

# **Fluxes of the NO-O<sub>3</sub>-NO<sub>2</sub> triad above a spruce forest canopy in south-eastern Germany**

A dissertation submitted to the  
FACULTY OF BIOLOGY, CHEMISTRY AND GEOSCIENCES,  
UNIVERSITY OF BAYREUTH

in partial fulfilment of the requirements of the degree of

DR. RER. NAT.

by

Anywhere Tsokankunku

MSc. Agricultural Meteorology

---

# **Fluxes of the NO-O<sub>3</sub>-NO<sub>2</sub> triad above a spruce forest canopy in south-eastern Germany**

A dissertation submitted to the  
FACULTY OF BIOLOGY, CHEMISTRY AND GEOSCIENCES,  
UNIVERSITY OF BAYREUTH

in partial fulfilment of the requirements of the degree of

DR. RER. NAT.

by

Anywhere Tsokankunku

MSc. Agricultural Meteorology

Supervisor:

Prof Dr. Thomas Foken

July 2014



Die vorliegende Arbeit wurde in der Zeit von Oktober 2009 bis März 2012 in Bayreuth an der Abteilung Mikrometeorologie unter Betreuung von Herrn Prof. Dr. Thomas Foken angefertigt.

Vollständiger Abdruck der von der Fakultät für Biologie, Chemie und Geowissenschaften der Universität Bayreuth genehmigten Dissertation zur Erlangung des akademischen Grades eines Doktor der Naturwissenschaften (Dr. Rer. Nat.).

Dissertation eingerichtsdatum 23.07.2014

Zulassung durch die Prüfungskommission: 06.08.2014

Wissenschaftliches Kolloquium: 17.11.2014

Dekan: Prof. Dr. Rhett Kempe

Prüfungsausschuss:

Prof Dr. Thomas Foken (*Erstgutachter*)

Prof Dr. Andreas Held (*Zweitgutachter*)

Prof Dr. Cyrus Samimi (*Prüfungsvorsitzender*)

Prof Dr. Anke Jentsch

## Summary

Nitrogen monoxide (NO) and nitrogen dioxide (NO<sub>2</sub>) (denoted together as NO<sub>x</sub>) are important compounds for the regulation of the tropospheric photochemical oxidant ozone (O<sub>3</sub>). Although they account for less than one millionth of the total constituents of the atmosphere, they play an important role in the composition and chemical processes of the atmospheric boundary layer. They affect the distribution of tropospheric O<sub>3</sub> and its natural background levels, which plays an active role in air pollution. Together the three reactive trace gases NO, NO<sub>2</sub> and O<sub>3</sub> undergo a series of interconnected reactions and are often referred to as the NO-O<sub>3</sub>-NO<sub>2</sub> triad. This triad has attracted attention from scientists in the recent past because of the role that it plays in causing problems such as acid rain, eutrophication of water bodies, and air pollution.

Within the global tropospheric O<sub>3</sub> budget the low NO<sub>x</sub> concentration levels over large rural forest ecosystems (0.2-10 ppb) are assumed to be important potential counterparts to the high NO<sub>x</sub> concentration levels over industrialized urban areas (10-1000 ppb). Being able to directly and simultaneously measure the concentrations of the triad and their corresponding biosphere-atmosphere exchange fluxes can give valuable information for policy makers and environmentalists about the NO<sub>x</sub>-O<sub>3</sub> budget of forest ecosystems and the troposphere.

The eddy covariance (EC) method is a well-known method for obtaining fast reliable fluxes within a large footprint and it has been successfully applied to measure CO<sub>2</sub> and water vapour fluxes for over fifty years. However, up to now, not many EC measurements of NO and NO<sub>2</sub> exchange fluxes above rural forest ecosystems have been conducted successfully because of a lack of analysers which meet the precision requirements for measuring the low concentrations of NO and NO<sub>2</sub> characteristic at these sites. The limit of detection of most available analysers is within the range of the measured concentration, making it impossible to resolve concentrations. Moreover, a lack of fast analysers and suitable photolytic converters until the last decade has also hindered progress in the turbulent measurement of these trace gases to obtain fluxes. Another problem is that the NO-O<sub>3</sub>-NO<sub>2</sub> triad are reactive trace gas compounds and the measurements of their fluxes tend to get affected by chemical transformations during turbulent transport.

To solve these problems, a unique approach was taken using a novel, fast (5 Hz), high precision, highly specific, 2-channel NO analyser to conduct EC flux measurements of NO and NO<sub>2</sub>. This analyser was deployed during the summer of 2008 in a spruce forest stand at the FLUXNET research site Waldstein-Weidenbrunnen (DE-Bay) in the rural Fichtelgebirge mountain range in north-eastern Bavaria, Germany, within the scope of the DFG-funded project EGER (Exchange Processes in Mountainous Regions). EC flux measurements of NO, NO<sub>2</sub> and also O<sub>3</sub> were conducted on a walk-up tower 32 m above ground level (9 m above the forest canopy) . For the first time in a spruce forest in central Europe, simultaneous EC fluxes of the NO-O<sub>3</sub>-NO<sub>2</sub> triad were measured. CO<sub>2</sub> and H<sub>2</sub>O EC fluxes were also measured as they were important for the verification of the EC method in use and for an insight into the biological response of the forest.

Vertical concentration profiles of NO, NO<sub>2</sub>, O<sub>3</sub>, CO<sub>2</sub> and H<sub>2</sub>O above (25m, 32m) and below the canopy (0.005 m, 1.000 m) were measured by an independently operated but simultaneously operational profile system. Profiles of

meteorological data were also available. From these profile measurements, concentration differences between 25 and 32 m above the forest were evaluated, from which fluxes using the aerodynamic gradient method (AGM) and the Modified Bowen Ratio (MBRM) were calculated for comparison with the EC fluxes.

A period of four ‘golden days’ of excellent meteorological conditions was chosen for data evaluation. Since I was dealing with very low concentrations of trace gases, data quality assessment and control was crucial and was applied using reliable state-of-the-art tools. Spectral analysis showed minimal flux losses at high frequency. However, cut-off frequencies for NO (1.11 Hz), and NO<sub>2</sub> (1.17 Hz), were higher than for O<sub>3</sub> (0.79 Hz) and the nonreactive trace gases – an indication of high frequency damping due to the long tubes from the tower to the NO/NO<sub>2</sub> analyser on the ground. Flux losses for the period 1100-1330 CET were acceptably low (NO: 2.1%, NO<sub>2</sub>:7.5%, O<sub>3</sub>: 1.8%). This result was a good indication of the good response and high quality of the measurement sensors. The losses were corrected for during data post-processing

During the golden days, fluxes of reactive and nonreactive trace gases showed distinct diurnal patterns. Between 0600 and 1200 CET, there was a distinct rise in the concentration and fluxes of all trace gases. This was attributed to external sources of the trace gases being advected to the site from the surrounding country roads. The NO flux was unexpectedly directed downwards throughout the day, ranging from -1.75 to 0.00 nmol m<sup>-2</sup> s<sup>-1</sup>. NO<sub>2</sub> flux was positive throughout, ranging from 0.0 to a maximum of 1.5 nmol m<sup>-2</sup> s<sup>-1</sup> at 1400 CET. The O<sub>3</sub> flux was directed into the canopy throughout the day, ranging from a minimum of 0 to a maximum of 20 nmol m<sup>-2</sup> s<sup>-1</sup> around 1100 CET. The strong peak of NO during the early to mid-morning period and the persistence of the NO<sub>2</sub> flux throughout the day was a strong indicator of the existence of an external source of NO<sub>x</sub> being advected towards the canopy from a nearby country road.

The relation between turbulent and chemical time scales (Damköhler numbers) and segregation intensities (indicators of the extent of mixing between chemical species by turbulence) suggest that there was a minimal influence of chemistry on above canopy fluxes of the NO-O<sub>3</sub>-NO<sub>2</sub> triad during the day. Although minimal, the chemistry might have been enough to create the NO sink evident in the above canopy fluxes. There is evidence of night-time conversion of soil biogenic NO to NO<sub>2</sub> as well as the possible formation of nitrous acid (HONO) and nitric acid (HNO<sub>3</sub>) below the canopy through heterogeneous processes in the presence of dew and fog. Vertical gradients and estimated fluxes below the forest canopy showed that the O<sub>3</sub> sink is so strong that none of the NO from the soil manages to reach the top of the canopy. The entire NO observed above the canopy is most likely due to horizontal advection and photochemical production.

This dissertation has proven that reliable, fast turbulent measurements of NO and NO<sub>2</sub> can be simultaneously made above a forest canopy. It has also demonstrated the importance of quality control and precision on reactive trace gas flux measurements. For central European forests with low soil NO emissions under moderate pollution, the forest canopy acts as a net source of NO<sub>2</sub> and a net sink of NO and O<sub>3</sub>. Issues such as advection make the evolution of the NO-O<sub>3</sub>-NO<sub>2</sub> triad in the trunk space a complicated issue to fully understand without additional, rigorous on-site measurements and analysis. Additional work should look at the possibility of partitioning the in-canopy and above canopy flux of the triad as well as reformulating the Damköhler number to include an advection term.

## Zusammenfassung

Stickstoffmonoxid (NO) und Stickstoffdioxid (NO<sub>2</sub>) (in der Summe als NO<sub>x</sub> bezeichnet) sind wichtige Verbindungen für die Regulierung von Ozon (O<sub>3</sub>) in der Troposphäre. Obwohl sie weniger als ein millionstel der gesamten Atmosphäre ausmachen, spielen sie eine wichtige Rolle für die Zusammensetzung und chemischen Prozesse der atmosphärischen Grenzschicht. Sie beeinflussen die Verteilung von troposphärischem O<sub>3</sub> und dessen natürliche Hintergrundkonzentration, was im Zusammenhang mit der Luftverschmutzung von großer Bedeutung ist. Zusammen gehen die drei reaktiven Spurengase eine Reihe von untereinander verbundenen Reaktionen ein und werden daher meist als NO-O<sub>3</sub>-NO<sub>2</sub>-Triade bezeichnet. Diese Triade hat in der jüngsten Vergangenheit aufgrund ihrer Rolle bei der Entstehung von Umweltproblemen wie saurem Regen, Eutrophierung von Gewässern oder Luftverschmutzung die besondere Aufmerksamkeit von Wissenschaftlern erlangt.

Im Hinblick auf das globale Vorkommen von troposphärischem O<sub>3</sub> werden niedrige NO<sub>x</sub>-Konzentrationen über großen Waldökosystemen (0.2-10 ppb) als wichtige mögliche Gegenstücke zu den hohen NO<sub>x</sub>-Konzentrationen über industrialisierten, urbanen Regionen (10-1000 ppb) gesehen. Die Möglichkeit die Spurengaskonzentrationen der Triade direkt und gleichzeitig zu messen sowie deren Biosphären-Atmosphären Austauschflüsse zu bestimmen, kann Umweltschützern und politischen Entscheidungsträgern wichtige Informationen über das NO<sub>x</sub>-O<sub>3</sub>-Budget in Waldökosystemen und der Troposphäre liefern.

Die Eddy-Kovarianz-Methode (EC) ist eine etablierte Methode, welche zeitlich hochaufgelöste und verlässliche Austauschflüsse über einen großen sog. „Footprint“ liefert und welche erfolgreich seit über 50 Jahren zur Bestimmung von CO<sub>2</sub>- und Wasserdampfströmen herangezogen wird. Allerdings wurden bisher nur wenig EC-Messungen zur Bestimmung von NO und NO<sub>2</sub> Flüssen über ländlichen Waldökosystemen durchgeführt, aufgrund eines Mangels an Gasanalysatoren, welche die Genauigkeitsanforderungen zur Messung von geringen NO- und NO<sub>2</sub>-Konzentrationen an solchen Standorten erfüllen. Die Nachweisgrenze vieler verfügbarer Gasanalysatoren ist im Bereich der gemessenen Konzentrationen, die daher nicht aufgelöst werden können. Zudem hat ein Mangel an schnellen Gasanalysatoren und an geeigneten photolytischen Konvertern zur NO<sub>2</sub>-Photolyse noch bis in das letzte Jahrzehnt den Fortschritt von Turbulenzmessungen dieser Spurengase für Flussmessungen gehindert. Ein weiteres Problem ist, dass die NO-O<sub>3</sub>-NO<sub>2</sub>-Triade aus reaktiven Spurengasen besteht, deren Flüsse durch chemische Umwandlungen während des turbulenten Austausches beeinflusst werden können.

Um diese Probleme zu lösen, wurde ein einzigartiger Ansatz verfolgt, bei dem ein neuer, zeitlich hochauflösender (5 Hz), äußerst genauer und hoch spezifischer Doppelkanal-NO-Analysator zur Messung von NO und NO<sub>2</sub>-Flüssen mit der EC-Methode verwendet wurde. Dieser Gasanalysator wurde im Sommer 2008 in einem Fichtenwaldbestand des Waldstein-Weidenbrunnen-Forschungsstandortes (DE-Bay) des FLUXNET-Netzwerkes im Fichtelgebirge im Nordosten Bayerns im Rahmen des DFG-Projekts EGER (Exchange Processes in Mountainous Regions) eingesetzt. Eddy-Kovarianz-Flussmessungen von NO, NO<sub>2</sub> und auch O<sub>3</sub> wurden an einem begehbaren, 32 m hohen Messturm (Höhe entspricht 9 m über dem Fichtenbestand) durchgeführt. . Zum ersten Mal wurden in einem Fichtenbestand in Mitteleuropa zeitgleich die EC-Flüsse der NO-O<sub>3</sub>-NO<sub>2</sub>-Triade gemessen. Daneben wurden die Austauschflüsse von

CO<sub>2</sub> and H<sub>2</sub>O gemessen, da sie wichtig für die Überprüfung der angewandten EC-Methode waren und Erkenntnisse über die biologischen Reaktionen des Fichtenbestandes lieferten.

Vertikale Profile der Spurengaskonzentrationen von NO, NO<sub>2</sub>, O<sub>3</sub>, CO<sub>2</sub> und H<sub>2</sub>O wurden über (32 m, 25 m) und innerhalb des Fichtenbestandes (1.000 m, 0.005 m) mit einem gleichzeitig aber unabhängig betriebenen Profilsystem gemessen. Aus den Profilmessungen konnten als Vergleich zu den EC-Messungen Austauschflüsse anhand der Konzentrationsdifferenzen zwischen 25 und 32 m mittels der Aerodynamischen Gradientenmethode (AGM) und der Modifizierten Bowen-Verhältnismethode (MBRM) bestimmt werden.

Eine Zeitspanne von vier Tagen mit exzellenten meteorologischen Bedingungen („golden days“) wurde zur Datenauswertung herangezogen. Für jede 30 min Periode wurden die EC-Flüsse mit einem Flussqualitätskriterium belegt, wobei nur die Flüsse mit der höchsten Qualität verwendet wurden. Eine Analyse der Spektralanteile der turbulenten Flüsse zeigte nur einen minimalen Flussverlust im hochfrequenten Bereich des Frequenzspektrums. Allerdings waren die Grenzfrequenzen für NO (1.11 Hz) und NO<sub>2</sub> (1.17 Hz) größer als für O<sub>3</sub> (0.79 Hz) und die nicht-reaktiven Spurengase – ein Hinweis für Dämpfungen hoher Frequenzen aufgrund der langen Einlassleitung von dem Messturm zu dem NO/NO<sub>2</sub>-Analysator am Boden. Die Flussverluste für die Zeitperiode von 1100 bis 1330 MEZ waren annehmbar gering (NO: 2.1%, NO<sub>2</sub>:7.5%, O<sub>3</sub>: 1.8%). Dies ist ein guter Hinweis auf die schnelle Ansprechzeit und gute Qualität der Messtechnik. Die Flussverluste wurden im Rahmen der Datenauswertung korrigiert.

Während der „golden days“ zeigten die Flüsse der reaktiven und nicht reaktiven Spurengase einen deutlichen Tagesgang. Zwischen 0600 und 1200 MEZ war in den Konzentrationen und Flüssen aller Spurengase ein deutlicher Anstieg zu beobachten. Dies war auf externe Spurengasquellen durch Landstraßen in der Umgebung zurückzuführen, von wo Spurengase an den Messstandort transportiert wurden. Tagsüber war der NO-Fluss unerwarteterweise abwärts gerichtet mit Werten zwischen -1.75 und 0.00 nmol m<sup>-2</sup> s<sup>-1</sup>. Der NO<sub>2</sub>-Fluss war tags positiv und erstreckte sich von 0 bis zu einem Maximum von 20 nmol m<sup>-2</sup> s<sup>-1</sup> gegen 1100 MEZ. Die hohen NO-Konzentrationen am Morgen nach Sonnenaufgang und die stetige NO<sub>2</sub>-Deposition über den ganzen Tag waren ein deutlicher Indikator für die Existenz einer externen NO<sub>x</sub>-Quelle.

Das Verhältnis von turbulenten und chemischen Zeitskalen (Damköhlerzahlen) und die Trennungsintensitäten (Indikatoren für das Ausmaß der Vermischung zwischen chemischen Spezies durch Turbulenzen) lassen darauf schliessen, dass tagsüber ein minimaler Einfluss von chemischen Reaktionen auf die Flüsse der NO-O<sub>3</sub>-NO<sub>2</sub>-Triade über dem Bestand gegeben war. Obwohl der Einfluss gering war, ist es möglich, dass chemische Reaktionen für die NO-Senke verantwortlich waren, welche durch die über dem Fichtenbestand gemessenen Flüsse aufzeigt wurde. Es gibt Hinweise für die Umwandlung von biogenem NO, welches aus Böden emittiert wird, zu NO<sub>2</sub> bei Nacht sowie für die mögliche Bildung von salpetriger Säure (HONO) und Salpetersäure (HNO<sub>3</sub>) im Fichtenbestand durch heterogene Prozesse beim Vorhandensein von Tau und Nebel. Die vertikalen Gradienten im Fichtenbestand und die über dem Waldboden abgeschätzten Spurengasflüsse zeigen, dass der abwärtsgerichtete Transport von O<sub>3</sub> in den Bestand so stark ist, dass vom Boden emittiertes NO zu NO<sub>2</sub> umgewandelt wird bevor es den obersten Teil des Bestandes erreicht. Das gesamte NO, welches über dem Fichtenbestand beobachtet wurde, ist höchstwahrscheinlich auf horizontale Advektion und auch photochemische Produktion zurückzuführen.

Diese Dissertation hat gezeigt, dass zuverlässige und schnelle Messungen von NO und NO<sub>2</sub> zur Bestimmung von turbulenten Spurengasflüssen zeitgleich durchgeführt werden können. Ebenso unterstreicht sie die Wichtigkeit der Kontrolle der Datenqualität und der Genauigkeit von Flussmessungen reaktiver Spurengase. Für Waldökosysteme mit geringen Boden NO-Emissionen in Mitteleuropa bei gemäßigter Luftverschmutzung stellt der Waldbestand eine Netto-Quelle für NO<sub>2</sub> und Netto-Senke für NO und O<sub>3</sub> dar. Probleme wie Advektion machen die Entwicklung der NO-O<sub>3</sub>-NO<sub>2</sub>-Triade im Stammbereich zu einem komplizierten Punkt, der ohne zusätzliche, umfassende Feldmessungen und Analysen nicht vollständig verstanden werden kann. Weitere Studien sollten die Möglichkeit der Zerlegung der Spurengasflüsse der Triade in ihre Anteile in und über dem Bestand betrachten sowie sich mit der Berücksichtigung eines Advektionsterms in der Damköhlerzahl beschäftigen.

## Acknowledgements

The idea to do a PhD was first put in my mind by Dr Ivonne Trebs and Dr Franz Meixner while on a visit to the University of Zimbabwe when I was writing my MSc thesis in 2006. It became a reality when I came to the Max Planck Institute for Chemistry to do my PhD research one and a half years later. I thank them both for the interesting PhD topic and the opportunity that they gave me to work with them in the biogeochemistry department. I thank them also for making me feel welcome during my early days in Germany. I thank Dr Meixner for his guidance and patience which was important in bringing this thesis to an end. I would like to express my sincere gratitude to the Max Planck Society through the International Max Planck Research School for funding the major part of my research through a scholarship and for providing world class research facilities.

I also thank Professor Thomas Foken who led the EGER project. I thank him also for his large contribution of ideas, guidance and suggestions for the major part of this thesis.

This thesis would not have been completed successfully without the contributions of Prof. Dr. Zhilin Zhu, Alexander Moravek and Daniel Plake. Zhilin Zhu provided the EC ozone fluxes while Alexander Moravek and Daniel Plake measured and provided the trace gas profile data that I used in this thesis. I also thank them for their friendship and welcoming attitude during my time in Mainz. I shall remember with fondness the many beers that we had together. I thank Michael Welling for some technical help. I also thank the University of Bayreuth crew who provided some of the meteorological data, SODAR data, and additional eddy covariance measurements from their Turbulence Tower.

The EGER measurement campaigns would have been dull and boring without the EGER crew. I thank them all for making the ever cold and wet days of the measurement periods seem warm with their warmth and friendliness.

I thank Alexander Moravek and Linda Voss for translating my summary and reading my draft, and Jens Mayer and Daniel Plake for reading earlier drafts of my thesis.

I thank my family in Zimbabwe, especially my mother for always giving me chance to explore my abilities and for teaching me how to be strong, patient, persevering and God-fearing. Their words of encouragement over the distance kept me going.

A big thank you goes to my wife Candy whose encouragement, love, patience and positivity kept me going especially during those periods when I could not see the light at the end of the tunnel.

Finally I would like to thank God who makes all things possible even when all hope is gone.

# Contents

<b>Summary</b> .....	iii
<b>Zusammenfassung</b> .....	v
<b>Acknowledgements</b> .....	viii
<b>Contents</b> .....	ix
<b>Chapter 1: Introduction</b> .....	1
1.1 Preamble .....	1
1.2 Motivation and background to the research.....	1
1.2.1 Chemistry of the NO-O <sub>3</sub> -NO <sub>2</sub> triad in the atmospheric boundary layer .....	3
1.2.2 Trace gas flux measurement techniques .....	9
1.3 Previous research on NO-O <sub>3</sub> -NO <sub>2</sub> triad fluxes.....	10
1.4 Research questions.....	14
1.5 Objectives of research.....	14
1.6 Challenges.....	15
1.7 Thesis outline .....	16
<b>Chapter 2: Theory</b> .....	18
2.1 Introduction.....	18
2.1.1 The atmospheric boundary layer.....	18
2.1.2 The Monin-Obukhov Similarity Theory .....	21
2.1.3 Exchange processes within and above a forest .....	22
2.1.4 Overview of trace gas measurement techniques .....	25
2.1.5 General requirements for flux measurements .....	27
2.2 Gradient Methods.....	28
2.2.1 Aerodynamic Gradient Method .....	28
2.2.2 Modified Bowen Ratio Method .....	30
2.2.3 Experimental Realization.....	31
2.2.4 Data Quality .....	34
2.3 Eddy Covariance Method .....	35
2.3.1 Theory .....	37
2.3.2 Experimental realisation .....	40
2.3.3 Data quality .....	42

---

2.4 Role of chemical reactions on the fluxes .....	47
2.4.1 Turbulence and chemical timescales – the Damköhler number.....	47
2.4.2 Intensity of segregation of the NO-O <sub>3</sub> -NO <sub>2</sub> triad.....	49
2.5 Designing the experiments.....	50
<b>Chapter 3: Experimental site and setup .....</b>	<b>51</b>
3.1 Site description.....	51
3.1.1 Location .....	51
3.1.2 Climate.....	51
3.2 Trace gas measurements .....	52
3.3 Experimental setup.....	53
3.4 Trace gas EC measurement instrumentation.....	54
3.4.1 NO and NO <sub>2</sub> – the CLD 790SR2 NO <sub>x</sub> analyser .....	56
3.4.2 Measurement of O <sub>3</sub> .....	62
3.4.3 Measurement of CO <sub>2</sub> and H <sub>2</sub> O.....	63
3.5 Data acquisition system .....	63
3.6 Supporting measurements.....	65
3.6.1 Trace gas profile measurements above and below the canopy .....	65
3.6.2 Meteorological profile measurements.....	65
3.6.3 EC measurements of CO <sub>2</sub> and H <sub>2</sub> O on the Turbulence Tower .....	66
3.7 System Operation and Maintenance .....	67
3.7.1 Calibration.....	67
3.7.2 Routine logging of instrument operational parameters.....	68
3.7.3 Changing of filters .....	69
3.7.4 Checking the alignment bubble level of CSAT3 .....	69
3.7.5 Changing of O <sub>3</sub> discs.....	69
3.8 Evaluation of above-canopy EC data.....	69
3.8.1 Data processing and quality assurance.....	70
3.9 Evaluation of above-canopy vertical profile data .....	74
3.9.1 Evaluation of absolute vertical profile data .....	75
3.9.2 Evaluation of vertical mixing ratio differences.....	75
3.10 Analysis and interpretation of the net fluxes of the reactive trace gases .....	79
3.10.1 Above canopy fluxes.....	79
3.10.2 Below canopy (1 m).....	80
<b>Chapter 4: Results and Discussion .....</b>	<b>81</b>
4.1 Data availability .....	81
4.2 Atmospheric conditions during measurement period .....	81

4.3	Variation of trace gas mixing ratios during IOP-2 golden days.....	85
4.3.1.	Weekdays .....	86
4.3.3	Weekend .....	88
4.3.3	Variation of the mixing ratios with wind direction.....	91
4.4	Evaluation of the trace gas fluxes using gradient methods .....	93
4.4.1	Precision of trace gas analysers – the sigma criteria.....	93
4.4.2	Distribution of vertical concentration differences.....	95
4.4.3	Applicability of the discontinuous sampling method for finding concentration differences.....	97
4.4.4	Gradient-derived fluxes.....	100
4.4.5	Limitations and shortfalls of the gradient methods.....	103
4.5	Evaluation of the trace gas fluxes using the EC method.....	103
4.5.1	Comparison of EC parameters .....	103
4.5.2	Turbulence spectra .....	107
4.5.3	Quality flags of fluxes.....	113
4.5.4	Error limits for EC fluxes.....	114
4.5.5	Diel variation of the EC fluxes .....	119
4.6	Comparison of gradient methods to the EC standard.....	121
4.7	Effect of transport and chemistry on the reactive trace gas fluxes.....	123
4.7.1	Forest-atmosphere coupling .....	124
4.7.2	Characteristic timescales of the NO-O <sub>3</sub> -NO <sub>2</sub> triad.....	126
4.7.3	Damköhler numbers .....	127
4.7.4	Intensity of segregation between NO and O <sub>3</sub> .....	129
4.8	Trace gas fluxes at the forest floor.....	130
4.9	Fluxes of O <sub>3</sub> , NO <sub>2</sub> and NO under low NO <sub>x</sub> advection conditions on 29 <sup>th</sup> of June 2008.....	136
4.9.1	Atmospheric conditions .....	136
4.9.2	Trace gas vertical concentration differences and absolute concentrations.....	138
4.9.3	Chemical and turbulent driving forces.....	138
4.9.4	Fluxes.....	142
<b>Chapter 5:</b>	<b>Summary and Conclusions .....</b>	<b>147</b>
5.1	Summary of data availability .....	148
5.2	Summary of atmospheric conditions during the experiment .....	148
5.3	Summary of mixing ratios of the NO-O <sub>3</sub> -NO <sub>2</sub> triad .....	149
5.4	Summary of EC fluxes.....	149
5.5	Summary of AGM and MBRM fluxes .....	151
5.5.1	Above-canopy (32 m – 25 m) .....	151
5.5.2	Below canopy (1 m – 0.005 m).....	151

5.6 Summary of chemical and turbulent effects on the net trace gas fluxes above the canopy .....	152
5.7 Conclusions.....	153
5.8 New contributions to science .....	155
5.9 Recommendations.....	155
<b>References</b> .....	157
<b>Appendices</b> .....	168
A1: Roughness sublayer enhancement factors.....	168
A2: Segregation intensities .....	169
A3: Mixing ratio profiles .....	171
<b>Table of abbreviations</b> .....	177
Abbreviations.....	177
Roman Symbols .....	179
Greek symbols .....	182
<b>(Eidesstattliche) Versicherungen und Erklärungen</b> .....	184

# Chapter 1: Introduction

## 1.1 Preamble

The thesis focuses on concentration and surface exchange flux measurements of the reactive trace gases nitrogen monoxide (NO), nitrogen dioxide (NO<sub>2</sub>) and ozone (O<sub>3</sub>) which were made above a 55 year old spruce forest canopy at a FLUXNET (Baldocchi et al, 2000) research site called Waldstein-Weidenbrunnen (FLUXNET name DE-Bay; ((50° 08'31" N, 11° 52'1"E, elevation 755 m a.s.l)) in the rural Fichtelgebirge mountains in north-eastern Bavaria, Germany. The Fichtelgebirge is a low mountain range characteristic of the mid-European region. The measurements were made as part of the EGER (Exchange Processes in Mountainous Regions) project. The EGER project (Foken et al., 2012) aims at the detailed quantification of exchange processes within the soil-vegetation-atmosphere (SVAT) system by observing diurnal and annual cycles of energy, water and trace gases. The main focus lies on the understanding of process interactions among different scales and their role for corresponding budgets.

This work is a part of one of the EGER subprojects that investigates canopy cycling of CO<sub>2</sub>, water vapour and reactive trace gases by undertaking flux measurements and plant ecology modelling. This dissertation in particular investigates the exchange processes of the reactive trace gases NO, NO<sub>2</sub> and O<sub>3</sub> above the forest canopy at the Weidenbrunnen research site.

## 1.2 Motivation and background to the research

Understanding forest ecosystems has been the focus of ecologists, micrometeorologists, biologists and atmospheric chemists since the last century because of the challenge that it presents. Hutchinson and Hicks (1985) emphasized the very complex character of forest-atmosphere exchange and the challenges faced in trying to understand it (such as counter-gradients) were publicised by Denmead and Bradley (1985). The roughness sublayer (Garratt, 1978, 1980, 1983) and the mixing layer hypothesis (Finnigan, 2000) have also become important topics to consider in understanding forest-atmosphere exchange. The mixing layer theory, which has recently been successfully unified with the roughness sublayer theory (Harman and Finnigan, 2007, 2008), is closely related to coherent structures (Collineau and Brunet, 1993b; Katul et al., 1997) which generate characteristic ramp-like structures observed in the time series of scalar quantities measured above a forest canopy. These structures are caused by Kelvin-Helmholtz instabilities (Helmholtz, 1868; Kelvin, 1871) due to extreme shearing above the top of the aerodynamically rough forest and have also been detected in trace gas concentrations (Rummel et al., 2002c).

The direct, fast-response eddy covariance method (Aubinet et al., 2000) is state-of-the-art for the measurement of turbulent fluxes of momentum, sensible heat, water vapour and carbon dioxide. Slow response flux measurement methods like the Aerodynamic Gradient Method (Arya, 2001; Monteith and Unsworth, 1990) or the Modified Bowen Ratio Method (Businger, 1986; Liu and Foken, 2001; Müller et al., 1993; Meyers et al., 1996) have been applied for most trace gases and aerosol particles. Advancements within the last decade have however seen the eddy covariance method becoming applicable for aerosol particles and a few trace gases, particularly nitrous oxide (N<sub>2</sub>O), methane (CH<sub>4</sub>), ozone (O<sub>3</sub>), nitric oxide (NO) and nitrogen dioxide (NO<sub>2</sub>) (e.g. (Farmer and Cohen, 2008; Fuentes et al., 2007; Horii et al., 2004; Rummel et al., 2002a; Rummel et al., 2007)).

The exchange of energy and carbon dioxide in and above tall vegetation has already been formulated using micrometeorological theories in such a way that associated occurrences like the roughness sublayer and mixing layers (Finnigan, 2000; Raupach et al., 1996), coherent structures (Collineau and Brunet, 1993b, a), as well as advection (Aubinet et al., 2003a; Lee, 1998) could be detected. Improved understanding of turbulence structures in and above forest canopies still necessitates the study of coherent structures in greater detail. Additionally, as shown by Raupach and Thom (1981) and Bergström and Högström (1989), coherent events of low frequency contribute considerably to the budgets of momentum, heat and trace gas constituents in and above forest canopies. Moreover, Karipot et al. (2008; 2006) found that low-level jets (vertical bands of strong winds in the lower part of the atmospheric boundary layer), which have a significant effect on the night time exchange of a forest, increase turbulence and mixing close to the ground due to increased shear.

Consequently part of the focus of this study was to investigate the contribution of coherent structures to the transfer of reactive trace gas compounds (nitric oxide (NO), nitrogen dioxide (NO<sub>2</sub>) and ozone (O<sub>3</sub>)).

An important aspect of atmospheric budgets of trace gases is the ability of forest canopies to take up trace gases, which are biogenically emitted by plants and/or by the soil below (Ganzeveld et al., 2002). Generally the amount of absorbed/escaping trace gases is regulated by the

- (a) physiological and/or surface characteristics of forest vegetation and soils and
- (b) interaction of turbulent transport (in and above canopy) with processes of the gas exchange itself as well as with atmospheric conversions of chemically reactive trace compounds.

This is principally valid for reactive nitrogen and carbon species and, as shown very recently, also for related compounds like radicals and peroxides (e.g. (Farmer and Cohen, 2008; Karl et al., 2010; Wolfe et al., 2011a; Wolfe et al., 2011b)). This issue can be concentrated on the question of coupling, namely how strongly is the entire forest-atmosphere (or parts of it) coupled to or decoupled from the surface layer above the canopy. This has substantial consequences for the mean residence time (hence the in-

canopy recycling) of trace gases (Aubinet et al., 2003b; Meixner et al., 2003). Weakly coupled (decoupled) situations, resulting in longer residence times, generally favour the efficiency of reactions and transformations between chemically reactive trace gases (e.g. triads of NO-O<sub>3</sub>-NO<sub>2</sub>). The limiting factor on the temporal scales to be considered originates from the Damköhler number (Damköhler, 1940), a ratio of two particular timescales, namely the characteristic turbulent transport time over the characteristic chemical reaction time (see 1.2). For the investigation of in-canopy storage, canopy coupling, and whole ecosystem exchange of reactive trace gases, measurements of vertical profiles of concentrations and fluxes are essential. While methodologies to measure vertical concentration profiles for NO, NO<sub>2</sub>, O<sub>3</sub>, NH<sub>3</sub>, HONO, HNO<sub>3</sub> (NH<sub>4</sub><sup>+</sup>, NO<sub>3</sub><sup>-</sup>) are state-of-the-art (Trebs et al., 2004), flux measurements of these compounds by the eddy covariance method have been (and still are) hampered by the unavailability of fast and specific chemical sensors. However, (Rummel et al., 2002b) have demonstrated functioning eddy covariance flux measurements of NO by applying a specific and fast chemiluminescence analyser. Horii et al. (2004) applied operational eddy covariance flux measurements of NO and NO<sub>x</sub> over a temperate deciduous forest.

Against this background, I will give an account of the results of the field measurements that I did within and during the EGER project, their design, the applied methods, and particularly the results from the second of the intensive observation periods (IOPs) which were IOP-1 (September-October 2007) and IOP-2 (June-July 2008). In IOP-2, the emphasis of the analysis was on (Foken et al., 2012) the coupling between above-canopy atmosphere and different layers in the canopy due to coherent structures and special atmospheric phenomena and its consequences for (i) the structure of the turbulent exchange (ii) the above-canopy fluxes (iii) the timescales of turbulent transport and chemical reactions, (iv) the concentration gradients of non-reactive and reactive trace gases between the top of the canopy and forest floor, and (v) the consequences for model parameterisations.

My main role was to investigate (ii), (iii) and (iv) for the NO, NO<sub>2</sub> and O<sub>3</sub> system of trace gas compounds (commonly referred to as the NO-O<sub>3</sub>-NO<sub>2</sub> triad).

### **1.2.1 Chemistry of the NO-O<sub>3</sub>-NO<sub>2</sub> triad in the atmospheric boundary layer**

The lowest part of the atmosphere influenced directly by the Earth's surface is called the atmospheric boundary layer (ABL). The gas-phase chemistry of the ABL involves the chemical and photochemical oxidation of organic molecules in the presence of nitrogen oxides and sunlight. Atmospheric oxidation involves a very dilute driving medium, at mixing ratios of parts per million (ppm) or parts per billion (ppb). Because of these very low concentrations, an external source of energy, provided by the sun, is required to drive the reactions. In the urban and continental ABL, a large number of other anthropogenic and biogenic hydrocarbons and organic species are present. As a result of combustion emissions, greatly enhanced levels of nitrogen oxides over those in the background ABL exist in

urban and continental areas. Table 1.1 shows the relative concentrations of  $\text{NO}_x$  ( $\text{NO}+\text{NO}_2$ ) for different regions.

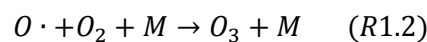
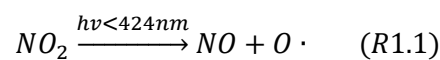
**Table 1.1.** Typical ABL mixing ratios of  $\text{NO}_x$  ( $\text{NO}+\text{NO}_2$ ). The bold font indicates the characteristics of the measurement site. After Seinfeld and Pandis (1998).

Region	$\text{NO}_x$ (ppb)
Urban-suburban	10-1000
<b>Rural</b>	<b>0.2-10</b>
Remote tropical forest	0.02-0.08
Remote Marine	0.02-0.04

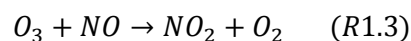
The nitrogen oxides  $\text{NO}$  and  $\text{NO}_2$  (denoted together as  $\text{NO}_x$ ) are important compounds for the regulation of the photochemical oxidant  $\text{O}_3$  in the ABL (Crutzen, 1979; Dickerson et al., 1979).

Although the reactive trace gas compounds  $\text{NO}$  and  $\text{NO}_2$  account for less than one thousandth of the total constituents of the atmosphere, they play an important role in the composition of and chemical processes in the atmosphere. They have an effect on the distribution of tropospheric ozone and its natural background levels, which plays – aside from the well-known role of ozone in the stratosphere – an important role in global warming. Together the three reactive trace gases  $\text{NO}$ ,  $\text{NO}_2$  and  $\text{O}_3$  undergo a series of interconnected reactions and are often referred to as the  $\text{NO}-\text{O}_3-\text{NO}_2$  triad. The  $\text{NO}-\text{O}_3-\text{NO}_2$  triad has attracted attention from scientists in the recent past because of the role that it plays in causing environmental problems such as acid rain ( $\text{HNO}_3$ , -formed by the oxidation of  $\text{NO}_2$  by  $\text{OH}$ , see equation R1.15), respiratory problems, and air pollution.

When  $\text{NO}$  and  $\text{NO}_2$  are present under sunlit conditions,  $\text{O}_3$  formation occurs as a result of the photolysis of  $\text{NO}_2$  at wavelengths  $< 424 \text{ nm}$  (Seinfeld and Pandis, 1998).



where  $\text{M}$  represents  $\text{N}_2$  or  $\text{O}_2$  or another third molecule that absorbs the excess vibrational energy and thereby stabilizes the  $\text{O}_3$  molecule formed. There are no significant sources of ozone in the atmosphere other than reaction R1.2 (Seinfeld and Pandis, 1998). Once formed,  $\text{O}_3$  reacts with  $\text{NO}$  to generate  $\text{NO}_2$ .



During daytime, NO, NO<sub>2</sub> and O<sub>3</sub> establish equilibrium of their mixing ratios known as a photo stationary state (PSS) (Leighton, 1961). For the NO/NO<sub>2</sub> ratio, the PSS occurs when

$$\frac{[\text{NO}]}{[\text{NO}_2]} = \frac{J_{\text{NO}_2}}{k_1[\text{O}_3]} \quad (1.1)$$

[NO], [NO<sub>2</sub>] and [O<sub>3</sub>] are the mixing ratios of NO, NO<sub>2</sub> and O<sub>3</sub> respectively, J<sub>NO<sub>2</sub></sub> is the photolysis frequency parameterized from shortwave radiation according to (Trebs et al., 2009), and k<sub>1</sub> is the rate constant for R1.3. The degree of deviation away from PSS may indicate the presence of external sources or sinks of the triad constituents.

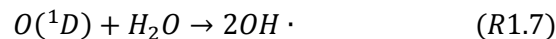
Photolysis of O<sub>3</sub> to produce both ground state O and excited singlet O(<sup>1</sup>D) oxygen atoms is important in the ABL (Seinfeld and Pandis, 1998),



The ground state O atom combines rapidly with O<sub>2</sub> by the second reaction to reform O<sub>3</sub>, so the first reaction followed by the second reaction has no net effect. However when O(<sup>1</sup>D) is produced, since the O(<sup>1</sup>D)→O transition is forbidden, it must react with another atmospheric species. Most often O(<sup>1</sup>D) collides with N<sub>2</sub> or O<sub>2</sub>, removing the excess energy and quenching O(<sup>1</sup>D) to its ground state,

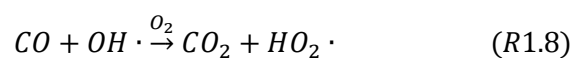


Since the O atom then just reacts with O<sub>2</sub> to replenish O<sub>3</sub>, this path consisting of reactions R1.4, R1.5, and R1.6, is a null cycle. Sometimes O(<sup>1</sup>D) collides with H<sub>2</sub>O and produces two hydroxyl radicals

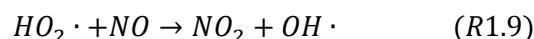


Because H<sub>2</sub>O is present in the lower troposphere at mixing ratios up to 10<sup>4</sup> ppm (1%) and because the reaction above has a rate constant about a factor of 10 larger than the quenching reaction with M=N<sub>2</sub> or O<sub>2</sub>, as much as 10% of the O(<sup>1</sup>D) produced reacts with H<sub>2</sub>O to generate OH. The OH radical is unreactive toward oxygen, and as a result, it survives to react with most atmospheric trace species.

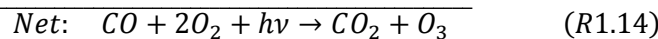
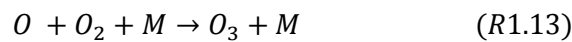
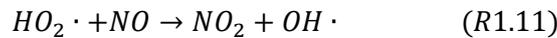
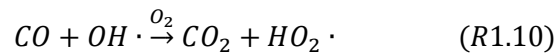
Carbon monoxide can react with the OH radical formed



When NO is present, the most important atmospheric reaction that the HO<sub>2</sub>· undergoes is with NO,



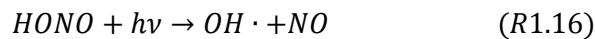
The atmospheric oxidation of CO<sub>2</sub> can then be summarized thus:



OH, HO<sub>2</sub>·, NO and NO<sub>2</sub> catalyse the oxidation of CO to CO<sub>2</sub>. Net O<sub>3</sub> formation is a by-product of the reaction. This is because the conversion of NO to NO<sub>2</sub> is performed by the HO<sub>2</sub>· rather than by O<sub>3</sub>. This set of reactions can occur repeatedly until one of the molecules is removed in a termination reaction. This occurs when either OH· reacts with itself or OH· and NO<sub>2</sub> react to form HNO<sub>3</sub>.



NO can be formed by the photolysis of HONO, which also produces OH· in the process. HONO is normally detected during night-time and is rapidly photolysed at wavelengths ≤400 nm during daytime to produce NO and OH· (Calvert et al., 1994),



HONO is formed by the reaction of OH· radicals with NO



HONO can also be formed by the reaction of NO<sub>2</sub> and water vapour (fog) (Jenkin et al., 1988).

For a forest, measuring the fluxes above the canopy gives an indication of the net trace gas exchange between the forest and the atmosphere. Within the global tropospheric ozone budget the low NO<sub>x</sub> concentration levels over large rural forest ecosystems (0.2-10 ppb) (see Table 1.1) are assumed to be important potential counterparts to the high NO<sub>x</sub> concentration levels over industrialized urban areas (10-1000 ppb) (Rummel et al., 2002a). Being able to directly and simultaneously measure the concentrations of the triad and their corresponding fluxes can give useful information about the NO<sub>x</sub>-O<sub>3</sub> budget above tall vegetation.

### **The Damköhler number**

Chemical reactions and turbulence simultaneously play a role in the exchange and transport of reactive trace gases in the atmosphere. The overall effect depends on the strength of the turbulence and that of the chemistry.

If atmospheric stability (the degree of vertical motion in the atmosphere) is neutral or near-neutral (Wyngaard et al., 1982),  $\tau_{turb}$ , the characteristic timescale of turbulence (characteristic residence time of an air parcel in an investigated air column) can be expressed according to Mayer et al. (2009). The chemical timescale (the lifetime of a species consumed in the respective reaction) for the whole NO-O<sub>3</sub>-NO<sub>2</sub> triad,  $\tau_{chem}$ , is defined according to Lenschow (1982).

The Damköhler number (Da), a dimensionless quantity being defined as the ratio of the characteristic timescales of turbulent transport to chemical reactions, for the NO-O<sub>3</sub>-NO<sub>2</sub> triad is represented as

$$Da = \frac{\tau_{turb}}{\tau_{chem}} \quad (1.2)$$

In order to determine a threshold below which there is certainty that there is no chemical influence during the transport process of reactive trace gases, a critical Damköhler number  $Da_{crit}$  can be defined. This is arbitrarily taken as 0.1 meaning that chemical transformations are proceeding at least ten times slower than turbulent processes for the data to be accepted as not having been influenced by chemistry. In the data quality check process, all data above  $Da_{crit}$  are flagged to ensure that all fluxes are not distorted by chemical influences.

### **Chemical processes in the soil which generate NO**

Fig. 1.1 shows the cycle of NO in the soil. Biogenic processes from soil microbes generate NO in the first few centimetres of the soil and release it. Nitrogen (N) is introduced into the soil via atmospheric deposition (through precipitation), by nitrogen fixing legumes, by industrial fixation e.g. Haber-Bosch process fertilizers (such as ammonium nitrate), and manure. Within the soil, the organic N components of manure, crop residues and soil organic matter are converted to inorganic N forms (ammonia (NH<sub>3</sub>) and ammonium (NH<sub>4</sub><sup>+</sup>)). The ammonia is then quickly converted to NH<sub>4</sub><sup>+</sup> in a process called *mineralisation*. Using enzymes, microbes in the soil convert NH<sub>4</sub><sup>+</sup> to NO<sub>2</sub><sup>-</sup> then immediately to NO<sub>3</sub><sup>-</sup> (nitrate) in a process called *nitrification*. This process is most rapid in the presence of warm, moist and well-aerated soil conditions.

*Denitrification* is the escape of N from the soil through the conversion of NO<sub>3</sub><sup>-</sup> into various gaseous forms of N. N<sub>2</sub> makes up 78% of the air we breathe while N<sub>2</sub>O and NO are greenhouse gases. Ammonia *volatilisation* occurs when ammonia gas (NH<sub>3</sub>) is produced from NH<sub>4</sub><sup>+</sup>. *Immobilisation* occurs when microbes consume the available N in the soil, making it part of their microbial biomass and making it temporarily unavailable. Leaching is the washing away of NO<sub>3</sub><sup>-</sup> below the root zone and is dependent on rainfall, soil drainage and concentration of NO<sub>3</sub><sup>-</sup> in the soil. Plants take up nitrates and NH<sub>4</sub><sup>+</sup> to form their own building blocks. The N is then consumed when the plants are harvested and eaten. Biomass burning also releases the N taken up by the plants back into the atmosphere in the form of NO and N<sub>2</sub>O.

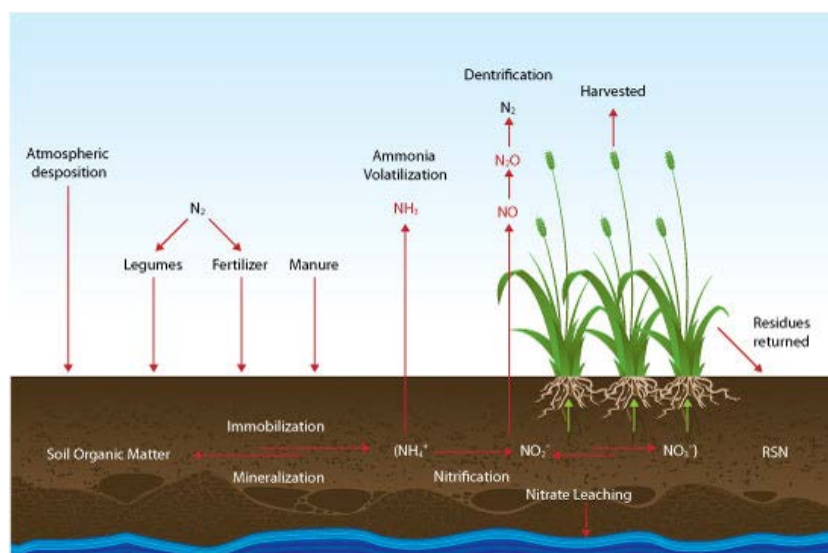


**Fig. 1.1.** Cycle of  $\text{NO}$  in the soil (source: <http://www.agr.gc.ca>, accessed: 07.05.2009).

### **Chemical processes of the $\text{NO-O}_3\text{-NO}_2$ triad for short vegetation surfaces**

Above short vegetation such as grassland,  $\text{NO}$  comes out of the forest from biogenic processes in the soil organic layer. There is already some  $\text{NO}$ ,  $\text{O}_3$  and  $\text{NO}_2$  above the grassland.  $\text{O}_3$  tends to deposit on the leaf surfaces and into the leaf stomata of the grass while  $\text{NO}_2$  is taken up by the stomata or deposited on the ground. Any  $\text{O}_3$  escaping the trap of the leaves tries to reach the ground. The  $\text{O}_3$  that eventually manages to reach the ground meets with  $\text{NO}$  coming from the soil. The  $\text{O}_3$  reaching the ground instantly reacts with the  $\text{NO}$  coming out of the soil to produce more  $\text{NO}_2$ . In the presence of sunlight, the  $\text{NO}_2$  reacts with  $\text{O}_2$  to produce more  $\text{NO}$ . The remainder of the  $\text{NO}_2$  present is either deposited on the ground, on the leaves and stomata, or escapes to the free atmosphere. Therefore we have a net flux of  $\text{NO}$  out of the ground and net fluxes of  $\text{NO}_2$  and  $\text{O}_3$  into the ground.

### **Chemical processes of the $\text{NO-O}_3\text{-NO}_2$ triad above tall vegetation**

Fig. 1.2 illustrates the  $\text{NO-O}_3\text{-NO}_2$  triad within and above a forest.  $\text{NO}$  comes out of the forest from biogenic processes in the soil organic layer. There is already some  $\text{NO}$  above the forest canopy where, for the EGER site, the ratio  $\text{NO}:\text{O}_3$  was 1:120 (Foken et al., 2012). Additionally there is also some  $\text{NO}_2$ ,  $\text{O}_3$  and VOCs above the canopy.  $\text{O}_3$  from above-canopy reactions of  $\text{NO}_2$  and  $\text{O}_2$  tends to deposit on the leaf surfaces and into the leaf stomata. Any  $\text{O}_3$  escaping the trap of the leaves tries to reach the ground. The  $\text{O}_3$  that eventually manages to reach the ground meets with  $\text{NO}$  coming from the soil. At the ground, the ratio  $\text{NO}:\text{O}_3$  was 1:40 (Foken et al., 2012), i.e. there was 3 times less  $\text{O}_3$  at the ground than above the canopy. The efficiency of photolysis of  $\text{NO}_2$  to  $\text{NO}$  (R1.1 and R1.2) is greatly reduced at the forest floor because there is insufficient light in the right wavelength for photolysis. Therefore only reaction R1.3 occurs to a larger extent to produce more  $\text{NO}_2$ . The

additional  $\text{NO}_2$  is either deposited on the ground, on the leaves and stomata, or escapes to the free atmosphere. The puzzle is what conditions and mechanisms within the canopy determine whether the canopy is a net source or sink for  $\text{NO}$ ?

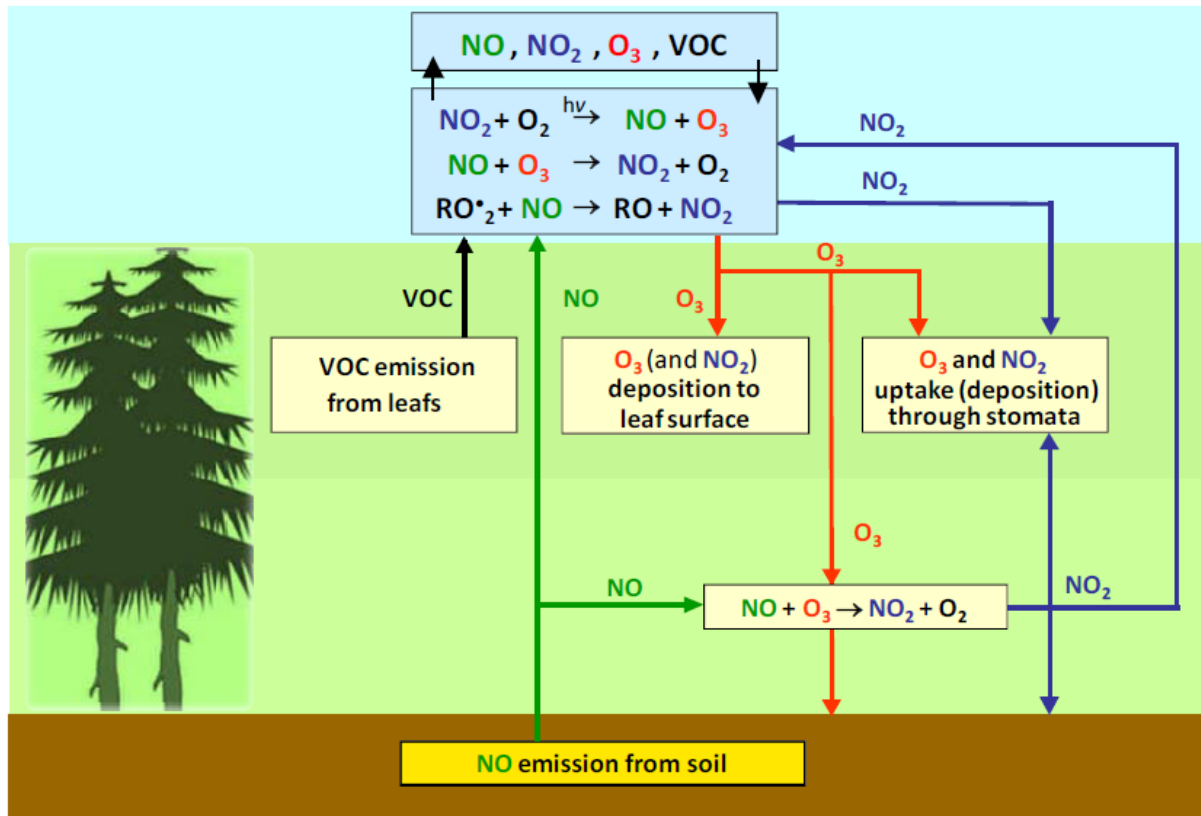


**Fig. 1.2.** Schematic diagram of the exchange of the  $\text{NO}$ - $\text{O}_3$ - $\text{NO}_2$  triad within and above a forest canopy (modified from Meixner et al., 2003).

### 1.2.2 Trace gas flux measurement techniques

This work will focus on three techniques for the measurement of reactive trace gas fluxes: the Eddy Covariance (EC) Method, the Aerodynamic Gradient Method (AGM), and the Modified Bowen Ratio Method (MBRM).

The EC method is presently the most reliable, direct, accurate, and widely used technique for quantifying exchange fluxes of trace gases and energy between the earth's surface and the atmosphere. In the EC method, a flux is determined by taking the long term mean of the covariance of the vertical wind fluctuations and the fluctuations of the trace gas under consideration. The wind fluctuations are measured using a 3 dimensional sonic anemometer which measures the fluctuations of the 3 components of the wind ( $u$ ,  $v$ , and  $w$ ). The sonic anemometer also measures the fluctuation of the sonic temperature ( $T_s$ ) which can be used to calculate the sensible heat flux. A fast analyser is used to measure the fluctuations in the concentration of the trace gas under study. Frequencies used for eddy covariance are typically 20 Hz but may be as low as 1 Hz. The EC method can only be

applied under steady state conditions in the surface layer. It also requires a homogeneous terrain with adequate fetch (distance upwind of the measurement point – should be at least 100 times the height of the tower), high frequency measurements of the vertical wind component and the trace gas under investigation, as well as a sufficiently tall tower. It is the standard and reference method used in this dissertation.

The Aerodynamic Gradient Method is a technique for determining exchange fluxes of momentum and scalars in the surface layer (layer directly under the influence of the earth's surface). The advantage of the aerodynamic method is that it can be used with slow measuring equipment. The challenges associated with the AGM are that difference between the values of the measured parameters of the upper sampling level ( $z_2$ ) and the lower sampling level ( $z_1$ ) are often below the limit of precision of the measuring system. Therefore instrument precision is important in the application of this method.

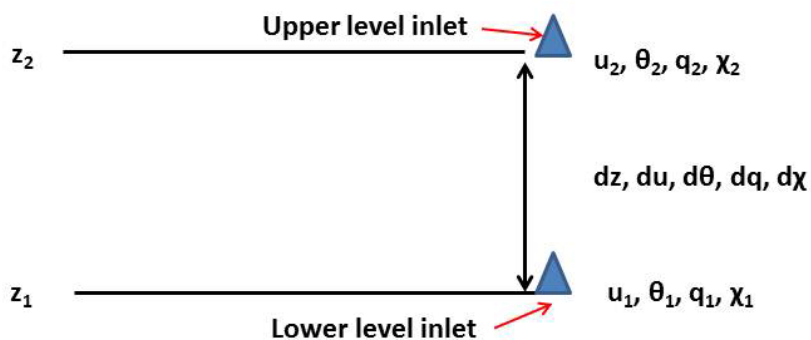


**Fig. 1.3.** A two point gradient measurement system where  $z$  is height,  $u$  is horizontal wind speed,  $\theta$  is the potential temperature,  $q$  is the humidity and  $\chi$  is any trace gas concentration.

The Modified Bowen Ratio Method (Businger, 1986; Liu and Foken, 2001; Müller et al., 1993; Meyers et al., 1996) is a flux measurement technique whereby one of the trace gas fluxes must be measured by the eddy-covariance method and the other can be determined from the vertical concentration difference between two measurement levels. Like the AGM, its usefulness is also dependent on instrument precision.

### 1.3 Previous research on NO-O<sub>3</sub>-NO<sub>2</sub> triad fluxes

The uptake of biogenically emitted trace gases by forest canopies has become known in the last few decades to play an important role in the budgets of atmospheric trace gases (Ganzeveld et al., 2002). Trace gases such as NO<sub>x</sub> from above or below (e.g. from the soil) a forest canopy are absorbed or recycled by the canopy vegetation before they are escape into the atmospheric boundary layer and further away into the troposphere (Rummel et al., 2007). The degree of absorption or emission is regulated by the turbulent transport of the reactive trace gases, the influence of chemical

transformations during that turbulent transport as well as the surface and physiological characteristics of the vegetation (Meixner et al., 2003).

While O<sub>3</sub> has been known to be exclusively deposited in plant canopies, there is still controversy (due to inconsistent results from different researchers) regarding the simultaneous upward and downward fluxes of NO and NO<sub>2</sub> between vegetation canopies and the atmosphere (Wildt et al., 1997). Reactive trace gases get affected by chemical transformations during turbulent transport in the forest while non-reactive trace gases are inert to chemical transformations. As a result, it is more difficult to determine the flux of reactive trace gases because of the potential for chemical divergence. Although eddy covariance (EC) flux measurements of CO<sub>2</sub> and H<sub>2</sub>O have been going on for decades, such measurements for the reactive trace gases have rarely been made. This is due to the unavailability of specific analysers that are fast enough. As a result of this limitation, EC fluxes of NO<sub>x</sub> have rarely been measured. Another limitation has been the lack of highly specific converters for determining NO<sub>2</sub> from NO<sub>x</sub>. In most cases (e.g. Wesley et al, 1982, Hicks et al., 1989), non-specific detection methods involving molybdenum or gold converters have been used. This has resulted in questionable fluxes of NO<sub>2</sub>. Furthermore full scale analyses of the exchange process within and above a forest using concentration profiles of the NO-O<sub>3</sub>-NO<sub>2</sub> triad in addition to the eddy covariance measurements have rarely been reported. As a result, the net exchange of NO-O<sub>3</sub>-NO<sub>2</sub> fluxes above a forest is still not satisfactorily quantified and understood.

With the advancement in portable trace gas detection methods within the last decade, several studies have been carried out on grassland, in-canopy, and above-canopy exchange fluxes of NO<sub>x</sub> and O<sub>3</sub> (Farmer and Cohen, 2008;Fuentes et al., 2007;Horii et al., 2004;Rummel et al., 2002a;Rummel et al., 2007).

One of the earliest publications on eddy covariance flux measurements of the NO-O<sub>3</sub>-NO<sub>2</sub> triad was by (Wesely et al., 1982). They measured NO, NO<sub>2</sub> and O<sub>3</sub> deposition velocities above a soybean canopy in 1979 with a then newly-developed NO analyser which worked on the gas phase chemiluminescence reaction of NO and O<sub>3</sub> (Stedman et al., 1972). The analyser had a molybdenum converter for reducing NO<sub>2</sub> in the air sample to NO. Their O<sub>3</sub> analysers were also chemiluminescence based. They found maximum deposition velocities of NO<sub>x</sub> (with NO<sub>2</sub> making up 90% of the NO<sub>x</sub>) of 0.006 m s<sup>-1</sup>, with O<sub>3</sub> having 0.009 m s<sup>-1</sup>. Additionally, the minimum surface resistance to NO<sub>x</sub> was larger than expected. This made them speculate that the release of NO from within the plant canopy or the emission of NO<sub>x</sub> from biogenic processes may have led to the reduced downward fluxes of NO<sub>x</sub> measured. They rejected the possibility of a mesophyll resistance to NO<sub>2</sub> during daytime as being the cause of the small daytime deposition velocities of NO<sub>2</sub>.

Delany et al. (1986) measured fluxes of  $\text{NO}_x$  and  $\text{O}_3$  over a short mature wheat grass. The site was under the influence of urban pollution. They found that  $\text{O}_3$  fluxes were always negative.  $\text{NO}_x$ , however, showed both deposition (predominating during morning hours) and emission (predominant in the afternoon) with  $\text{NO}_x$  ranging from  $-0.3$  to  $+0.2$   $\text{ppb m s}^{-1}$ . They concluded that the flux of  $\text{O}_3$  to the vegetation is determined by its atmospheric concentration, while for  $\text{NO}_x$ , deposition is similar to that for  $\text{O}_3$  but emission is controlled by physical, chemical, and biological factors.

Hicks et al. (1989) were among the first investigating  $\text{NO}_x$  and  $\text{O}_3$  fluxes to come up with a data selection technique to eliminate flux data that had been influenced by chemical reactions that compromise data quality. They recognized that flux divergence associated with spatial and temporal changes in concentrations of reactive trace gases can occur. They set some criteria that the divergence has to be much smaller than the flux for the flux to be considered meaningful. Additional work by Kramm et al. (1991) found that for  $\text{NO-O}_3\text{-NO}_2$ , chemical reactions have a considerable influence on the downward fluxes.

de Arellano and Duynkerke (1992) quantified the work started by Hicks et al. (1989) by deriving some relationships linking the turbulence timescale of reaction ((Wyngaard et al., 1982) with the chemical timescale (Lenschow, 1982)) of the  $\text{NO-O}_3\text{-NO}_2$ . They showed that the exchange by gradient-derived methods have to be modified for chemical systems that react with timescales similar to the turbulence timescale. Using a surface layer model, they found out that the effective turbulent exchange coefficients for reactive trace gases are not similar to those for nonreactive trace gases, with  $\text{NO}$  showing the largest difference, but smaller differences for  $\text{O}_3$  and  $\text{NO}_2$ . Moreover, they showed that the fluxes of the  $\text{NO-O}_3\text{-NO}_2$  triad, besides depending on their own gradients, are coupled to the gradients of the other chemical species within the triad.

From this result de Arellano and Duynkerke (1992) derived a chemical Damköhler number ( $\text{Da}$ ) - which is the ratio of the atmospheric turbulence timescale to the chemical transformation timescale (Damköhler, 1940) (see 2.4.1) for the  $\text{NO-O}_3\text{-NO}_2$  triad. It gives an idea of the degree of reaction during the turbulent transport of a chemically reactive compound. It is a tool that can help in deciding whether chemical corrections should be applied in determining flux-gradient relationships of the  $\text{NO-O}_3\text{-NO}_2$  triad.

Padro (1993) observed daytime  $\text{O}_3$  deposition velocities of  $0.01$   $\text{m s}^{-1}$  over a deciduous forest in summer and  $0.003$   $\text{m s}^{-1}$  in winter. They also observed mostly negative deposition velocities for  $\text{NO}_2$ . Their model (Venkatram et al., 1988) could not simulate the negative deposition velocity values observed.

Measurements of  $\text{NO}_2$  and  $\text{O}_3$  fluxes at the soil surface and 11 m above the ground in the Amazonian rainforest were conducted by (Gut et al., 2002a; Gut et al., 2002b) and Rummel et al. (2002a). They

observed small but negative fluxes of both O<sub>3</sub> (-0.5 nmol m<sup>-2</sup> s<sup>-1</sup> average daytime; -1.2 nmol m<sup>-2</sup> s<sup>-1</sup> maximum) and NO<sub>2</sub> (-0.11 nmol m<sup>-2</sup> s<sup>-1</sup> mean daytime; -0.12 nmol m<sup>-2</sup> s<sup>-1</sup> mean night time). However the NO<sub>x</sub> flux showed net emission during both day and night. Contrary to most other authors, they attributed mesophyllic resistance (with the same order of magnitude as the stomatal resistance) to part of the control of the uptake of NO<sub>2</sub>. They also reported NO flux measurements from soil chambers of up to 0.29 nmol m<sup>-2</sup> s<sup>-1</sup> at the same site.

Munger et al. (1998;1996) measured above-canopy eddy covariance flux measurements of NO, NO<sub>2</sub> (indirectly) and O<sub>3</sub> at the Harvard Forest (mixed deciduous forest) in Massachusetts. Horii et al. (2004) also made above-canopy eddy covariance flux measurements of NO, NO<sub>2</sub> and O<sub>3</sub> at the same site and found net deposition of NO<sub>x</sub> (~0.002 m s<sup>-1</sup>). They suggested that their results were consistent with an NO<sub>2</sub> compensation point in the region of 1.5 nmol m<sup>-2</sup> s<sup>-1</sup>. They suggested that surface uptake also accounts for NO<sub>2</sub> downward directed fluxes when stomata are closed and that nitrous acid (HONO) production may be an important factor. In both cases NO and NO<sub>2</sub> were derived from unreliable methods involving the use of empirical equations.

Farmer et al. (2006) and Farmer and Cohen (2008) observed upward fluxes of NO<sub>2</sub> and downward fluxes of NO<sub>x</sub> in a ponderosa pine forest in the Sierra Nevada Mountains. NO<sub>x</sub> fluxes were downward into the canopy which they attributed to the conversion of NO<sub>x</sub> to nitric acid (HNO<sub>3</sub>) and peroxyacetyl nitrate (PAN). However, there are a lot of simplifying assumptions in their application of the aerodynamic gradient method (AGM) (see 2.2.1).

The reported results of (Kortner, 2005) from simultaneous, high frequency eddy covariance measurements of the NO-O<sub>3</sub>-NO<sub>2</sub> triad above a mixed deciduous forest canopy are the most experimentally comparable ones to this study. They measured direct fluxes and profiles of the full NO-O<sub>3</sub>-NO<sub>2</sub> triad above a mixed deciduous forest at a complex terrain site in Jülich, Germany. They also had a highly specific photolytic converter for the detection of NO<sub>2</sub> from NO<sub>x</sub>. The difference with this study is that in this study measurements were made at a rural site where O<sub>3</sub> concentrations are expected to be at least 10 times greater than NO<sub>x</sub> concentrations. In such cases, local conditions are near photochemical equilibrium.

Stella et al. (2013) measured the eddy covariance fluxes of the NO-O<sub>3</sub>-NO<sub>2</sub> triad at a grassland using the NO/NO<sub>2</sub> analyser used in this dissertation. They discovered that plant physiology was unaffected by changes of turbulent conditions which occur when chamber methods are used.

Unfortunately only a few of these studies have focused on directly determining resolved fluxes of the triad above a forest. Additionally most of the research on the gradient-derived fluxes of the triad does not take into consideration the effect of the roughness sublayer on the magnitude of the fluxes. The major limitation has been the lack of availability of fast analysers for reactive nitrogen compounds.

As a result of this limitation, fast turbulent fluxes of  $\text{NO}_x$  have rarely been measured.  $\text{O}_3$  analysers have however been available for at least three decades. Another limitation has been the lack of highly specific converters for determining  $\text{NO}_2$  from  $\text{NO}_x$ . In most cases (Wesley et al, 1982, Delany et al., 1986., Hicks et al., 1989), non-specific detection methods involving molybdenum or gold converters have been used. This has resulted in questionable derived values of fluxes of  $\text{NO}_2$ . Furthermore full scale analyses of the exchange process within and above a forest using concentration profiles of the  $\text{NO-O}_3\text{-NO}_2$  triad in addition to the eddy covariance measurements have rarely been reported. As a result, the net exchange of  $\text{NO-O}_3\text{-NO}_2$  fluxes above a forest is still not satisfactorily understood. It is the aim of this work to fill in part of the gap in the knowledge by analysing the exchange processes of the reactive trace gases in a more comprehensive manner. This is done by incorporating eddy covariance flux measurements with gradient-derived flux methods.

It is the aim of this work to fill in part of the gap in the knowledge by analysing the exchange processes of the reactive trace gases in a more comprehensive manner. This is done by tackling the problem from two perspectives – the robust reference direct EC flux measurements and the gradient-derived flux methods. It is hoped that by filling this gap, more knowledge will be added to the field of atmospheric chemistry with the potential to improve atmospheric chemistry models and the research into mitigating air pollution in all parts of the world. For instance, the direction and range of magnitude of the  $\text{NO}_x$  fluxes in a spruce forest would be very useful for atmospheric chemistry models.

#### **1.4 Research questions**

Results of previous research leaves some questions about the canopy-atmosphere exchange processes of the  $\text{NO-O}_3\text{-NO}_2$  triad still unanswered:

- (1) Are rural forest ecosystems a source or sink of  $\text{NO}$  and  $\text{NO}_2$ ?
- (2) What are the source/sink relationships of the constituents of the  $\text{NO-O}_3\text{-NO}_2$  triad to each other above a forest canopy?
- (3) Can we quantify how much of the soil biogenic  $\text{NO}$  emission is escaping from the forest and reaches the atmosphere?

#### **1.5 Objectives of research**

The objectives of this research were:

- (1) to present and report reliable simultaneous high frequency, high resolution measurements of the fluxes of the full  $\text{NO-O}_3\text{-NO}_2$  triad and to investigate the source/sink relationship between its

constituents and the canopy-atmosphere system at *Waldstein-Weidenbrunnen* using a novel EC measurement system;

(2) to investigate the influence of chemical reactions on turbulent transport and *vice versa* on the fluxes of the NO-O<sub>3</sub>-NO<sub>2</sub> above the forest ecosystem;

(3) to investigate the performance and applicability of flux-gradient techniques to the measurement of reactive trace gas fluxes in the roughness sublayer at *Waldstein-Weidenbrunnen*; and

(4) to compare the results from the flux-gradient techniques to the reference eddy covariance results.

## 1.6 Challenges

### Challenge 1: The precision problem

Sometimes the concentration differences measured are in the same range as the precision with which the difference can be measured by the instrument. Careful calibrations and error analyses are necessary to overcome this problem.

### Challenge 2: Cycle time of trace gas analysers

The analysers for most trace gases, NO<sub>x</sub> in particular, are up to now still too slow for detecting fast changes in concentrations, which are important in determining fluxes using the EC technique. To solve this problem, we used a novel fast NO<sub>x</sub> analyser operating at 5 Hz.

### Challenge 3: Temporal resolution of discontinuously measured concentration differences

Measurement of reactive trace gas fluxes using flux-gradient techniques is usually based on discontinuous gradient measurements of the concentration at two sampling levels. This is achieved by using a switched valve system which switches the sampled air between the two levels of interest. In this way the analyser measures sequentially the concentration at one level during a defined time period before switching to the other level and back again. The temporal resolution of the measurements at each level depends on the response time of the system, and the time needed per level. Direct measurement techniques for measuring the concentration difference between two levels are available for CO<sub>2</sub> and H<sub>2</sub>O (e.g. with LI-6262 and LI-7000).

Unfortunately, such direct methods are still not readily available for most other reactive trace gases such as NO, NO<sub>2</sub> and O<sub>3</sub>. As a result, the switching method has remained the method of choice for measuring reactive trace gas concentration gradients. The problem of poor temporal resolution can be partially solved by using two independent instruments for sampling at the two measurement levels. However, even with very careful side-by-side characterization of the two instruments, calibration differences between the two instruments can be the same order of magnitude as the concentration

difference being measured, especially when small concentration differences are present. Although temporal resolution is reduced, switching is the best compromise. In addition the costs incurred in acquiring two instruments are avoided. Therefore it is necessary to make a thorough quality analysis of this measurement method in order to determine its applicability for measuring reactive trace gas concentration differences and deriving fluxes from them.

#### **Challenge 4: Gradient-derived flux measurements under the influence of the roughness sublayer**

The RSL is the layer immediately above the forest canopy where the roughness elements modify the flow of air (Kaimal and Finnigan, 1994). The main characteristics of the RSL are horizontally and vertically varying flux densities. Measurement of reactive trace gas fluxes using flux-gradient techniques is usually based on discontinuous gradient measurements as described above. Often one or both of the measurement levels are under the influence of the roughness sublayer because of one or both of the following reasons:

- (a) If measurement heights above the roughness sublayer were to be chosen, the concentration difference  $\Delta\chi$  between the two sampled levels would be too low or unresolvable (especially for reactive trace gases) using the available instruments.
- (b) Limitations (in terms of both cost and logistics) in the height of the available tower.

Therefore gradient-derived flux measurements near roughness elements are often a compromise. Nevertheless, gradient techniques are useful to apply in places or conditions where EC measurements are not available.

#### **Challenge 5: Effect of chemistry during turbulent transport of reactive trace gases**

The turbulence timescale (see 2.4) can be slower than the characteristic timescale of chemical reaction (see 2.4). Therefore appropriate measures have to be taken to correctly interpret mixing ratios of the measured reactive trace gas data according to chemistry. Tools that are useful for determining the influence of chemistry include the Damköhler number criterion and the intensity of segregation criterion (see 2.4).

### **1.7 Thesis outline**

This monograph thesis consists of six chapters. **Chapter 2** looks into detail at the possibilities of measuring reactive trace gases. In this chapter, the main aspects of micrometeorological theories and techniques encompassing measurement and data quality control and assessment relevant to this study

are explained in detail. It also looks at other micrometeorological concepts which are not directly related to the measurement of reactive trace gases but are used in the interpretation of the results and the discussion in the results chapter.

**Chapter 3**, the Materials and Methods chapter describes the instruments and methods used to satisfy the objectives of this thesis as well as give a detailed analysis of specific experimental adaptation of the instrumentation.

**Chapter 4** presents and discusses the results of the work carried out.

**Chapter 5** concludes the thesis by summarizing what has been done and what has been discovered. It explains to what extent the objectives of the thesis were met.

## Chapter 2: Theory

### 2.1 Introduction

This chapter explains the theory behind the three flux evaluation methods used in this thesis (the Aerodynamic Gradient Method, the Modified Bowen Ratio Method and the eddy covariance technique). Emphasis is placed on how each method was applied, including some modifications to some formulations to suit the objectives of this thesis. Another aim of this chapter is to explain micrometeorological terms and phenomena which are relevant to this thesis and which will be used often in the results and discussion section of the thesis.

Having discussed the importance and role of trace gases in surface-atmosphere interactions in Chapter 1, it is important to know how to quantify the magnitudes and directions of these trace gases in their exchange between the surface and the atmosphere. A number of possibilities exist when it comes to choosing a method for quantifying the concentrations and fluxes of trace gases. Before discussing further about these three methods of evaluating trace gas fluxes, a brief introduction to the turbulent transport of trace gases in the ABL is presented. This will help to explain why the methods that were used in this study were chosen.

#### 2.1.1 The atmospheric boundary layer

Processes in the ABL undergo a diurnal cycle (ABL) (see Fig. 2.1 and 2.2). Except for a thin layer of air close to the surface known as the molecular diffusion layer, the ABL's mechanism of mass and energy transfer is turbulent. Turbulent transfer is composed of thermal or free convection and mechanical or forced convection. It is characterized by random fluctuations in wind speed direction caused by eddy motion of the air. The driving forces for this turbulence are shear stress of the horizontal wind  $u$  (mechanical convection), and buoyancy due to air density variations with height (thermal convection) (Kaimal and Finnigan, 1994). The buoyancy effects occur mainly during daytime when the surface is heated by solar radiation. This creates forced and free convection as well as turbulent diffusion in the ABL. The ABL height is influenced by synoptic scale motions as well as mechanical and buoyant mixing.

#### *Diurnal cycle of the ABL*

Above terrestrial surfaces in high pressure regions the ABL structure's diurnal cycle consists of three main components: the mixed layer (ML), the residual layer (RL), and the stable boundary layer (SBL). These three layers are unstable, neutral, and stable respectively. The ABL is called the ML or convective boundary layer (CBL) during daytime as a result of convectively driven turbulence. The mean daytime ABL height ranges between 1 and 3 km. At the top of the ABL the entrainment zone

(EZ) is a boundary between the turbulence in the CBL and the streamlined flow of the free atmosphere (FA) above. Matter can enter or leave the EZ in processes called entrainment and detrainment respectively. At night, a SBL (called the nocturnal boundary layer (NBL)) with mechanically driven turbulence forms under the RL with a height that can become very low (tens of metres).

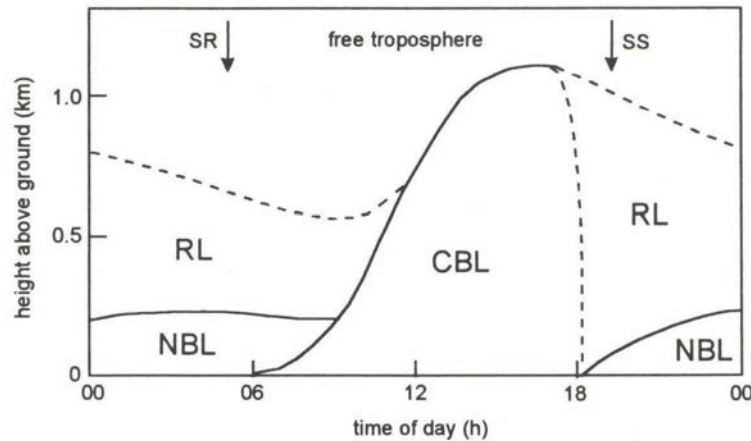


**Fig. 2.1.** Idealised diurnal course of boundary layer structure under clear sky conditions; SR: sunrise, SS: sunset, CBL: convective boundary layer, NBL: nocturnal boundary layer, RL: residual layer (after Stull, 1988).

### **Fragmentation of the ABL**

The surface layer (SL) is the lowest 10% of the ABL where turbulent fluxes are steady state with respect to height, i.e. turbulence and stress vary by less than 10% of their magnitude with height (Stull, 1988). Wind speed, humidity, and air temperature, show their largest gradients in the SL. Over rough surfaces such as forests the SL is subdivided into an inertial sublayer (ISL) and a roughness sublayer (RSL) (Garratt, 1992; Graefe, 2004).

The RSL is the layer immediately above the roughness elements where the roughness elements modify the flow of air (Kaimal and Finnigan, 1994). At the canopy level, the roughness effects of vegetation predominate, creating a well-mixed region extending up to three times the height of the canopy. The height of this roughness sublayer from the ground is denoted by  $z^*$ . The main characteristics of the RSL are horizontally and vertically varying flux densities. Furthermore, wake turbulence caused by the roughness elements and thermal effects enhance turbulence in the RSL over the turbulence in the ISL. Turbulent exchange coefficients (see 2.1.4) are also increased above their logarithmic values encountered in the ISL.

In the ISL the influence of surface properties on airflow properties decreases, e.g. the wind direction is increasingly modified by the Coriolis force (an inertial force created by the rotation of the Earth),

and vertical flux densities are considered to be constant with height (Cellier and Brunet, 1992; Garratt, 1992; Kaimal and Finnigan, 1994; Oke, 1987).

Additionally, a canopy layer (CL) forms near the ground. The height of the CL is roughly the mean height of the roughness elements (Oke, 1987). Just above the soil-canopy interface is a small layer called the molecular diffusion layer. In this layer, molecular diffusion predominates over turbulent diffusion.

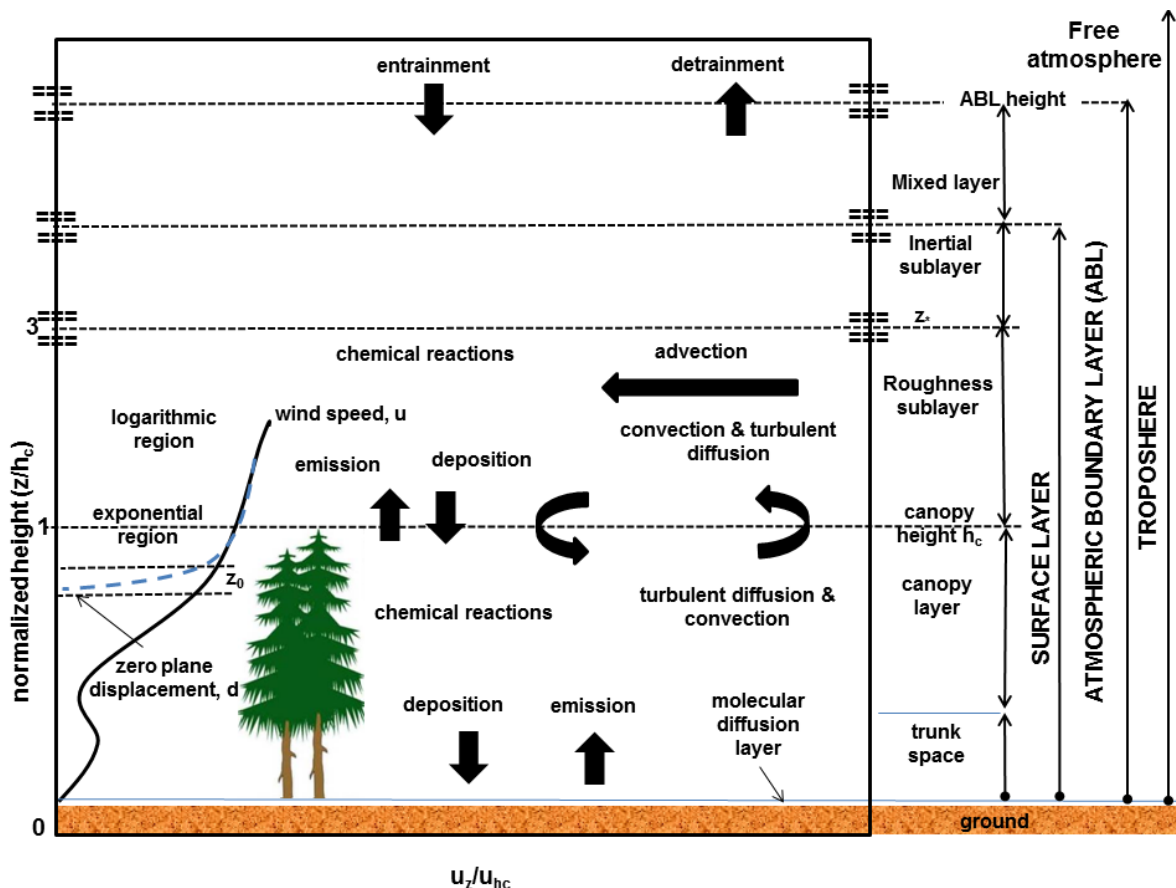


**Fig. 2.2.** Physical and chemical processes of the Atmospheric Boundary Layer in and above a forest canopy. The wind profile characteristic is also illustrated. After Enders *et al.* (1992) and Amiro (1990).

Within the canopy, chemical processes of deposition and emission predominate. There are also convective and diffusive exchanges at the canopy-atmosphere interface. The horizontal wind profile shows a rapid exponential decrease of horizontal wind speed in this region due to the retarding effect of the roughness elements. This exponential decrease extends all the way to the trunk space at which point there is a region in which the horizontal wind speed increases with height, leading to a secondary wind maximum before it starts to decrease again, finally reaching zero at the ground. The presence of the canopy displaces the canopy wind profile from the ground by a distance  $d$ , known as

the *zero plane displacement*. It is like having the wind profile coordinate system being transformed vertically due to the presence of the canopy.

### 2.1.2 The Monin-Obukhov Similarity Theory

Monin and Obukhov (1954) theorized that for the SL, non-dimensional relations exist between the fluxes of momentum and heat and the gradients of velocity and temperature, respectively. The theory was postulated for atmospheric turbulence in the SL and has some basic assumptions:

- (1) The mean turbulent fluxes do not change with height, with the horizontal flow being homogeneous and the fluxes of momentum and heat independent of height within the surface layer.
- (2) Influences of surface properties and height are fully represented by the surface shear stress parameter.

These assumptions make up the basis for the Monin-Obukhov Similarity Theory (MOST). From these assumptions, Monin and Obukhov (1954) concluded that the SL wind and temperature field depend only on four independent variables: the kinematic sensible heat flux  $\frac{Q_H}{\rho c_p}$  ( $\text{K m s}^{-1}$ ), the height above the ground (m), the buoyancy parameter  $\frac{g}{T}$  ( $\text{m K}^{-1} \text{s}^{-2}$ ) and the surface shear stress  $\tau_0/\rho$  ( $\text{m}^2 \text{s}^{-2}$ ). These fundamental surface parameters involve only 3 dimensions: length (m), temperature (K) and time (s). According to Buckingham's  $\Pi$ -theorem (Stull, 1988), the chosen combination for these fundamental parameters which produces a dimensionless group is the dimensionless height  $\zeta=z/L$ , where  $L$  is the Obukhov length (Obukhov, 1971) defined as:

$$L = -\frac{u_*^3}{\kappa \frac{g}{T} \frac{Q_H}{\rho c_p}} \quad (2.1)$$

where  $T$  denotes the average absolute temperature of the profile,  $u_*$  is the friction velocity,  $g$  is the acceleration due to gravity,  $\kappa$  is the von Karman constant and other symbols are as defined earlier.  $L$  has the dimensions of length (m). The magnitude of  $L$  is proportional to the thickness of the layer in which shear and friction induced turbulence is greater than buoyancy induced turbulence. In this layer the influence of stratification is negligible.  $L$  is positive when the atmospheric surface layer is convectively stable, negative in unstable conditions, and infinite under neutral conditions. A detailed description of the theory can be found in Stull (1988).

Furthermore, experimental work done on profiles of wind, humidity and temperature in the surface layer found that the flux at a point can be scaled to the gradient using the universal functions (Businger et al., 1971) of the scaling dimensionless parameter  $z/L$ . The formulations for the universal

functions used are according to Businger et al. (1971) and modified by Högström (1988). They shall be described in detail in 2.2.

$$\frac{\partial u(z)}{\partial z} \frac{\kappa z}{u_*} = \varphi_M \left( \frac{z}{L} \right) \quad (2.2)$$

$$\frac{\partial q(z)}{\partial z} \frac{\kappa q_*(z)}{w'q(z)'} = \varphi_Q \left( \frac{z}{L} \right) \quad (2.3)$$

$$\frac{\partial T(z)}{\partial z} \frac{\kappa T_*(z)}{w'T(z)'} = \varphi_H \left( \frac{z}{L} \right) \quad (2.4)$$

$u_*$  is the friction velocity(  $= \sqrt{-u'w'}$ ),  $q(z)$  is humidity and  $\varphi_M$  and  $\varphi_H = \varphi_Q$  are the universal functions for momentum and sensible heat (including scalars) and humidity respectively. All the three functions are dependent on  $z/L$  only.

It has been found that the Monin-Obukhov similarity theory fails when applied above a forest, other roughness elements and inhomogeneous surfaces, such as above tall vegetation in the roughness sublayer (Garratt, 1992;Graefe, 2004). Fluxes of momentum and scalars are corrected by pre-multiplying the right-hand-side of the three equations above by an enhancement factor which is peculiar to each site and must be determined experimentally. Even when conditions are ideal, the MOST is known to have an accuracy of not more than 20% (Foken, 2006).

### 2.1.3 Exchange processes within and above a forest

Exchange of energy and matter occurs continuously between the trunk space, the forest canopy and the atmosphere during the day for high vegetation. Eddies generated by turbulence can link or couple the lowest part of the canopy with the higher parts, and the ABL above. Decoupled states may as well be found. The degree of coupling between the canopy and the atmosphere varies with stability and is also influenced by the presence of the roughness sublayer (Foken, 2008;Raupach and Thom, 1981). The high roughness above the canopy weakens the wind velocity field and the canopy stability. As a result, the trace gases within the canopy and those above the canopy are enhanced by the decoupling effect, particularly during stable conditions when there is reduced turbulent mixing. The state of mixing between the atmosphere and the forest is variable and depends on a number of mechanical and buoyancy forces which influence parameters such as the horizontal wind and the vertical wind. The stronger the driving force, the greater the degree of mixing or coupling between the atmosphere and the forest canopy.

Stable isotopic chemical tracers have been used to determine the canopy-atmosphere coupling state by releasing them from the canopy interior and determining their concentrations above the canopy. A

commonly used isotope is  $^{13}\text{C}$  (Wichura et al., 2004). Rummel et al. (2002a) used the reaction of NO with  $\text{O}_3$  as a tracer to determine turbulent mixing within a forest canopy.

Coherent structures (Holmes et al., 1996) are well-organized, relatively stable long-living eddy structures which occur mostly with regularity in either time or space. They can be used to determine the canopy-atmosphere turbulent exchange regime if measurements are made at several heights within and above the canopy (Thomas and Foken, 2007). The degree of penetration into the canopy by coherent structures can be classified into five exchange regimes called coupling states (Thomas and Foken, 2007):

- Wave motion (Wa):* The flow above the canopy is dominated by gravity waves rather than by turbulence.
- Decoupled canopy (Dc):* The air above the canopy is decoupled from the canopy and subcanopy.
- Decoupled subcanopy (Ds):* The atmosphere is coupled with the canopy, but decoupled from the subcanopy. The region of coherent exchange is limited to the canopy.
- Coupled subcanopy by sweeps (Cs):* The exchange between the above-canopy air and the subcanopy is forced by the strong sweep motion of coherent structures only.
- Fully coupled canopy (C):* The atmosphere, the canopy and the subcanopy are in a fully coupled state.

Canopy coupling states were used as a tool for the interpretation of the trace gas fluxes.

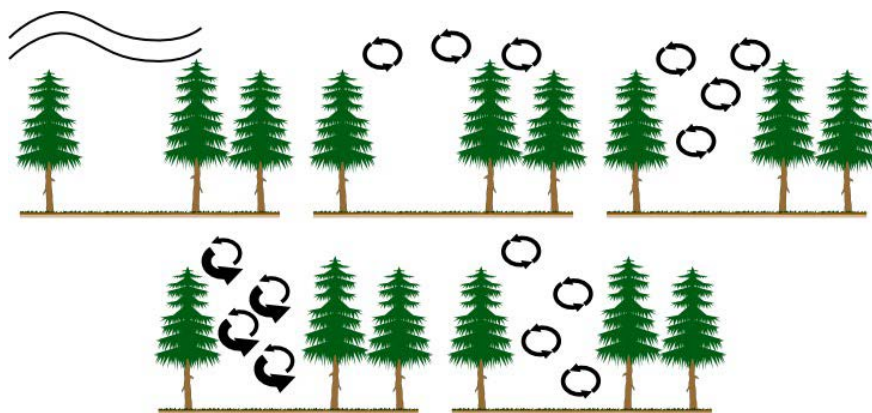


**Fig. 2.3.** The five canopy coupling states (diagram courtesy of A. Serafimovich - Thurnau 2009 [poster page 13](#)) clockwise from the top left we have Wa, Dc, Ds, C, and Cs.

### **Dynamic processes in the ABL**

The flow of matter can be described to a larger extent by the Navier-Stokes equations of motion. They are a set of equations of state and conservation of mass, momentum, heat and moisture, consisting of a superposition of mean and turbulent flow. Reynolds decomposition (see 2.3) is a tool that is applied to simplify the Navier-Stokes equations by splitting the variables into their mean and turbulent components.

Momentum exchange:

$$\frac{\partial \bar{u}_i}{\partial t} + \frac{\partial}{\partial x_j} (\bar{u}_j \bar{u}_i + \overline{u_j' u_i'}) = -\frac{1}{\rho} \frac{\partial \bar{p}}{\partial x_i} + \nu \frac{\partial^2 \bar{u}_i}{\partial x_i^2} + g \delta_{i3} \quad (2.5)$$

Heat exchange:

$$\frac{\partial \bar{T}}{\partial t} + \frac{\partial}{\partial x_i} (\bar{u}_i \bar{T} + \overline{u_i' T'}) = a_T \frac{\partial^2 \bar{T}}{\partial x_i^2} + Q \quad (2.6)$$

and transport of trace gases:

$$\frac{\partial \bar{\chi}}{\partial t} + \frac{\partial}{\partial x_i} (\bar{u}_i \bar{\chi} + \overline{u_i' \chi'}) = D \frac{\partial^2 \bar{\chi}}{\partial x_i^2} + S \quad (2.7)$$

where  $u_i$  is the component of wind velocity in direction  $i$ ,  $t$  is the time,  $x_i$  and  $x_j$  are the components of the position in direction  $i$  or  $j$ ,  $p$  is the pressure,  $\rho$  is the density,  $\nu$  is the viscosity,  $g$  is the acceleration due to gravity ( $9.81 \text{ m s}^{-2}$ ),  $T$  is the mean thermodynamic temperature ( $K$ ),  $a_T$  is the molecular heat conduction coefficient,  $D$  is molecular diffusion coefficient.  $Q$  is a source term and  $S$  is a sink term.

The terms which are not in bold are part of the Navier-Stokes equations but are not included in the surface layer analysis because of simplifying assumptions (Foken, 2008; Kaimal and Finnigan, 1994; Stull, 1988):

- Horizontal fluctuations of density, pressure and temperature are negligible.
- The layer of air is considered incompressible.
- Molecular diffusivity is small enough to be neglected.
- The mean flow is in hydrostatic equilibrium.

The assumptions simplify the Navier-Stokes equations and allow them to be used to derive the EC formulations. We can parameterize Equation 2.7 directly as a function of space and time. In this case the proportionality constant between flux and gradient is the turbulent exchange coefficient.

$$\overline{u_i' \chi'} = -K \frac{\partial \bar{\chi}}{\partial x_i} \quad (2.8)$$

$u_i'$  is the fluctuation of the wind velocity component  $i$ ,  $\chi'$  is the fluctuation of the horizontal wind velocity  $u$  or a scalar,  $K$  is the turbulent exchange coefficient,  $\bar{\chi}$  is the mean value of the local gradient of  $\chi$ , and  $\partial x_i$  is the distance of separation of the local gradient. This method is called gradient transport theory or K-theory. It is one of the least complex parameterizations but fails in the presence of large eddies (Foken et al., 2008). Different  $K$  values are associated with different types of variables. For momentum,  $K_M$  is used, which is referred to as the eddy diffusivity. For heat and humidity,  $K_H$  and  $K_Q$  are used.  $K_H$  is used generally for scalars. The application of this technique to calculate fluxes will be encountered in the discussion of the MBR method in 2.1.3.

One of the limitations associated with using gradient or K-theory techniques inside a forest is *counter-gradient fluxes*, a phenomenon whereby the fluxes are opposite to the local gradients of the state parameters (Denmead and Bradley, 1985). Contributions of coherent structures may be large enough to create such observed fluxes (Bergström and Högström, 1989; Gao et al., 1989).

#### 2.1.4 Overview of trace gas measurement techniques

One of the objectives of this work was to determine fluxes of scalars for which no fast sensors were available to determine the fluxes using the EC method. The Aerodynamic Gradient Method (AGM) is a technique for determining the fluxes of momentum and scalars in the surface layer (see Equations 2.2-2.4). The advantage of the aerodynamic method is that it can be used with slow measuring equipment and it does not require a large fetch. The challenges associated with the AGM are that concentration difference between the upper sampling level and the lower sampling should are often below the detection limit of the measuring system. Therefore instrument precision is important in the application of this method.

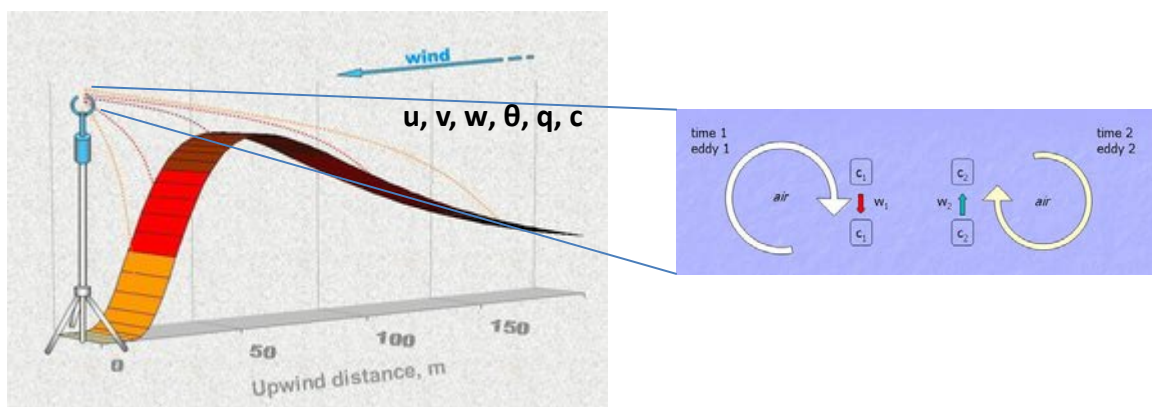


**Fig. 2.4.** An illustration of the EC flux measurement principle.  $c$  represents the trace gas concentration (adapted from George Burba poster [image 1](#) and [image 2](#). Accessed 07.05.2010)

The MBR method (Businger, 1986; Liu and Foken, 2001; Müller et al., 1993; Meyers et al., 1996) is a zero order local closure technique based on the universal flux-profile relationships according to the Monin-Obukhov similarity theory. The starting point is equation 2.8 for two different trace gases.

$$\overline{u_i' \chi_1'} = -K_1 \frac{\partial \bar{\chi}_1}{\partial x_i}, \overline{u_i' \chi_2'} = -K_2 \frac{\partial \bar{\chi}_2}{\partial x_i} \quad (2.9)$$

The main assumption is that  $K_1 = K_2$ , i.e. the exchange coefficients are similar:

$$\frac{\overline{w_1' \chi_1'}}{\overline{w_2' \chi_2'}} = \frac{\Delta \chi_1}{\Delta \chi_2} \quad (2.10)$$

One of the trace gas fluxes must be measured by the eddy-covariance method and the other can be determined from the concentration. This method was used to evaluate fluxes of reactive trace gases (NO, NO<sub>2</sub>) for which there were no fast measurements.

The chamber method (Reikosky et al., 1990) is an enclosure method which relies on the mass balance technique. The sample is enclosed in a cuvette or chamber and the rate of assimilation or emission of a trace gas by the material enclosed in the chamber is equal to the rate of change of concentration of the trace gas flowing across the chamber. Therefore the flux of a trace gas through the chamber will be equal to the area of the chamber times the rate of change of concentration of the trace gas in the chamber.

Eddy covariance is the most direct method available for determining trace gas fluxes using high frequency turbulent measurements of the vertical wind speed and the trace gas under study. It is based on the Navier-Stokes equations. In the EC method, a flux is determined by taking the long term mean of the covariance of the vertical wind fluctuations and the fluctuations of the trace gas under consideration. The EC method can only be applied under steady state conditions in the surface layer. It also requires a homogeneous terrain with adequate fetch, high frequency measurements of the vertical wind component and the trace gas under investigation, as well as a sufficiently tall tower.

The relaxed eddy accumulation method (REA), was proposed by Businger and Oncley (1990). In this method the conditional sampling of the trace gas is determined by positive or negative vertical wind velocity and the sample flow rate is constant. The surface layer flux is then assumed to be directly proportional to the standard deviation of the vertical wind component times the difference of the updraft concentration (c+) and the downdraft concentration (c-) of the trace gas. The constant of proportionality depends on the stability parameter z/L. Table 2.1 gives a brief summary of flux measurement techniques for reactive trace gases.

**Table 2.1.** Overview of various flux measurement methods. The bold printed methods are used in this thesis.

<b>Method</b>	<b>Response time of the sensors; Application possibility</b>	<b>Limitations</b>
<b>AGM</b>	Long response time; calculating fluxes below or above RSL	Limited by RSL
<b>MBR</b>	Long response time; calculating fluxes under conditions where MOST is fulfilled	Limited by availability of EC flux measurements
Chamber/Cuvette	Long response time; soil flux measurements, leaf/branch flux measurements	Not suitable above forest; needs upscaling of fluxes which reduces the accuracy of the measurements
<b>Eddy Covariance</b>	Short response time; surface layer flux measurement	Expensive
REA	short response time; nonreactive trace gas flux measurements	Not suitable for fast reacting trace gases (reaction in reservoir)

### 2.1.5 General requirements for flux measurements

The general requirements for flux measurements are that (Aubinet et al., 2012):

- 1) The turbulent flow must be stationary
- 2) The turbulent flow must be isotropic
- 3) The flow must also be homogeneous

Point (1) is achieved by choosing appropriate averaging intervals by analysing turbulence spectra using ogive functions. Point (2) and (3) are site dependent and can be checked for by doing a footprint analysis of the chosen site to verify if it meets the requirements for eddy covariance measurements.

To be able to measure fluxes with confidence, several requirements have to be met. One of these assumptions is that the terrain within the fetch has to be homogeneous, leading to steady-state flows

and no advection (Vesala et al., 2008). This assumption cannot be met, particularly when measuring in complex terrain such as a forest where there are different types of vegetation and other structures that create inhomogeneity such as clearings and footpaths. In such terrain, it is difficult to know which vegetation type or part of the terrain is represented by the fluxes.

## 2.2 Gradient Methods

### 2.2.1 Aerodynamic Gradient Method

#### *Profile equations for unvegetated surfaces*

For momentum or trace gases of concentration  $\chi$  at height  $z$  under the influence of neutral stratification, the relationship of the gradient to the Monin-Obukhov stability parameter can be used to find the flux. The differential profile relationships can be used for determining  $u_*$ , the latent heat flux  $LE$ , and the sensible heat flux  $H$ . A direct determination of wind, temperature and other scalar gradients requires measurements at several, closely separated heights.

Therefore it is necessary to use integrated profile relationships. Integrating the differential equations 2.11 and 2.12 above from the lower sampling height  $z_1$  to the upper sampling height  $z_2$  of interest yields:

$$\Delta u(z) = \frac{u_*}{\kappa} \left[ \ln \left( \frac{z_2 - d}{z_1 - d} \right) - \psi_M \left( \frac{z_2 - d}{L} \right) + \psi_M \left( \frac{z_1 - d}{L} \right) \right] \quad (2.11)$$

for the horizontal wind difference between two sampling inlets  $z_1$  and  $z_2$ , and

$$\Delta \chi(z) = \frac{\chi_*}{\kappa} \left[ \ln \left( \frac{z_2 - d}{z_1 - d} \right) - \psi_H \left( \frac{z_2 - d}{L} \right) + \psi_H \left( \frac{z_1 - d}{L} \right) \right] \quad (2.12)$$

for the vertical concentration difference between the same sampling inlets  $z_1$  and  $z_2$ .

The  $\psi$  term denotes the stability function (integrated) under stratification. Its value depends on the stability conditions. Table 2.2 shows a summary of the values of  $\psi$  for stable and unstable conditions.

**Table 2.2.** The  $\psi$  functions for different stability conditions according to the formulations of Businger et al. (1971), modified by Högström (1988).

$z/L$	$\psi_M$	$\psi_H$
$<0$	$\ln \left[ \left( \frac{1+x}{2} \right)^2 \left( \frac{1+x^2}{2} \right) \right] - 2 \arctan(x) + \frac{\pi}{2}$	$2 \ln \left[ \frac{1 + 0.95 \left( 1 - 11.6 \frac{z}{L} \right)^{0.5}}{2} \right]$
$>0$	$-6 \frac{z}{L}$	$-7.8 \frac{z}{L}$

where  $x = \left( 1 - 19.3 \frac{z}{L} \right)^{0.25}$

### Profile equations above tall vegetation

The effect of above-canopy roughness elements has to be accounted for when measuring fluxes above tall vegetation. The roughness sublayer effects mentioned earlier lead to a situation where a correction term  $\varphi_*$  has to be applied to the Monin-Obukhov stability parameters because the MOST does not hold in the roughness sublayer.

$$\frac{\partial u(z)}{\partial z} \frac{\kappa z}{u_*} = \varphi_M \left( \frac{z}{L} \right) \varphi_{*M} \left( \frac{z}{z_*} \right) \quad (2.13)$$

and in general for scalars:

$$\frac{\partial \chi(z)}{\partial z} \frac{\kappa \chi_*}{F_\chi} = \varphi_H \left( \frac{z}{L} \right) \varphi_{*H} \left( \frac{z}{z_*} \right) \quad (2.14)$$

The same universal function  $\varphi_H$  is used for heat, moisture and other trace gases.

In integrated form:

$$\Delta u(z) = -\frac{u_*}{\kappa} \left[ \ln \left( \frac{z_2 - d}{z_1 - d} \right) - \psi_M \left( \frac{z_2 - d}{L} \right) + \psi_M \left( \frac{z_1 - d}{L} \right) + \int_{z_1}^{z_2} \varphi_M (1 - \varphi_{*M}) \frac{dz}{z} \right] \quad (2.15)$$

$$\Delta \chi(z) = -\frac{F_\chi}{\kappa u_*} \left[ \ln \left( \frac{z_2 - d}{z_1 - d} \right) - \psi_H \left( \frac{z_2 - d}{L} \right) + \psi_H \left( \frac{z_1 - d}{L} \right) + \int_{z_1}^{z_2} \varphi_H (1 - \varphi_{*H}) \frac{dz}{z} \right] \quad (2.16)$$

where the correction function is given as (Garratt, 1980, 1983):

$$\varphi_* \left( \frac{z}{z_*} \right) = e^{-0.7 \left( 1 - \frac{z}{z_*} \right)} \quad (2.17)$$

**Table 2.3.**  $\varphi_*$  functions as derived and used by several authors

Author	$\varphi_{*M}$	$\varphi_{*H}$
(Garratt, 1980, 1983)	$e^{-0.7\left(1-\frac{z}{z_*}\right)}$	$e^{-0.7\left(1-\frac{z}{z_*}\right)}$
Cellier and Brunet (1992); Mölder et al. (1999)	$\left(\frac{z}{z_*}\right)^n$	$\frac{z}{z_*}$
	n=0,1, 2,....	

### 2.2.2 Modified Bowen Ratio Method

High time resolution measurement instruments and techniques for reactive trace gases are still in their infancy. Most techniques employ sampling methods which are based on slow measurement techniques such as accumulation and chromatography. This is especially true for determining mixing ratios of VOCs and water-soluble compounds, such as  $\text{NH}_3$  and  $\text{HNO}_3$ . Therefore an alternative method to the AGM, which failed due to the roughness sub layer limitation at the experimental site of this work, had to be used. The MBR method (Businger, 1986; Liu and Foken, 2001; Müller et al., 1993; Meyers et al., 1996) was a good alternative. It is a zero order local closure technique based on the universal flux-profile relationships according to the Monin-Obukhov similarity theory.

#### **Unvegetated surfaces**

To avoid profile fitting and profile equations the Modified Bowen Ratio Method may be a good alternative in some instances. It is a useful tool which can be applied in the inference of fluxes of quantities that would otherwise be too difficult to determine using conventional methods. The Modified Bowen Ratio method (Businger, 1986; Liu and Foken, 2001; Müller et al., 1993; Meyers et al., 1996) is based on the scalar similarity principle and it can be used to infer fluxes of trace gases from slow, gradient-based measurements. It states that the ratio of two fluxes is similar to the ratio of the gradients of those two fluxes. This assumes that the turbulent Schmidt number, the universal function and also the universal function of the roughness sublayer are identical for both trace gas fluxes.

One of the trace gas fluxes must be measured by the eddy-covariance method and the other can be determined from the concentration gradients. Unfortunately the application of the method is not as simple because both scalars must be similar.

$$F_{\chi_1} = -K_{\chi_1} \frac{\Delta\chi_1}{\Delta z} = \overline{w'\chi_1'} \quad (2.18)$$

$$F_{\chi_2} = -K_{\chi_2} \frac{\Delta\chi_2}{\Delta z} = \overline{w'\chi_2'} \quad (2.19)$$

If the similarity principle holds the turbulent exchange coefficients will be the same:

$$K_{\chi_1} = K_{\chi_2}.$$

Therefore

$$F_{\chi_1} = F_{\chi_2} \frac{\Delta\chi_1}{\Delta\chi_2} \quad (2.20)$$

This relationship means that if we have measured a flux  $F_{\chi_2}$  by EC (e.g.  $q$ ) and we also have the gradient of  $q$  ( $\Delta\chi_2$ ), then if we also have a gradient of another gas (e.g.  $\text{NO}_2$ ) at the same levels as  $q$ , then the flux of that trace gas can be calculated using the equation above. Periods where the similarity principle was fulfilled, i.e. where the exchange coefficients were similar for water and temperature are looked for. Equation 2.20 can then be used to calculate the unknown fluxes from the gradients of the trace gas measurements.

### ***Above tall vegetation***

The MBR method is applied above tall vegetation the same way as for unvegetated surfaces. However, the MBR method does not work for momentum flux above tall vegetation. This is because momentum flux is derived from a horizontal gradient whose characteristics will be different from a vertical gradient. Therefore in such a case no similarity can be achieved. The roughness sublayer has no net influence on the scalar fluxes because any effect affecting one of the concentration differences will equally affect the other and the overall ratio between the two concentration differences will remain the same. This is, however, not entirely true for reactive trace gas concentration differences which may be subjected to different intensities of chemical reaction

## **2.2.3 Experimental Realization**

### ***Aerodynamic Gradient Method***

Since one of our aims is to test the applicability of the gradient-derived flux determination methods, there was need to find the friction velocity and the stability parameters independently of EC methods. We therefore used an iterative approach for finding  $u^*$  and  $z/L$  as described below.

From equation 2.1, the Obukhov length can be modified by using a similarity theory approximation

$$\frac{H}{\rho c_p} \approx \overline{w'T'} = -u_* \theta_* \quad (2.21)$$

to give

$$L = \frac{\bar{T} u_{p*}^2}{g \kappa \theta_*} \quad (2.22)$$

Where  $\bar{T}$  denotes the average temperature of the profile,  $u_{p*}$  is the friction velocity derived from the profile (to differentiate it from  $u_*$  from EC), and  $\theta_*$  is the potential temperature scale. The modification is necessary when using the pure AGM because there is no eddy covariance data of heat flux required by Equation 2.1.

The potential temperature is that temperature which a hypothetical parcel of fluid at a pressure  $P$  would reach if it was transported adiabatically to a pressure of 1000 hPa.

$$\theta = T \left( \frac{P_0}{P} \right)^{\frac{R_L}{c_p}} \quad (2.23)$$

where  $\theta$  is the potential temperature,  $T$  is the air temperature,  $P_0$  is the reference pressure (1000 hPa),  $P$  is the atmospheric pressure,  $R_L$  is the universal gas constant for dry air (287.058655 J kg<sup>-1</sup>K<sup>-1</sup>) and  $c_p$  is the specific heat capacity at constant pressure. Potential temperature is used instead of actual temperature because, unlike ordinary temperature, it is not affected by vertical fluctuations caused by large-scale turbulence.

Substituting for  $u_*$  and  $\theta_*$  in the integrated profile equations for momentum (Equation 2.11) and for heat (Equation 2.12) respectively yields:

$$L = \frac{\bar{T} (\Delta u)^2 \left[ \ln \left( \frac{z_2 - d}{z_1 - d} \right) - \psi_H \left( \frac{z_2 - d}{L} \right) + \psi_H \left( \frac{z_1 - d}{L} \right) \right]}{g \kappa \Delta \theta \left[ \ln \left( \frac{z_2 - d}{z_1 - d} \right) - \psi_M \left( \frac{z_2 - d}{L} \right) + \psi_M \left( \frac{z_1 - d}{L} \right) \right]^2} \quad (2.24)$$

where  $\Delta u$  and  $\Delta \theta$  are wind and potential temperature differences between the two heights where the gradients are measured. The set of equations making up  $L$  has more variables than equations and therefore needs to be solved numerically.

When wind and temperature are measured at the same heights,  $L$ , and hence  $z/L$ , can be found by using the bulk Richardson number ( $Ri$ ) approach:

$$Ri = \frac{g}{\bar{\theta}} \frac{\Delta \theta}{(\Delta u)^2} \Delta z \quad (2.25)$$

$$L = z_2 \left[ \frac{z_2 - z_1 \ln\left(\frac{z_2}{z_1}\right)}{2\gamma \left(1 - \frac{Ri}{Ri_c}\right)} \right] \left[ -\left(1 - \frac{2 Ri}{Pr_t Ri_c}\right) + \sqrt{\left(1 - \frac{2 Ri}{Pr_t Ri_c}\right)^2 + \frac{4 Ri}{Pr_t^2 Ri_c} \left(1 - \frac{Ri}{Ri_c}\right)} \right]^{-1} \quad (2.26)$$

$Pr_t$  is the turbulent Prandtl number ( $\sim 0.74$ ) and  $Ri_c$  is the critical value of  $Ri$  ( $=0.2$ ). The derivation of the equation above is according to Sharan et al. (2003) and is shown in Chapter 4.

Alternatively, the following iterative method can be used (Berkowicz and Prahm, 1982):

- (1) First the iteration is started with an initial estimate of  $-\infty$  for  $L$ . This value is substituted into the equation for  $u_{p^*}$  and  $\theta_*$ :

$$\Delta u(z) = \frac{u_{p^*}}{\kappa} \left[ \ln\left(\frac{z_2 - d}{z_1 - d}\right) \right] \quad (2.27)$$

$$\Delta \theta(z) = \frac{\theta_*}{\kappa} \left[ \ln\left(\frac{z_2 - d}{z_1 - d}\right) \right] \quad (2.28)$$

- (2) Next  $L$  is computed from the initial values of  $u_{p^*}$  and  $\theta_*$  obtained when  $L = -\infty$ .
- (3) The new value of  $L$  was used to calculate new values of  $u_{p^*}$  and  $\theta_*$ . The new values of  $u_{p^*}$  and  $\theta_*$  are then used to calculate an improved value of  $L$ . The steps are repeated until the difference between subsequent values of  $L$  was less than 0.1%.

For *stable cases*, i.e.  $\Delta\theta < 0$  the iteration is always converging. However, for *unstable cases* ( $\Delta\theta > 0$ ) valid solutions ( $L > 0$ ) are obtained for bulk Richardson numbers less than the critical value of 0.215. This condition is added to the algorithm and is applied whenever a stable case is encountered by the iteration subroutine.

- (4)  $L$  and  $u_{p^*}$  were then used to calculate the fluxes of the various scalars as well as momentum using the integrated flux-gradient equations:

$$F_M = -u_{p^*}^2 \quad (2.29)$$

$$F_\chi = -\frac{\kappa u_{p^*} \Delta\chi}{\ln\left(\frac{z_2 - d}{z_1 - d}\right) - \psi_H\left(\frac{z_2 - d}{L}\right) + \psi_H\left(\frac{z_1 - d}{L}\right)} \quad (2.30)$$

To account for the influence of the roughness sublayer, the flux equations above are modified by multiplying them by enhancement factors:

$$F_M = -u_{p*}^2 \left[ \varphi_{M*} \left( \frac{z}{z_*} \right) \right]^{-1} \quad (2.31)$$

$$F_\chi = - \frac{\kappa u_{p*} \Delta\chi}{\ln \left( \frac{z_2 - d}{z_1 - d} \right) - \psi_H \left( \frac{z_2 - d}{L} \right) + \psi_H \left( \frac{z_1 - d}{L} \right)} \cdot \left[ \varphi_{H*} \left( \frac{z}{z_*} \right) \right]^{-1} \quad (2.32)$$

where  $\varphi_{M*}$  is the enhancement factor for momentum and  $\varphi_{H*}$  is the enhancement factor for scalars. The term in the denominator multiplied by the friction velocity is known as the transfer velocity ( $v_{tr}$ ).  $\chi$  denotes scalars such as temperature, CO<sub>2</sub>, NO, etc., and  $\Delta\chi = \chi_2 - \chi_1$  where  $\chi_2$  is the upper level of measurement and  $\chi_1$  is the lower level of measurement.

Out of the two methods for calculating  $L$ , I used the Berkowicz and Prahm method. The gradient Richardson approach also gave good results but not as well as those from the Berkowicz and Prahm method.

### **Modified Bowen Ratio Method**

For the MBR method, the starting point is to apply Equation 2.20 first on simple, nonreactive scalars (e.g. T and CO<sub>2</sub>) for which EC fluxes and gradients are available. The next would be to identify those periods, indicated by similar exchange coefficients, where the Monin-Obukhov similarity theory is fulfilled. When those suitable periods have been found, the unknown fluxes of other scalars for which gradients are available can then be evaluated using Equation 2.20 for those periods. There were periods where the AGM worked better than the MBR method and vice versa.

### **2.2.4 Data Quality**

When applying the AGM or any other gradient-derived flux measurement method, the accurate measurement of the 2-point vertical concentration difference is of paramount importance. It is also the most difficult part since for most forest sites concentrations of trace gases are very low and vertical gradients are up to 20% of the mean concentration (Businger et al., 2006; Foken, 1998; Wolff et al., 2010).

### **Precision requirements**

Several preliminary procedures have to be implemented before measured data can be considered to be of high quality:

- 1) Periods where the data is below the precision of the instrument ( $\sigma$ ,  $2\sigma$  or  $3\sigma$ ) should be removed.
- 2) Data where the conditions are obviously non-stationary should be removed
- 3) Finally, only data showing fully coupled (Thomas and Foken, 2007) (Cs and C) conditions should be allowed to remain.

### **Error propagation method**

The quantity being derived is usually a result of several measured variables. The error propagation principle states that the total error in the derived quantity is equal to the propagation of the separately considered error contributions in each of the measured variables. In considering the error from each variable separately, the variables have to be independent of each other; otherwise the covariance between the variables has also to be considered in the error propagation. The total error in  $f$  is the quadrature sum of the individual error contributions. The measured quantities are assumed to have Gaussian distributions.

Therefore the following simplification can be used to estimate the flux relative error for gradient data:

$$\sigma_F(t) = |F| \left[ 2 \left( \frac{\sigma_{\psi_H}}{\psi_H} \right)^2 + 2 \left( \frac{\sigma_{u_{p^*}}}{u_{p^*}} \right)^2 + \left( \frac{\sigma_{\Delta\chi}}{\Delta\chi} \right)^2 \right]^{0.5} \quad (2.33)$$

Where  $\Delta\chi$  is the concentration gradient and  $K_\chi$  is the turbulent exchange coefficient;  $\sigma_{\Delta\chi}$  is derived from side-by-side measurements taken during calibrations.  $\sigma_{\psi_H}$  is applied according to Wolff et al. (2010). This was the method used for determining errors in the gradient-derived fluxes.

According to a method by Foken (1998), for all flux calculations from gradients, it should be demonstrated that the measuring accuracy is at least 10 times greater than the expected difference between the two measuring heights so that the flux can at least be determined with an accuracy of  $\pm 20\%$ . The profile equations can be divided into a turbulence-caused part and into the difference of the concentration between the two heights. This was an alternative method that was tested for the precision analysis of the flux-gradient data. I found the  $10\sigma$  criteria for this method to be too stringent to the point where over 95% of the concentration differences failed to satisfy the criteria. Therefore I used the  $1\sigma$  criteria.

## **2.3 Eddy Covariance Method**

The eddy covariance method is based on the principle that the flux of a scalar quantity can be derived from the long term mean of the correlation between the fluctuation of the vertical wind velocity ( $w$ )

and the fluctuation of a scalar. The EC method relies on a number of simplifying assumptions which are described in detail by Aubinet et al. (2012) and Baldocchi et al. (1988). In this section, emphasis shall be limited only to the EC theory and corrections that were relevant to this study.

Reynolds postulated that a propagating wave,  $x$ , can be decomposed into its mean and turbulent terms i.e.  $x = \bar{x} + x'$  where  $\bar{x}$  is the mean component of the wave and  $x'$  is the fluctuating component. He also postulated other relationships for decomposing turbulent flow:

$$\overline{w'} = 0 \quad (2.34)$$

$$\overline{w\chi} = \bar{w} \bar{\chi} + \overline{w'\chi'} \quad (2.35)$$

$$\overline{\overline{w\chi}} = \bar{w} \bar{\chi} \quad (2.36)$$

$$\overline{a\chi} = a\bar{\chi} \quad (2.37)$$

$$\overline{\overline{w + \chi}} = \bar{w} + \bar{\chi} \quad (2.38)$$

where  $a$  is a constant.

The total flux as a function of the covariance between  $w$  and  $\chi$  is given by

$$\overline{w'\chi'} = \frac{1}{N-1} \sum_{i=0}^{N-1} [(w_i - \bar{w})(\chi_i - \bar{\chi})] \quad (2.39)$$

where  $N$  is the number of data samples.  $\bar{w} \bar{\chi}$  is accounted for by coordinate rotation which has the effect of reducing its net contribution to zero.

The Navier-Stokes equations (Equation 2.7, 2.8 and 2.9) decompose into the flux equations when the following assumptions of the EC principle are applied:

- 1) a constant flux layer (i.e.  $\frac{\partial \bar{\chi}}{\partial z}, \frac{\partial \bar{u}_i}{\partial z}$  and  $\frac{\partial \bar{T}}{\partial z} \approx 0$ )
- 2) one of the Reynolds's postulates ( $\overline{u_i \bar{\chi}} = 0$ )
- 3) the mean vertical wind velocity component  $\bar{w} = 0$ .

The fluxes are described as:

$$\text{Momentum flux:} \quad u_*^2 = -\overline{u'w'} \quad (2.40),$$

$$\text{Sensible heat flux:} \quad \frac{H}{\rho c_p} = \overline{w'T'} \quad (2.41),$$

$$\text{Latent heat flux:} \quad \frac{LE}{\rho \lambda} = \overline{w'q'} \quad (2.42), \text{ and}$$

Trace gas flux: 
$$\frac{F_{\chi}}{\rho} = \overline{w'\chi'} \quad (2.43)$$

$F$  is the flux,  $\rho$  is the density of the air,  $\overline{w'\chi'}$  is the covariance between the long term means of the fluctuations of the vertical wind ( $w'$ ) measured by a 3D sonic anemometer and the volume mixing ratio ( $\chi'$ ) of a scalar quantity (e.g. CO<sub>2</sub> or NO<sub>2</sub>).

### 2.3.1 Theory

#### **Coordinate rotation**

Wind speed has can be broken down into its three components  $u$ ,  $v$  and  $w$  in the Cartesian coordinates system directions  $x$ ,  $y$  and  $z$  respectively. One of the assumptions of the eddy covariance method which was mentioned above is that the mean vertical wind velocity  $\bar{w} = 0$ . This is not true in reality but must be corrected for by rotating the coordinate system such that the mean vertical wind velocity is 0. This technique also corrects for misalignment of turbulence measurement instruments.

There are three main types of coordinate rotation methods; *double rotation*, *planar fit* and *triple rotation*. Only double rotation and planar fit were used in this study and therefore triple rotation will not be discussed further.

In *double rotation* a series of two rotations are involved:

- 1)  $\bar{v}$  is set to zero by rotating the  $x$  and  $y$  axes about the  $z$  axis.

$$u_1 = u_m \cos\theta + v_m \sin\theta \quad (2.44)$$

$$v_1 = -u_m \sin\theta + v_m \cos\theta \quad (2.45)$$

$$w_1 = w_m \quad (2.46)$$

where

$$\theta = \tan^{-1}\left(\frac{\bar{v}_m}{\bar{u}_m}\right) \quad (2.47)$$

the subscript 1 denotes the velocities after the first rotation.

- 2)  $\bar{w}$  is set to zero by rotating  $x$  and  $z$  axis about the  $y$  axis so that the  $x$  axis is aligned with the mean horizontal streamline direction.

$$u_2 = u_1 \cos\phi + w_1 \sin\phi \quad (2.48)$$

$$v_2 = v_1 \quad (2.49)$$

$$w_2 = -u_1 \sin\phi + w_1 \cos\phi \quad (2.50)$$

where

$$\phi = \tan^{-1} \left( \frac{\bar{w}_1}{\bar{u}_1} \right) \quad (2.51)$$

The above rotation aligns the  $x$ -axis with the mean wind vector, but allows the  $y$  and  $z$  axis to rotate freely about  $x$ , i.e. there are an infinite number of rotations that satisfy  $\bar{v} = \bar{w} = 0$ . The anemometer's final orientation in the  $y$ - $z$  plane after the double rotation depends on its initial orientation. Figure 2.4 illustrates the double rotation procedure.

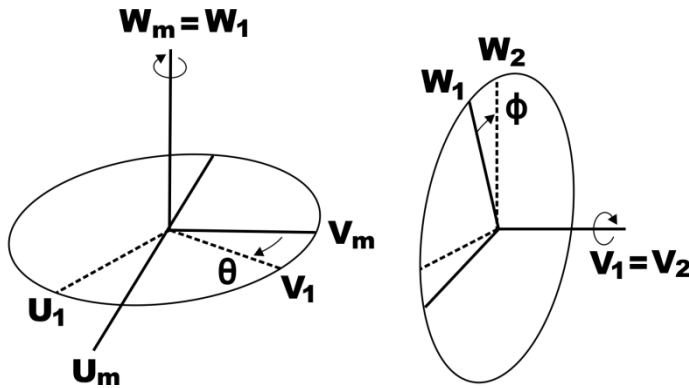


**Fig. 2.5.** Illustration of the double rotation method (Foken, 2008).

The advantage of the double rotation method is that rotation is done for each 30 minute sampling interval, thereby avoiding a cumulative error. Its disadvantage is that low wind speed conditions lead to unrealistically large rotations when using the double rotation method. Therefore a wind threshold has to be set. Ambiguity in the  $y$ - $z$  orientation after rotation is also another disadvantage of the double rotation method. McMillen (1988) suggested that over land a third rotation can be applied to remove this ambiguity by setting  $\bar{v}\bar{w} = 0$  by rotating the new  $y$  and  $z$ -axes around  $x$  (Kaimal and Finnigan, 1994).

The *planar fit method* calculates tilt angles for a given data set. It uses 3 plane factors  $\alpha$ ,  $\beta$ , and  $\gamma$ . More details on the theory can be found in Wilczak et al. (2001). The following is a summary of the principle of the planar fit method according to Wilczak et al. (2001):

A sonic anemometer oriented with its vertical axis perpendicular to the local terrain slope, so that its  $x$  and  $y$ -axes measure the two components of the streamwise flow, when tilted, can be represented by:

$$\vec{u}_p = P(\vec{u}_m - \vec{c}) \quad (2.52)$$

where  $u_m$  is the measured wind vector,  $u_p$  is the wind vector in the mean unrotated streamline coordinate system,  $P$  is a partial rotation matrix which rotates the  $z$ -axis perpendicular to the plane of the mean streamlines, and  $c$  is the mean offset error in the measured winds due to the instrument error.

The mean wind components can then be written as:

$$\bar{u}_p = p_{11}(\bar{u}_m - c_1) + p_{12}(\bar{v}_m - c_2) + p_{13}(w_m - c_3) \quad (2.53)$$

$$\bar{v}_p = p_{21}(\bar{u}_m - c_1) + p_{22}(\bar{v}_m - c_2) + p_{23}(\bar{w}_m - c_3) \quad (2.54)$$

$$\bar{w}_p = p_{31}(\bar{u}_m - c_1) + p_{32}(\bar{v}_m - c_2) + p_{33}(\bar{w}_m - c_3) \quad (2.55)$$

Setting  $w_p=0$  to align the coordinate system into the mean streamline yields

$$\bar{w}_m = c_3 - \frac{p_{31}}{p_{33}}\bar{u}_m - \frac{p_{32}}{p_{33}}\bar{v}_m \quad (2.56)$$

$$= b_0 + b_1\bar{u}_m + b_2\bar{v}_m \quad (2.57)$$

$b_0$ ,  $b_1$  and  $b_2$  can be obtained using linear regression. This procedure was used to calculate the planar fit coefficients as a test of the stability of the sonic anemometer mounting boom. The steps involved in doing the rotations have been included as an appendix. Substitution gives all the elements of the matrix P in terms of  $b_1$  and  $b_2$ .

The advantages of the planar fit method are that several iterations are made when determining the inclination angles, thereby reducing sampling errors. The fact that the planar fit method gives finite mean vertical wind velocities makes it useful for investigations such as large eddy simulation.

The disadvantages of the method are that, the inclination angles produced are a function of the direction of the mean flow. Above fast-growing vegetation, errors may be incurred by the assumption of constant setup conditions over the measurement period. Shaking masts, booms and other equipment mountings affects the stationarity of the equipment and will lead to systematic errors in the planar fit coefficients. The resultant mean wind direction will therefore not be the same as that in the actual setup. A solution to this problem may be to restrict the planar fit calculations to individual periods not longer than a day (Wilczak et al., 2001). The use of inclinometers (sensors that can detect deviations from a horizontal position in the  $x$  and  $y$  horizontal axes) also solves this problem.

### **WPL correction**

In section 2.2 an assumption was made on the mean vertical wind velocity using Reynolds' averaging. This assumption was that only the fluctuating part of the mean vertical wind velocity contributes to the total flux, with the mean vertical velocity being considered to be zero. This simplifying assumption was corrected for by rotating the coordinate system into the mean horizontal wind direction. However because of the different densities of rising and falling particles due to mass balance maintenance, it can be deduced that the mean vertical velocity is not zero (Liebethal and Foken, 2003, 2004).

Webb et al. (1980) came up with the following parameterization for the mean vertical wind velocity:

$$\bar{w} = \frac{\overline{w' \rho_v'}}{\rho_a} + (1 + \mu\sigma) \frac{\overline{w' T'}}{\bar{T}} \quad (2.58)$$

$$\mu = \frac{m_a}{m_v} \quad (2.59)$$

$$\sigma = \frac{\overline{\rho_v}}{\rho_a} \quad (2.60)$$

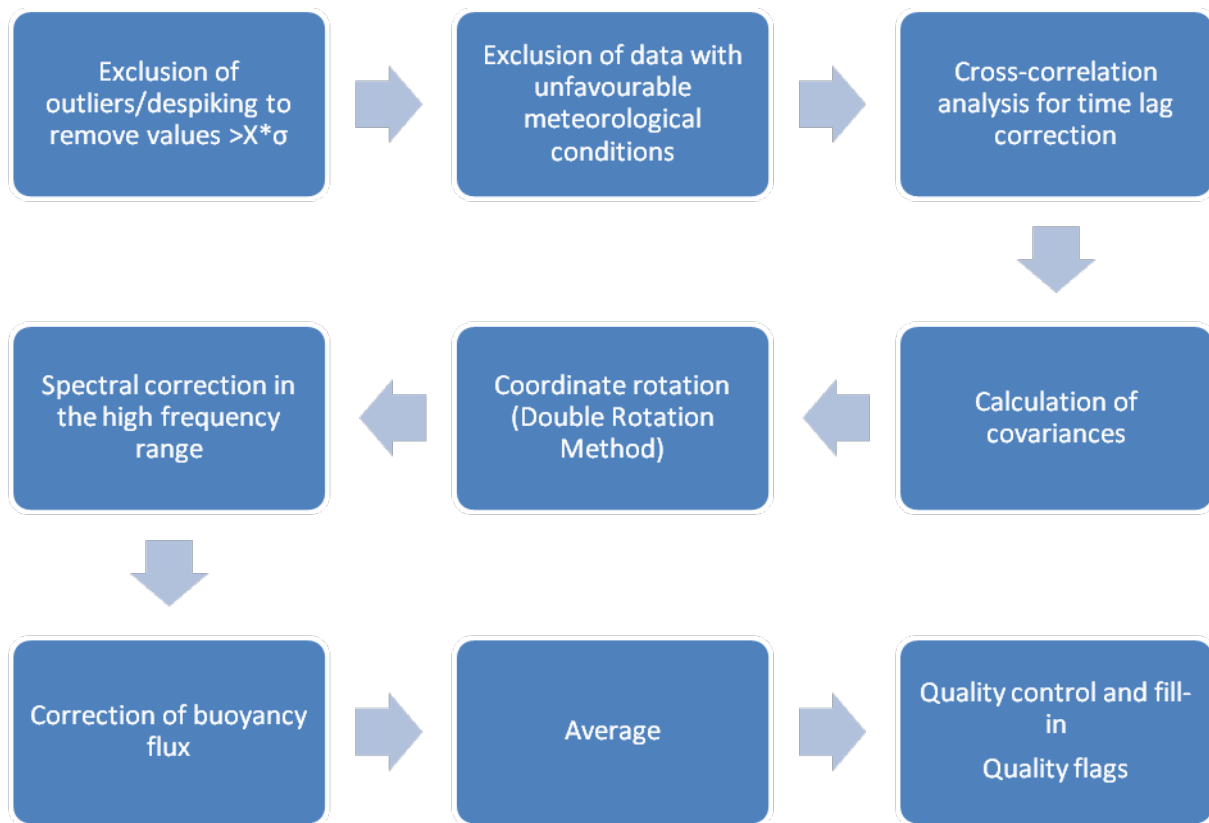
where the subscripts  $v$  and  $a$  refer to water vapour and dry air respectively;  $T$  is the thermodynamic air temperature and  $m$  is the molecular mass of the representative constituent.

The Webb-Pearman-Leuning (WPL) (Leuning, 2007) correction in its corrected form is used in open-path sensors to correct the vertical flux of water vapour density. Without this correction, fluxes derived from open-path sensors can have large errors, especially when the amount of water vapour in the air is high.

### 2.3.2 Experimental realisation

Experimental realisation of the EC method involves finding a suitable site with a tower of the appropriate height for the measurements, setting up the analysers and the sonic anemometer on the tower away from obstacles which can change the wind direction, measuring and logging the measured high frequency data, and performing routine maintenance of the instruments during the measurements. The data processing, post-processing, and analysis are the last steps.

The instrumentation must be set up in such a way that the minimum requirements for EC measurements are met. One thing to consider is the orientation of the sonic anemometer. A more detailed explanation of that will be given in Chapter 4. For the data processing and post-processing, software programs are usually used. Most of the basic EC data processing was done using the Turbulence Knight Version 2 (TK2) EC software (Mauder and Foken, 2004) (see Fig 2.5).

**TK2 data processing and analysis**

**Fig 2.6.** Flowchart of the TK2 EC analysis procedures.

High frequency data is input into the TK2 program. The program calculates averages, covariance and variance for 30 minute data intervals. Cross-correlation to maximize covariance between  $w$  and any of the trace gases or wind vectors is then performed. It considers the corrected time delay between the sensors. Physically impossible data and spikes are rejected using plausibility criteria according to Vickers and Mahrt (1997).

The program then loops through the 30 minute data blocks and performs the following corrections:

- Coordinate rotation with the choice of double rotation, triple rotation or planar fit according to Wilczak et al. (2001).
- Correction of spectral loss due to path length averaging, spatial separation of sensors and the frequency responses of the sensors' signals (Moore, 1986). This is done by the applying transfer functions on the input signals.
- Conversion of sonic temperature fluctuations into fluctuations of actual temperature for calculation of the sensible heat flux according to Schotanus et al. (1983).
- Correction for density fluctuations to determine fluxes of scalar quantities according to Webb et al. (1980).

The corrections are iterated until the change for each correction between successive iterations is less than 0.01%.

After that, post-field quality control is performed according to the Foken et al. (2004) method. This method involves test for steady state conditions using 5 minute subsets of the 30 minute data blocks (Foken and Wichura, 1996) and test for developed turbulence (See 2.3.3) using integral turbulence characteristics (Foken and Wichura, 1996). The end results are the corrected results of the turbulent fluxes (Mauder and Foken, 2006) with quality flags.

### **2.3.3 Data quality**

The main reason for data quality control is to validate if, under the given meteorological conditions, the simplifications of the eddy covariance flux equations are valid. The final aim is to have reliable fluxes after all the post-processing has been done.

The EC technique is valid only for horizontally homogeneous, stationary, and isotropic turbulent airflow. Meteorological measurements fulfil stationarity conditions for short periods roughly up to one hour only (Foken and Wichura, 1996). The requirement for horizontal homogeneity and isotropy means that the quality of the EC measurements is strongly dependent on the measuring site, its terrain and relief.

Empirical methods can be used to investigate whether the processed fluxes meet certain plausibility criteria. For instance these methods are built into TK2 and give output quality flags for each parameter analysed (see Chapter 4). As part of the manual quality control the EC input and output data should also be checked for consistency.

#### ***Systematic flux errors***

In evaluating EC fluxes, several limitations in the available instrumentation have to be accounted for and measures have to be taken to correct for those limitations. For instance, there may be errors associated with the length of the sampling tube, sensor separation, and the frequency response of the analyser.

The length of the sampling tube induces a lag time (which is proportional to the residence time of the sample in the tube) between the sensor and the closed path analyser. This lag time can be determined by carrying out a response test (See Chapter 4) and/or doing a cross-correlation between the vertical wind and each sensor for each high frequency data block. The point of maximum covariance will be equal to the lag time. The lag is then corrected for by shifting the relevant data to match the vertical wind component.

Sensor separation and the frequency response of the analyser require spectral analysis (see next section) for correction. Sensor separation can be corrected for using the Moore correction method (Moore, 1986).

## Spectral analysis

### Lag times

Lag occurs when the vertical velocity sensor and the scalar sensor are mounted apart. The distance between the two instruments then causes a delay from when the individual air parcel (eddy) is measured by each of the two sensors (Moore, 1986). Lag time can be induced by both horizontal and vertical separation as well as electronic delays in the measurement instruments and leads to underestimation of the smallest fluxes.

### Turbulence spectra

It is really important before starting EC measurements, to know if the instruments are suitable enough for the task. For this reason, it is necessary to characterize the frequency range of the analysers. Turbulence spectra are widely used for doing this. A turbulence spectrum describes how energy or flux is distributed among different time scales or magnitudes of turbulence elements. A time series can be decomposed into a superposition of sin and/or cosine waves with different period ( $1/\text{frequency}$ ) and wavelength  $\lambda$ . The most commonly used representations of turbulence spectra are the power spectral density and the cospectral density graphs. The power spectral density (Stull, 1988) of a signal describes how the variance of the signal ( $\chi$ ) is distributed with frequency. The cospectral density (Stull, 1988) of two signals describes how the covariance between the two signals is distributed with frequency.

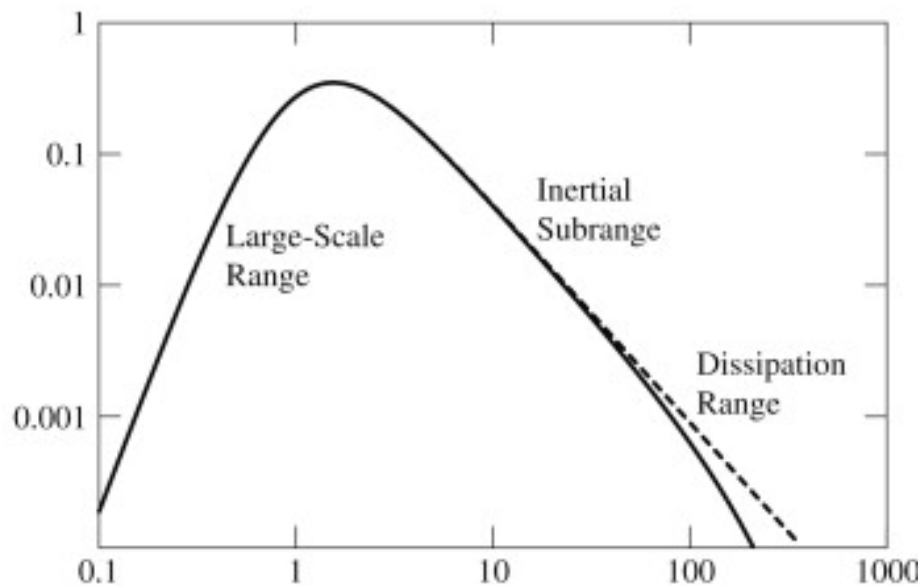


**Fig. 2.7.** Energy spectrum schematic with energy on the vertical axis and arbitrary frequency or wavenumber on the horizontal axis. The dashed line shows an ideal model, which extends the inertial subrange to infinity (after (Lysak et al., 2008)).

The kinetic energy spectrum ( $E(k)$ ) of the ABL in wavenumber space can be divided into three parts (see Fig. 2.7):

- The *large scale range* or *energy production range* where energy is produced by buoyancy and shear.
- The *inertial subrange* where the energy is transferred from larger to smaller scales at a constant rate  $\varepsilon$ . This is known as Kolmogorov's second hypothesis (Kolmogorov, 1991). Dimensional analysis shows that the power spectrum ( $S(k)$ ) follows a universal power law:

$$E_i(k) = S_i(k) = \alpha_i \varepsilon^{2/3} k^{-5/3} \quad (2.61)$$

$i=u, v, w$

In the inertial subrange, power spectra ideally have a  $-5/3$  slope and cospectra have a  $-7/3$  slope.

- The *viscous subrange* where energy of very small eddies is irreversibly converted into kinetic energy of molecular motions and removed from the system as heat.

The area enclosed by the spectral curve and the frequency axis is then a measure of the energy content.

### Ogives

An ogive test (Desjardins et al., 1989; Foken and Oncley, 1995; Oncley et al., 1990) can be used to check if the averaging time of 30 minutes is long enough to measure the low frequency part of the fluxes. It is the cumulative integral of the cospectral density of the vertical wind  $w$  and the quantity of interest  $\chi$  from the highest frequency to the lowest frequency  $f_0$ .

$$\text{Og}_{w,\chi}(f_0) = \int_{\infty}^{f_0} \text{Co}_{w,\chi}(f) df \quad (2.62)$$

The ogive function can be used to test if the flux measured has its maximum value within the averaging time (Foken, 2008) as well as:

- to test of adequate flux averaging interval (Brooks and Rogers, 1997; Oncley, 1989);
- to carry out tests and adjustment of delay time between vertical wind speed and a scalar quantity (Beier and Weber, 1992);
- to test for stationarity of turbulence – (Schulz and Sanderson, 2004), and
- for testing and correction of high frequency damping – (Spirig et al., 2005)

### **Quality control through analysis of Integral Turbulence Characteristics (ITCs)**

Direct verification of EC measurements is not possible since there is no alternative method for measuring the fluxes at the same spatial and temporal scale. Therefore it is necessary to choose empirical methods to investigate whether the fluxes meet certain plausibility criteria. Integral

turbulence characteristics (ITCs) of the vertical wind velocity and temperature can be used to do that (Foken and Wichura, 1996). Integral turbulence characteristics are defined as the normalised standard deviations of fluctuating turbulent parameters (Tillman, 1972). Equation (2.63) is a general form.

$$\frac{\sigma_\chi}{X_*} = \varphi_\chi \left( \frac{z-d}{L} \right) \quad (2.63)$$

where  $\sigma_x$  is the standard deviation of the parameter  $\chi$ ,  $X_*$  is the normalizing factor and  $\varphi_x$  is a function of  $x$ . All other symbols have their usual meanings described earlier.

The word ‘integral’ indicates the turbulence characteristics represent the integral over all frequencies of the turbulent spectrum of the considered parameter. The variable  $\chi$  is the observed parameter and can stand for the vertical wind component  $w$ , the horizontal wind component  $u$ , and the absolute temperature of the air  $T$  or the specific humidity of the air  $q$ .

Experimental observations have found that the ITCs of the wind components and temperature under neutral stratification have the following values:

$$\sigma_w/u_* \approx 1.25, \sigma_u/u_* \approx 2.45, \sigma_v/u_* \approx 1.9, \sigma_T/T_* \approx \text{constant} \quad (2.64)$$

Therefore analysing ITCs and observing the deviations from these values can be useful in assessing the quality of measured data. Tests were made for all stratifications.

### **Random flux errors and precision requirements**

When determining a flux  $F$ , what is really measured is  $x = F + \delta + \varepsilon$ , where  $\delta$  is a random measurement error whose characteristics are generally unknown and  $\varepsilon$  is any systematic error. The random error is therefore distinct from potential systematic errors due to incomplete spectral response or lack of nocturnal mixing (Richardson et al., 2006). Correction for the systematic errors is discussed in the previous sections. The final flux error analysis has to account for both systematic and random errors. In this section, the focus is on the random flux error  $\delta$ . Three possible methods (the correlation coefficient method, the simultaneous flux (two-tower) method and the daily differencing method) for determining the random flux error are discussed here.

#### *Correlation coefficient method*

Based on the relative error from aircraft measurements developed by Lenschow et al. (1994) and Mann and Lenschow (1994). Richardson et al. (2006) defined the random flux error as (also Farmer et al. (2006), Dlugi et al. (2010)):

$$\sigma_F(t) = |F| \left( \frac{2\tau_t}{T} \right)^{0.5} \left( \frac{1 + (\overline{w'\chi'}/\sigma_w\sigma_\chi)^2}{(\overline{w'\chi'}/\sigma_w\sigma_\chi)^2} \right)^{0.5} \quad (2.65)$$

Where  $T$  is the averaging time (30 minutes),  $F$  is the flux;  $\tau$  is the integral time scale which is a measure of how long turbulence remains correlated with itself. It signifies the scale of most flux-carrying eddies (Finnigan, 2000; Richardson et al., 2006). The squared term in the denominator and the numerator of the last bracket in equation 2.64 is the correlation coefficient between the vertical wind velocity  $w$  and the scalar  $\chi$ . Wyngaard et al. (1973) made the assumption that the integral timescales  $\tau_x = \tau_t = \tau_c = z/\bar{u}$ . The indices  $x$ ,  $t$  and  $c$  denote momentum, temperature and scalar quantities respectively. Pryor et al. (2007) found that  $(z - d)/\bar{u}$  where  $z$  is the inlet height,  $d$  is the displacement length and  $\bar{u}$  is the mean horizontal wind speed, gives a better measure of the integral timescale.

Therefore substituting this into Equation 2.65 gives us a reformulation of the random flux error formula:

$$\sigma_F(t) = |F| \left( \frac{2(z-d)}{T\bar{u}} \right)^{0.5} \left( \frac{1 + (\overline{w'\chi'}/\sigma_w\sigma_\chi)^2}{(\overline{w'\chi'}/\sigma_w\sigma_\chi)^2} \right)^{0.5} \quad (2.66)$$

#### *Simultaneous flux method*

Based upon the method suggested by Finkelstein and Sims (2001) and implemented by Hollinger et al. (2004), Hollinger and Richardson (2005), and Richardson et al. (2006), the random error of flux measurements can also be evaluated from simultaneous measurements in one place using two towers. The main assumption in this method of repeated sampling is that the random variables at each tower are independent and have the same distribution.

Suppose we measure the flux  $F$  simultaneously from two towers:

$$F_1 = F + \varepsilon_1 \quad (2.67)$$

$$F_2 = F + \varepsilon_2 \quad (2.68)$$

$\varepsilon_1$  and  $\varepsilon_2$  are random variables. The variance of the difference of the measurements  $F_1$  and  $F_2$  is

$$\sigma^2(F_1 - F_2) = \sigma^2(F_1) + \sigma^2(F_2) + 2cov(F_1, F_2) \quad (2.69)$$

Using the formulation by Hollinger and Richardson (2005), and Richardson et al. (2006) and their assumption that  $\varepsilon_1$  and  $\varepsilon_2$  are independent and have the same distribution we get the random flux error as:

$$\sigma(\varepsilon) = \frac{\sigma(F_1 - F_2)}{\sqrt{2}} \quad (2.70)$$

*Daily differencing method*

An alternative approach to this method for determining  $\sigma(\varepsilon)$ , which is applicable when only 1 tower is available, is to use daily differencing (Hollinger and Richardson, 2005). This method uses fluxes measured on two consecutive days at the same time of day to mimic fluxes made on two different towers simultaneously. A measurement ( $F_1, F_2$ ) is considered valid if the environmental conditions on those two consecutive days (so-called golden days) are the same to within  $\pm 75 \mu\text{mol m}^{-2} \text{s}^{-1}$  photosynthetic photon flux density (PPFD),  $\pm 3 \text{ }^\circ\text{C}$  air temperature, and wind speed within  $1 \text{ m s}^{-1}$ . This is to ensure that the differences in the measured fluxes are as a result of random error and not due to differences in driving forces.

## 2.4 Role of chemical reactions on the fluxes

### 2.4.1 Turbulence and chemical timescales – the Damköhler number

Chemical reactions and turbulence simultaneously play a role in the exchange and transport of reactive trace gases in the atmosphere. The overall effect depends on the strength of the turbulence and that of the chemistry.

If conditions are neutral or near-neutral (Wyngaard et al., 1982),  $\tau_{\text{turb}}$ , the characteristic timescale of turbulence (characteristic residence time of an air parcel in an investigated air column) can be expressed according to Mayer et al. (2009) as

$$\tau_{\text{turb}} = \frac{\Delta z^2 \varphi_M(\zeta) S c_t}{\kappa z_m u_*} \quad (2.71)$$

where  $\Delta z$  is the thickness of the layer under consideration,  $\kappa=0.4$  and  $z_m$  is the mean height above the ground,  $S c_t$  is the turbulent Schmidt number ( $=0.8$ ). All other symbols have their usual meaning as used in this thesis.

From the equation above it is possible to use the relationship between the universal function for momentum exchange and the integral turbulence characteristic for vertical wind velocity

$$\left(\frac{\sigma_w}{u_*}\right)^2 = [\varphi_M(\zeta)]^{-1} \quad (2.72)$$

Therefore  $\tau_{\text{turb}}$  can be reformulated to become:

$$\tau_{\text{turb}} = \frac{\Delta z^2 S c_t}{\kappa z_m u_*} \left(\frac{\sigma_w}{u_*}\right)^{-2} \quad (2.73)$$

This simplifies the calculation of  $\tau_{\text{turb}}$  when using EC for  $u_*$  and  $\sigma_w$ .

For in-canopy measurements, Rannik et al. (2003) proposed a parameterization for the integral turbulence characteristics while measuring at the Hyytiälä site in Finland

$$\frac{\sigma_i}{u_*} = a_i \left\{ \exp \left[ -\alpha_i \left( 1 - \frac{z}{h_c} \right)^{\beta_i} \right] (1 - \gamma_i) + \gamma_i \right\} \quad (2.74)$$

for  $i=u, v, w$  and  $z < h_c$

Only the vertical wind velocity is of interest in this study. Parameterization of Equation 2.74 for the Weidenbrunnen site during EGER IOP-1 produced the following parameter values (Foken et al., 2012):

$$a_i=1.13, \alpha_i=0.9, \beta_i=1.2, \gamma_i=-0.63.$$

This means that below the canopy:

$$\frac{\sigma_w}{u_*} = 1.13 \left\{ \exp \left[ -0.9 \left( 1 - \frac{z}{23} \right)^{1.2} \right] (1 + 0.63) - 0.63 \right\} \quad (2.75)$$

And above the canopy

$$\frac{\sigma_w}{u_*} = 1.13 \quad (2.76)$$

The characteristic chemical timescales (the lifetime of a species consumed in the respective reaction) of NO, NO<sub>2</sub> and O<sub>3</sub> are defined according to Lenschow (1982) as:

$$\tau_{NO} = \frac{1}{k_1 N_{O_3}} \quad (2.77)$$

$$\tau_{NO_2} = \frac{1}{J_{NO_2}} \quad (2.78)$$

$$\tau_{O_3} = \frac{1}{k_1 N_{NO}} \quad (2.79)$$

and the chemical timescale for the whole NO-O<sub>3</sub>-NO<sub>2</sub> triad,  $\tau_{chem}$ , is defined according to Lenschow (1982) as:

$$\tau_{chem} = 2 \left[ J_{NO_2}^2 + k_1^2 (N_{O_3} - N_{NO})^2 + 2k_1 J_{NO_2} (N_{O_3} + N_{NO} + 2N_{NO_2}) \right]^{-0.5} \quad (2.80)$$

where  $J_{NO_2}$  is calculated from parameterization of incoming shortwave radiation measurements according to Trebs et al. (2009) as:

$$J_{NO_2} = B_1 G + B_2 G^2 \quad (2.81)$$

$B_1 = (1.47 \pm 0.03) \times 10^{-5} \text{ W}^{-1} \text{ m}^2 \text{ s}^{-1}$ ,  $B_2 = (-4.84 \pm 0.31) \times 10^{-9} \text{ W}^{-2} \text{ m}^4 \text{ s}^{-2}$ ,  $G$  is the global solar irradiance,  $k_1$  (taken from Atkinson et al. (2004)) is the rate constant for the NO-O<sub>3</sub>-NO<sub>2</sub> forward reaction (R3 in Chapter 1)),  $N_{NO}$ ,  $N_{NO_2}$  and  $N_{O_3}$  are the number densities of NO, NO<sub>2</sub> and O<sub>3</sub> respectively.

A useful tool for determining whether fluxes are diverged by chemical reactions is the Damköhler number (Da), a dimensionless quantity being defined as the ratio of the characteristic timescales of turbulent transport to chemical reactions.

For a species  $x$ ,

$$Da_x = \frac{\tau_{turb}}{\tau_x} \quad (2.82)$$

and for the whole NO-O<sub>3</sub>-NO<sub>2</sub> triad

$$Da = \frac{\tau_{turb}}{\tau_{chem}} \quad (2.83)$$

In order to determine a threshold below which there is certainty that there is no chemical influence during the transport process of reactive trace gases, a critical Damköhler number  $Da_{crit}$  can be defined. This is arbitrarily taken as 0.1 meaning that chemical transformations are proceeding at least ten times slower than turbulent processes for the data to be accepted as not having been influenced by chemistry. In the data quality check process, all data above  $Da_{crit}$  are flagged to ensure that all fluxes are not distorted by chemical influences.

#### 2.4.2 Intensity of segregation of the NO-O<sub>3</sub>-NO<sub>2</sub> triad

Another useful tool for studying the effect of chemistry on concentrations and fluxes of matter is the intensity of segregation. The intensity of segregation ( $I_s$ ) is the long-term (30 minutes) covariance of the fluctuations of two species normalized by the long-term product of their means (Danckwerts, 1952):

$$I_s = \frac{\overline{\chi_1' \chi_2'}}{\overline{\chi_1} \overline{\chi_2}} \quad (2.84)$$

where  $\chi_1'$  and  $\chi_2'$  are the fluctuations of the mean (30 minute) concentrations  $\chi_1$  and  $\chi_2$  respectively. The overbar denotes that the long term mean of the fluctuations is considered. (de Arellano and Duynkerke, 1993)

The intensity of segregation is an indicator of the extent of mixing between two chemical species by turbulent motion (Brodkey, 1981; Kramm and Meixner, 2000). Its magnitude ranges from 0 to -1 with 0 indicating perfect mixing between the two species and -1 indicating perfect separation between the two species. Any value of  $I_s$  not equal to zero indicates that the covariance of the fluctuations between the two species has to be taken into account. A positive intensity of segregation value indicates that the reactants are correlated or are premixed.

For the NO-O<sub>3</sub>-NO<sub>2</sub> triad, the intensity of segregation is therefore given as

$$I_s = \frac{\overline{NO'O_3'}}{\overline{NO} \overline{O_3}} \quad (2.85)$$

## 2.5 Designing the experiments

A number of questions had to be asked before designing the experiments:

- are the available instruments fast enough, sensitive enough for the measurement we want to carry out?
- what are the implications of having such long tubes running from the top of the tower to the container in terms of high frequency losses and in-situ chemical reactions?
- does the site meet the EC and gradient flux requirements?

To start with the first question, it was necessary to ensure that the EC measurement system was carefully calibrated and that the setup was installed correctly in a way which meets the requirements of the EC method (see 2.3). In addition, care was taken to ensure that the measured data was plausible as well as to ensuring that the reactive trace gas measurements of NO<sub>x</sub> were significant in a rural environment where concentrations of NO<sub>x</sub> are known to be low (see Table 1.1). The procedures are outlined in 3.8.

For the second objective, an approach which involved rigorous data quality analysis of the mixing ratios as well as concentration differences of the reactive trace gases was taken. This was necessary because concentration differences of reactive trace gases dominated by low background mixing ratios of such compounds are most likely to be very small and may be insignificant. The procedures followed for handling the gradient data are outlined in 3.9. The third and fourth objectives are all related to the work carried out in fulfilling the first and second objective.

## Chapter 3: Experimental site and setup

### 3.1 Site description

#### 3.1.1 Location

Measurements were carried out at the FLUXNET site Waldstein-Weidenbrunnen (DE-Bay, 50°8'N, 11°52'E). The forest site is predominated by Norway spruce, with the average canopy height being 25 m. The site is described in detail by Gerstberger et al. (2004) and further information can also be found in Staudt and Foken (2007).

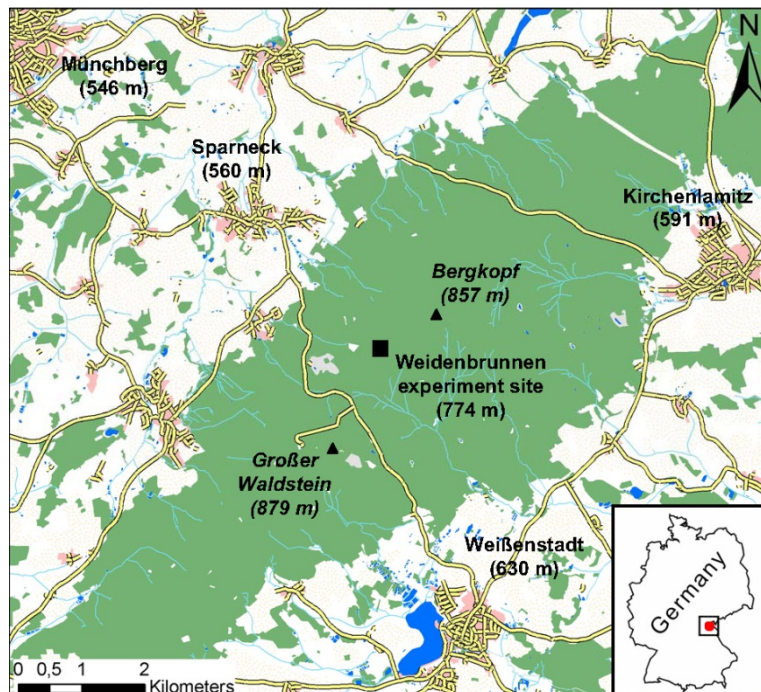


**Fig. 3.1.** Map of the EGER experimental site and surroundings (after Moravek (2008))

#### 3.1.2 Climate

According to the effective climate classification by Köppen modified by Trewartha (Hupfer, 1996), the site can be classified as having a continental temperate climate (Foken, 2003; Gerstberger et al., 2004). It is in climate class Dc according to the classification by Köppen/Trewartha/Rudloff (Hendl, 1991). Eiden et al. (1989) classified it alternatively as moist continental with high precipitation.

The mean annual temperature at the site is 5.3 °C with the temperature amplitude being 18.1 K. Mean winter temperatures have been increasing at the rate of 0.33 K per decade, while for the other seasons, the mean temperature increase is 0.52 K per decade. Total annual precipitation has been estimated at 1162.5 mm per year. December and July have been observed to have the highest precipitation for at

the site. The area is covered by snow for approximately 80 days per year according to records of measurements at Fichtelberg-Hüttstadl (662 m a.s.l.). Statistics indicate that the annual snow cover period is declining at a rate of 10 days per decade. The climate data (period 1971-2000 Foken, 2003) and trends (Foken, 2004; Seifert, 2004) is for the period 1971-2000 measured at a clearing, “the Pflanzgarten”, very close to the measurement site.

### 3.2 Trace gas measurements

Measurements were divided into two **I**ntensive **O**bservation **P**eriods (IOPs), namely IOP-1 (Autumn 2007) and IOP-2 (Summer 2008). Measurements during IOP-2 focused on determining EC fluxes of the reactive trace gases CO<sub>2</sub>, H<sub>2</sub>O, O<sub>3</sub>, NO, and NO<sub>2</sub>. In addition, EC flux measurements of CO<sub>2</sub>, H<sub>2</sub>O and the energy fluxes were carried out. The purpose of the IOP-2 investigation was to study the effect of chemical and turbulent exchange processes on the magnitude and direction of the EC fluxes of the NO-O<sub>3</sub>-NO<sub>2</sub> triad. In addition, it was sought to find the effect of chemistry and turbulence on the gradient-derived fluxes.

In order to meet the objectives of this thesis, the experimental work had to be designed and carried out with these objectives in mind:

- (1) To present and report reliable simultaneous high frequency, high resolution measurements of the fluxes of the full NO-O<sub>3</sub>-NO<sub>2</sub> triad and to investigate the source/sink relationship between its constituents and the canopy-atmosphere system at *Waldstein-Weidenbrunnen* using a novel EC measurement system.
- (2)
- (3) To investigate the influence of chemical reactions on turbulent transport and *vice versa* on the fluxes of the NO-O<sub>3</sub>-NO<sub>2</sub> above the forest ecosystem.
- (4) To investigate the performance and applicability of flux-gradient techniques to the measurement of reactive trace gas fluxes in the roughness sublayer at *Waldstein-Weidenbrunnen*.
- (5) To compare the results from the flux-gradient techniques to the reference eddy covariance results.

This chapter therefore aims to present a chronological account of how the objectives of the thesis were approached.

The main challenge of this work was that the investigation involved measurement of reactive trace gases where the background levels are very low. In addition, there is a strong likelihood of chemical transformations of the reactive trace gases during turbulent transportation. Vertical concentration

gradients measured during IOP-1 (Foken et al., 2012) had shown that even for the non-reactive trace gases ( $\text{CO}_2$  and  $\text{H}_2\text{O}$ ) it was difficult to resolve the concentration differences above the forest canopy. In addition, previous work on reactive trace gas gradients (Foken, 1998) had shown that the gradients above the forest canopy at this site cannot be resolved with the available instrumentation.

### 3.3 Experimental setup

For the measurements involving eddy covariance of reactive trace gases, data were obtained in the period of June-July 2008 during the second intensive measurement campaign of the field experiment EGER conducted at Weidenbrunnen.

High-frequency turbulence measurements (20 Hz) of horizontal and vertical wind components  $u$ ,  $v$ ,  $w$ , and sonic temperature  $T_s$  were performed using a sonic anemometers (CSAT3 Campbell Scientific, Inc.), and a fast-response gas analyser (LI-7000, LI-COR Biosciences) for mixing ratios of carbon dioxide  $\text{CO}_2$  and water vapour  $\text{H}_2\text{O}$ . The system was installed at the top of the 32-m high walk-up tower, the “Main Tower” – henceforth referred to as MT. The “Turbulence Tower” shall henceforth be referred to as TT.

To make it easier to follow the text, the following nomenclature shall be used when referring to the measurement complexes:

**Table 3.1.** *Abbreviations used to refer to the measurement complexes relevant to this study*

Measurement system	Height of measurement (m)	Abbreviation
Max Planck Institute (MPI)	32.5 m (MT)	MPI32
University of Bayreuth (UBT)	36 m (TT)	UBT36
	32 m (MT)	UBT32
	23 m (TT)	UBT23
MPI reactive trace gas profile system	31 m -24 m (IOP-2)	RETGAP2

---

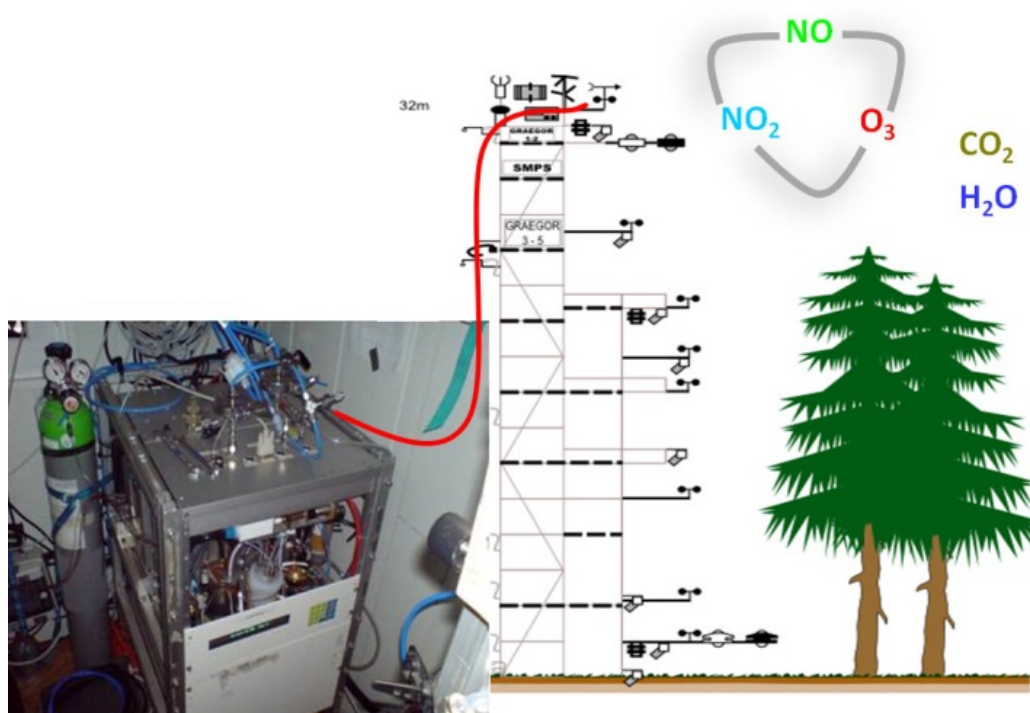


**Fig. 3.2.** Setup of the CLD 790SR2 NO analyser (left) and the MT at the measurement site during IOP-2.

Fluxes of NO and NO<sub>2</sub> were derived from highly resolved, high frequency time series (5 Hz) of NO and NO<sub>2</sub> measured by a fast response, chemiluminescence-based (see 3.4.1) 2-channel NO detector (CLD 790 SR2, ECO PHYSICS GmbH, Switzerland). One channel was connected to 2 solid-state blue light converters for high efficiency conversion of NO<sub>2</sub> to NO (indirect method of detecting NO<sub>2</sub>). The limit of detection (LOD) of NO for the instrument was  $0.010 \pm 0.005$  ppb.

A 53 m long insulated bundle containing the Teflon® inlet tubes, 2 spare tubes, tube heating as well as interface cables from the data logger ran from the top of the tower to the instruments and control computers in the container. Filters and flow restrictors were installed in front of the inlets to ensure that the residence time in the tubes was as short as possible as well as to ensure that fully turbulent conditions were maintained during transportation of the air samples in the tubes.

### 3.4 Trace gas EC measurement instrumentation

The EC measurement system consisted of a CR3000 data-logger, the CSAT3 sonic anemometer, the LI-7000 CO<sub>2</sub>/H<sub>2</sub>O gas analyser, the CLD 790SR2 NO analyser. In addition, 5 O<sub>3</sub> EC flux instruments were simultaneously data-logged together with the other analysers of my EC system but independently maintained by Zhilin Zhu (Zhu et al., 2009). Figure 3.3 shows a schematic of the instrumentation and data acquisition system setup.

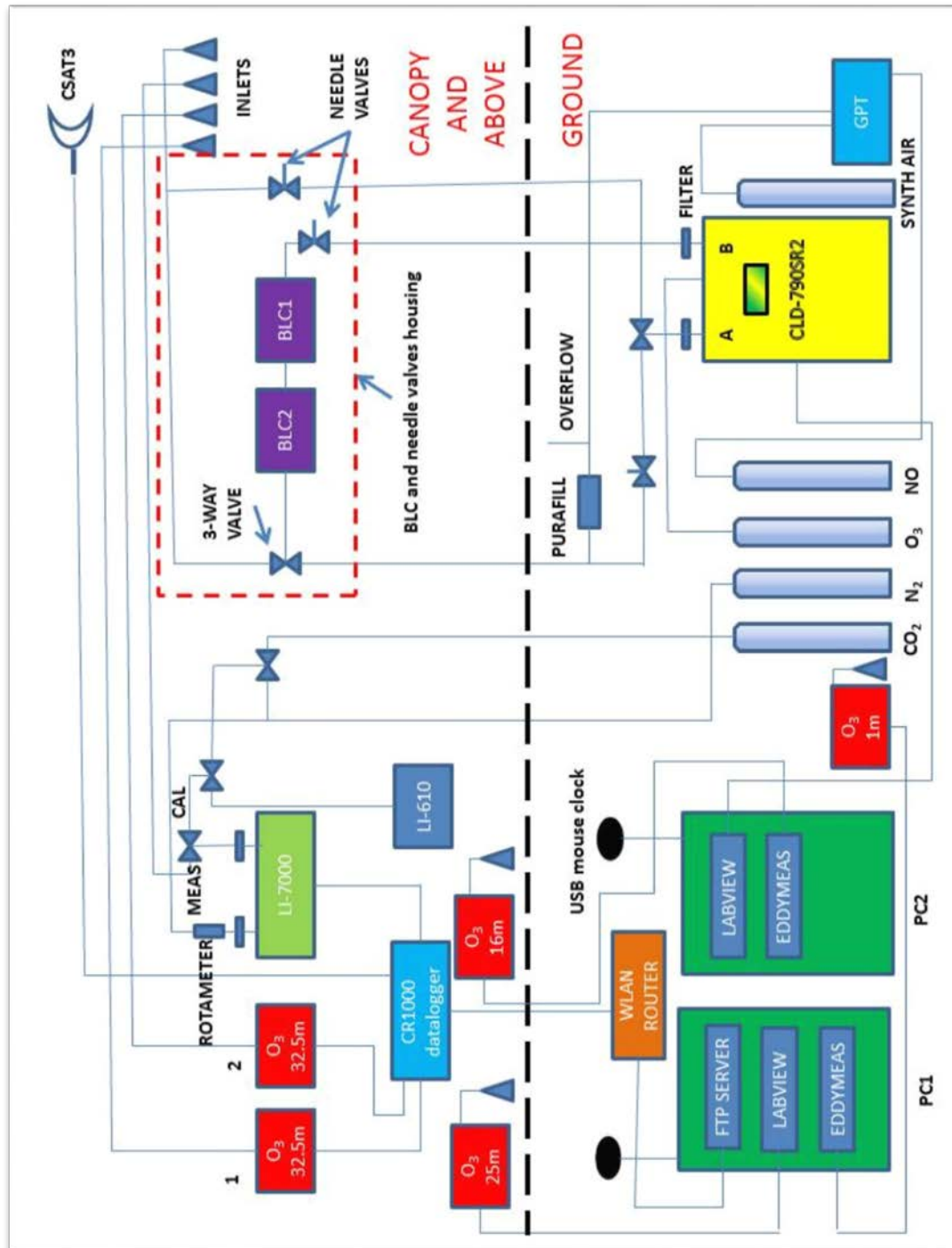


Fig. 3.3. Diagram of the main instrumentation and data acquisition system for this research during IOP-2.

**Table 3.2.** A summary of the specifications of the main instruments used

Parameter	Sampling height (m)	Sampling frequency (Hz)	Technique/sensor	Model, manufacturer	Detection limit or precision
NO	32.5	0.2	Dry chemiluminescence	CLD790SR2, ECO PHYSICS GmbH	$\pm 0.010 \text{ nmol mol}^{-1}$ ( $3\sigma$ , continuous mode)
NO <sub>2</sub>	32.5	0.2	Dry chemiluminescence	CLD790SR2	$\pm 0.020 \text{ nmol mol}^{-1}$ ( $3\sigma$ , continuous mode)
CO <sub>2</sub>	32.5	0.05	Infrared absorption	LI-7000, LI-COR Biosciences	$0.06 \text{ } \mu\text{mol mol}^{-1}$
H <sub>2</sub> O	32.5	0.05	Infrared absorption	LI-7000	$0.0015 \text{ mmol mol}^{-1}$
O <sub>3</sub>	32.5	0.05	chemiluminescence	GFAS OSG-2, ENVISCOPE GmbH	variable*
wind vector	32.5	0.05	ultrasound	CSAT3 Campbell scientific	$0.05 \text{ m s}^{-1}$
Sonic temperature	32.5	0.05	ultrasound	CSAT3 Campbell scientific	$0.05 \text{ K}$

\* the detection limit depended on the length of use of the organic dye plate.

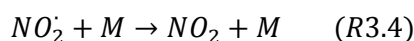
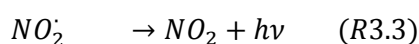
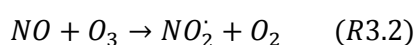
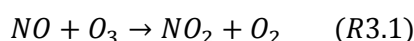
### 3.4.1 NO and NO<sub>2</sub> – the CLD 790SR2 NO<sub>x</sub> analyser

As shown in the experimental setup diagram (Fig. 3.3), the NO<sub>x</sub> analyser used was the CLD 790SR2. This instrument works on the chemiluminescence principle as applied to the reaction between NO and O<sub>3</sub>. It has previously been used for the measurement of NO<sub>x</sub> concentrations at sea (Hosaynali Beygi et al., 2011) and the measurement of NO<sub>x</sub> fluxes on a grassland site (Stella et al., 2013).

**Measurement of NO – the chemiluminescence principle**

Chemiluminescence is the process whereby electromagnetic energy in the form of photons is emitted by the reaction between two chemical substances. The chemiluminescence method gives the best results whenever the difficult analysis of the tiny molecule NO in air samples is required. The chemiluminescence method allows the detection of extremely low concentrations of NO, being not only fast but also very sensitive and specific to NO.

In the chemiluminescent reaction between NO and O<sub>3</sub> nitrogen oxide reacts with O<sub>3</sub> under very low pressure conditions to produce NO<sub>2</sub> and O<sub>2</sub>:



The radiation emission from the photons ( $h\nu$ ) is in the wavelength range 600 – 3000 nm with a peak intensity corresponding to ~1200 nm. This radiation can be detected by a photo-multiplier tube (PMT) which is a photosensitive vacuum -filled tube that can highly multiply the low current generated by weak incident light (e.g. from individual photon emissions) . In the presence of excess O<sub>3</sub>, the intensity of the photon emission is directly proportional to the concentration of NO in the air sample.

Most of the NO<sub>2</sub><sup>\*</sup> (excited NO<sub>2</sub>) returns to the ground state without radiation emission because of collisions with other molecules (M) (R3.4) in an unwanted process called quenching. It is unwanted because it results in less chemiluminescence occurring, hence leading to an underestimation of the NO signal in the air sample. In measurement systems, the presence of a pre-chamber (see Fig. 3.4) solves this problem. The extent to which quenching occurs depends on the characteristics of the colliding molecule M. For instance water (H<sub>2</sub>O), carbon dioxide (CO<sub>2</sub>), and hydrocarbons quench NO chemiluminescence more effectively than N<sub>2</sub> and O<sub>2</sub>.

**Measurement of NO<sub>2</sub>**

In order to measure NO<sub>2</sub> in the sample air, it has to be converted first into NO. This is accomplished by passing the sample air through a converter, which converts the NO<sub>2</sub> component of the sample air into NO. It is important that the converter be very specific to NO<sub>2</sub>, otherwise conversion of other nitrogen oxides to NO might result, leading to erroneous concentration of NO<sub>2</sub>. A widely used and effective way for doing this is by using a photolytic converter, the so-called “blue light converter” (BLC) with a very specific spectral emission range corresponding to the energy required to convert NO<sub>2</sub> to NO with minimal interference with from e.g. HONO and NO<sub>3</sub>.

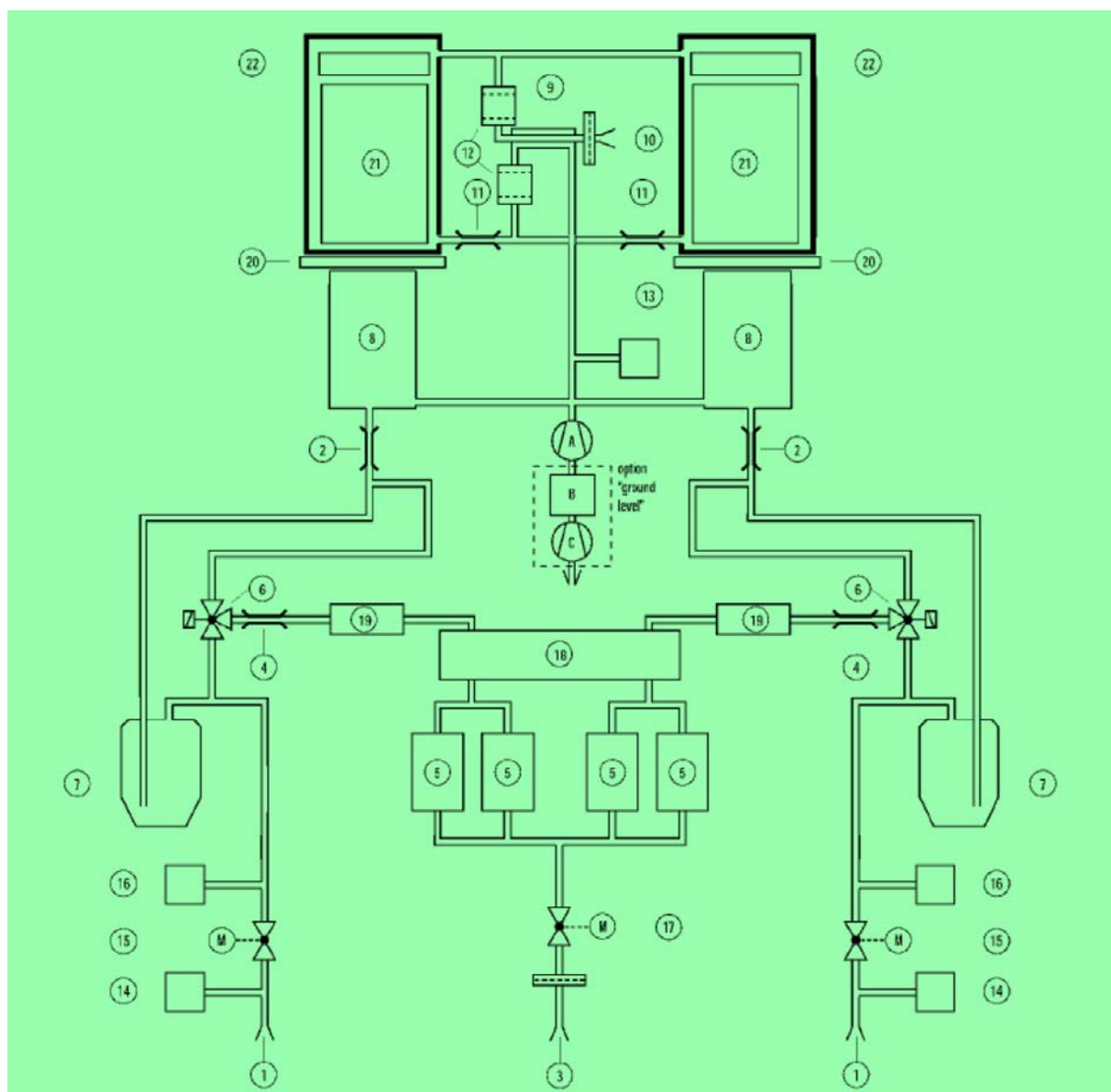


**Fig. 3.4.** Schematic of a 2-channel CLD 790 SR2 (source: ECO Physics CLD 790 SR manual, ECO Physics, Switzerland). The two channels above are for NO and NO<sub>2</sub> measurements. (A) Scroll pump, (B) ozone scrubber, (C) membrane pump, (1) sample inlet, (2) sample flow restrictor, (3) O<sub>2</sub> inlet with filter, (4) ozone flow restrictor, (5) ozone generators, (6) solenoid valves, (7) pre-chambers, (8) main chamber, (9) permeation tube, (10) dry air inlet with filter, (11) PMT flushing outlet with flow restrictor, (12) filter with drying agent, (13) pressure sensor 'reactor', (14) pressure sensor 'inlet', (15) pressure regulator 'sample', (16) pressure sensor 'back', (17) pressure regulator, O<sub>2</sub> inlet, (18) damper, (19) pre-volume, (20) red filter, (21) photomultiplier (PMT), (22) high-voltage module. Adapted from CLD790SR2 manual; ECOPHYSICS, Switzerland.

For this purpose a highly specific BLC, the AQD (MetCon GmbH, Germany) was used. Two such converters were mounted inside special ventilated boxes to protect them from rain and large external temperature fluctuations. The boxes also sheltered the flow restrictors for the NO/NO<sub>2</sub> inlets from the

weather. The spectral range of the AQD BLC is shown in Fig. 3.5 below. Generally, the conversion efficiency of an  $\text{NO}_2$  converter is an important property and will be discussed in the instrument calibration section (3.7.1). To increase the conversion efficiency, two BLCs mounted in series were used. The series configuration also has the advantage that it does not damp the turbulence signal during transportation through the tubes, something that might occur if a parallel configuration (which would involve splitting the airflow) were to be used.

In this case,  $\text{NO}_2$  is measured indirectly as  $\text{NO}_2 = \text{NO}_x - \text{NO}$ . The NO is taken from the NO measuring channel (Channel A on the CLD) and the  $\text{NO}_x$  from the channel connected to the photolytic converter (Channel B on the CLD). The two channels had to be intercalibrated with respect to NO to ensure that the NO from Channel B matches that in Channel A; otherwise erroneous measurements of  $\text{NO}_2$  would have resulted.

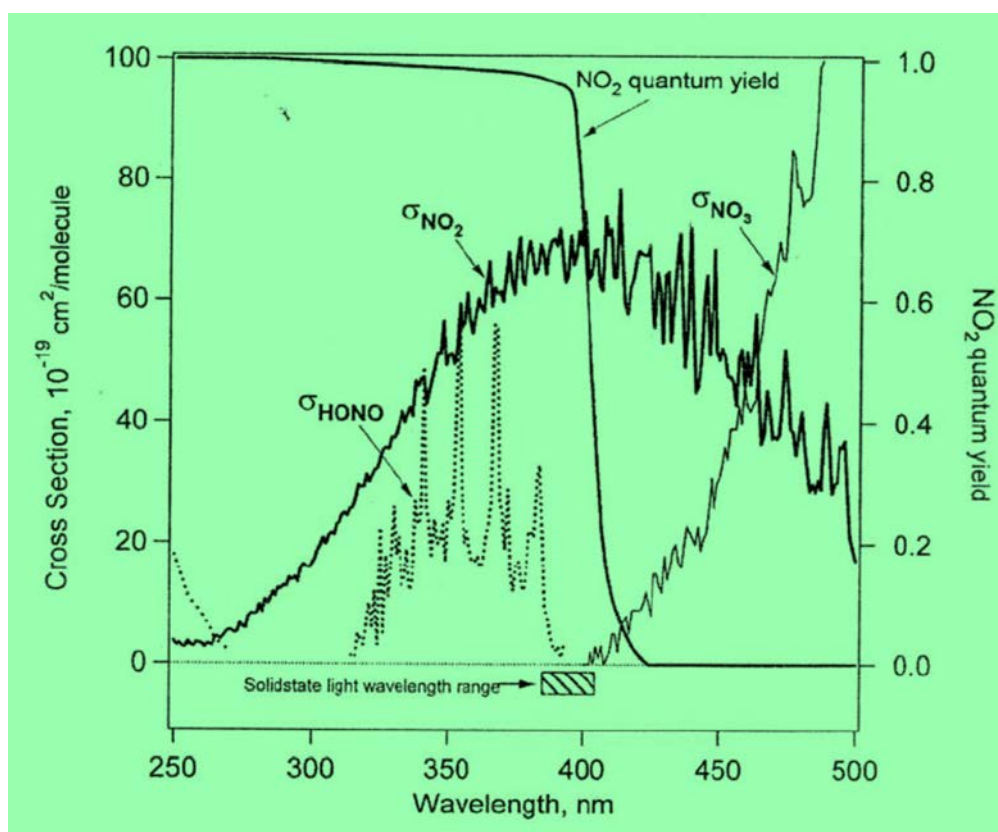


**Fig. 3.5.** Illustration of the absorption cross-section of the BLC. The wavelength range of the BLC's LEDs is such that the interfering species are not simultaneously photolysed. Adapted from the AQD manual; MetCon GmbH, Germany.

#### **Modifications to the CLD to fit the specific experimental requirements**

The instrument was specifically designed for airborne measurements in the troposphere. Therefore to be able to use it successfully for ground-based measurements, some modifications were necessary to make it suitable for the experimental environment.

- The instrument will not power up unless the pressure is below 1000 mbar because it was designed for operation in airborne aircraft where pressures are lower than that. To be able to use it on or near the ground level, a pressure below 1000 mbar had to be mimicked. This was achieved by placing a small tube at the inlet of the pressure sensor and sucking out some air and then sealing the tube.
- The analyser comes mounted with a built in scroll pump to make it easier to operate in an aircraft. The whole instrument is powered off a 28V, 5A source. Initially, the instrument was operated using its built-in internal pump. The internal pump had the advantage that the connecting tubes from the pump to the reaction chambers were very short, and therefore the reaction chamber pressure was very low (~6 mbar per channel). The lower the reaction chamber pressure, the less noise there is in the signal of the instrument. However, operating the analyser in the container using the internal pump resulted in a gradual temperature rise which the air conditioning system could not cope with. This temperature increase in the container had a negative effect not only on the analyser's performance, but also on the other instruments from the other measurement systems that were housed in the container.

Therefore to solve this problem, an external scroll pump (Edwards, UK) with similar specifications as the one built-in one was used. A hole was made in the side of the container and the external pump was mounted at the back of the container directly behind the CLD 790 SR2. The metal tubing from the reaction chambers had to be extended each by another tube. The shortest possible tube extensions for this purpose were 98 cm long each. Adding these tube extensions increased the reaction chamber pressure to ~13 mBar per channel. Subsequent calibrations showed that the interference signals in the pre-chambers had increased from ~900 cps to ~1000 cps. This did not have any noticeable effect on the overall precision of the instrument.

- Besides having a built-in pump, the analyser has a built-in ozone destroyer. The ozone destroyer converts ozone from the pump's exhaust (being sucked away from the reaction chambers) into oxygen by heating it to a temperature of over 600 °C. It was found that the ozone destroyer was an additional source of heat in the container and it was disconnected at the same time that the internal pump. Therefore an external ozone destroyer (Ecophysics, Dürnten, Switzerland) was used.
- The safety electronics of the CLD 790 SR2 are designed in such a way that the instrument will not power up its ozone generators and hence get into operating mode until the ozone destroyer reaches a temperature of over 600°C. This is to ensure that no O<sub>3</sub>, which is dangerous when inhaled, is allowed to escape before it is destroyed. After studying the instrument's ozone power distribution electronics (which was on a circuit board called PONOX) and measuring the resistance of the thermistor connected to the O<sub>3</sub> destroyer, it was

identified that reaching a temperature of over 600 °C coincided with a thermistor resistance above 100  $\Omega$ . Therefore the power supply to the ozone destroyer heating element was disconnected and the thermistor and replaced with a 1 k $\Omega$  resistor. This allowed the CLD 790 SR2 to operate with an external ozone destroyer mounted at the back of the container directly downstream of the external scroll pump. In this way, the container heat problem was solved.

### ***Temperature sensitivity analysis***

The temperature range during the EGER IOP-2 measurements was quite high (up to 10 °C). The CLD 790 SR2 was housed in a container where a lot of other instruments were also present. As a result, the level of heat generated in the container, despite the presence of an air conditioning system, was quite high. Preliminary observation of the counts per second (cps) from the NO analyser during calibrations showed that there was a dependence of the cps on the ambient temperature during the calibration. Higher temperatures produced more noise in the photomultipliers of the analyser. The LI-7000 CO<sub>2</sub>/H<sub>2</sub>O analyser was situated in a ventilated, temperature-controlled shielded box at the top of the MT. The temperature control was achieved via a thermostat-controlled fan with a heating element. The set temperature was 25°C. The temperature control mechanisms were useful but insufficient. Therefore a temperature sensitivity analysis was conducted on the CLD 790 SR2 as well as the LI-7000 after the measurement campaign. The analysis was conducted in a large temperature controlled chamber over the range 5 °C – 35 °C in 5 °C steps. For each temperature point, data was continuously logged from both analysers while first zero air, then the span gas (NO at 10, 20, 30, 40 and 50 ppb for the CLD 790 SR2 and 400 ppm and 700 ppm for the LI-7000) were administered.

### ***Residence time of trace gases in the Teflon® tubes – response test and needle valves***

The sample air for the CLD had to travel 53 m in the ¼ inch Teflon® tubes from the top of the MT to the inlets of the analyser. A theoretical calculation for the residence time of the air sample in the tubes gives 35.4 s. This figure is too high when compared to the average turbulence timescale at the site. As a result there is a strong possibility of loss of turbulence during transport of the trace gas in the inlet tubes. The residence time of a reactive trace gas in a tube must be shorter than the chemical timescale of the reactive trace otherwise losses can occur due to the trace gas reacting during transport and being reduced to other chemical substances. To solve this problem, flow restrictors (in the form of needle valves) were installed at the NO and NO<sub>2</sub> sample inlets (see Fig. 3.3). For NO, the flow restrictor was installed just in front of the inlet while for NO<sub>2</sub>, it was installed downstream of the BLCs. This was done to ensure that the residence time of the sample air inside the BLCs was not too low so that conversion efficiency would not be compromised. The purpose of the flow restrictors is to create a low pressure condition inside the inlet tube downstream of the flow restrictor. As a result of the low pressure condition, the flow rate inside the tube increases, and hence the residence time inside

the tube according to the Bernoulli principle. The pressure between the flow restrictors and the analyser (the backpressure) was monitored daily and kept stable at 87 hPa.

Furthermore, a response test was done to check the residence time of the air sample in the 53 m long inlet tubes for NO and NO<sub>2</sub> with the flow restrictors installed. A three way valve (see Fig. 3.3) was used to shunt either 50 ppb NO or zero air into the NO or NO<sub>2</sub> inlet at the top of the tower. The exact time at which NO or zero air was switched on was noted down. On the ground, the CLD 790 SR2 NO analyser was continuously logging the concentration from the inlets.

The clock used at the top of the tower was synchronized with the CLD 790 SR2 data logging computer. The results showed a residence time of 7.8 s for NO and 7.9 s for NO<sub>2</sub>. Comparison with a theoretical calculation showed agreement to within 2%. In addition, cross-correlation analyses were done between the vertical wind component  $w$ , and NO and NO<sub>2</sub> respectively. The results obtained were on average similar to those from the response test.

### 3.4.2 Measurement of O<sub>3</sub>

The O<sub>3</sub> part of the system was jointly managed with Prof Dr Zhilin Zhu during IOP-2. The GFAS OS-G-2 ozone sensor can only measure relative concentrations of O<sub>3</sub> in the atmosphere as a voltage signal. Therefore to obtain calibrated O<sub>3</sub> concentrations, it is necessary to calibrate the system with simultaneous absolute O<sub>3</sub> measurements. This was done using O<sub>3</sub> concentrations at 32 m from the TEI 49c O<sub>3</sub> analyser which was part of the RETGAP2 system. The procedure involved using the equation outlined below:

$$F_{O_3} [ppb] = \frac{\overline{w'O_3'} [mV]}{O_3 [mV]} \cdot O_3 [ppb] \quad (3.1)$$

$F_{O_3} [ppb]$  is the calibrated O<sub>3</sub> flux,  $w'O_3' [mV]$  is the covariance between the vertical wind and the uncalibrated O<sub>3</sub> relative signal (mV), and  $O_3 [ppb]$  is the absolute O<sub>3</sub> signal at 32 m from the RETGAP2 TEI49c ozone analyser. Muller et al. (2010) tested various methods for calibrating fast ozone sensors and also found this technique to be effective.

The GFAS OS-G-2 ozone sonde maintenance is detailed in Zhu et al. (2009). In summary it works on the chemiluminescence principle using a thin film of Coumarin® based organic dye on small circular discs. A plate is inserted into the instrument and provides the medium for chemiluminescence which lasts typically 3-5 days before the instrument loses sensitivity and the disc has to be replaced.

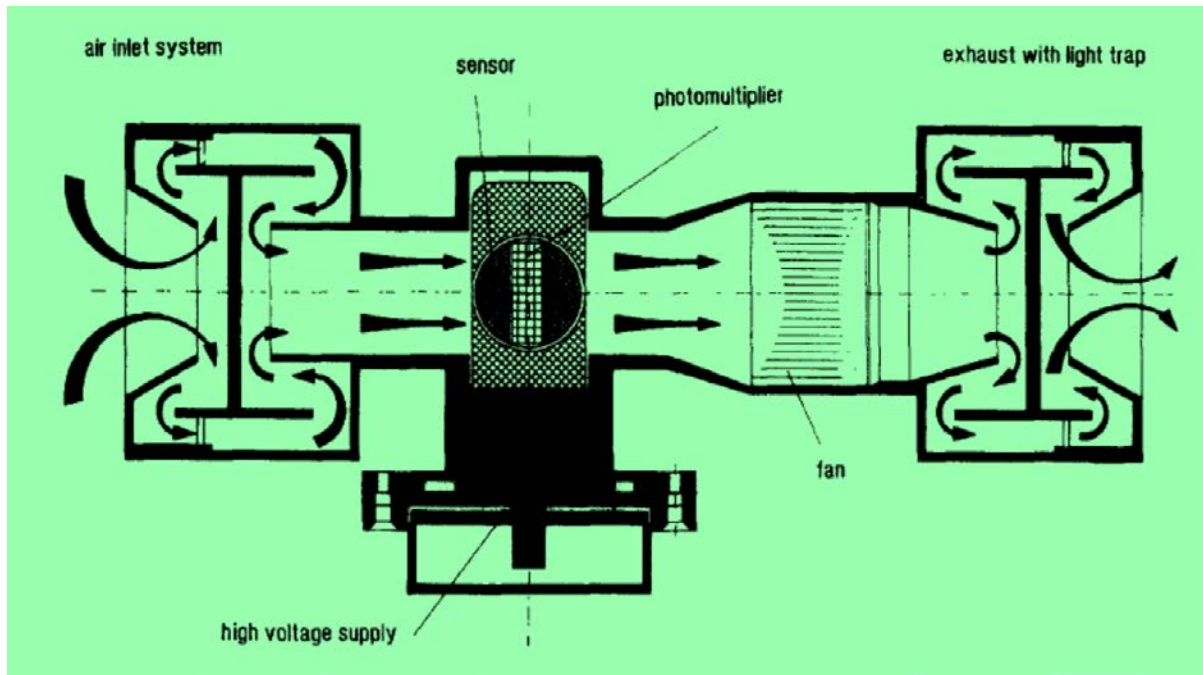


**Fig. 3.6.** A schematic diagram of the GFAS OS-G-2 fast response ozone sensor. Adapted from GFAS OS-G-2 manual; GFAS, Germany.

### 3.4.3 Measurement of CO<sub>2</sub> and H<sub>2</sub>O

High frequency CO<sub>2</sub> and H<sub>2</sub>O mixing ratios were measured using the LI-7000 infrared gas analyser whose operational principles are outlined below.

A LI-COR LI-7000 infrared gas analyser was used during IOP-2 to sample 20 Hz mixing ratios of CO<sub>2</sub> and H<sub>2</sub>O at 32.5 m. It was situated on the 30 m measurement platform at the top of the MT. To protect it from external conditions and ensure reproducible results, it was kept in a temperature-controlled housing, together with the data logger. The inlet tubes for the CO<sub>2</sub> and H<sub>2</sub>O channels were 6 m long each. Rotameters were used in front of each channel to maintain a constant flow rate.

### 3.5 Data acquisition system

Data acquisition was carried out by using a datalogger (CR3000, Campbell Scientific, USA) and two workstation computers (Hewlett Packard Computers, USA). Figure 3.3 shows a schematic of how the data acquisition system was linked to the measurement instruments. The CR3000 data logger was responsible for logging the data from the CSAT3 sonic anemometer (via an RS232 interface capturing wind vectors and sonic temperature). It was also responsible for logging the data from the two fast O<sub>3</sub> sensors at the top of the MT. The sensors were logged at 20 Hz using the CR3000's differential inputs (to avoid grounding problems). The data logged were the relative voltage signals (in mV).

The LI-7000 data was logged as DAC (Digital to Analog Converter) voltage signals using differential channels on the CR3000. The data was logged at 20 Hz and consisted of the LI-7000 temperature, pressure, CO<sub>2</sub> mixing ratio, and H<sub>2</sub>O mixing ratio.

For easy access to the logged data, and because the CR3000 has a limited amount of memory, an external memory card was used for storing the raw data (8 GB CompactFlash® card). This was connected through a memory card/Ethernet module (NL-120 module; Campbell Scientific, USA). The Ethernet module was used to transmit all the collected data to an FTP client on one of the workstations at the ground via a 70 m cross-over Ethernet cable, with the CR3000 acting as an FTP server through a set of additional commands. The data from the CR3000 CompactFlash® card was polled regularly to the FTP client on the workstation PC. That way, data could be downloaded from the PC without interrupting the logger. In addition, the data from the CR3000 was connected to a wireless network through a router from which data on the CR3000 or its memory card could be accessed from a radius of 100 m around the measurement site. This had the added advantage of making it easy to edit the CR3000 running programs without having to go up the tower (thereby disrupting measurements). It also enabled the CR3000 clock to remain synchronized with the PCs and laptops used.

Time synchronisation was an important part of the whole measurement procedure. This is because there were several independent measurement systems. For instance, the NO<sub>x</sub> analyser was independent of the CR3000 data logger. Therefore to reduce time related errors, high precision USB radio clocks (Expert mouseCLOCK USB II; GUDE Analog und Digitalysteme GmbH, Cologne, Germany) synchronised to a time server transmitter at Mainflingen near Frankfurt were used. The radio time signal (77.5 kHz) is known as the DCF77 and belongs to one of the most accurate caesium atomic clocks in the world (less than one second deviation in 300,000 years) (*Physikalisch-Technische Bundesanstalt (PTB)*, Braunschweig; <http://www.ptb.de>). These automatically updated the PCs and laptop clocks which tended to drift with time. The same USB clocks were used to synchronise the clocks of the data logging PCs for all the supporting measurements (see 3.6) to ensure that the same time was kept.

The two workstation PCs also played the role of hosting data logging software for the CLD NO<sub>x</sub> analyser as well as the O<sub>3</sub> sensor/sonic anemometer combinations at 24 m, 16 m, and 1 m. For the O<sub>3</sub> EC systems at 24 m and 16 m, the EddyMeas component of the multifunctional EddySoft (Kolle and Rebmann, 2007) EC software was used to log the data from the R3 sonic anemometers and the O<sub>3</sub> sensors (each connected to its respective the R3 sonic anemometer via a 14-bit analogue input channel. The O<sub>3</sub> sensor on the ground, which had an R2 sonic anemometer, was logged using a LabVIEW® program. All the ozone EC systems at 24 m, 16 m, and 1 m were logged at 20.8 Hz and

the signals were later filtered to 20 Hz. This was because the R3 and R2 sonic anemometers operate at 20.8 Hz.

The CLD signals for NO and NO<sub>2</sub> were also logged using a LabVIEW® program (www.ni.com). The original program was developed by Axel Thiemann for use with an R2 sonic anemometer. In this case, the aim was to log the CLD signal independently of a sonic anemometer, hence the program was rewritten to accommodate that. Logging was done at 5 Hz via an RS232 interface. Logged signals were the Channel A (NO) and Channel B (NO<sub>2</sub>) counts per second. During calibration mode, logged signals included the pre-chamber signals for both channels.

### **3.6 Supporting measurements**

The supporting measurements for this work were from both the MT and the TT. The main supporting measurements were the trace gas profile measurements above the canopy on the main tower from which vertical concentration differences could be found; the EC measurements above the canopy on the TT; and the meteorological profile measurements on the MT. These measurements were used in a comparative and qualitative sense as part of the analysis and interpretation of the results of the work done in this research. The measurements are described briefly in the following sections. Table 3.3 summarises the supporting measurements.

#### **3.6.1 Trace gas profile measurements above and below the canopy**

Carbon dioxide and H<sub>2</sub>O mixing ratios for the profile system were measured using a LI-7000 IRGA (LI-COR Biosciences). Nitrogen oxide and NO<sub>2</sub> were measured using a chemiluminescence based CLD780TR NO analyser. Nitrogen dioxide was measured indirectly by first converting it to NO using a very specific blue light converter just in front of the inlet into the analysers. The multi-point trace gas profile system was known as the RETGAP (short for reactive trace gas profile) (Foken et al., 2012). The O<sub>3</sub> profile was measured using a TEI 49C (Thermo Environment, USA) UV absorption O<sub>3</sub> analyser. Detailed information about the profile system is found in (Foken et al., 2012).

The profile system was managed by Daniel Plake see (Foken et al., 2012) and consisted of two independent systems the upper system and the lower system, operating at two different sequences of levels. Only the upper system (32 m and 25 m during IOP-2) was relevant to this thesis.

#### **3.6.2 Meteorological profile measurements**

On the MT were also in and above canopy meteorological profile measurements of wind speed, temperature (wet and dry bulb) and humidity. Incoming shortwave (global) radiation measurements were taken at the top of the MT and at 2 m within the canopy. These measurements were important for further interpretation and analysis of the primary data of this work. Most of the data was available in 10 minute and half-hour resolution, although in some instances, one minute resolution data for

psychrometers was available. Two separate profile systems were available – one belonging to MPI and the other to UBT. The data were used interchangeably depending on needs.

### 3.6.3 EC measurements of CO<sub>2</sub> and H<sub>2</sub>O on the Turbulence Tower

The data from two EC systems installed on the TT at 23 m, and 36 m were also used in this study. They consisted of CSAT3 (Campbell Scientific, USA) sonic anemometers. The systems had fast LI-7500 open path CO<sub>2</sub>/H<sub>2</sub>O analysers and LI-7000 closed path CO<sub>2</sub>/H<sub>2</sub>O analysers. Again the sampling rates were 20 Hz. The TT setup is described in detail in Serafimovich et al. (2010). The EC systems on the TT provided the wind vectors; EC fluxes of CO<sub>2</sub>, latent heat, sensible heat and momentum; and mixing ratios of CO<sub>2</sub> and H<sub>2</sub>O.

**Table 3.3.** A summary of the supporting measurements during both IOPs.

Parameter	Sampling height (m)	Sampling Frequency (Hz)	Model, manufacturer	Detection limit or precision
NO [nmol mol <sup>-1</sup> ]	25 & 32 (IOP-2)	1/30	CLD780TR, ECO PHYSICS GmbH	± 0.010 nmol mol <sup>-1</sup> (3σ, cont. mode)
NO <sub>2</sub> [nmol mol <sup>-1</sup> ]	25 & 32 (IOP-2)	1/30	CLD780TR	± 0.020 nmol mol <sup>-1</sup> (3σ, cont. mode)
CO <sub>2</sub> [nmol mol <sup>-1</sup> ]	25 & 32 (IOP-2)	1/30	LI-7000, LI-COR Biosciences	0.06 μmol mol <sup>-1</sup>
	23, 36	1/30		
CO <sub>2</sub> [g m <sup>-3</sup> ]		20	LI-7500, LI-COR Biosciences	
H <sub>2</sub> O [nmol mol <sup>-1</sup> ]	25 & 32 (IOP-2)	1/30	LI-7000	0.0015 nmol mol <sup>-1</sup>
	23, 36	1/30		
H <sub>2</sub> O [g m <sup>-3</sup> ]		20	kH-20, Campbell Scientific, Inc.	
O <sub>3</sub> [nmol mol <sup>-1</sup> ]	25 & 32 (IOP-2)	1/30	TEI 49i, Thermoenvironment GmbH	-
Wind vector [m s <sup>-1</sup> ]	36	20	USA-1, METEK GmbH	-
	23, 32	20	CSAT3, Campbell Sci.	
Mean wind speed [m s <sup>-1</sup> ]	21, 25, 31		Cup anemometer, Friedrichs & Co.	-
Global radiation [W m <sup>-2</sup> ]	2, 30		CM14 pyranometer, Kipp & Zonen	-
Long wave radiation	2, 30		CG2 net pyrgeometer, Kipp & Zonen	-
Dry bulb temperature [°C]	21, 31		Aspirated psychrometer, Theodor Friedrichs & Co.	-
Wet bulb temperature [°C]	21, 31		Aspirated psychrometer, Theodor Friedrichs Co.	-
Soil temperature [°C]	-0.02, -0.05, -0.1, -0.2, -0.5, -0.7, -1.0, -2.0		Pt-100 thermometers, Electrotherm GmbH	-
Soil moisture [%]	-0.1, -0.5		TRIME-EZ TDR sensors, IMKO GmbH	-
Precipitation rate	1		OMC 212, Adolf Thies GmbH & Co. KG	-
Air pressure	2		Barometric pressure sensor, Ammonit Gesellschaft für Messtechnik mbH	-

## 3.7 System Operation and Maintenance

### 3.7.1 Calibration

#### ***NO and NO<sub>2</sub>***

The calibrations coincided with bad conditions for measurement. All calibrations were done from the container via 53 m long tubes. A Gas Phase Titration (GPT) unit (Thermo Environment GmbH) was used to create the low mixing ratios between 10 and 40 ppb that were used to calibrate NO. The NO<sub>2</sub> was inferred from the NO calibration by calibrating first with the blue light converter off, then with the blue light converter on.

$$NO = \frac{\lambda_{NO}(S_{NO} - ZERO_{NET})}{f_{NO}} \quad (3.2)$$

where NO is the calibrated NO signal in ppb,  $\lambda_{NO}$  is the interference factor (the ratio of the total signal which reacts in the pre-chamber to that which reacts in the main chamber),  $ZERO_{NET}$  is the prechamber signal when zero air is sampled,  $S_{NO}$  is the NO signal produced by the CLD790SR2 (main chamber signal),  $f_{NO}$  is the sensitivity of the reactor in cps/ppb

$$NO_2 = \frac{NO_c - NO_{BA}}{f_{NO} \cdot CE} \quad (3.3)$$

NO<sub>2</sub> is the calibrated NO<sub>2</sub> signal in ppb, NO<sub>c</sub> is the NO from the blue light converter in ppb and NO<sub>BA</sub> is the NO from channel A matched to channel B by using the regression line of NO from channel A against NO from channel B. This matching was done because the two channels had different sensitivities and therefore different calibration factors. CE is the combined conversion efficiency of the blue-light converters connected in series. The conversion efficiency was calculated as the ratio of the difference between titrated and untitrated NO<sub>c</sub> and titrated and untitrated NO. The titration gas used was O<sub>3</sub> which was produced by the GPT.

Possible sources of error in the measurement of NO and NO<sub>2</sub> include flow rate errors due to the GPT as well as the vacuum pump, fluctuations in sensitivity, as well as errors in the conversion efficiency CE. Daily logs of flow rates and pressures in the tubes did not show any significant changes, and when changes were found, these were corrected immediately. Therefore such errors were expected to be minimal.

#### **Ozone**

As mentioned before, a disc consisting of an organic dye provides the chemiluminescence medium for the GFAS. Chemiluminescence can occur for up to 5 days before the dye is used up and the plate has to be replaced. As the dye on the plate gets depleted, the sensitivity of the analyser is reduced due to

less chemiluminescence. Therefore the plates were routinely replaced every 4-5 days (Zhu et al., 2009). A detailed description of the operating principles of the O<sub>3</sub> instrument can be found in Güsten and Heinrich (1996).

When high frequency calibrated data of O<sub>3</sub> from the GFAS was required, a calibration procedure involving regression fitting to the absolute O<sub>3</sub> concentration was performed. This involved taking one minute resolution data of O<sub>3</sub> absolute mixing ratios (with gaps due to discontinuous sampling) and also taking the relative O<sub>3</sub> signal from the GFAS and averaging it to 1 minute resolution. After that, regression factors were evaluated for 30 minute blocks of data using the robust regression (Holland and Welsch (1977); Street et al. (1988)) algorithm. Using the robust regression algorithm ensured that spiky or spurious data where the correlation between the absolute and the relative measurement was below 0.5 were not included in the regression calculation. After the linear regression coefficients  $m$  and  $c$  were calculated for each 30 minute block, they were applied back on the high frequency relative concentrations for each respective 30 minute interval according to the formulation below:

$$O_3[ppb] = m_{robust} \cdot O_3[mV] + c_{robust} \quad (3.4)$$

$m_{robust}$  is the slope of the relative O<sub>3</sub> signal against the absolute O<sub>3</sub> signal and  $c_{robust}$  is the y-intercept of the curve.  $O_3[ppb]$  and  $O_3[mV]$  are the 30 minute arrays of high frequency O<sub>3</sub> signals in ppb and millivolts respectively.

### **CO<sub>2</sub> and H<sub>2</sub>O**

The LI-7000 (LI-COR Biosciences, USA) was calibrated every 2 weeks at the same time as the CLD790SR2 analyser. It was calibrated by running the calibration gases (CO<sub>2</sub> and N<sub>2</sub>) to the top of the tower from the container via 53 m long calibration lines. For H<sub>2</sub>O calibration, the LI-610 was taken to the top of the tower and then the calibration was done there. This was because it was impractical and erroneous to set dew points through long tubes. The CO<sub>2</sub> calibrations were performed using NIST-traceable nitrogen gas as zero air and two span gases of 400 ppm and 700ppm CO<sub>2</sub>. The calibration procedure was carried out exactly as recommend by LI-COR in the LI-7000 manual using the DAC (digital to analogue converter) outputs method. The calibrations coincided with bad conditions for measurement.

### **Supporting measurements**

Information about the calibration procedures and system maintenance of the supporting measurements can be found in Foken et al.(2012) and Serafimovich et al. (2011a;2011b).

#### **3.7.2 Routine logging of instrument operational parameters**

The CLD790SR2's operating parameters such as reactor temperatures, inlet pressures, O<sub>2</sub> inlet pressure and PMT temperatures were carefully logged and, where necessary controlled, daily to

ensure that the instrument was operating as optimally as possible (see Appendix A3). The instrument's photomultipliers are very expensive as well as fragile. Therefore it was very important to ensure that all the set point parameters were always within the range for creating a good PMT operating environment. In addition, flow checks were performed daily on parameters such as the PMT flush to ensure that the PMTs were dry all the time. Indicator silica gel drier cartridges for the PMTs were also monitored to ensure that they remained deep blue. Turning pink would be an indication of humidity in the PMT housing, a condition that can lead to damage of the PMT. Two additional silica gel drier cartridges were placed in front of the PMT flush inlet to complement the built-in Nafion® drier.

The ozone generators of the CLD require 30 ml of distilled water every day for generating O<sub>3</sub> from the reaction with O<sub>2</sub>. Water was refilled every two days. The design of the water reservoir is such that excess water is released through an overflow mechanism. In that way, there is no danger to the instrument associated with administering too much water.

### **3.7.3 Changing of filters**

Inlet filters for the EC system were changed every 4 week to ensure that the inlets did not become clogged with dirt. Traces of soot were found on all used up filters. All inlet funnels also had mosquito net type additional filters in front of them. These were checked regularly and to ensure that they had not been damaged by birds or insects. They were replaced when it was necessary.

### **3.7.4 Checking the alignment bubble level of CSAT3**

The CSAT3 has a 3-axis bubble level which is used to keep it aligned with all the three Cartesian coordinate axes. The spirit level was checked routinely to see if the CSAT3 was still aligned with the horizontal plane. Realignment was conducted were necessary and the time noted in the logbook.

### **3.7.5 Changing of O<sub>3</sub> discs**

The chemiluminescent reaction in the GFAS O<sub>3</sub> sensors depletes the Coumarin® organic dye on the discs. As the dye gets depleted the sensitivity of the sensor towards O<sub>3</sub> is reduced. Therefore the organic dye discs used by the ozone sensors were changed every four to five days. This way, the sensitivity of the sensors was kept above an acceptable value.

## **3.8 Evaluation of above-canopy EC data**

Eddy covariance data evaluation consisted of initially an investigation into the quality of the measured data. The next step was the evaluation of the error limits of the eddy covariance fluxes. This was followed lastly by the analysis and interpretation of the quality controlled EC fluxes. Tools such as the

canopy-atmosphere turbulence exchange regimes were used as part of the analysis and interpretation. Figure 3.7 is a flowchart of the evaluation procedure for the EC data.

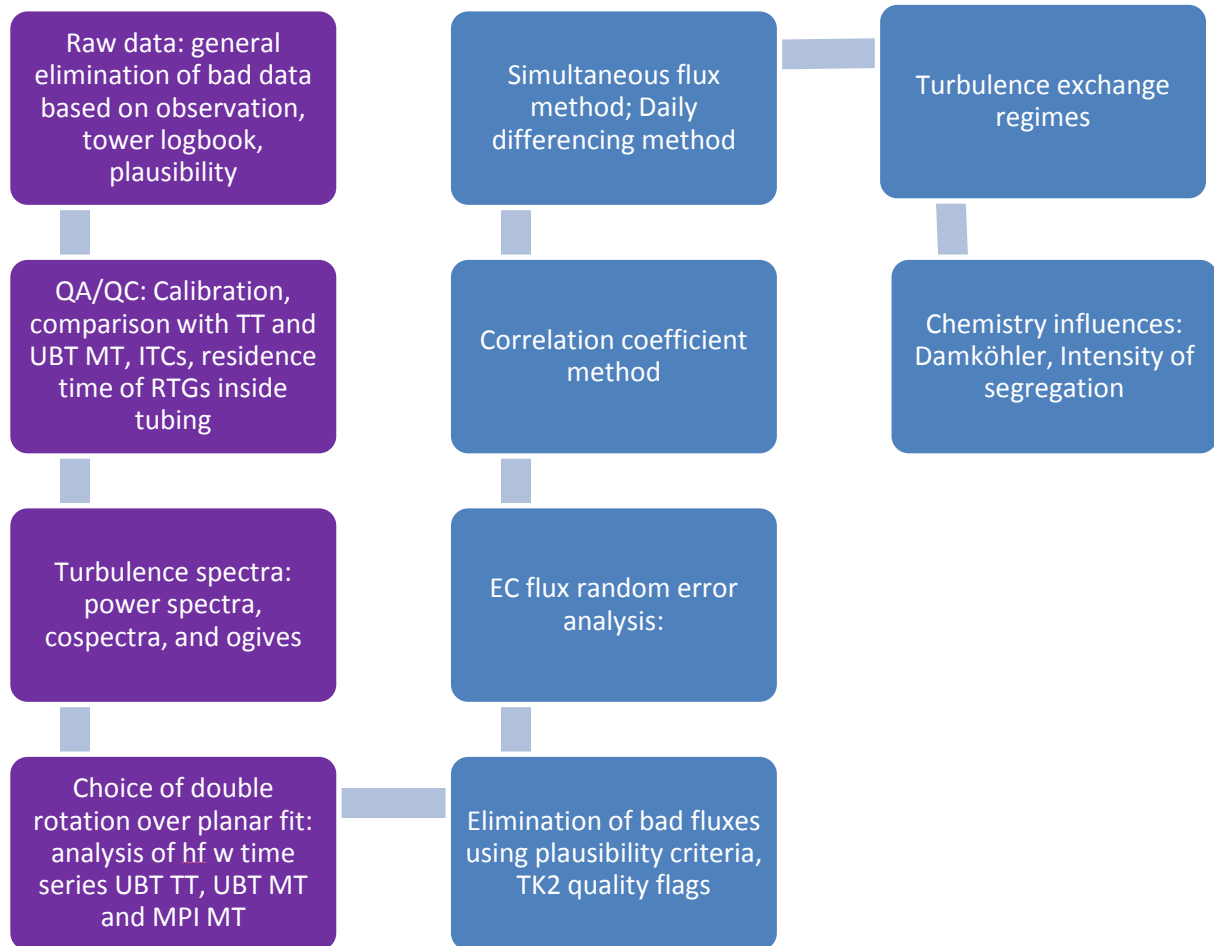


**Fig. 3.7.** Flow chart of the steps involved in acquiring and analysing the EC data. The violet blocks show the steps applied on the raw data while the blue blocks show the procedures on the fluxes.

### 3.8.1 Data processing and quality assurance

#### **Data plausibility**

Raw data was preliminarily quality checked and quality assured by elimination of bad data periods according to a data logbook in which all records of people moving on the tower for the purpose of instrument maintenance and checks were recorded. Instances where lumberjack trucks passed by the access footpath to the site were also recorded in this logbook, as were all other incidences that had the possibility to compromise data quality. Data outside the plausibility range (Table 3.4) were either flagged or eliminated.

**Table 3.4.** A list of the plausibility criteria used to flag raw data during IOP-2.

Parameter	Acceptance window	Units
$u$	$-50 \leq u \leq 50$	$\text{m s}^{-1}$
$v$	$-50 \leq v \leq 50$	$\text{m s}^{-1}$
$w$	$-10 \leq w \leq 10$	$\text{m s}^{-1}$
$T$	$-20 \leq T \leq 50$	$^{\circ}\text{C}$
$\text{CO}_2$	$0 \leq \text{CO}_2 \leq 500$	$\mu\text{mol mol}^{-1}$
$\text{H}_2\text{O}$	$0 \leq \text{H}_2\text{O} \leq 30$	$\text{mmol mol}^{-1}$
$\text{NO}$	$0 \leq \text{NO} \leq 5$	$\text{nmol mol}^{-1}$
$\text{NO}_2$	$0 \leq \text{NO}_2 \leq 10$	$\text{nmol mol}^{-1}$
$\text{O}_3$	$0 \leq \text{O}_3 \leq 200$	$\text{nmol mol}^{-1}$
Wind direction	$0 \leq \theta \leq 360$	$^{\circ}$
Air pressure	$950 \leq P_{\text{air}} \leq 1050$	$\text{hPa}$
Global radiation	$0 \leq G \leq 1500$	$\text{W m}^{-2}$

### Comparison

The LI-7000  $\text{CO}_2$  and  $\text{H}_2\text{O}$  fluxes were compared to the fluxes of the LI-7000 UBT EC system at 32 m on the same tower and to the fluxes of the open path LI-7500 on the TT. This was an additional method of data quality checking and proved useful in realizing that there was a need to use the double rotation method for the EC fluxes. Inter-comparisons of  $\text{CO}_2$ ,  $\text{H}_2\text{O}$ , H and LE fluxes were made with the UBT32 and UBT36.

### Tube response tests for NO and NO<sub>2</sub>

Tube response tests were done to estimate lag time for NO and NO<sub>2</sub>. They were not necessary for the other trace gases because the other analyser were mounted at the top of the tower, close to the sonic anemometer. Additionally, lag time (see 2.3.3) was calculated by finding the maximum covariance between the vertical wind velocity and the trace gas of interest (see Moore (1986)). The results are shown and discussed in 4.5.2.

### Test for developed turbulence – ITCs

Comparative tests were made on sigma  $\sigma_w/u_*$ ,  $\sigma_v/u_*$ ,  $\sigma_T/T_*$  on MPI32, UBT32 and UBT36. The results are presented in 4.5.

### Turbulence spectra

The cospectral density of a parameter  $\chi$  is the cospectrum (see 2.3.3) between the vertical wind component  $w$  and  $\chi$  divided by the covariance between  $w$  and  $\chi$ , i.e.:

$$Cod_{w\chi} = \frac{\int_{\infty}^{f/2} Co_{w\chi}}{w'\chi'} \quad (3.5)$$

where the cospectrum is

$$Co_{w\chi} = Re \left( \left( \frac{FFT(\chi)}{Ls} - \frac{FFT(\chi)i}{Ls} \right) \cdot \frac{FFT(\chi)}{Ls} \right) \quad (3.6)$$

and  $f$  is the sampling frequency, FFT is the fast Fourier transform (computed using the MATLAB programming software) and  $Ls$  is the length of the sampling period.

Data for all spectra (power spectra, cospectra and ogives) were taken between 1100 and 1300 during the ‘Golden Days’. This time period was chosen because it is when turbulence is at its maximum (due to maximum solar radiation) and therefore it is easiest to observe all the energy ranges of the eddies.

Graphs of power spectral and cospectral density against the frequency (up to the Nyquist frequency) and the corresponding ogive for each parameter are shown in Chapter 4. To make enhance the inertial subrange, the spectra were pre-multiplied by the frequency.

#### ***Choice of double rotation over planar fit - analysis of planar fit coefficients***

When the high frequency time series of MT CSAT3 sonic anemometer  $w$  component were plotted and compared to those for UBT MT32 and UBT TT36, it was found that there were periodic, short-lived spikes in the MPI32 data. Further inspection of these spikes showed that their duration was too short to be flagged as spikes by TK2. A possible cause of this was the fact that the EC mast for the CSAT3 was a boom extending out 2 m from the MT which might have vibrated as the tower moved due to wind perturbations and people walking up the tower for routine maintenance of their instruments. Using the planar fit method under these conditions would have resulted in additional flux errors due to unrealistic planar fit matrices being generated by the spikes. To solve this problem, the double rotation method was used instead of the planar fit method for rotating the wind components. Although the double rotation method is known to have limitations, it was the best method of coordinate rotation that could be used for this dataset.

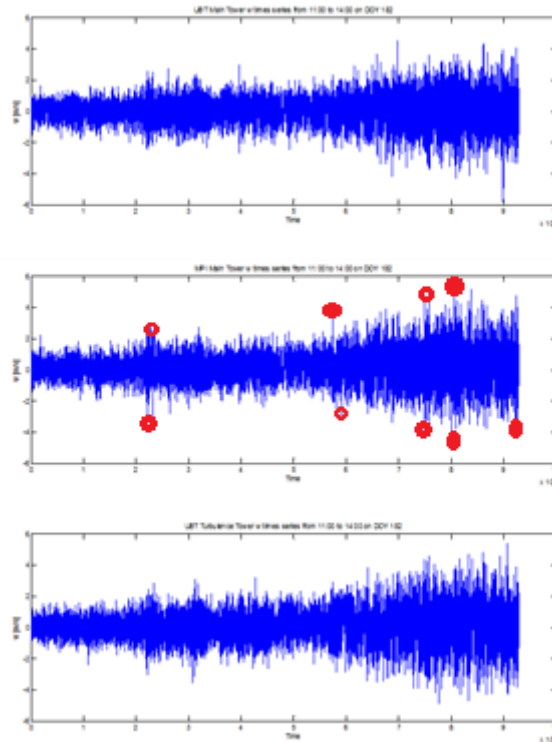


**Fig. 3.8.** Time series of  $w$  for the UBT32 (top), MPI32 (middle), and the UBT36 (bottom) stations. The red dots show the spikes in the MPI32  $w$  time series.

### Quality assurance of fluxes using data quality flags

The data quality of energy and matter fluxes from EC measurements was classified according to the scheme developed by Foken and Wichura (Foken and Wichura, 1996) and (Foken et al., 2004).

**Table 3.5.** Stationarity and ITC quality flag classification according to Foken et al. (2004).

Stationarity class	Stationarity % deviation	ITC Class	ITC % deviation
1	0-15	1	0-15
2	16-30	2	16-30
3	31-50	3	31-50
4	51-75	4	51-75
5	76-100	5	76-100
6	101-250	6	101-250
7	251-500	7	251-500
8	501-1000	8	501-1000
9	>1000	9	>1000

**Table 3.6.** Overall quality flags classification after Foken et al. (2004). The greyed out classes were excluded.

Overall class	Stationarity class	ITC Class
1	1-2	1-2
2	1-2	1-2
3	3-4	3-4
4	1-2	1-2
5	3-5	3-5
6	5	< 5
7	$\leq 6$	$\leq 6$
8	$\leq 8$	$\leq 8$
9	$\leq 9$	$\leq 9$

To ensure that the data was of the highest quality, only data with overall flags 1-3 was used.

### 3.9 Evaluation of above-canopy vertical profile data

Focus was limited to the last two levels above the canopy on the MT and the TT as explained earlier. Here we look at the quality assessment and control of the absolute data as well as the vertical differences between the absolute data of the two levels above the canopy. The data under investigation consists of CO<sub>2</sub>, H<sub>2</sub>O, NO, NO<sub>2</sub>, O<sub>3</sub>, temperature and specific humidity (from the psychrometers). Figure 3.9 is a flowchart summarising the data evaluation procedure for the profile data.

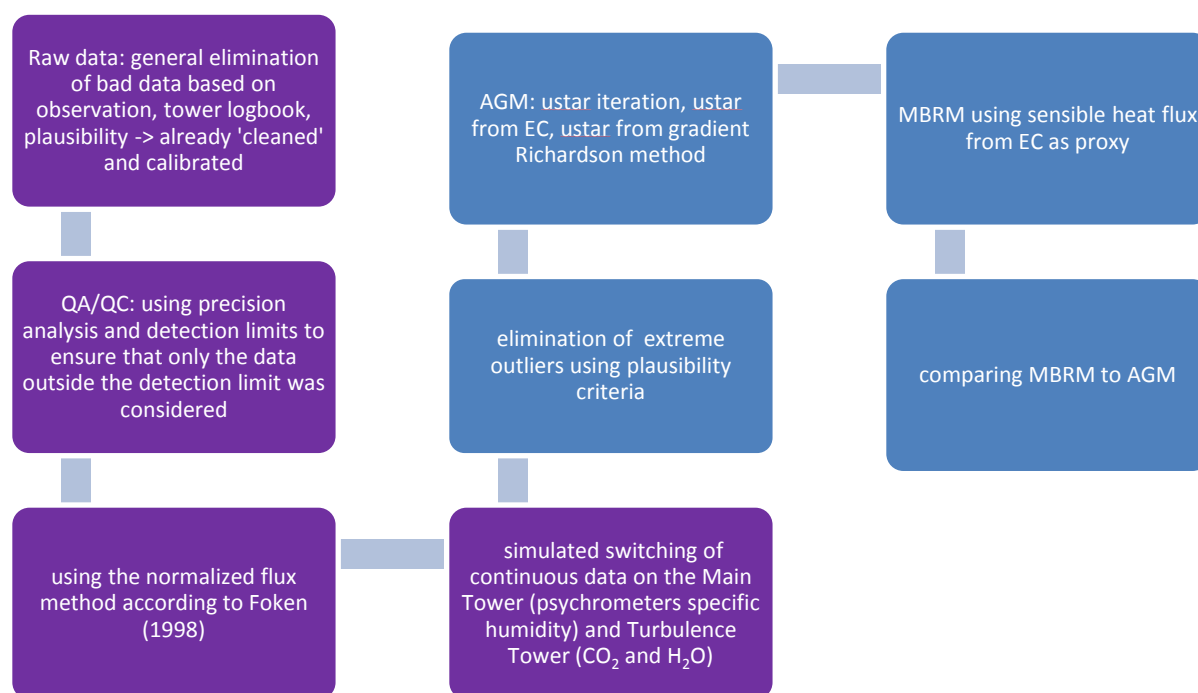


**Fig. 3.9.** Flow chart of the steps involved in manipulating and analysing the reactive trace gas profile data. The violet blocks show the steps applied on the raw data while the blue blocks show the procedures on the fluxes.

### 3.9.1 Evaluation of absolute vertical profile data

The plausibility criteria used was the same as that used for the EC data (see Table 3.4). Mixing ratio measurements from the EC station at 32.5 m (NO, NO<sub>2</sub>, CO<sub>2</sub>, H<sub>2</sub>O, O<sub>3</sub>) were matched to the RETGAP2 to ensure a consolidated, consistent dataset (Plake, 2009). A temperature sensitivity analysis for the RETGAP2 measurement system was carried out (Plake, 2009) in the same way as described for the EC system in 3.4.1.

### 3.9.2 Evaluation of vertical mixing ratio differences

Vertical differences between the absolute mixing ratios above the forest were calculated by taking the difference between the upper level height 32 m) and the lower level height (25 m).

It is well known from statistics (already discussed in 2.2.4) that for the difference between two measurements to be significant, the difference must be greater than the combined uncertainty of each measurement. Therefore precision analysis and detection limits were used to ensure that only the data outside the detection limit was considered. In addition, the normalized flux method according to (Foken, 1998) was tested on the differences.

To check for the effect of switching on vertical concentration differences, tests using simulated switching of continuous data on the MT (specific humidity from the psychrometers) and the TT (CO<sub>2</sub> and H<sub>2</sub>O) were performed. The simulated switched differences in comparison with the switching profile differences were used to show the effect of switching on data quality and the extent to which stationarity plays a role in the stability of the gradients.

Finally, the effect of turbulent exchange regimes and the Damköhler numbers on the vertical differences was analysed qualitatively and quantitatively. Details of the evaluation of the vertical differences are outlined below.

### ***Distribution of differences***

The distributions of vertical concentration differences for all the reactive and non-reactive trace gases under investigation were evaluated. The normal and Laplace probability density functions were fitted to the distributions to check how well the data fitted to each of these two distributions.

### ***Quality check on differences***

Directly and indirectly measured concentration differences needed to be checked to ensure that they were significant enough to be used for further analyses such as the calculation of fluxes. Therefore precision analysis was done to ensure that only the data outside the detection limit was considered.

### ***Application of precision criteria on the differences***

The limit of detection (LOD) or precision of an instrument is the standard deviation,  $\sigma$ , of its output signal when sampling zero air under steady state conditions. It can be interpreted as the noise level of the instrument. The LOD can be defined as a factor of  $\sigma$ . Commonly used variations are  $2\sigma$  and  $3\sigma$ .

Given the mixing ratio difference

$$\Delta\chi = \chi_2 - \chi_1 \quad (3.7)$$

then using the Gaussian error propagation method in 2.1.4, the precision with which the concentration difference can be measured becomes

$$\delta\Delta\chi = \sqrt{(\sigma\chi_2)^2 + (\sigma\chi_1)^2} \quad (3.8)$$

where  $\sigma\chi_2$  is the precision in the measurement of the concentration at level 2 ( $\chi_2$ ) and  $\sigma\chi_1$  is the precision in the measurement of the concentration at level 1 ( $\chi_1$ ).

The RETGAP switched profile system uses the same analyser for sampling both inlet levels, therefore  $\sigma\chi_1 = \sigma\chi_2 = \sigma\chi$

$$\delta\Delta\chi = \sigma\chi\sqrt{2} \quad (3.9)$$

$\sigma$ ,  $2\sigma$ ,  $3\sigma$  and  $10\sigma$  criteria were set for determining the LOD and the resultant errors in the precisions were used to determine the significant concentration difference data for each of the four criteria. 4.4 shows a summary of the precisions of the instruments for concentration differences used in this study. The results of this test were used to decide on the further usefulness of data. All data below  $2\sigma$  was considered unreliable and therefore rejected.

### **Minimum measurable flux method**

According to a method by Foken (1998), for all flux calculations from gradients, it should be demonstrated that the measuring accuracy is at least 10 times greater than the expected difference between the two measuring heights so that the flux can at least be determined with an accuracy of  $\pm 20\%$ . Wolff et al. (2010) used a similar method but with less stringent requirements on the measuring accuracy. The procedure for investigating this precision method was as follows:

1. Representing the normalized flux equation in terms of stability parameters from the AGM:

According to Foken (1998;2008)

$$F = F_N \Delta\chi \quad (3.10)$$

where  $F$  is the flux,  $F_N$  is the normalised flux (otherwise known as the transfer velocity) and  $\Delta\chi$  is the concentration difference

The minimum detectable flux is given as

$$F_{min} = F_N \Delta\chi_{min} \quad (3.11)$$

where  $\Delta\chi_{min}$  is the minimum measurable difference between the two levels of interest.

Using flux-gradient relationships from 2.2:

$$F_N = - \frac{\kappa u_*}{\ln(m) - \psi_H\left(\frac{z_2 - d}{L}\right) + \psi_H\left(\frac{z_1 - d}{L}\right)} \quad (3.12)$$

$$\text{where } m = \frac{z_2 - d}{z_1 - d} \quad (3.4)$$

Therefore

$$F_N = - \frac{\kappa u_*}{\ln(m) - \psi_H\left(\frac{z_2 - d}{L}\right) + \psi_H\left(\frac{z_2 - d}{mL}\right)} \quad (3.13)$$

$$\text{Let } \frac{z_2 - d}{L} \text{ represent } \frac{z}{L}$$

which implies that

$$F_N = - \frac{\kappa u_*}{\ln(m) - \psi_H\left(\frac{z}{L}\right) + \psi_H\left(\frac{z}{L} \cdot \frac{1}{m}\right)} \quad (3.14)$$

2. The next step was to find  $F_N$  for different cases of  $\frac{z}{L}$  and  $u_*$ . Variations of the normalized flux at different stability conditions and friction velocities were plotted.
3. The minimum concentration difference required in the roughness sublayer was then found by multiplying the minimum concentration difference by the enhancement factor.
4.  $F_{min}$  in the roughness sublayer was then found by multiplying the result in (3) by the normalized flux  $F_N$ .

### ***Investigation into the applicability of the discontinuous profile method for the site - validity of discontinuously measured differences***

#### *Artificial switching of psychrometers*

In order to understand the effect of discontinuous sampling on mixing ratio differences, an experiment was devised. Continuous 1 minute resolution measurements of water vapour mixing ratios at 31 m and at 25 m were matched with discontinuous water vapour mixing ratios from the RETGAP, also at 31 m and 25 m. For each of the two levels, data points were removed from the continuous data for all time periods where the RETGAP had no data. That way a switching system was artificially simulated on the continuous psychrometer mixing ratios. After that, concentration differences (31 m – 25 m) were found between the mixing ratios of the switched psychrometer.

#### *Simulated switching of turbulence tower data (36 m and 23 m) for CO<sub>2</sub> and H<sub>2</sub>O using Main Tower RETGAP data.*

Having looked at the concentration differences of discontinuous H<sub>2</sub>O data on the MT, I developed an idea to extend this analysis further by studying the differences of the mixing ratios of CO<sub>2</sub> and H<sub>2</sub>O across the MT and the TT. The aim was to verify if discontinuous sampling has the same effect on CO<sub>2</sub> mixing ratios like it does on H<sub>2</sub>O mixing ratios. In addition, finding out if concentration differences are consistent across spatial variability was also of interest. The heights of interest on the TT (TT) were 36 m and 23 m on which were mounted open-path LI-7500 analysers for measuring 20 Hz densities of CO<sub>2</sub> and H<sub>2</sub>O.

The 20 Hz densities of CO<sub>2</sub> and H<sub>2</sub>O at 23 m and 36 m were first averaged to one minute data and calibrated using the calibration information in the EGER implementation plans for the UBT (Serafimovich et al., 2011a; Serafimovich et al., 2011b). After that the 1 minute densities were converted into mixing ratios of CO<sub>2</sub> and H<sub>2</sub>O for easier comparison with the MT mixing ratios of CO<sub>2</sub> and H<sub>2</sub>O at 31 m and 25 m.

Differences (36 m – 23 m) for continuous data and for simulated discontinuous data (using the method used for the psychrometers) were then evaluated and compared to the mixing ratio differences on the MT (31 m - 25 m). The results are shown in Chapter 4.

### ***Comparison of AGM and MBRM to the EC method.***

The results of the AGM and MBR method were compared to the EC reference method. Within this comparison was the discussion of whether the gradient derived methods when applied to reactive trace gases at this site can be used as an alternative to the EC method.

## **3.10 Analysis and interpretation of the net fluxes of the reactive trace gases**

### **3.10.1 Above canopy fluxes**

In Chapter 2, it was mentioned how chemistry can influence the magnitude and direction of trace gas fluxes. Therefore characteristic timescales of chemical reaction were calculated for the individual species of the NO-O<sub>3</sub>-NO<sub>2</sub> triad according to Equations. 2.75 – 2.77. Finally, the chemical timescale for the whole triad was calculated using the Lenschow formula (Equation. 2.78). The turbulence timescale was calculated using the formulation of Wyngaard modified by Mayer et al. (2009) (Equation. 2.72). From the chemical timescale of the triad and the turbulence timescale, the Damköhler numbers for the individual species of the triad and for the whole triad were found.

In order to understand further the degree of reaction between the triad species, the segregation intensity between O<sub>3</sub> and NO, as discussed in 2.4.2 was found as follows:

- High frequency time series of NO (5 Hz) and O<sub>3</sub> (20 Hz averaged to 5 Hz) mixing ratios from EC measurements were taken for the golden days of the IOP-2 campaign.
- The lag time between the NO and the O<sub>3</sub> time series was found by cross-correlation. This was necessary because the O<sub>3</sub> signal was measured independently of the NO signal. The tube lengths of the NO measurement system were much more than that for the O<sub>3</sub> system. Therefore a lag time was expected to exist between the O<sub>3</sub> and NO signal.
- The O<sub>3</sub> signal was taken as the reference signal and the NO signal was shifted to match the time of the O<sub>3</sub> signal for each 30 minute interval. After that, the covariance between the NO and the O<sub>3</sub> mixing ratios was found for each 30 minute interval.
- From the 30 minute covariances and the 30 minute averages of the NO and the O<sub>3</sub> mixing ratios, the segregation intensity,  $I_s$ , was found according to Equation. 2.86.

The DA and  $I_s$  were then used together to analyse and interpret the vertical concentration differences of the reactive trace gases.

After all the corrections and error analysis had been done, the cumulative result of all the corrections and analysis were plotted for the flux of each reactive trace gas. This was also done for CO<sub>2</sub>, H<sub>2</sub>O and the energy fluxes. These final results could be considered as the net fluxes above the canopy and were discussed and interpreted.

### 3.10.2 Below canopy (1 m)

Vertical concentration differences between 0.9 m and 0.005 m above the ground were evaluated from the trace gas profile measurements and the results were used to assist in the interpretation of the above canopy fluxes. Additionally, using the vertical gradient between 0.005 m and 0.9 m and the O<sub>3</sub> EC flux at 1 m, fluxes were calculated using the MBRM for CO<sub>2</sub>, H<sub>2</sub>O, NO and NO<sub>2</sub>. Fluxes were picked only for those periods where: (i) the coupling state was  $Cs/C$ ; (ii) the vertical gradient was above  $2\sigma$  of the detection limit for gradients derived from the trace gas sensor's detection limit. (iii) the friction velocity ( $= \sqrt{-u'w'}$ ), at 1 m was above  $0.1 \text{ m s}^{-1}$ .

For verification of this method, the modelled soil NO flux results of Falge et al. (2010) were used, which were:

- laboratory results of soil NO flux (net potential NO fluxes from the four different (understory) vegetation covered soils (i.e. blueberries, young spruces, grass, and moss)),
- soil temperature- and soil moisture data (2008) for these four different (understory-) vegetation covered soils (calculated by Falge et al. (2010)'s SVAT-model (Surface Vegetation Atmosphere Transfer-model)), and
- the understory-vegetation map of the Waldstein-Weidenbrunnen experimental site (Behrendt, 2009).

With the help the net potential NO fluxes and the soil temperature and moisture data, Falge et al. (2010) calculated actual NO fluxes (for EGER IOP-2) for each of the (understory) vegetation covered soils. Finally, this result was “weighted” by the area contributions of the four different (understory-) vegetation covered soils to the entire Waldstein-Weidenbrunnen experimental site.

For the EC flux measurements one never knows from which individual part of the Waldstein experimental site the soil emitted NO is coming from (i.e., where the fetch of these flux measurements is and particularly from which vegetation covered soil type the soil emitted NO is coming from). Therefore, the temporal average (DOY 146 to DOY 191, 2008) of the soil emission flux from Falge et al. (2010) was used. As a measure of this average soil emission NO flux, the temporal average of the corresponding standard deviation was used.

## Chapter 4: Results and Discussion

Here the main results obtained from the methods explained in Chapter 3 are discussed in detail. Emphasis is placed on those results that are directly linked to the objectives of this thesis. This chapter is subdivided into 7 important parts:

- (1) atmospheric conditions during selected evaluation periods
- (2) variation of trace gas mixing ratios
- (3) trace gas fluxes using gradient methods
- (4) trace gas fluxes using the eddy covariance method
- (5) comparison of trace gas fluxes evaluated using the gradient methods and those evaluated using the eddy covariance method
- (6) physical and chemical influences on the fluxes of the NO-O<sub>3</sub>-NO<sub>2</sub> triad
- (7) trace gas fluxes under reduced advection conditions

### 4.1 Data availability

The evaluated data were chosen from those days (so-called ‘golden days’) when the skies were clear, with a lot of sunlight and no precipitation. The reason for choosing such days is that the trace gases NO, NO<sub>2</sub> and O<sub>3</sub> are reactive – therefore the absence of precipitation was required to ensure that there were no additional reactions with precipitation such as raindrops during the day. Chemical reactions of the NO-O<sub>3</sub>-NO<sub>2</sub> triad are driven by photolysis (see 1.1) – therefore the presence of clear skies during the day to provide a continuous source of sunlight was required to make an unbiased analysis.

Suitable periods that fulfilled these conditions were used for all the evaluations in this chapter and were IOP-1; 29.09-03.10.2007; IOP-2: 29.06 – 02.07.2008; total measurement period: 03.06-10.07.2008. IOP-1 data will be used mainly to study the influence of meteorology on the site under two different seasons. Available data consisted of all the parameters listed in Table 3.2 and the parameters from the supporting measurements listed in Table 3.3. Henceforth all data and results discussed here pertain to the golden days for each IOP.

### 4.2 Atmospheric conditions during measurement period

Atmospheric conditions for the ‘golden days’ periods of both IOPs were favourable for data analysis because they were characterized by lack of precipitation, moderate wind speeds, very low and infrequent cloud cover, and high radiation (see Fig. 4.1 and Fig. 4.2). These conditions, especially the

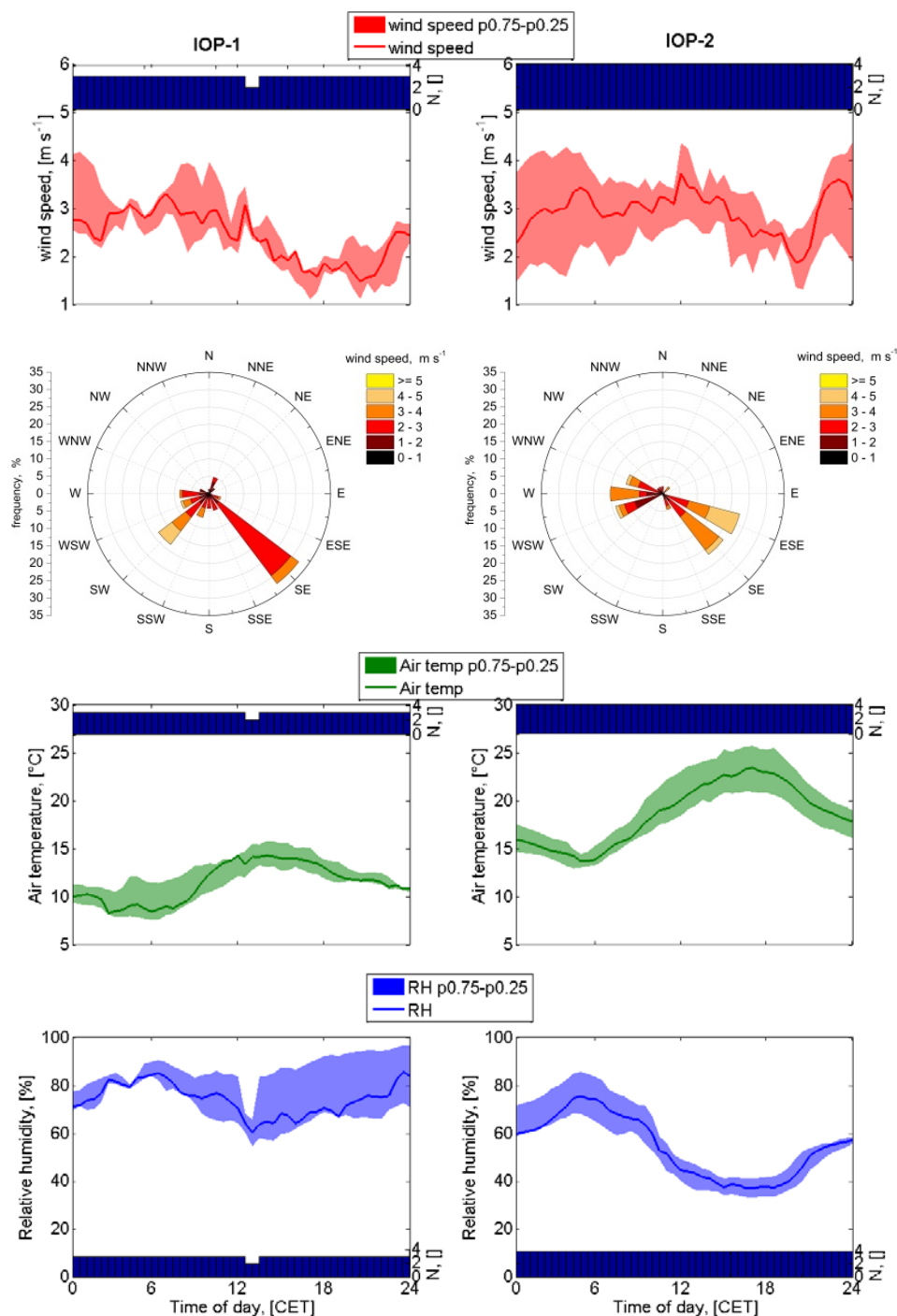
high global radiation (and therefore high  $j\text{NO}_2$  (see Eq. 2.79)) and the low cloud cover were important for the analysis of the light-dependent chemical reactions of the NO-O<sub>3</sub>-NO<sub>2</sub> triad.

Figure 4.1 and Fig. 4.2 show the mean diel variation of selected atmospheric parameters during the “golden days” periods. The IOP-1 was an autumn experiment while IOP-2 was a summer experiment. As a result of the seasonal temperature differences, the IOP-2 period was warmer than the IOP-1 period, with the average maximum temperature during IOP-2 (24 °C) being roughly 10°C higher than during IOP-1 (14 °C). The year 2007 was on average the warmest in the region since 1850 (see Staudt and Foken, 2008), even though the summer temperatures for that year were not as warm as those in 2008.

Both IOP-1 and IOP-2 were dominated by cyclonic conditions, with the IOP-1 golden days’ period occurring just after the anticyclone *Katrin* had swept across the mid-European region. The IOP-2 period was under the influence of warmer air encircling cold air masses in the north. However, the golden days’ period for IOP-2 was characterised by dry summer weather conditions.

Horizontal wind speeds reported here were measured at 31 m (a.g.l) on top of the MT. This height was chosen because the meteorological standard of 11 m was within the canopy and would not give an accurate indication of the horizontal wind speed. Median diel wind speeds (Fig. 4.1) during IOP-1 peaked at 3 m s<sup>-1</sup> around 0600 CET in the morning and declined after midday, reaching levels of about 1.5 m s<sup>-1</sup> at 2200 CET. A similar pattern was observed for the wind speeds during the IOP-2 period (Fig 4.1). On the other hand, IOP-2 was predominated by moderate wind speeds most of the day, only declining slightly in the evening. The wind speeds can be summarised as being moderate and comparable for the two IOPs. Mean diel wind direction (Fig. 4.1) was in the East-Southeast to South-Southeast sector during most of the day.

For both IOPs, atmospheric conditions were unstable during the course of the day (indicating the development of turbulence) and slightly stable during the night. IOP-1 showed higher levels of night-time stability than IOP-2, a condition that is also shown by the much lower friction velocities (< 0.1 m s<sup>-1</sup>) between 1800 CET and 0600 CET the next morning. Friction velocities during both IOPs followed the same diel course with IOP-2 friction velocities being on average 20% higher than for IOP-1. The low night-time friction velocities and neutral to stable night-time conditions were expected to favour accumulation of those trace gases that are normally emitted from the forest and the deposition of those trace gases that are normally deposited to the forest floor.



**Fig. 4.1.** Plots of the diel atmospheric conditions during the golden days of IOP-1 (29.09-03.10.2007) and IOP-2 (29.06-02.07.2008). Shown are the wind speeds (red), wind direction roses, air temperature (green), and relative humidity (blue). The shaded areas depict the interquartile range over the measurement days for each data point and the dark blue bar graphs show the number of data points ( $N$ ) for each 30 minute period.

The IOP-1 was relatively more humid than IOP-2 (see Fig. 4.1), with more variability in the humidity after midday. The IOP-2 had much lower daytime relative humidity, with values of 35% on average after midday. These differences are all directly related to the autumn-summer differences; the autumn conditions during IOP-1 were characterised by more precipitation than IOP-2. In addition, the period

leading to the golden days had been characterised by a lot of rainfall. Therefore an accumulation of moisture in the soil and the canopy, as well as the transport of moist autumn air masses to the site can be the reason for the higher relative humidity during the IOP-1 golden days when compared to the IOP-2 golden days.

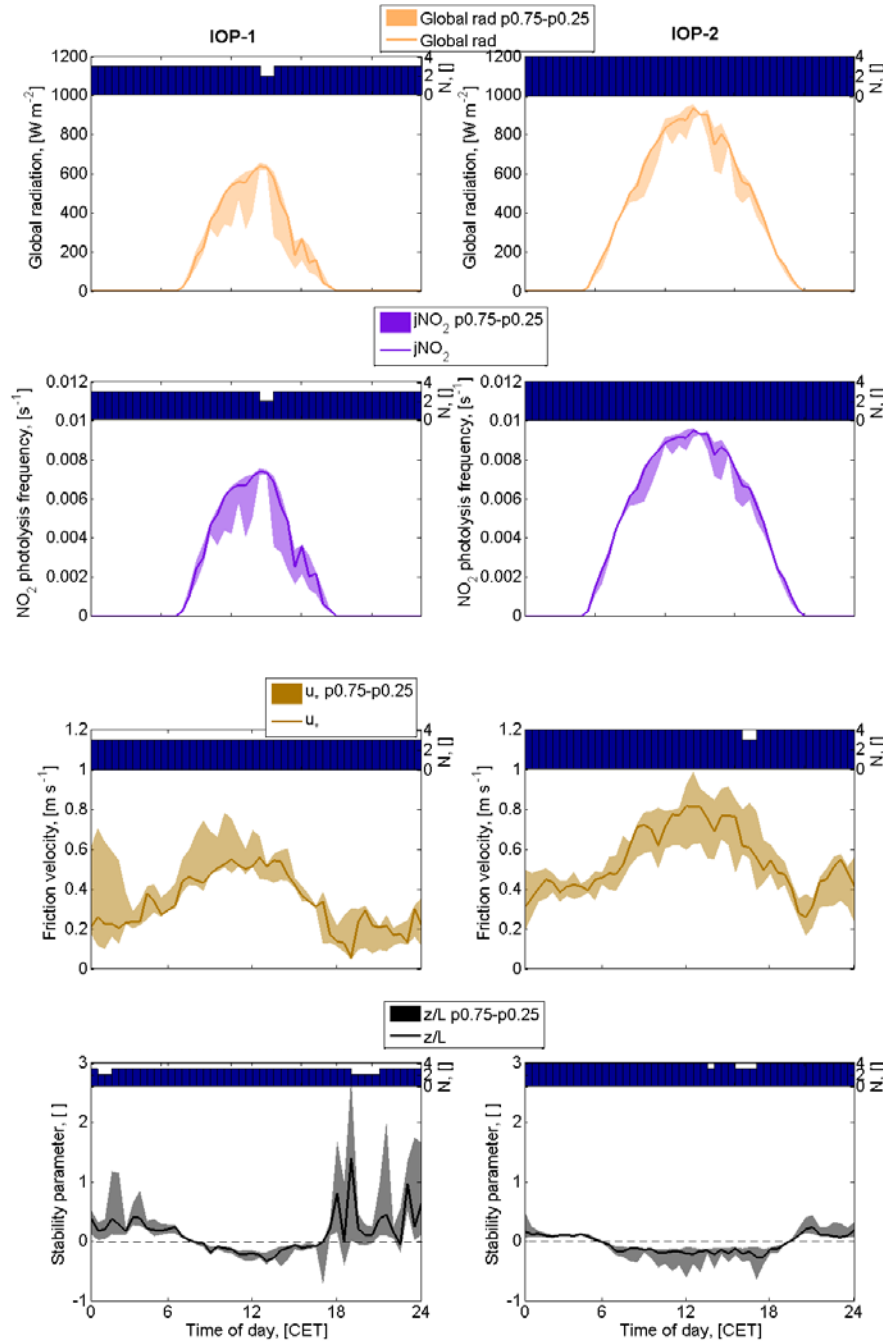


**Fig. 4.2.** Plots of the diel atmospheric conditions during the golden days of IOP-1 (29.06-03.07.2008). Shown is the global radiation (orange),  $j\text{NO}_2$  (violet), friction velocity (brown), and the stability parameter (black). The shaded areas depict the interquartile range over the measurement days for each data point and the dark blue bar graphs show the number of data points ( $N$ ) for each 30 minute period.

The average time of sunrise was 0345 CET and sunset was 2030 CET. Median diel cycles of global radiation (Fig. 4.2) showed well defined almost bell shaped curves indicative of clear skies. These were the optimum conditions for studying photochemistry. Midday values of global radiation and  $j\text{NO}_2$  (see Fig. 4.2) were about 33% higher during IOP-2 than during IOP-1. This is due to the difference in the seasons (solar angle) between the two measurement periods. As a result, higher production of  $\text{O}_3$  by photolysis (see R1.1 and R1.2) was expected.

### 4.3 Variation of trace gas mixing ratios during IOP-2 golden days

The distribution of the mixing ratios of the  $\text{NO-O}_3\text{-NO}_2$  triad above the forest canopy (32 m) were analysed and the results grouped into all weekdays (Monday to Wednesday) and weekends (Sunday). The aim of such a grouping was to identify to what extent anthropogenic sources of  $\text{NO}_x$  (such as cars and trucks on the country roads surrounding the measurement site) influence the mixing ratios of the reactive trace gases reaching the site because the traffic density is generally higher during the week than during weekends due to people commuting to and from work and trucks moving on the roads.

Median diel variations of the mixing ratio of the  $\text{NO-O}_3\text{-NO}_2$  triad were calculated from 1 minute resolution averages. The data was classified according to percentiles with the 25th percentile, the 50th percentile (median) and the 75th percentile used. The results were plotted in Fig. 4.3 separately for weekdays (Monday to Wednesday), and weekends (Sunday).

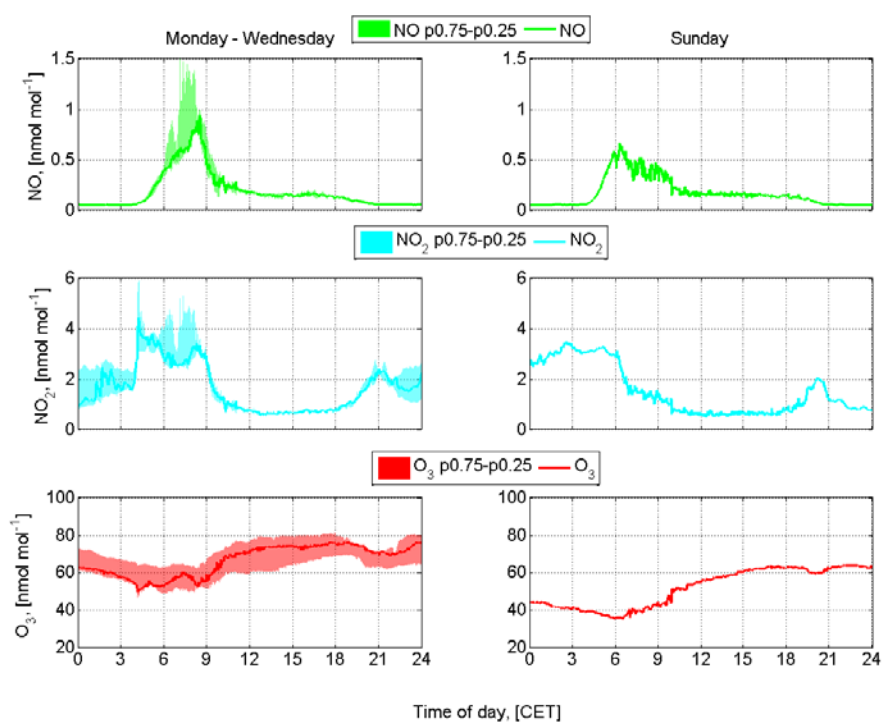


**Fig. 4.3.** Median diel variation of  $\text{NO}$  (red),  $\text{NO}_2$  (cyan), and  $\text{O}_3$  (red) mixing ratios for the time periods Monday-Wednesday (30.06-02.07.2008) (left) and Sunday (29.06.2008) (right) during IOP-2 golden days. The shaded areas indicate the interquartile range of the data.

The classification was also done for the nonreactive ( $\text{NO}_x$ ,  $\text{CO}_2$  and  $\text{H}_2\text{O}$ ) trace gases (Fig. 4.4). The reason for including the nonreactive trace gases was so that the possibility of chemical reaction during transport as well as advection could be investigated.

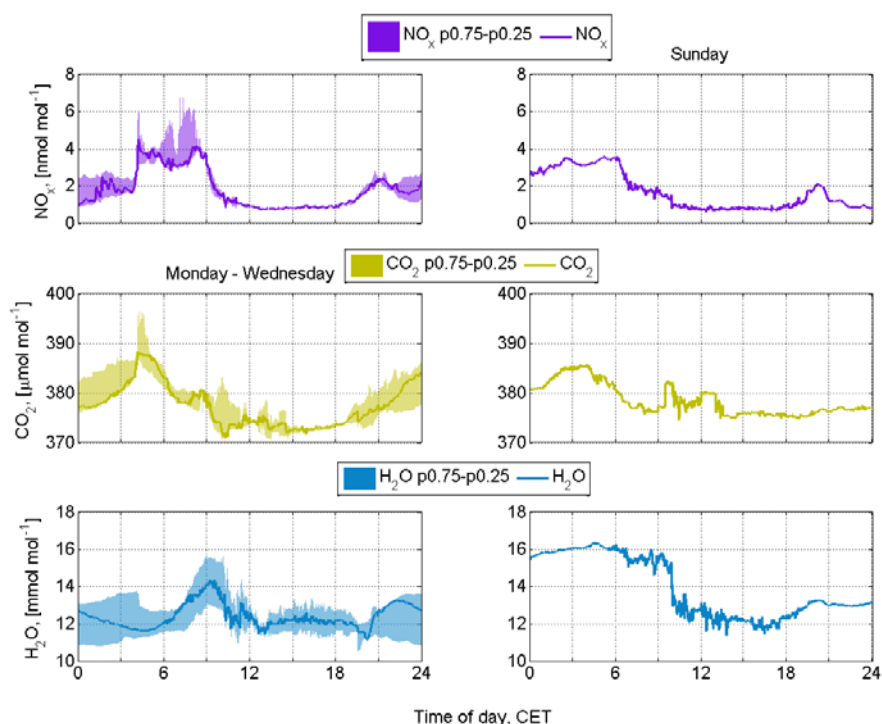


**Fig. 4.4.** Median diel variation of the  $\text{NO}_x$  (violet),  $\text{CO}_2$  (olive), and  $\text{H}_2\text{O}$  (blue) mixing ratios for the time periods Monday-Wednesday (30.06-02.07.2008) (left) and Sunday (29.06.2008) (right) during IOP-2 golden days. The shaded areas indicate the interquartile range of the data.

#### 4.3.1. Weekdays

Diel variation of the  $\text{NO}$ - $\text{O}_3$ - $\text{NO}_2$  triad for all the weekdays of the available data during IOP-2 showed a distinct pattern for all three constituents of the triad (Fig. 4.3).

The most distinct pattern was shown by the  $\text{NO}$  mixing ratios whereby levels of  $\text{NO}$  started to rise from zero as early as 0400 CET in the morning, reaching a distinct peak of  $1 \text{ nmol mol}^{-1}$  (median) at 0900 CET in the morning before levelling out to an almost steady state value of  $0.3 \text{ nmol mol}^{-1}$  (median) at 1130 CET. This steady state mixing ratio rapidly decayed from 1730 CET, reaching zero around 2000 CET in the evening. The characteristic peak can be assumed to have been caused by a strong source of  $\text{NO}$  which was rapid enough to overcome the strong  $\text{NO}$  sink provided by the high concentration of  $\text{O}_3$  present. Biogenic  $\text{NO}$  emissions from the soil were not assumed to be strong and rapid enough to overcome the  $\text{O}_3$  sink. Therefore advection of  $\text{NO}_x$  from the nearby country road was singled out as the course of the peak. The peak coincided with the period when there is a high traffic density due to people going to work. In addition the timber trucks and delivery trucks were expected

to be busy on the roads at that time. A traffic survey for the country road 1 km away from the site conducted in 2005 showed that the road encounters 3000 cars per hour.

Nitrogen dioxide underwent a similar increase at the same time, rising from a steady state value of about  $1 \text{ nmol mol}^{-1}$  at 0000 CET to a peak median value of  $4 \text{ nmol mol}^{-1}$  at 0430 CET before declining to  $3 \text{ nmol mol}^{-1}$  at 0700 CET. After that, the  $\text{NO}_2$  mixing ratio started to rise simultaneously with the NO mixing ratio, reaching a median peak of  $3.5 \text{ nmol mol}^{-1}$  at 0830 CET, the same time that NO reached its peak. This was also assumed to be the advection induced peak described for NO in the previous subsection. After that, there was a rapid decline, reaching a steady-state value of  $0.5 \text{ nmol mol}^{-1}$  at 1100 CET. The  $\text{NO}_2$  mixing ratios started to rise again after 1800 CET, coinciding with the point at which  $j\text{NO}_2$  became zero. This indicates that there was no more destruction of  $\text{NO}_2$  by photolysis and therefore it could accumulate. Additionally, the NBL depth was becoming shallow and therefore the  $\text{NO}_2$  mixing ratios could increase above the canopy. The NO still present above the canopy as well as the NO coming out of the soil were also being converted to  $\text{NO}_2$ , hence the increase of  $\text{NO}_2$ . At 2100 CET, after reaching a peak of  $2 \text{ nmol mol}^{-1}$ , the  $\text{NO}_2$  mixing ratio started to decrease again, reaching a minimum of  $1.8 \text{ nmol mol}^{-1}$  at close to midnight.

Ozone showed a steady decrease from a midnight value of  $60 \text{ nmol mol}^{-1}$  to a minimum of  $50 \text{ nmol mol}^{-1}$  at 0430 CET before rising steadily to a maximum of  $80 \text{ nmol mol}^{-1}$  at 1800 CET. It then decreased to  $70 \text{ nmol mol}^{-1}$  at 2200 CET before rising again to  $80 \text{ nmol mol}^{-1}$  close to midnight. The steady decrease of  $\text{O}_3$  in the early morning can be assumed to be a result of the shallow nocturnal boundary layer already slowly starting to rise and thereby diluting the mixing ratios, releasing the trapped  $\text{O}_3$ , since at that time there is no NO present in the ABL to account for the destruction of  $\text{O}_3$ . Another reason is the depletion of  $\text{O}_3$  by surface deposition on leaves, etc. as well as stomatal uptake after 0345 CET when the sun comes up and the stomata open.

After sunrise, the decrease of  $\text{O}_3$  was also caused by the rapid increase of NO which provided a strong sink for  $\text{O}_3$ . In the same way, the increase of  $\text{O}_3$  after 2200 CET can be assumed to be due to the development of a shallow nocturnal boundary layer which traps the  $\text{O}_3$ . The daytime steady-state rise in  $\text{O}_3$  mixing ratios was assumed to be due to the photolytic oxidation of  $\text{O}_2$  to  $\text{O}_3$  (see R1.2).

The result of this investigation suggests that the driving forces for the distribution of the triad compounds were predominant during the weekdays. It adds strength to the proposition that there is a strong influence of external sources of  $\text{NO}_x$  on the distribution of the triad mixing ratios.

The median diel cycles of  $\text{NO}_x$ ,  $\text{CO}_2$  and  $\text{H}_2\text{O}$  also showed distinct diel patterns as shown in Fig. 4.4. Mixing ratios of  $\text{NO}_x$  followed the same diel course as  $\text{NO}_2$ . This is not surprising since  $\text{NO}_2$  was more abundant than NO. The same bimodal peaks seen in the  $\text{NO}_2$  diel variation is also seen in the

NO<sub>x</sub> variation. The maximum median value of NO<sub>x</sub> was about 4.2 nmol mol<sup>-1</sup> while the minimum value was approximately 1 nmol mol<sup>-1</sup>.

Carbon dioxide rose from midnight, reaching a peak (387 μmol mol<sup>-1</sup>) at 0430 CET before starting to decrease, reaching about 371 μmol mol<sup>-1</sup> at 1030 CET where it remained until 1800 CET when it started to increase again, reaching 385 μmol mol<sup>-1</sup> close to midnight.

The two periods of CO<sub>2</sub> increase can be attributed to respiration by the trees and from the soil creating an increase in CO<sub>2</sub>. In addition, the shallow NBL increased the concentration of CO<sub>2</sub>. Early morning decrease of CO<sub>2</sub> can be assumed to have been due to the onset of photosynthesis due to the rising of the sun and the lifting of the NBL. In the evening, photosynthesis ended with the setting of the sun and the resulting respiration created the increased CO<sub>2</sub> mixing ratios. No diel pattern was expected from the H<sub>2</sub>O mixing ratios. However an early to mid-morning rise in H<sub>2</sub>O mixing ratios can be assumed to be due to evaporation of dew from leaves as well as the soil.

### 4.3.3 Weekend

For the weekends, only one day of ideal conditions data was available for analysis. This day was a Sunday (29.06.2008). Analyses in the following sections will cover reactive, then nonreactive trace gases in a similar manner to the analyses for the weekdays.

Mixing ratios of NO on Sunday showed the same variation as that described for the weekdays. The only difference was the magnitude of the NO peak. The peak had its maximum of 0.6 nmol mol<sup>-1</sup> at 0600 CET before declining to a steady value of 0.2 nmol mol<sup>-1</sup> at 1000 CET (the same time as weekdays). The NO mixing ratio remained at 0.2 nmol mol<sup>-1</sup> until 1800 where it declined to 0.1 nmol mol<sup>-1</sup>. The Sunday peak can be assumed to be due to baker's trucks delivering bread early in the morning (supported by the fact that the peak was at 0600 CET, the time around which most bakeries deliver bread on Sundays). The rest of the advection period can be assumed to be due to the low density Sunday traffic which declined steadily. Therefore the nominal value of 0.2 nmol mol<sup>-1</sup> NO which was observed during the period after the advection until sunset can be assumed to be the NO mixing ratio due to the exchange between the forest and the atmosphere. The same value was also observed during the same time period for weekdays. It can be assumed that low NO levels cannot reach the site from the country road before they are converted by the high O<sub>3</sub> background concentrations.

Weekend (Sunday) mixing ratios of NO<sub>2</sub> did not show the advection peak that was observed in the weekday mixing ratios. It may be that the peak was present but was lower than the night-time to early morning high mixing ratios of NO<sub>2</sub> which were assumed to be due to a shallow NBL and storage. NO<sub>2</sub> started at mixing ratios of approximately 3 nmol mol<sup>-1</sup> at midnight and started to decrease at 0600 CET, reaching a steady state value of 0.5 nmol mol<sup>-1</sup> at 1000 CET. Shortly after 1800 CET NO<sub>2</sub>

started to rise again, reaching a peak of 2 nmol mol<sup>-1</sup> at 2000 CET before going back down to 0.5 nmol mol<sup>-1</sup> for the rest of the night. The NO<sub>2</sub> mixing ratio started the day high due to the storage of NO<sub>2</sub> caused by high anthropogenic activity expected on the previous night (Saturday).

Sunday O<sub>3</sub> mixing ratios showed an almost identical pattern to that observed on weekdays with the only difference being that the Sunday mixing ratios were 66% less than those during the weekdays. The low O<sub>3</sub> levels were assumed to be a result of the correspondingly low NO and NO<sub>2</sub> levels on this day.

In summary, three identifiable phases in the diel evolution of the reactive trace gases exist - *storage*, *source* and *sink*.

### **NO<sub>2</sub>**

*Storage* of below canopy NO<sub>2</sub>, *sink* above the canopy (by the photolysis of NO<sub>2</sub>), and *source* of NO<sub>2</sub> below canopy from the reaction between in-canopy O<sub>3</sub> and soil biogenic emissions of NO.

### **NO**

There is no *storage* of NO because O<sub>3</sub> is a very strong *sink* for any NO present. The *source* of NO is below canopy microbiological activity and photolysis of NO<sub>2</sub> above the canopy.

### **O<sub>3</sub>**

There is *storage* of O<sub>3</sub> in the shallow NBL during absence of a sink. The *sink* for O<sub>3</sub> is NO, stomatal uptake, and dry deposition while the *source* is the secondary reaction of NO<sub>2</sub> photolysis (photolytic oxidation of O<sub>2</sub>).

### **NO<sub>x</sub>**

The mixing ratios of NO<sub>x</sub> followed the same diel pattern exhibited by the weekday mixing ratios. Again the only difference was that the magnitude was lower. In the absence of advection, the mixing ratio of NO<sub>x</sub> was constant at 1 nmol mol<sup>-1</sup> during the day.

Carbon dioxide mixing ratios on Sunday followed an almost similar diel course to that observed from the weekdays. However minimum daytime CO<sub>2</sub> mixing ratios were slightly higher than those on weekdays (376 μmol mol<sup>-1</sup> compared to 371 μmol mol<sup>-1</sup>). In addition there was no night time storage of CO<sub>2</sub> on Sunday. It is unclear why this was so but it may be due to a higher NBL or a stronger forest atmosphere coupling on that night. This will be investigated further when the exchange processes on this day will be analysed in detail (4.7). Water vapour mixing ratios on Sunday started out higher than those on weekdays until 1200 CET, apparently due to the formation of early morning dew on that day. There was however no distinct diel pattern.

To investigate further the extent to which external sources of  $\text{NO}_x$  may be influencing the mixing ratios of the triad, the Leighton ratio was used (see Equation. 1.1 and Figs. 4.5, 4.6, and 4.7). Weekday values of the Leighton ratio ranged between 2 and 7, with Tuesday showing the highest maximum Leighton ratio. These figures are indicative of a slightly  $\text{NO}_x$  polluted environment, i.e. there is a small contribution of  $\text{NO}_x$  into the environment which is pushing the Leighton ratio up, indicating that there are additional sinks of  $\text{NO}$  in the environment other than the  $\text{O}_3$ .

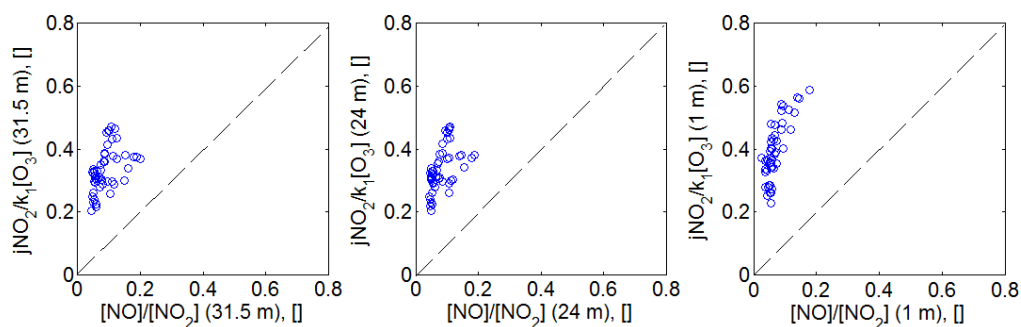


**Fig. 4.5.** Leighton ratio relationship for the  $\text{NO}-\text{O}_3-\text{NO}_2$  triad at 31.5 m, 24 m, and 1 m for the golden days weekdays. The dashed line shows the 1:1 relationship where the PSS is achieved.

Sunday had a higher minimum but lower maximum Leighton ratio (2.5 and 4.2). The overall implication of the Leighton ratios on Sunday was the same as for weekdays.

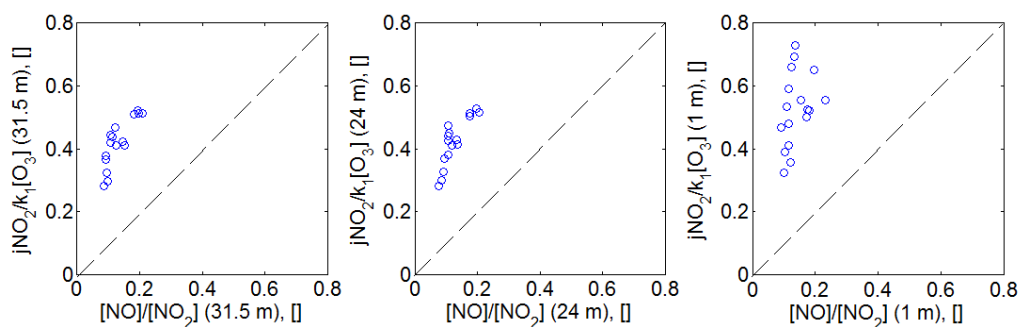


**Fig. 4.6.** Leighton ratio relationship for the  $\text{NO}-\text{O}_3-\text{NO}_2$  triad at 31.5 m, 24 m, and 1 m for the golden days weekend. The dashed line shows the 1:1 relationship where PSS is achieved.

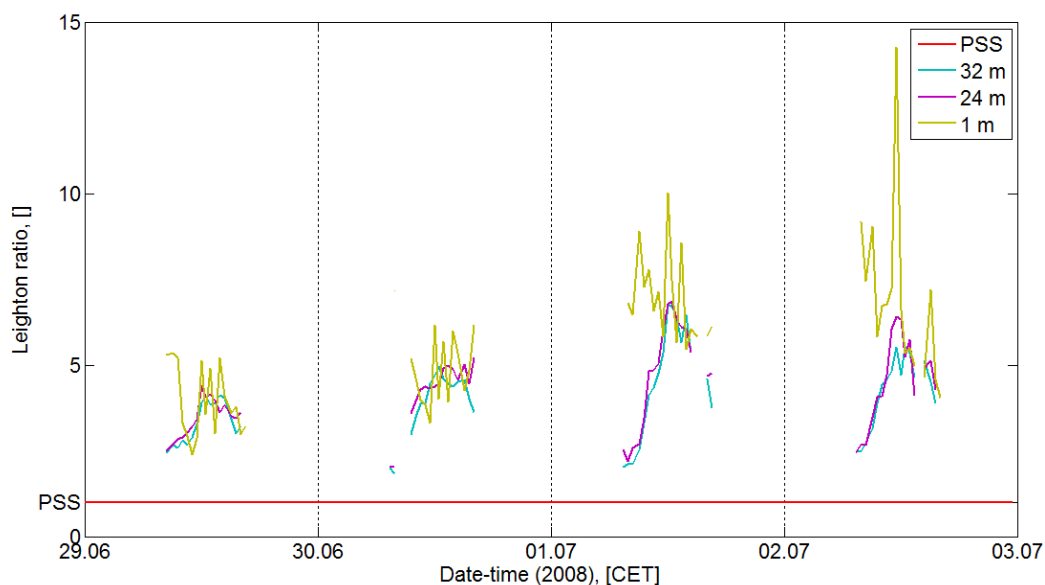


**Fig. 4.7.** Time series of the Leighton ratio distribution during the Golden Days of IOP-2. The red line shows the point at which the photostationary state (PSS) is achieved.

The results of the Leighton ratio investigation indicated that the environment was indeed moderately polluted and that there were additional sources of  $\text{NO}_x$ . The next investigation aimed to confirm whether advection of  $\text{NO}_x$  from the surrounding busy country roads was responsible for bringing in fresh  $\text{NO}_x$  to the measurement site.

### 4.3.3 Variation of the mixing ratios with wind direction

In order to complete the analysis above and gain some insight into the possibility of advection playing a role in the diel variability of the mixing ratios of the trace gases, plots of the distribution of the mixing ratios of the reactive trace gases with wind direction are shown (Fig. 4.8).

The  $\text{NO}$  and  $\text{NO}_2$  mixing ratios showed higher mixing ratios when the wind was coming from sectors close to the country roads from the measurement site. This observation should be treated cautiously because the wind did not blow equally from all directions, with south-easterly winds being predominant during the weekdays and westerly winds on Sunday. Mixing ratios of  $\text{O}_3$  were largely not influenced by the wind direction.

Now that we have seen the distribution of the mixing ratios of the trace gases above the forest canopy at the site, the question to answer from the objectives is: what is the magnitude of the biosphere-atmosphere exchange of the reactive trace gases? Can we quantify and/or partition the fluxes?

The first step towards answering this question is to present the results of the analysis of the data quality which will show whether the instruments available could be used further for flux measurements.

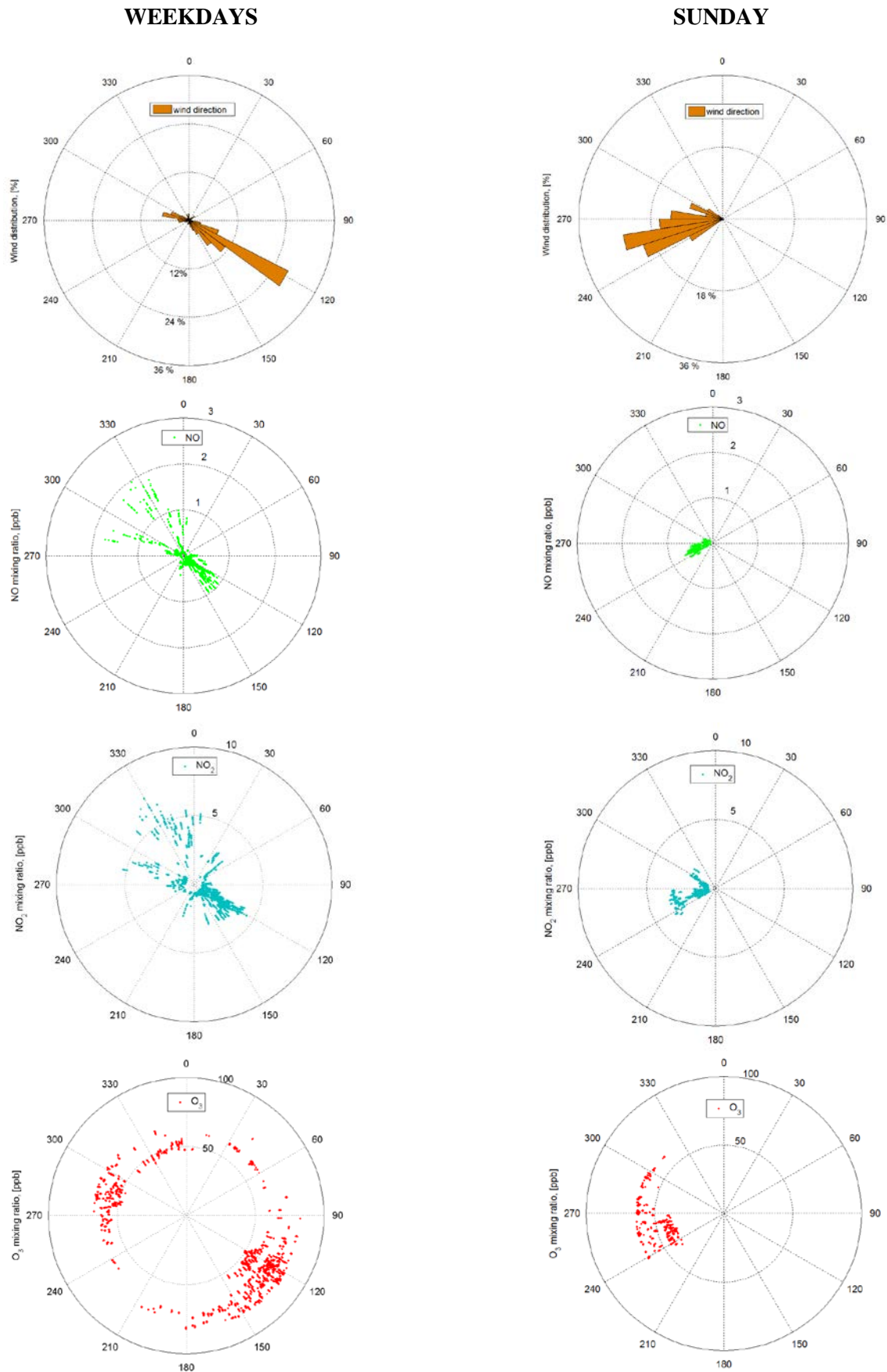


Fig. 4.8. Distribution of mixing ratios according to wind direction for the golden days of IOP-2.

#### 4.4 Evaluation of the trace gas fluxes using gradient methods

For the evaluation of trace gases using the gradient method, it was important to assess the limits of precision of the concentration differences evaluated from the measurement instruments. This is because the concentration difference is the most important determining factor for both the MBRM and the AGM. To recap, the trace gas measurement concentration differences for this study were between 32 m and 25 m.

In order to verify the suitability of the instruments used in this study for gradient-derived measurement of trace gas fluxes above the forest, a comprehensive quality analysis of trace gas vertical concentration difference ( $\Delta\chi$ ) data was carried out and the results are reported in the following sections. This is in line with one of the challenges associated with measuring trace gases brought out in 1.3. This section is subdivided into 2 important parts: the data quality analysis part (4.4.1 to 4.4.3) and the flux results part (4.4.4 to 4.4.5).

##### 4.4.1 Precision of trace gas analysers – the sigma criteria

The sigma precision criteria were used to investigate the precision limits of the instruments at 4 different levels of precision ( $\sigma$ ,  $2\sigma$ ,  $3\sigma$  and  $10\sigma$ ). Recall that sigma was described in 3 as the standard deviation of the measurements over a period of time when an instrument is sampling zero air.

Table 4.1 shows the precision for concentration differences associated with each precision criterion. Also shown are the minimum hypothetical fluxes (according to the AGM) associated with each respective precision criterion. The fluxes are calculated assuming friction velocity  $u_* = 0.2 \text{ m s}^{-1}$  and neutral conditions ( $z/L=0$ ). The investigation is also carried out for the same hypothetical fluxes when assuming that the effect of the roughness sublayer is present.

**Table 4.1.** Limits of precision of concentration differences measurement instruments. Minimum fluxes were calculated for neutral conditions and  $u_* = 0.2 \text{ m s}^{-1}$ ;  $F_N(z/L=0, u_* = 0.2) = 0.178$ ;  $m = 1.8$ .

quantity, $\chi$	units	$\sigma_\chi$	$\delta\Delta\chi(\sigma_\chi)$	$\delta\Delta\chi(2\sigma_\chi)$	$\delta\Delta\chi(3\sigma_\chi)$	$\delta\Delta\chi(10\sigma_\chi)$	Flux, $F_\chi$ units	$F_\chi(\sigma_\chi)$	$F_\chi(2\sigma_\chi)$	$F_\chi(3\sigma_\chi)$	$F_\chi(10\sigma_\chi)$	$F_N$	$F_{\text{Froben}}$
Dry temp	K	0.05	0.071	0.142	0.213	0.71	$\text{W m}^{-2}$	0.0097	0.0193	0.0290	0.0966	0.7125	0.1268
CO <sub>2</sub> (7000)	$\mu\text{mol mol}^{-1}$	0.06	0.0848	0.1696	0.2544	0.848	$\mu\text{mol m}^{-2}\text{s}^{-1}$	0.0115	0.0231	0.0346	0.1154	0.848	0.1509
H <sub>2</sub> O (7000)	$\text{mmol mol}^{-1}$	0.001 5	0.0021	0.0042	0.0063	0.021	$\text{mmol m}^{-2}\text{s}^{-1}$	0.0003	0.0006	0.0009	0.0029	0.021	0.0037
NO	$\text{nmol mol}^{-1}$	0.022	0.031	0.062	0.093	0.31	$\text{nmol m}^{-2}\text{s}^{-1}$	0.0042	0.0084	0.0127	0.0423	0.31	0.0552
NO <sub>2</sub>	$\text{nmol mol}^{-1}$	0.133	0.1881	0.3762	0.5643	1.881	$\text{nmol m}^{-2}\text{s}^{-1}$	0.0256	0.0512	0.0768	0.2560	1.881	0.3348
O <sub>3</sub>	$\text{nmol mol}^{-1}$	0.2	0.2828	0.5656	0.8484	2.828	$\text{nmol m}^{-2}\text{s}^{-1}$	0.0385	0.0770	0.1155	0.3849	2.828	0.5034

Table 4.2 shows the four precision criteria when applied to the concentration differences derived from the trace gas measurements for IOP-2.

Results showed that the reactive trace gases (NO, NO<sub>2</sub> and O<sub>3</sub>) are affected the most by any form of data elimination criteria. Even at  $\sigma$  criterion, NO, NO<sub>2</sub> and O<sub>3</sub> retain only 6.9%, 0% and 25.5% respectively of their data over the four golden days of IOP-2. More stringent criteria ( $2\sigma$ ,  $3\sigma$ ,  $10\sigma$ ) resulted in progressively higher losses of data. Nonreactive trace gases had acceptable significant data up to  $2\sigma$ . The  $10\sigma$  criterion yields almost zero retention for all trace gases.

This result exposes the limitation associated with measuring reactive trace gases when mixing ratios are low. It brings out the need for higher precision instruments. An investigation by Foken (1998) on reactive trace gas concentration differences concluded that the minimum reactive trace gas flux measurable is only significant at the  $10\sigma$  criterion.

As can be seen from the results in Table 4.1 and 4.2, getting adequate significant data at  $10\sigma$  and for RSL measurements requires either (a) large concentration gradients (larger inlet separation) or (b) highly precise instruments. Both requirements were impractical for the measurements in this study. Therefore a decision was made to evaluate the reactive trace gas concentration differences without using any precision criteria and the nonreactive trace gas fluxes using the  $2\sigma$  criterion.

**Table 4.2.** Number of data points remaining after applying four precision criteria on concentration differences of various trace gases during IOP-2. Values are given out of a possible 192 (4 days of 30 minute data points). The numbers in brackets are the corresponding percentages.

Trace gas difference, $\Delta\chi$	N( $\sigma$ ) (%)	N( $2\sigma$ ) (%)	N( $3\sigma$ ) (%)	N( $10\sigma$ ) (%)
CO <sub>2</sub> Li-7000	142 (74)	118 (61.5)	81(42.2)	6 (3.1)
H <sub>2</sub> O Li-7000	156 (81.3)	145 (75.5)	136 (70.8)	88 (45.8)
NO	10 (6.9)	3 (1.6)	1 (0.5)	0 (0)
NO <sub>2</sub>	0 (0)	0 (0)	0 (0)	0 (0)
O <sub>3</sub>	49 (25.5)	8 (4.2)	0 (0)	0 (0)
T <sub>dry</sub> (psychrometer)	172 (89.6)	137(71.3)	106 (55.2)	15 (7.8)

#### 4.4.2 Distribution of vertical concentration differences

Vertical differences of u, T, CO<sub>2</sub>, H<sub>2</sub>O, NO, NO<sub>2</sub> and O<sub>3</sub> between 25 m and 32 m are shown in Fig. 4.9. Data used was for the golden days of IOP-2. A Laplace double-exponential as well as a normal distribution was fitted to each histogram. The results show that horizontal wind velocity and temperature fit better to the normal distribution than the Laplace distribution. However, all the trace gases fitted to the Laplace distribution better than to the normal distribution. O<sub>3</sub> and CO<sub>2</sub> in particular

fitted very well to the Laplace distribution. Wolff et al. (2010) found a similar double exponential distribution while evaluating vertical concentration differences of the  $\text{NH}_3\text{-HNO}_3\text{-NH}_4\text{NO}_3$  triad.

A yellow shaded region was added to the plots to show the precision limit at  $\sigma$ . This region shows more the amount of insignificant data for each parameter.

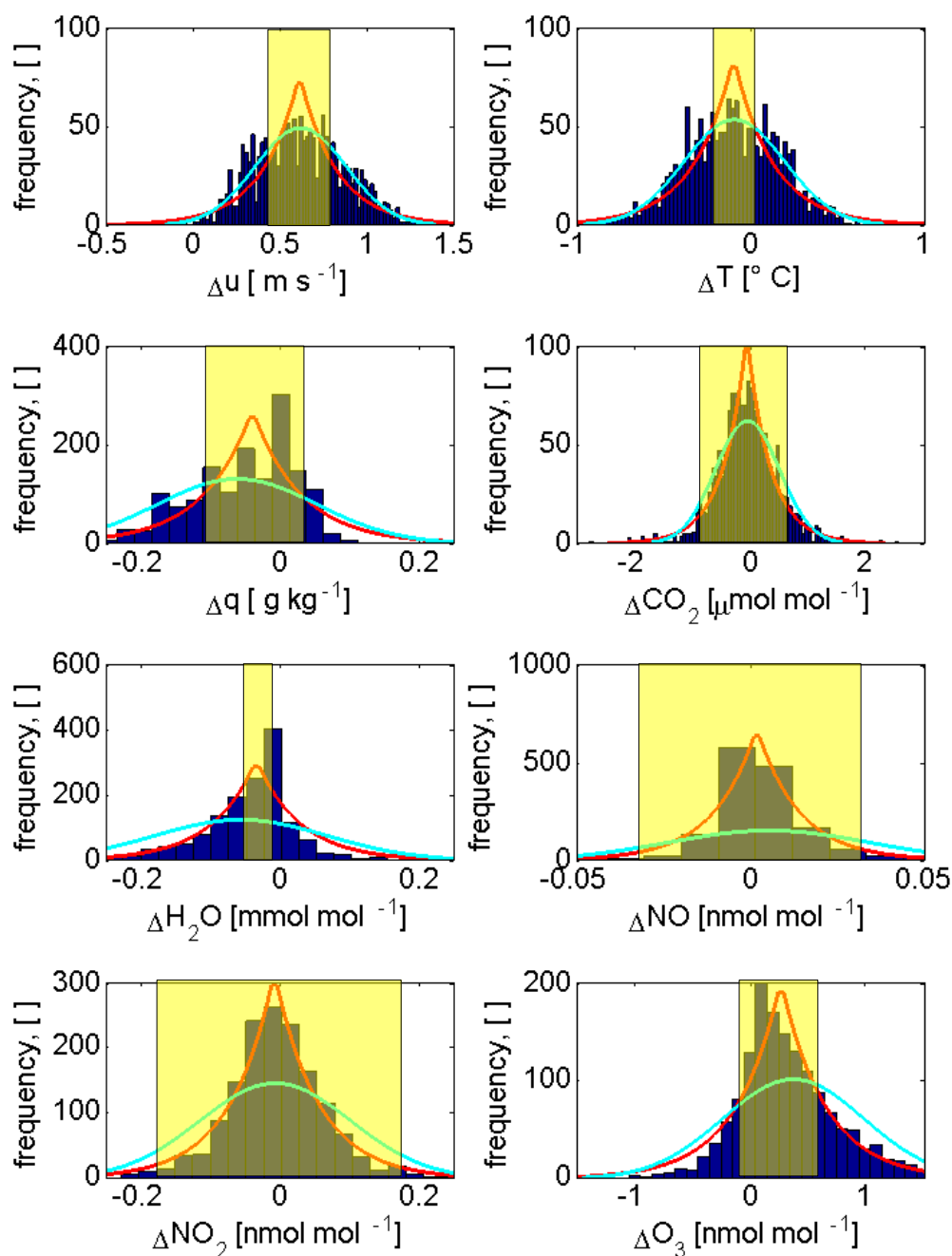


**Fig. 4.9.** Distribution of vertical concentration differences of meteorological parameters, reactive, and nonreactive trace gases EGER during IOP-2. The red line shows the double-exponential (Laplace) fit while the light blue line shows the normal distribution probability density. The yellow filled areas indicate the detection limit of the respective instrument at  $1\sigma$ .

When the statistical moments of each parameter were evaluated (see Table 4.3), the results showed, as expected, that those parameters with predominantly negative differences had negative skewness and vice versa.

**Table 4.3.** Summary of the statistical moments for the vertical differences on the MT. Usual units are assumed.

Parameter	Mean	Standard deviation	Skewness	Kurtosis
$\Delta u$	0.617	0.260	0.190	2.79
$\Delta T$	-0.095	0.287	0.322	3.98
$\Delta q$	-0.062	0.115	-6.910	104.00
$\Delta CO_2$	-0.061	0.548	0.058	5.34
$\Delta H_2O$	-0.057	0.124	-5.770	69.40
$\Delta NO$	0.005	0.029	-5.910	231.00
$\Delta NO_2$	-0.007	0.108	2.300	52.50
$\Delta O_3$	0.363	0.605	3.150	28.00

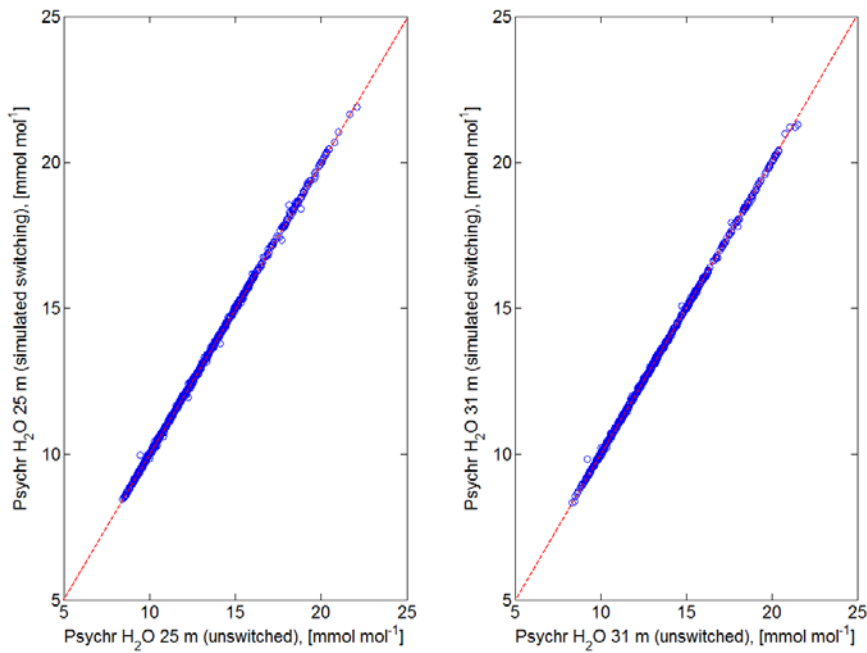
#### 4.4.3 Applicability of the discontinuous sampling method for finding concentration differences

This analysis was performed by simulated switching of continuous data on the MT (psychrometers specific humidity) and TT ( $CO_2$  and  $H_2O$ ). The simulated switched data in comparison with the switching profile gradients show the effect of switching on data quality and the extent to which stationarity places a role in the stability of the gradients.

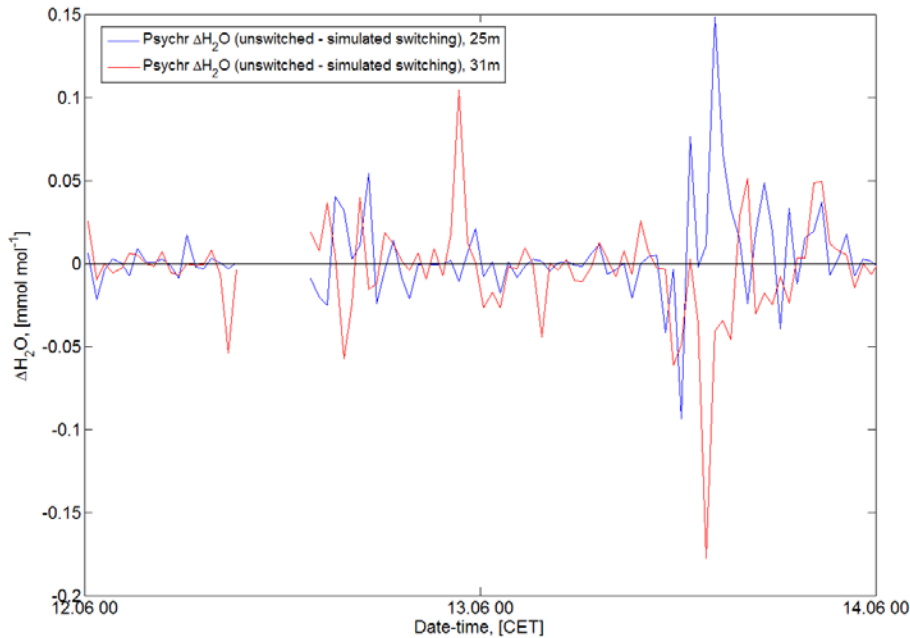
Figure 4.10 shows the relationship because continuous and discontinuous absolute  $H_2O$  mixing ratios as measured by the psychrometer at 25 m (left figure) and 31 m (right figure). The discontinuous psychrometer values were simulated by using the same time step as the RETGAP for both heights i.e. data for the psychrometer were removed at every instance where there was no data from the RETGAP (which occurred when it switched to a different height). The deviation caused by simulated switching is less than 3% of the absolute mixing ratios and can be considered insignificant.

Fig. 4.11 shows the 30 minute averages of the differences between the normal (unswitched) psychrometer measurements and the simulated (switched) measurements for both the 25 m level and the 31 m level. The implication of Fig, 4.11 is that deviations between a continuous profile measurement system and a discontinuous measurement system are apparent mostly during the day and at times when stability is high. In these cases, the discontinuous measurement system does not have

enough time to achieve a steady mixing ratio value before the system switches to another measurement level (its response time is not fast enough to deal with highly variable mixing ratios).



**Fig. 4.10.** Scatter plots illustrating the relationship between continuous and discontinuous  $H_2O$  mixing ratios at 25 m and 31 m on the MT between 12 and 14 June 2008.



**Fig. 4.11.** Mixing ratio differences between continuous measurements and simulated discontinuous measurements of  $H_2O$  on the MT at 25 m and 31 m between 12 and 14 June 2008.

When the vertical differences between the 31 m and the 25 m levels were evaluated, it was found that the differences for the switched psychrometer were comparable to those for the continuously sampling

psychrometer. However, larger differences were found for the continuous psychrometer when compared to the RETGAP. When the switched psychrometer was compared to the RETGAP, there was a very good correlation (see Fig. 4.12).

To investigate further the effect of switching on the mixing ratio differences, psychrometer data at 31 m and 25 m (both continuous and discontinuous) were further analysed by evaluating the difference between the continuous data and the discontinuous data at each of the two levels. The differences were found to be on average  $\pm 0.05 \text{ mmol mol}^{-1}$ , with occasional daytime spiking up to approximately  $\pm 0.2 \text{ mmol mol}^{-1}$ . The average deviation was more than 10 times higher than the precision limit of the LI-7000 analyser.

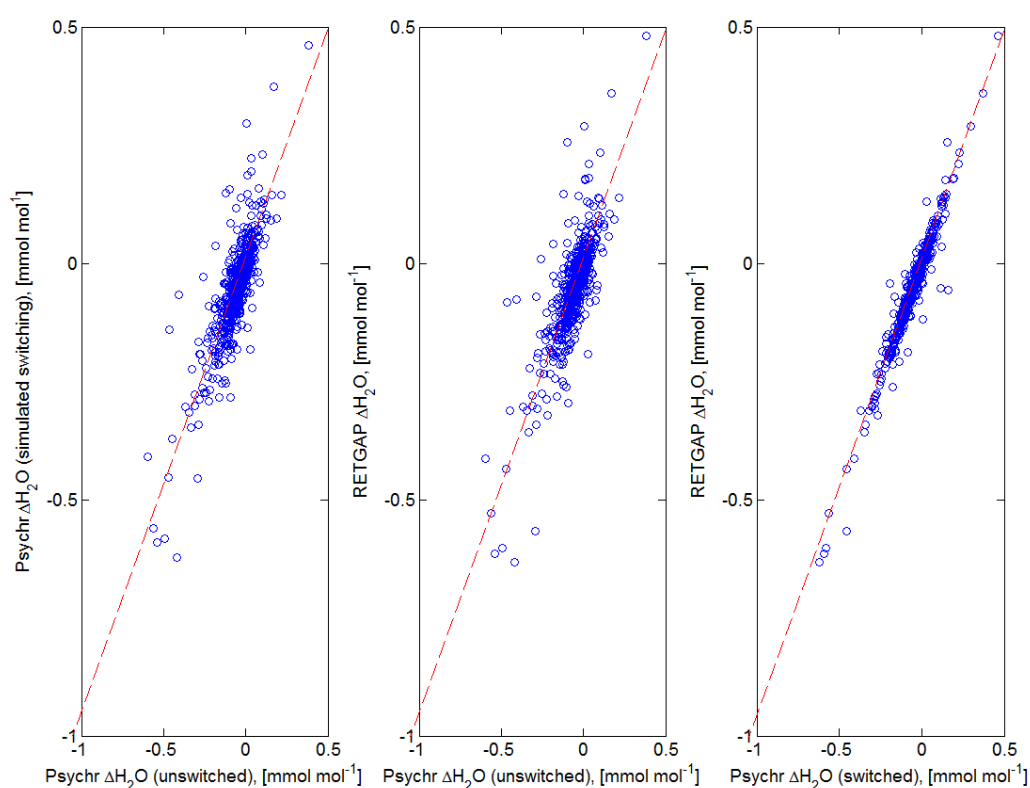


**Fig. 4.12.** Scatter plots illustrating the relationship between continuous and discontinuous  $\text{H}_2\text{O}$  mixing ratio differences (31 m -25 m) on the MT between 12 and 14 June 2008.

An average difference between continuous differences and discontinuous differences of  $\pm 0.025 \text{ mmol mol}^{-1}$  was found for the psychrometers. This was higher than the limit of precision for measuring  $\text{H}_2\text{O}$  differences at  $2\sigma$  ( $0.0042 \text{ nmol mol}^{-1}$ ). The differences of the continuous and discontinuous psychrometer mixing ratios against the RETGAP  $\text{H}_2\text{O}$  differences had similar values.

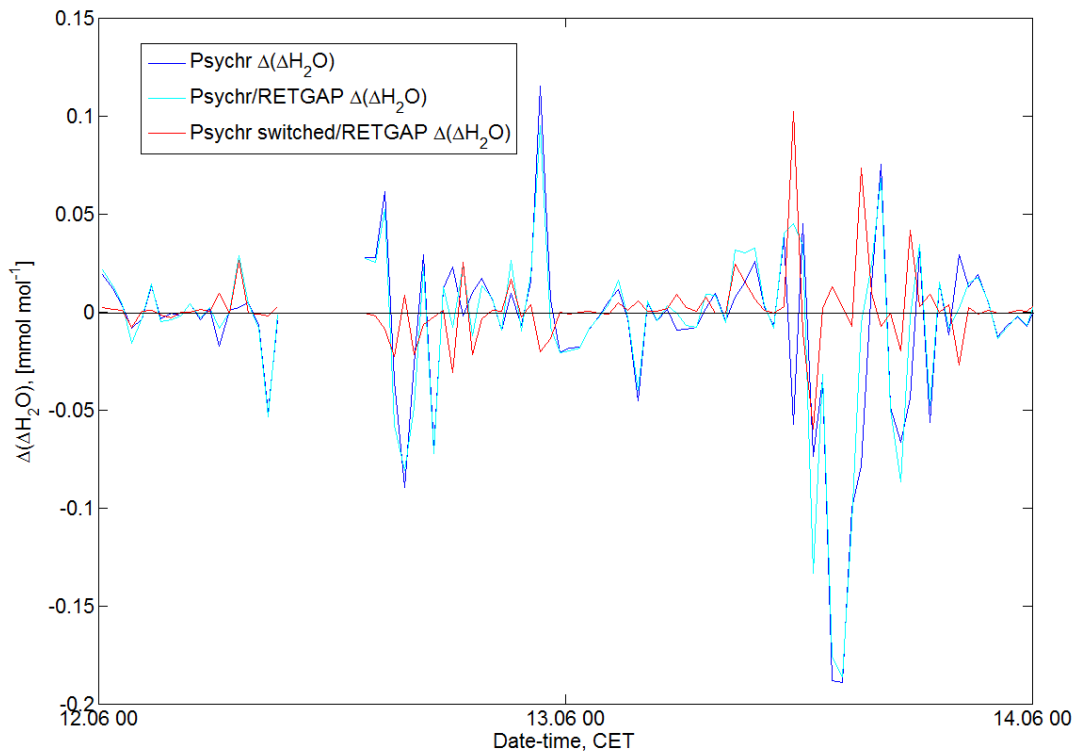


**Fig. 4.13.** Differences between  $H_2O$  mixing ratio differences. The blue line shows the difference between the continuous  $H_2O$  difference and the discontinuous  $H_2O$  difference of the psychrometer. The black line illustrates the difference between the continuous psychrometer  $H_2O$  difference and the RETGAP  $H_2O$  difference. The red line illustrates the difference between the discontinuous psychrometer  $H_2O$  difference and the RETGAP  $H_2O$  difference.

The conclusion from this analysis is that discontinuous sampling has an effect on measurements of  $H_2O$  at limits of precision of  $2\sigma$  for  $H_2O$  concentration differences. Therefore, in order to exclude the effect of switching in the case of  $H_2O$  differences, the precision criteria should be set higher than  $2\sigma$ . The fact that the vertical difference of  $H_2O$  obtained from the continuous psychrometer was comparable to that obtained from the RETGAP indicates that the ramp-like structures in the vertical differences may be induced by other phenomena. They may be coherent structures induced by forest atmosphere exchange regimes. This shall be explored further in this chapter in the analysis of vertical gradients and the spatial applicability of the flux-gradient method.

#### 4.4.4 Gradient-derived fluxes

In this section the results from the gradient-derived flux methods tested, namely the AGM and the MBR method are reported. As detailed in Chapter 3, the gradients fluxes were quality controlled by applying the precision criteria at  $1\sigma$  after tests on concentration differences using also  $2\sigma$ ,  $3\sigma$  and  $10\sigma$  criteria showed a loss of more than 50% of the data. The coupling criterion was also applied on the concentration differences in order to study the effects of canopy-atmosphere turbulent on the concentration differences.

Comparisons are also made to the EC CO<sub>2</sub> and H<sub>2</sub>O fluxes measured on the same tower (UBT32 station).

### **Finding $u^*$ and $z/L$**

Three methods of finding  $L$  (and hence  $z/L$  and  $u^*$ ) were primarily tested for applying the AGM. The three methods were the Berkowicz and Prahm method, the Gradient Richardson method, and the direct application of  $L$  and  $u^*$  from EC measurements. The difference between the three methods is only in the way  $L$  is found.

When  $u^*$  was evaluated from  $L$  derived from the gradient Richardson method, the result were almost similar to those obtained using the iterative method of Berkowicz and Prahm (1982) . Both methods correlated very well with the  $u^*$  and  $z/L$  obtained from EC. The iterative method of finding  $L$  and  $u^*$  was chosen for calculating  $u^*$  and  $z/L$  when the AGM method was applied because of its simplicity.

The friction velocity and  $z/L$  calculated from the AGM and from EC are shown in Fig. 4.14. The results from the two methods show a strong resemblance, which is a strong validation of the applicability of the AGM. The iteration for  $z/L$  failed to converge for some data points but those periods made up less than 3% of the whole data set.

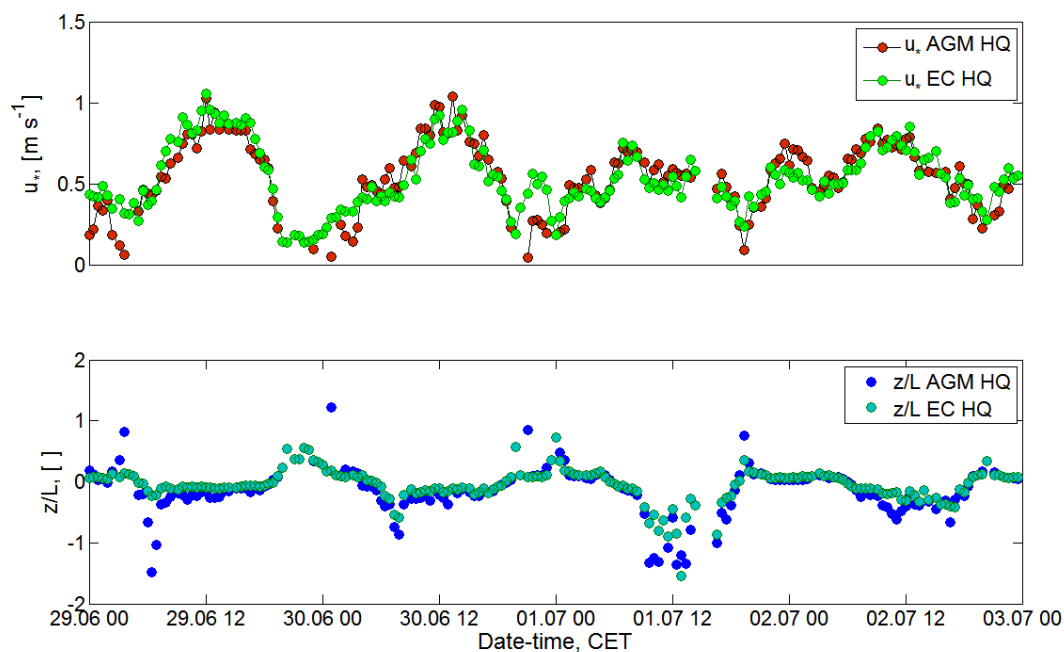


**Fig. 4.14.** Diel variation of the friction velocity (top) and the stability parameter using EC and the AGM. HQ denotes that quality flags were used to select the best data.

### Above canopy AGM and MBRM fluxes

The MBRM performed very well and the results were comparable to those obtained from the AGM (see Fig. 4.15). Distortion of  $\text{NO}_2$  and  $\text{O}_3$  fluxes was also present since it was dependent on the vertical concentration differences.

#### Unexpected result:

The flux of  $\text{NO}$  was found to be directed downwards into the forest while  $\text{NO}_2$  was mostly directed out of the forest in contradiction to most previous results for fluxes of  $\text{NO}$  and  $\text{NO}_2$ . The reason for such fluxes could be (a) the strong  $\text{O}_3$  sink sweeping up all  $\text{NO}$  emissions from the soil, (b) the same  $\text{O}_3$  sink converting all  $\text{NO}$  produced during the advection period to  $\text{NO}_2$ , (c)  $\text{NO}_2$  emission from the forest canopy due to conversion of biogenic  $\text{NO}$  to  $\text{NO}_2$ , and (d) additional  $\text{NO}_2$  from advection during the peak period. Later sections of this chapter will examine this result in greater detail

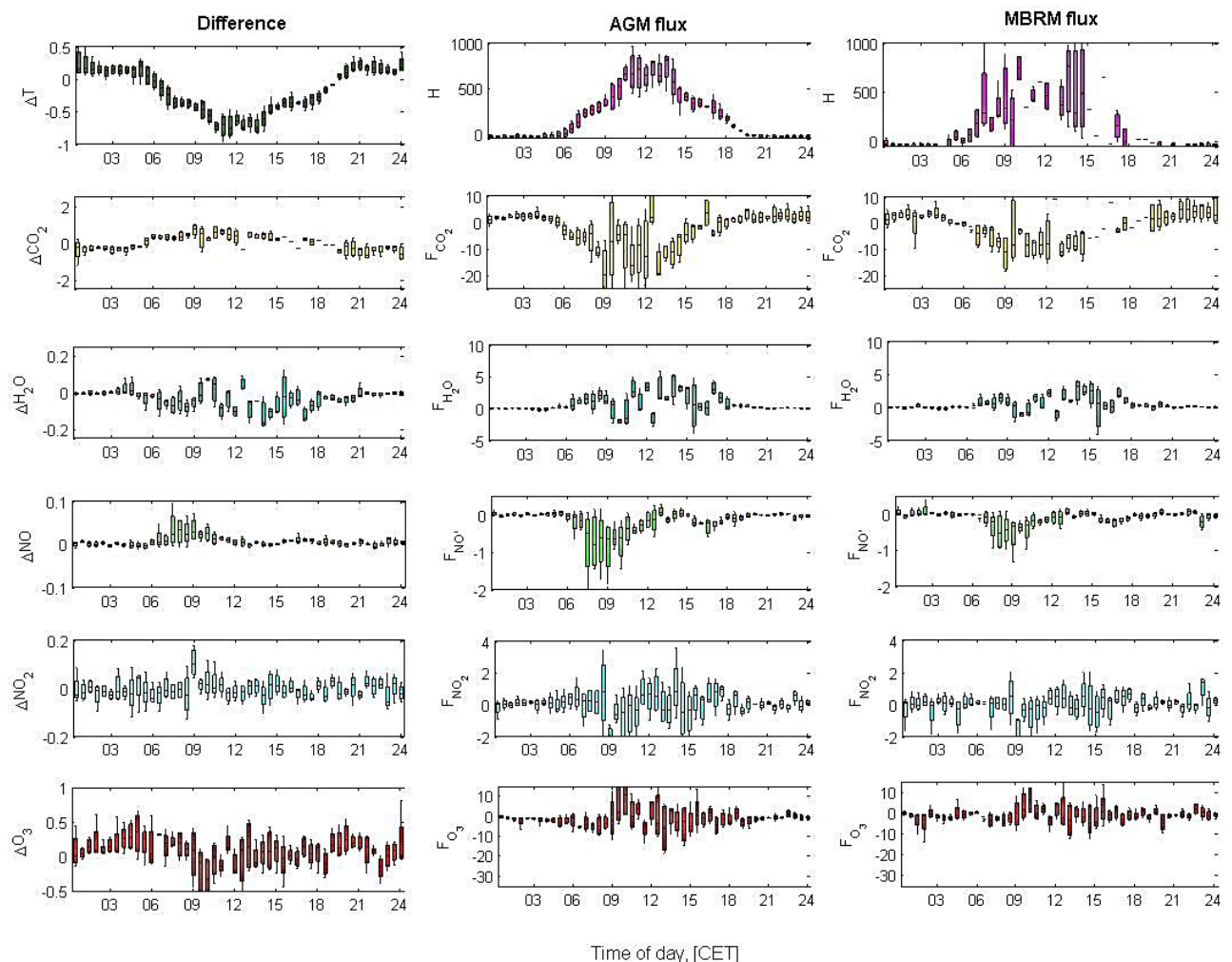


**Fig. 4.15.** Median diel variations of the vertical differences of temperature and concentrations (left column), RSL-corrected AGM fluxes (middle column), and MBRM fluxes (right column) for the IOP2 Golden Days.

#### 4.4.5 Limitations and shortfalls of the gradient methods

The MBRM and the AGM showed highly comparable fluxes for all trace gases in terms of the median diel values and the direction of the fluxes. Both methods performed well for CO<sub>2</sub>, H<sub>2</sub>O and to an extent for NO but were inconclusive for NO, NO<sub>2</sub> and O<sub>3</sub> gradients and fluxes (see Fig. 4.15) where some bidirectional behaviour was observed. This is an important result in the sense that it tells us that it is some effect on the concentration differences that is responsible for this phenomenon. The switching process has an indirect effect on the sign of concentration differences as shown earlier in this chapter. However, looking at the results from the nonreactive trace gases CO<sub>2</sub> and H<sub>2</sub>O shows that these artefacts are not as strongly present as they are in the NO<sub>2</sub> and O<sub>3</sub> data. Moreover NO hardly exhibits these artefacts. Therefore it is proposed that there is another interaction that, together with the switching effects, causes the bidirectional vertical differences and fluxes of NO<sub>2</sub> and O<sub>3</sub>. This is non-stationarity due to chemical conversions of the reactive trace gases

#### 4.5 Evaluation of the trace gas fluxes using the EC method

Having analysed the results from the gradient-derived methods for evaluating trace gas fluxes, more questions than answers came up, particularly concerning the downward-directed fluxes of NO. Furthermore, realizing the limitations when it comes to above canopy fluxes where trace gas concentration differences (vertical) are very small, the direct EC method was adopted. The results for some of the reactive trace gas fluxes, especially O<sub>3</sub> and NO<sub>2</sub> were not convincing, probably because of rapid chemical transformations above the forest canopy, something which will be investigated later in this study. This section is subdivided into a data quality analysis subsection and a flux analysis subsection.

##### 4.5.1 Comparison of EC parameters

Besides using plausibility criteria as a first check to the quality of measured data, comparisons with identical, independently measured parameters give a first impression of the quality of the data. Therefore the EC parameters  $z/L$  and  $u_*$  were compared in the form of scatter plots (Fig. 4.16) to those on the TT at 36 m (UBT36) and the other EC station on the MT at 32 m (UBT36). The results showed good correlation ( $r^2 > 0.85$ ) between each of the parameters measured by the independent EC systems with respect to MPI32. Within the same comparison, a check was made on the correlation when the parameters were under the influence of fully coupled conditions (Cs and C) as well as when the conditions were weakly coupled (Wa, Dc, and Ds). Only  $u_*$  and  $z/L$  showed a stronger correlation between MPI32/UBT32 and MPI32/UBT36 at fully coupled conditions. Friction velocities showed a strong correlation which was independent of magnitude while  $z/L$  showed better correlation at neutral to unstable conditions. The other parameters did not show a strong relationship between correlation and coupling state. The good correlation between the MT and the TT parameters shows that

horizontal homogeneity was good during the measurement period. As a result, the spatial variability was small.

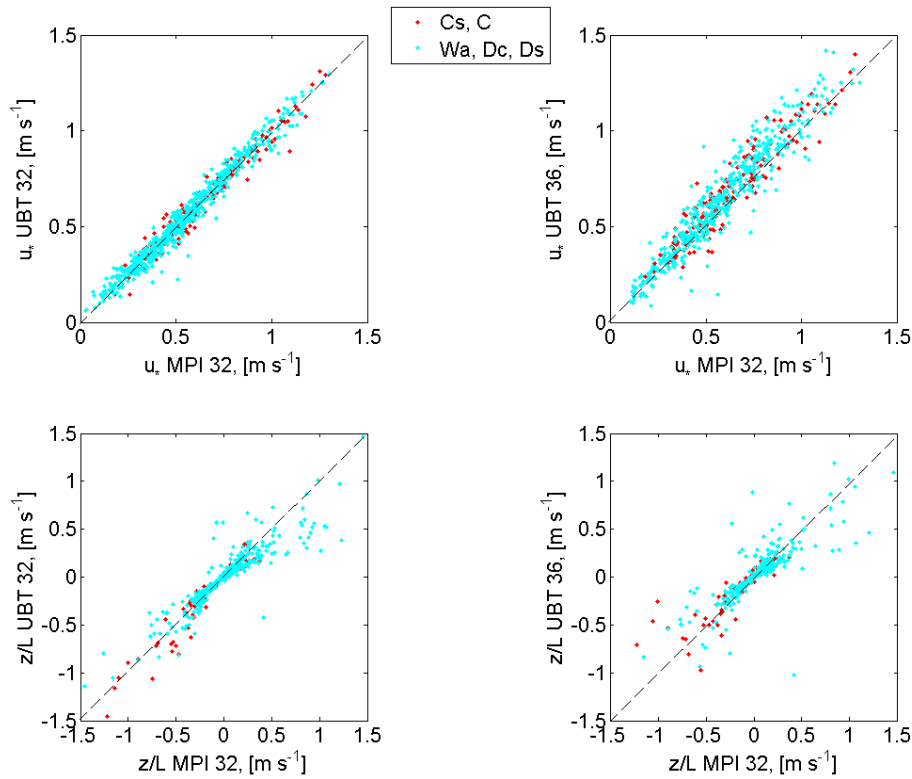


**Fig. 4.16.** Relationship between the two EC systems (MPI and UBT) on the MT for the parameters  $z/L$ ,  $u^*$ . The points marked in red denote data for coupled conditions (Cs and C) while the points in cyan denote data belonging to the coupling classes Wa, Dc and Ds).

Part of the work on EC flux error calculation involved using fluxes from two measurement stations. In this work the two additional EC stations were the UBT32 and the UBT36. As a starting point, the fundamental EC parameters were compared across the three stations with the reference station being MPI32. Results of the comparison are presented in Fig. 4.17 (H and LE), and Fig. 4.18 ( $\text{CO}_2$  and  $\text{H}_2\text{O}$  fluxes). In all cases, good correlation was obtained, including between the MT and the TT. Sensible heat flux, however, showed a poorer correlation relative to the other parameters.

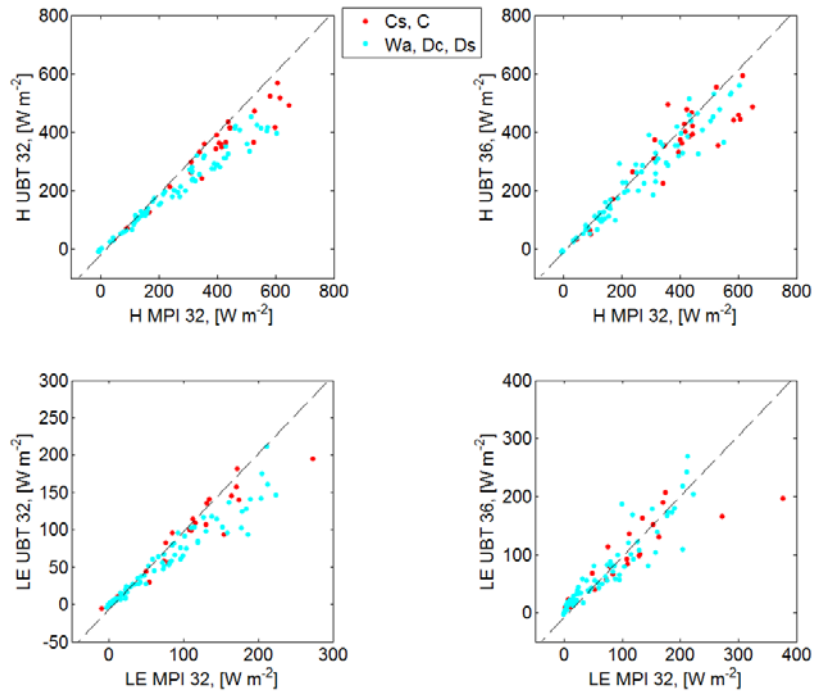


**Fig. 4.17.** Relationship between the two EC systems (MPI and UBT) on the MT and the TT for the parameters H and LE. The points marked in red denote data for coupled conditions (Cs and C) while the points in cyan denote data belonging to the coupling classes Wa, Dc and Ds).

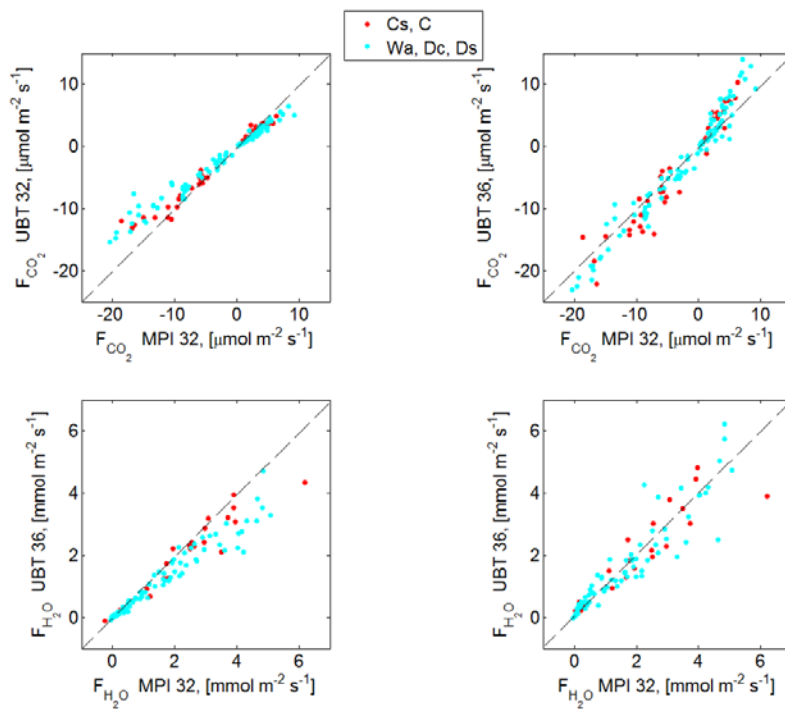


**Fig. 4.18.** Relationship between the between two EC systems (MPI and UBT) on the MT and the TT for the CO<sub>2</sub> and H<sub>2</sub>O fluxes. The points marked in red denote data for coupled conditions (Cs and C) while the points in cyan denote data belonging to the coupling classes Wa, Dc and Ds).

Although the correlation between MPI32 and UBT32 for H, LE,  $F_{CO_2}$  and  $F_{H_2O}$  was good, there was evident deviation from the correlation obtained between MPI32 and UBT36. Calibration differences cannot explain this (except for heat flux) because the  $H_2O$  and  $CO_2$  mixing ratios for UBT32 and MPI32 were inter-calibrated. A possible explanation for this is the difference in sensitivity of the sonic anemometers used. MPI32 and UBT36 used the CSAT3 while UBT32 used the METEK USA-1.

The integral turbulence characteristics (see 2.3.3) were also compared. The expected values of the ITCs according to Panofsky and Dutton (1984) were used for the reference values (see Fig. 4.19). Results showed that the ITCs compared well for the three EC systems and are indicative of the high quality of the data. They followed the Panofsky and Dutton (1984) values very well except for  $ITC_u$ .

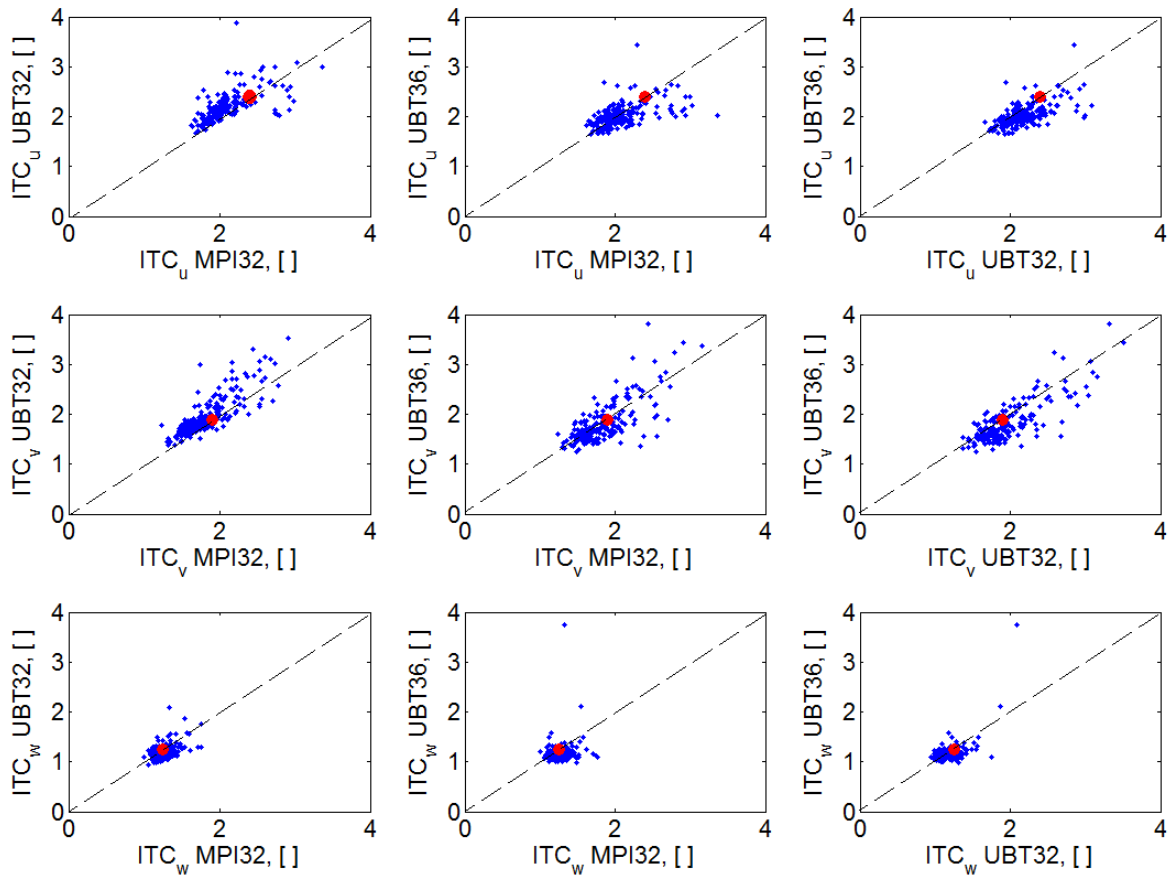


**Fig. 4.19.** Variation of the ITCs of  $u$ ,  $v$ , and  $w$  across the three EC systems MPI32, UBT32, and UBT36.  $u=2.4$ ,  $v=1.9$ ,  $w=1.25$

## 4.5.2 Turbulence spectra

Eddy covariance fluxes measured showed good fluctuations as seen in Fig. 4.20.

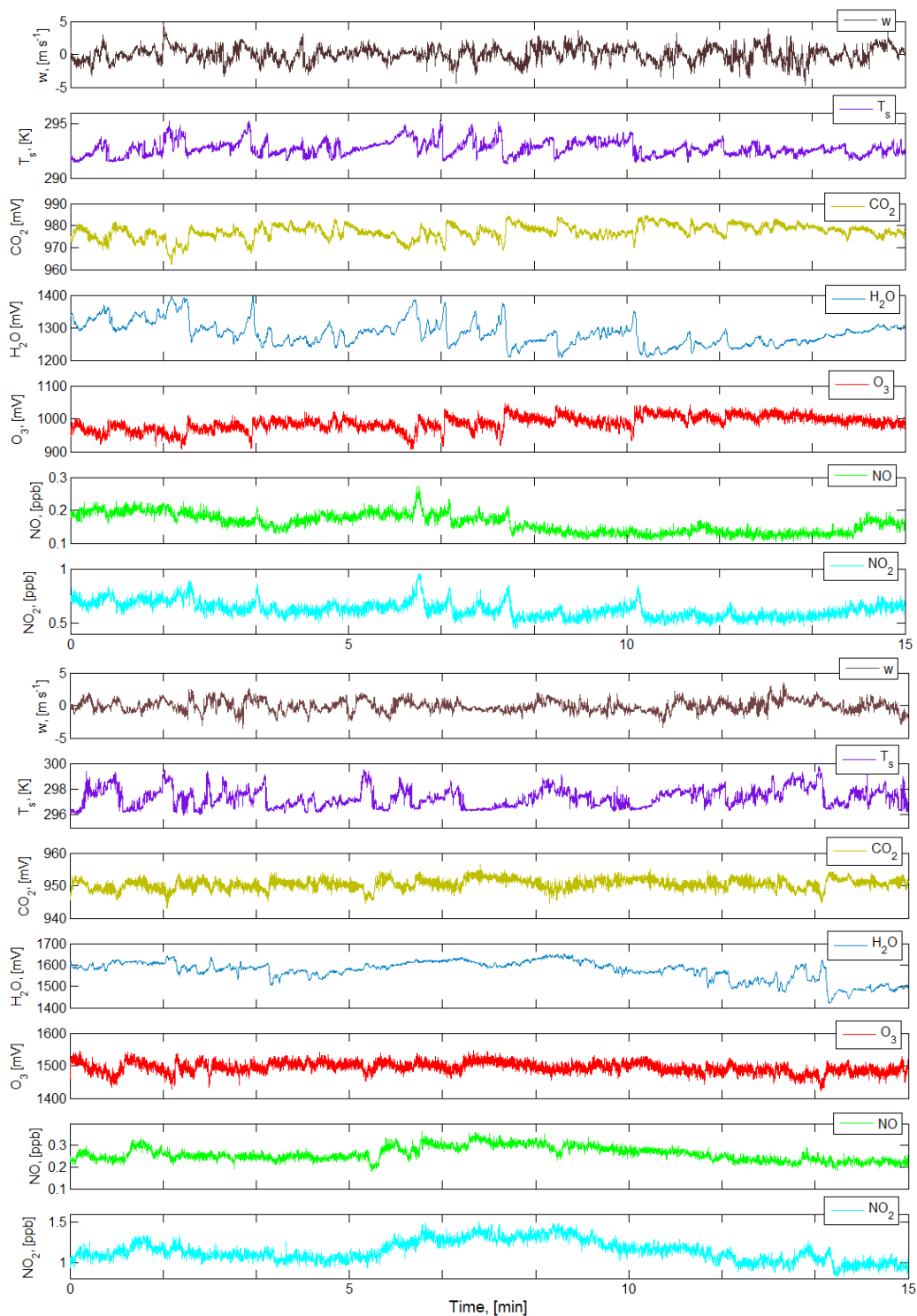


**Fig. 4.20.** Time series of raw 20 Hz eddy covariance signals for (top) 30 June 2008 1200-1215 CET and (bottom) 2 July 2008 1100-1115 CET. The parameters shown from top to bottom are  $u$ , sonic temperature  $T_s$ ,  $\text{CO}_2$ ,  $\text{H}_2\text{O}$ ,  $\text{O}_3$ ,  $\text{NO}$ , and  $\text{NO}_2$ . The ramp-like formations in some of the time series on the left are indicative of the presence of coherent structures.

The ramp-like formations observed in the time series of Ts, CO<sub>2</sub>, H<sub>2</sub>O and O<sub>3</sub> on the 30<sup>th</sup> of June 2008 between 1200 and 1215 CET (Fig. 4.21) are indicative of the presence of convective forces and coherent structures. The structures for CO<sub>2</sub> and O<sub>3</sub> are anti-correlated to those for Ts and H<sub>2</sub>O, an indication that the fluxes of CO<sub>2</sub> and H<sub>2</sub>O were expected to be negative. The duration of these structures was between 30 s and 1 minute. The same structures were not observed on 2 July 2008 except for Ts.

### ***Residence time inside tubes and inlet-sensor delay time***

Here the results of the evaluation of the residence time inside the trace gas inlet tubes are detailed. In addition the results of the lag times between the trace gases concentrations with respect to the vertical wind component measured by the CSAT3 are also presented. Table 4.5 shows the obtained residence times for the trace gases measured at the top of the MT.

The results from the tube response test showed a residence time of 7.8 s for NO and 7.9 s for NO<sub>2</sub>. Comparison with a theoretical calculation showed agreement to within 10%. In addition, cross-correlation analyses were done between the vertical wind component  $w$ , and NO and NO<sub>2</sub> respectively. The results obtained were on average similar to those from the response test.

The tubing used for O<sub>3</sub> was very short (3 m). Therefore the response test was neglected. Instead only the cross-correlation to find the lag time was performed. Cross-correlation tests yielded an average lag time of 1.6 s between the O<sub>3</sub> high frequency time series and the high frequency vertical wind time series. The resultant average lag time was used for the O<sub>3</sub> EC flux calculation. The results from the cross-correlation tests are show in Fig. 4.22.

The Teflon® tubing used for the CO<sub>2</sub>/H<sub>2</sub>O closed path measurements was short (6 m each) since the analyser was located at the top of the tower. Cross-correlation tests against the vertical wind velocity for CO<sub>2</sub> and H<sub>2</sub>O yielded lag times of 3.15 and 3.75 s respectively.

Lag times were calculated by finding the maximum covariance between each signal and the vertical wind  $w$ . The times series for the signals were then matched with  $w$  by being shifted back by steps equal to their respective delay times. Figure 4.21 below shows the calculated lag times. The maximum correlation coefficients for CO<sub>2</sub>, NO, and O<sub>3</sub> were negative but their absolute values were used in plotting Fig. 4.22 for a clearer illustration of the delay time. These negative correlation coefficients support the anti-correlations observed in Fig. 4.20. The longest lag times were observed for NO and NO<sub>2</sub> (9 s and 9.15 s respectively) due to the relatively longer inlet tubes used.

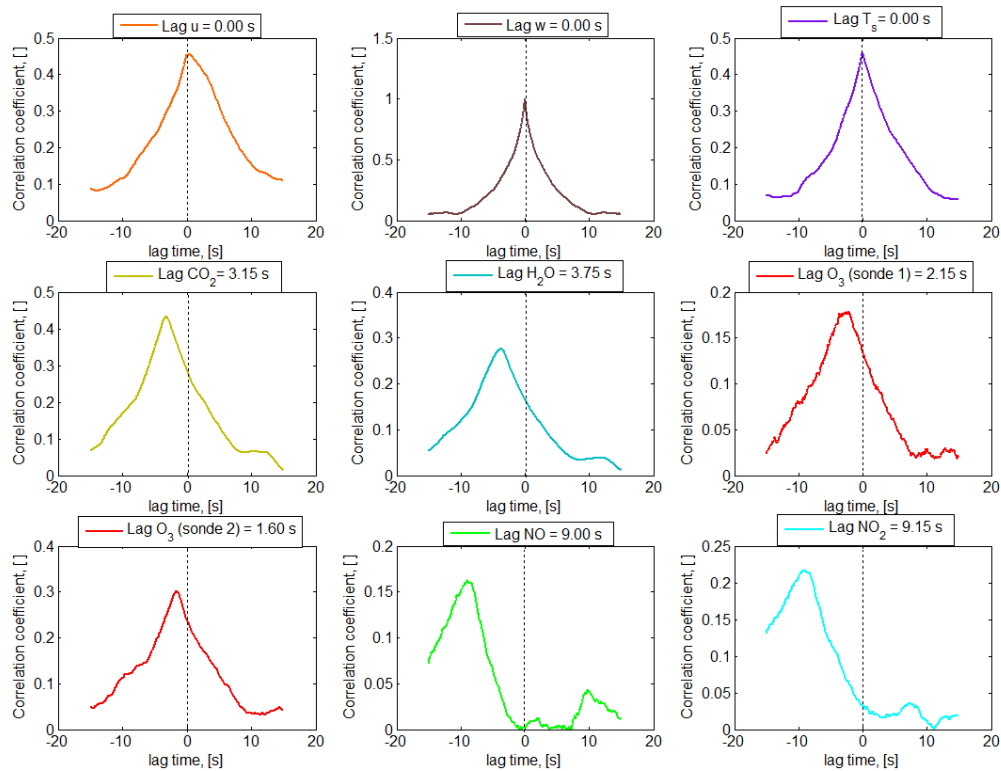


**Fig. 4.21.** Lag times between  $w$  and  $u$ ,  $w$ , sonic temperature  $T_s$ ,  $CO_2$ ,  $H_2O$ ,  $O_3$ ,  $NO$  and  $NO_2$  on 29 June 2008 between 1100-1130 hrs CET. The vertical axes show the absolute correlation coefficients while the vertical axes show the lag times.

**Table 4.4.** A summary of the residence times of the trace gases

Trace gas	Tube length (m)	Residence time (s)	Lag time (s) (cross (response test method) corr.)
NO	53	7.8	9.0
$NO_2$	53	7.9	9.15
$O_3$	3	-	1.6
$CO_2$	6	-	3.15
$H_2O$	6	-	3.75

The turbulence spectra for momentum, temperature and the trace gases are presented in this section. The analysis is grouped into:

- Power spectra for  $u$ ,  $T_s$ ,  $CO_2$ ,  $H_2O$ ,  $NO$ ,  $NO_2$  and  $O_3$
- Cospectra between the vertical wind component  $w$  and  $u$ ,  $T_s$ ,  $CO_2$ ,  $H_2O$ ,  $NO$ ,  $NO_2$  and  $O_3$
- Ogives constructed from the cumulative sum of the cospectra in (2) over the natural frequency of the sonic anemometer

All spectra were constructed from the 30 minute periods between the time 1100 CET and 1300 CET over the four golden day periods of IOP-2. The choice for this time period is that around midday the conditions are more stationary than the rest of the day. In addition there is well developed turbulence at this time. This was confirmed by the high quality stationarity flags which were found during these time periods. Additionally distortions resulting from the advection period described earlier are avoided by choosing the 1100-1300 CET time period for the spectral analyses.

### ***Power spectra***

Momentum and the vertical wind  $w$  showed (see Fig. 4.22) well developed power contributions at low frequencies ( $10^{-2}$  to  $10^{-1}$  Hz). The power dissipation followed perfectly the Kolmogorov  $-2/3$  law in the inertial sub-range. This was an indication that the sonic anemometer was operating fast enough to capture all the eddies in its footprint and that the 20 Hz sampling frequency was adequate for measurement at the site.

### *Temperature*

The temperature power spectrum showed close to ideal behaviour in the range of energy production, the inertial sub-range and the range of energy dissipation. The  $-2/3$  power law was also matched very closely in the inertial sub-range. Temperature spectra are often used as the standard spectrum for comparing the quality of other turbulence spectra measured in combination with the same sonic anemometer.

### *Non-reactive trace gases*

The power spectrum of  $\text{CO}_2$  showed a narrow, unstable range of energy production. The inertial sub-range followed the  $-2/3$  power law but was narrower than that for T. There was then rapid energy dissipation in the viscous region which had a slope of  $-1$  followed lastly by a slope of  $1/2$  at 5 Hz. This last range had a lot of white noise.

The  $\text{H}_2\text{O}$  power spectrum was similar to the  $\text{CO}_2$  power spectrum with the only difference being that the dissipation range had a lower minimum energy and much more rapid energy dissipation at higher frequencies. This is a characteristic feature of water vapour spectra and indicates the effects of viscous damping at high frequencies. The positive slope of  $1/2$  within the dissipation range was also present.

The positive slope may be indicative of the start of a first harmonic for the power spectra. This would mean that the 30 minute averaging interval is too long for the nonreactive trace gases at this site.

### *Reactive trace gases*

The power spectral densities for NO,  $\text{NO}_2$  and  $\text{O}_3$  (Fig. 4.22) all had similar shapes. Ozone had however lower power than NO and  $\text{NO}_2$  for the entire frequency range. The range of energy dissipation was higher than that for energy production for all three trace gases, a fact that can be attributed to high energy noise at higher frequencies.

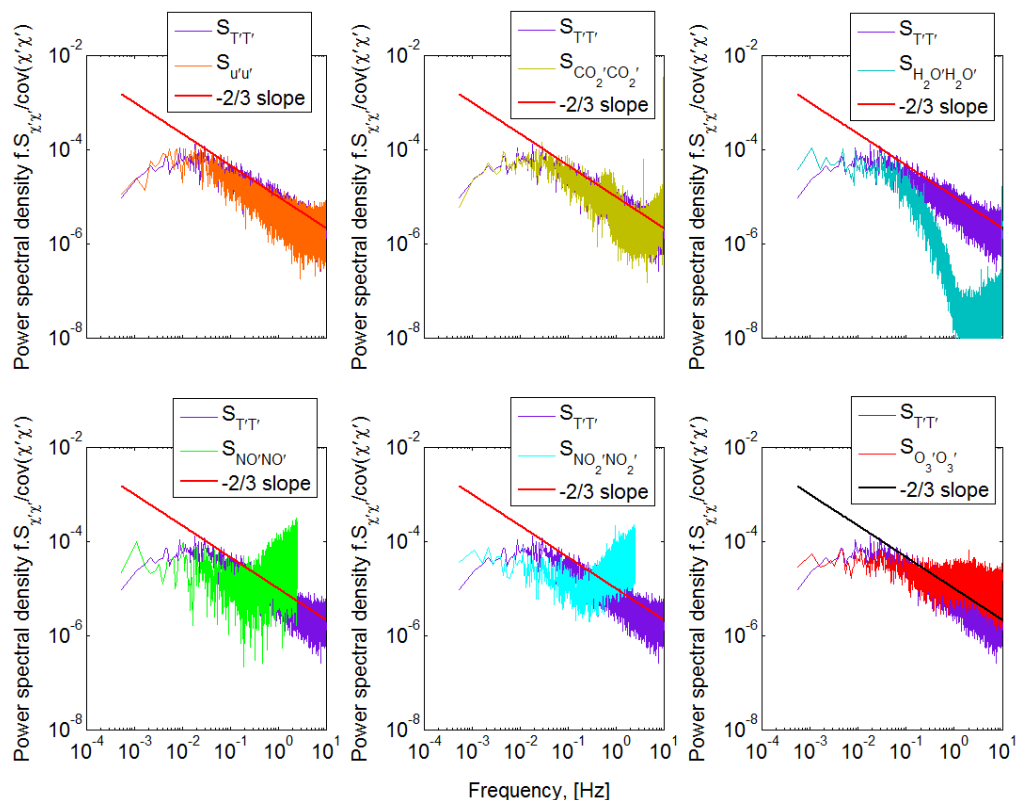


**Fig. 4.22.** Power spectral densities for momentum,  $\text{CO}_2$ ,  $\text{H}_2\text{O}$ ,  $\text{NO}$ ,  $\text{NO}_2$  and  $\text{O}_3$  during IOP-2. The values used were the mean half-hourly ogives taken between 1100-1300 CET for all the golden days.

### Cospectra

The cospectra were all constructed between the vertical wind and  $u$  divided by the covariance between  $w$  and  $u$ . In other words they represented the normalized vertical flux. The cospectra were multiplied by the frequency  $f$  in order to emphasize the slope in the inertial sub-range. Therefore the theoretical Kolmogorov inertial subrange slope becomes  $-4/3$ . The cospectrum of  $w$  with itself was left out because it is the same as the power spectrum of  $w$  shown in the previous section.

The cospectrum of  $w$  with  $u$  showed that the highest contribution to the momentum flux occurs in the low frequency range of the spectrum between  $10^{-2}$  and  $10^{-1}$  Hz.

### Temperature

The cospectrum between  $w$  and  $T$  also showed ideal behaviour and followed the  $-4/3$  law in the inertial sub-range.

### Non-reactive trace gases

The cospectra were all constructed between the vertical wind and the high frequency trace gas mixing ratios (also temperature) divided by the covariance between  $w$  and the trace gas (or temperature). In other words they represented the normalized vertical flux. The cospectra were multiplied by the frequency  $f$  in order to emphasize the slope in the inertial sub-range.

The CO<sub>2</sub> cospectrum had the same slope in the inertial sub-range and the dissipation range, with only a slight change towards the Nyquist frequency. The H<sub>2</sub>O cospectrum was the same as the CO<sub>2</sub> cospectrum in form and shape.

### Reactive trace gases

The turbulence cospectrum for NO had a narrow inertial sub-range and a large dissipation range. The same pattern is shown by the NO<sub>2</sub> and the O<sub>3</sub> cospectra. The range of dissipation has more energy than the range of energy production for all three reactive trace gases. It may be due to the fact that the noise had a lot of energy. The high frequency noise was probably due to path length errors, hence its absence in the temperature spectra. These were later corrected for in TK2.

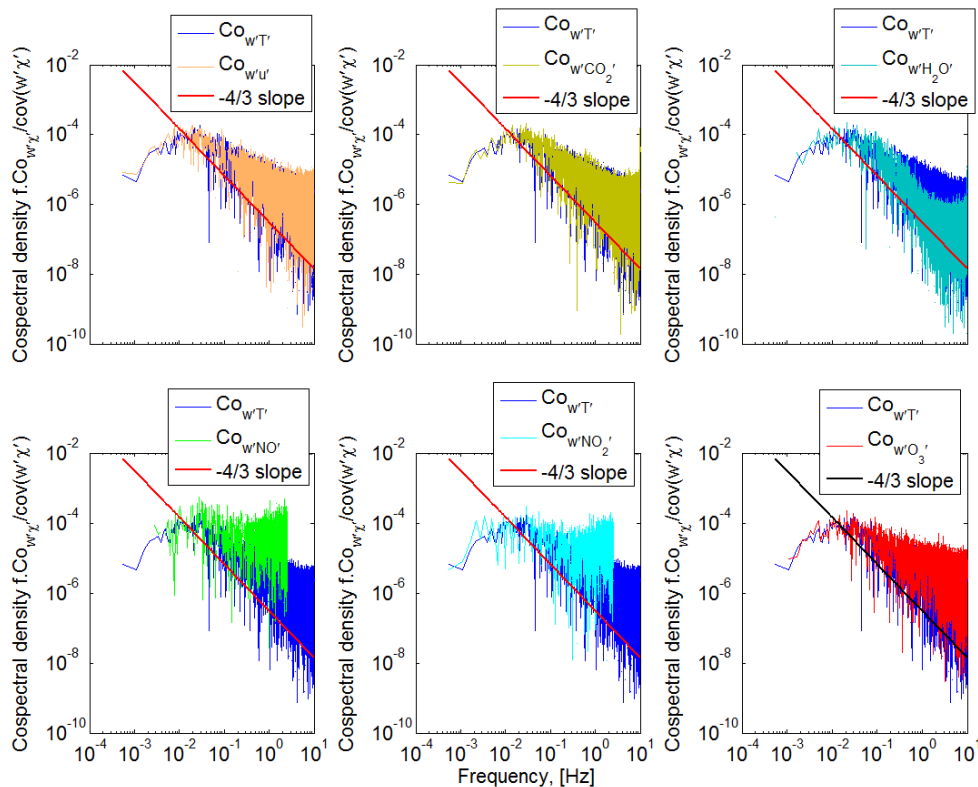


**Fig. 4.23.** Cospectral densities for momentum, CO<sub>2</sub>, H<sub>2</sub>O, NO, NO<sub>2</sub> and O<sub>3</sub> during IOP-2. The values used were the mean half-hourly ogives taken between 1100-1300 CET for all the golden days.

### Ogives

To find out if the trace gas analysers' frequency responses were enough to capture all the eddies at the measurement level, ogives showing the cumulative flux contribution over the range of frequencies of the sonic anemometer were constructed (see Fig. 4.24). Cut-off frequencies for the fluxes were as follows: Momentum – 1.1 Hz, Sensible heat – 1.3 Hz, CO<sub>2</sub> – 0.96 Hz, H<sub>2</sub>O – 0.65 Hz, NO – 1.1 Hz, NO<sub>2</sub> – 1.17 Hz, O<sub>3</sub> – 0.79 Hz. They are indicative of high frequency damping. The fluxes of H<sub>2</sub>O, NO, and NO<sub>2</sub> suffered the most damping due to high frequency losses in the tubes during transport as well as sensor separation which were later corrected for using the Moore correction (Moore, 1986).

Flux losses were calculated from one minus the mean ratio of the sensible heat flux ogive to the ogive for each parameter at two different frequencies (0.067 Hz and 0.1 Hz). The results using mean half hourly ogives for the period 1100-1330 CET over 3 golden days were as follows: Momentum – 7.7%, CO<sub>2</sub> – 2.6%, H<sub>2</sub>O – 5.1%, NO – 2.1%, NO<sub>2</sub> – 7.5%, O<sub>3</sub> – 1.8%. At lower frequencies, the NO flux contribution lagged behind the heat flux contribution while the NO<sub>2</sub> flux contribution was always higher than the sensible heat flux contribution. This is evidence of downward-directed NO flux predominating at lower frequencies with NO<sub>2</sub> emission predominating at all frequencies. Momentum also shows the same characteristic shape as NO<sub>2</sub> possibly due to the enhancement of momentum by the roughness sublayer. Typically, flux losses below 15% are indicative of high quality fluxes (Spirig et al., 2005). Therefore the results obtained are evidence of the very high quality of the sensors in carrying out EC measurements.

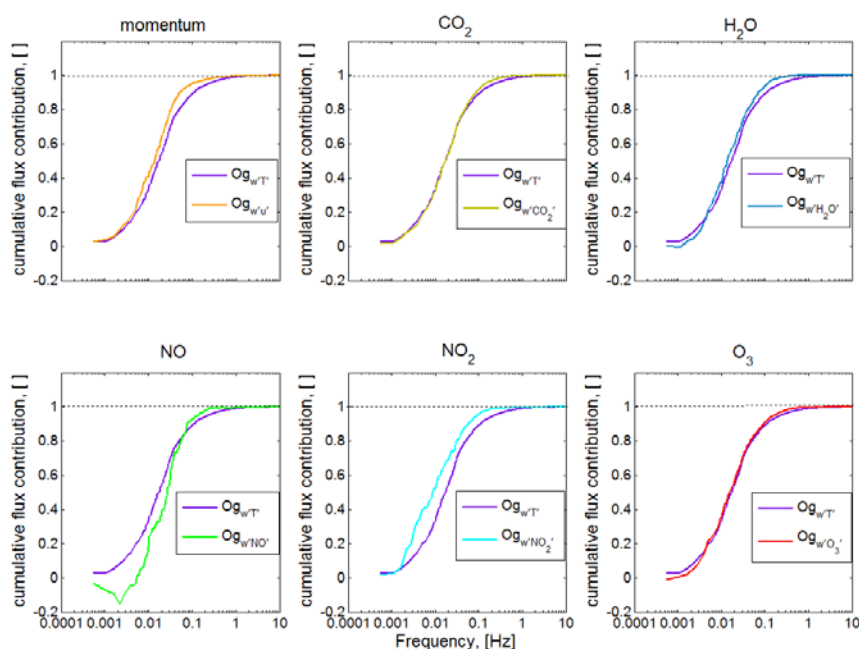


**Fig. 4.24.** Normalized cumulative flux contribution ogives for momentum, CO<sub>2</sub>, H<sub>2</sub>O, NO, NO<sub>2</sub> and O<sub>3</sub> during IOP-2. The values used were the mean half-hourly ogives taken between 1100-1300 CET for all the golden days.

### 4.5.3 Quality flags of fluxes

Eddy covariance fluxes of the non-reactive and reactive trace gases that were measured using the methods described are reported in this subsection. The quality of the fluxes as a whole is first looked at before reporting in detail the results of the non-reactive trace gases. Finally the reactive trace gases are investigated.

Results of quality checks performed using quality flags according to the method of Foken and Wichura (described in 3.8) are presented in Fig. 4.26 below. The flags shown are the overall flags whose derivation is shown in Table 3.7.

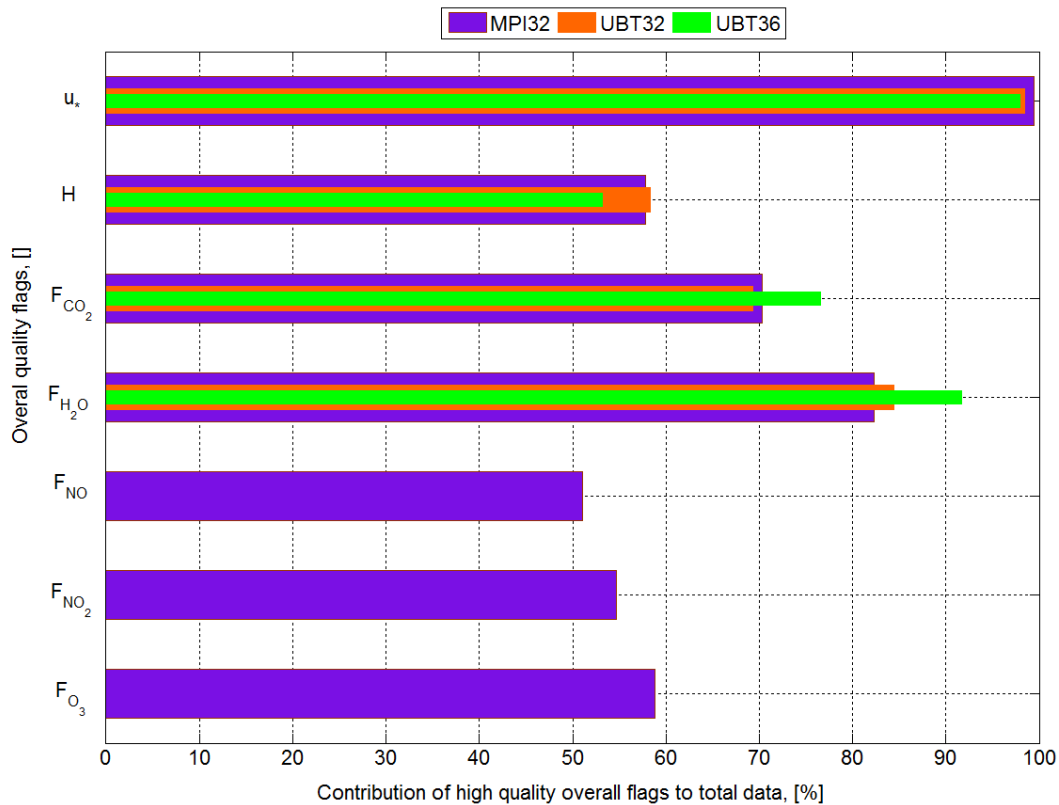


**Fig. 4.25.** Overall flux quality flags for momentum, H, CO<sub>2</sub>, H<sub>2</sub>O, NO, NO<sub>2</sub>, and O<sub>3</sub> calculated using TK2. The flags are shown for the EC stations MPI32 with UBT32 and UBT36 as comparisons.

All the high quality flags (1-3) were above 50% of the total fluxes for each parameter which was a confirmation that the EC data was of a high quality that was good enough for fundamental research.

Siebicke et al. (2008) showed that the footprint of the fluxes was mainly homogenous except for the small clearing which was made by hurricane-like Kyrill cyclone.

#### 4.5.4 Error limits for EC fluxes

With the raw fluxes having been calculated and the quality of the fluxes having been assured using the quality flag criteria outlined in the section above, it was a necessity to understand the limitation and error margins of the flux results. Section 4.5.3 showed the Foken and Wichura flux quality distribution. While knowing the data quality distribution is important, it does not give us adequate information about the extent of the significance of our flux results. Therefore a comprehensive error analysis regimen was performed on all the fluxes and the results are reported in this section. The techniques used to study the EC flux errors of the trace gases are the correlation coefficient, the simultaneous flux method and the daily differencing method as elaborated in 2.3.3.

##### **Correlation coefficient method**

Figure 4.26 shows the relative uncertainties observed when the correlation coefficient method for determining random EC flux errors was applied to the MPI32 station. For all cases, the data was

grouped into 24 bins. The sensible heat flux showed the smallest errors over the whole of its flux range. Its modal relative error was 15% while those for  $\text{CO}_2$ ,  $\text{H}_2\text{O}$ ,  $\text{NO}$ ,  $\text{NO}_2$ , and  $\text{O}_3$  were 20%, 20%, 40%, 40%, and 40% respectively. The relative errors were found to increase as the fluxes tended towards zero. The fact that the reactive trace gases had double the errors observed in the nonreactive trace gases may be linked to the fact that the reactive trace gases were much smaller in magnitude than the non-reactive trace gases.

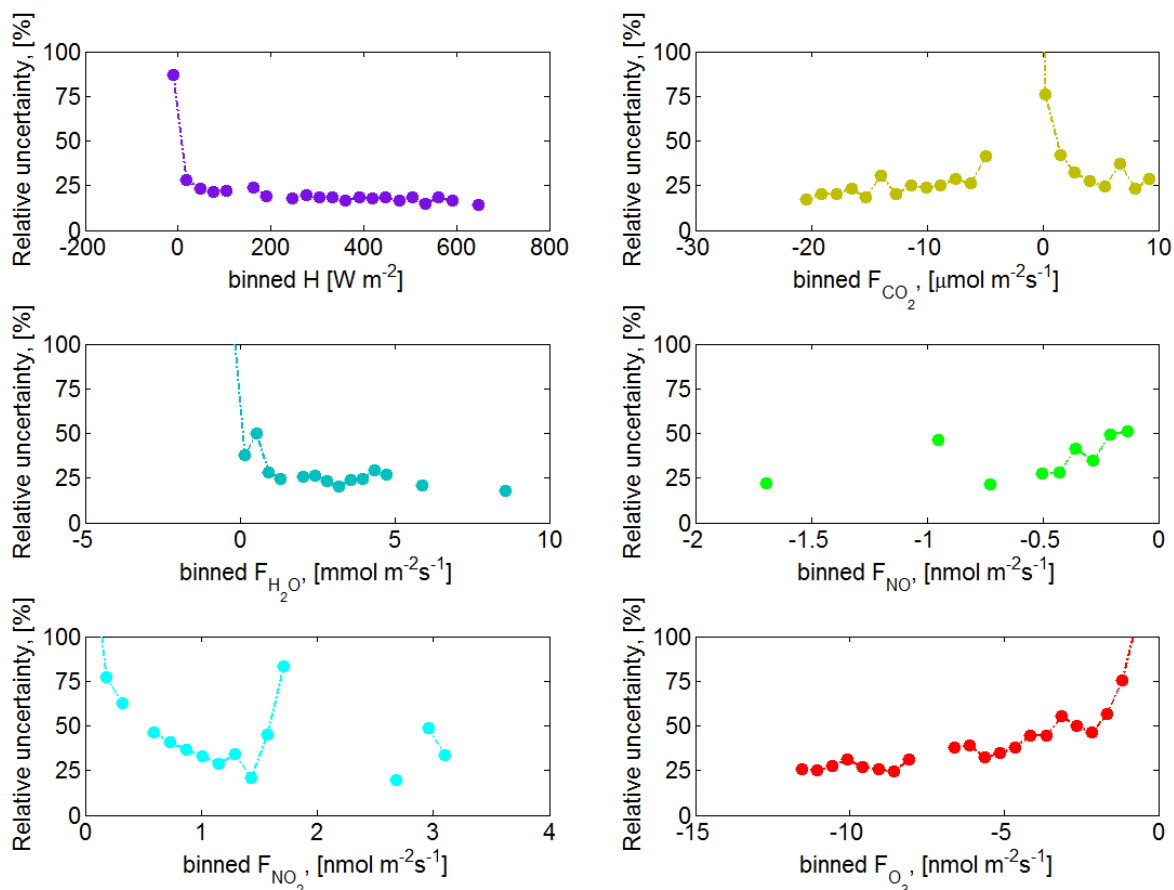


**Fig. 4.26.** Variation of relative uncertainty in the flux for  $H$ ,  $LE$ ,  $NO$ ,  $NO_2$ ,  $O_3$ ,  $H_2O$ , and  $CO_2$  on the  $MT$  using the correlation coefficient method during the golden days.

The EC station UBT32 showed a pattern similar to that for MPI32. The modal relative uncertainties for  $H$ ,  $\text{CO}_2$ , and  $\text{H}_2\text{O}$  were 20%, 25%, and 25% respectively for  $H$ ,  $\text{CO}_2$ , and  $\text{H}_2\text{O}$ . Fig. 4.27 shows the results.

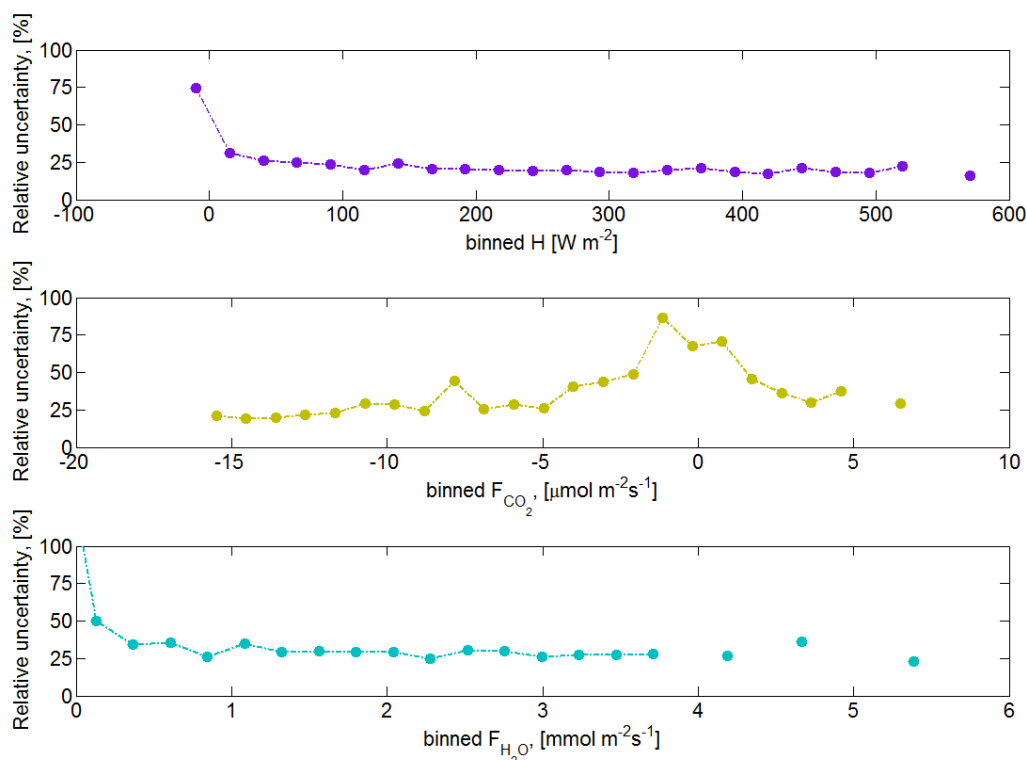


**Fig. 4.27.** Variation of relative uncertainties for sensible heat flux  $H$ ,  $\text{CO}_2$  flux, and  $\text{H}_2\text{O}$  flux against their respective fluxes each grouped into 24 bins from UBT32 during the golden days.

On the turbulence tower, UBT36 showed modal relative uncertainties of 20%, 50% and 25% for  $H$ ,  $\text{CO}_2$ , and  $\text{H}_2\text{O}$  respectively (see Fig. 4.28). It was unclear why the  $\text{CO}_2$  relative uncertainty tended to be so high, especially between  $-5$  and  $5 \mu\text{mol m}^{-2}\text{s}^{-1}$ . However,  $H$  and  $\text{H}_2\text{O}$  were in the normal range exhibited by the other two EC stations. The reactive trace gases were not measured on UBT32 and UBT36 and are therefore not reported for these two stations.

### **Simultaneous flux method**

This method was applied as described in 2.3.2 on the data from the MPI32 and UBT36. The data analysed included  $\text{CO}_2$ , sensible heat, and  $\text{H}_2\text{O}$  fluxes. The relative flux errors obtained (Fig. 4.29) from this method were about 50% smaller than those obtained using the correlation coefficient method. The modal relative errors were 10%, 15%, and 15% for  $H$ ,  $\text{CO}_2$  and  $\text{H}_2\text{O}$  respectively. The smaller errors are an indication of the similarity of the fluxes measured by the two towers and are in agreement with the comparison of the EC parameters for the two towers shown in 4.5.1.

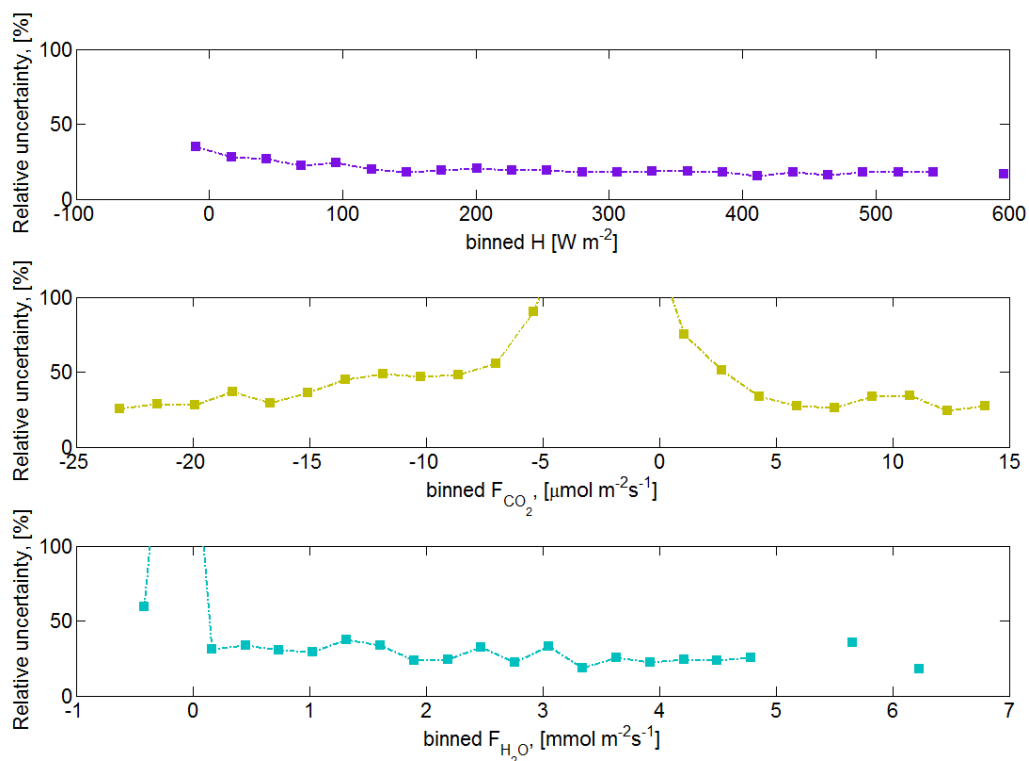


**Fig. 4.28.** Variation of relative uncertainties for sensible heat flux  $H$ ,  $\text{CO}_2$  flux, and  $\text{H}_2\text{O}$  flux against their respective fluxes each grouped into 24 bins from UBT36 during the golden days.

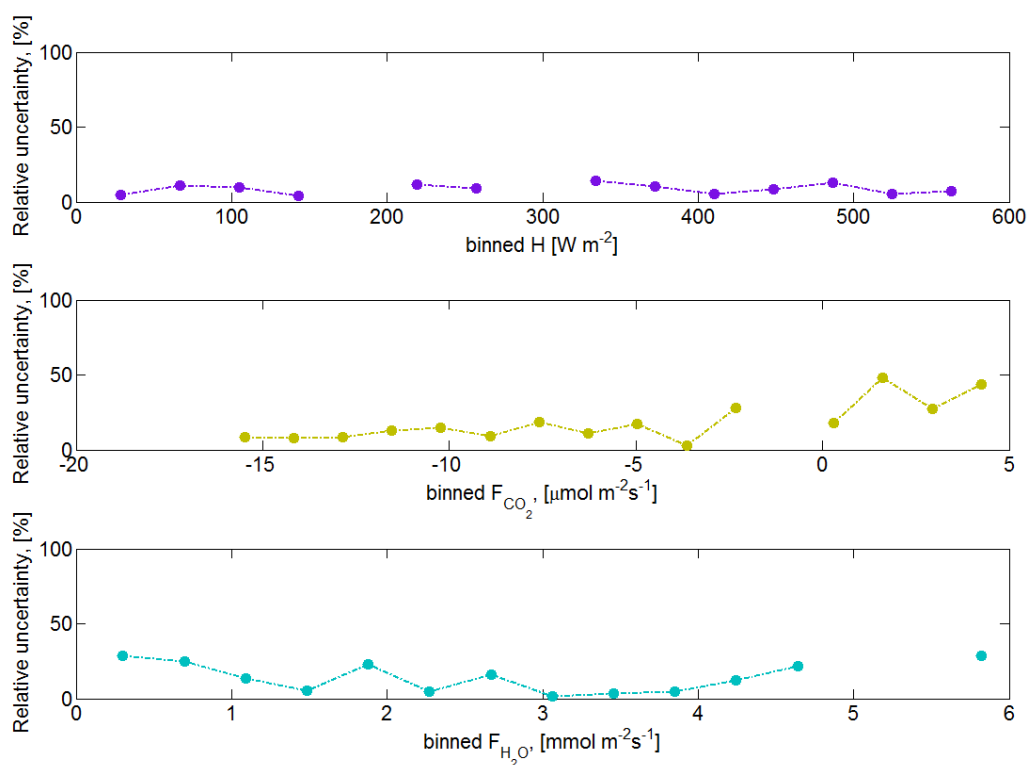


**Fig. 4.29.** Variation of relative uncertainties for sensible heat flux  $H$ ,  $\text{CO}_2$  flux, and  $\text{H}_2\text{O}$  flux against their respective fluxes each grouped into 24 bins calculated from the flux differences between UBT36 and MPI32 during the golden days.

### Daily differencing method

The daily differencing as described in 2.3.3 was applied on fluxes from MPI32. The temperatures and solar radiation differences on the 30<sup>th</sup> of June and on the 1<sup>st</sup> of July were the most closely matched. To minimize additional errors caused by large differences in the driving forces those two days were therefore used for the daily differencing procedure.

Results of the daily differencing method showed that the flux uncertainty is decreased when the daily differencing method is used as compared to the Richardson Two Tower approach and the Lenschow approach. The relative difference is in the order of 50%. The results were good because the atmospheric driving forces were comparable on the two days that were most similar (for both towers). Again it was difficult to get a good distribution of the error because of the small sample size.

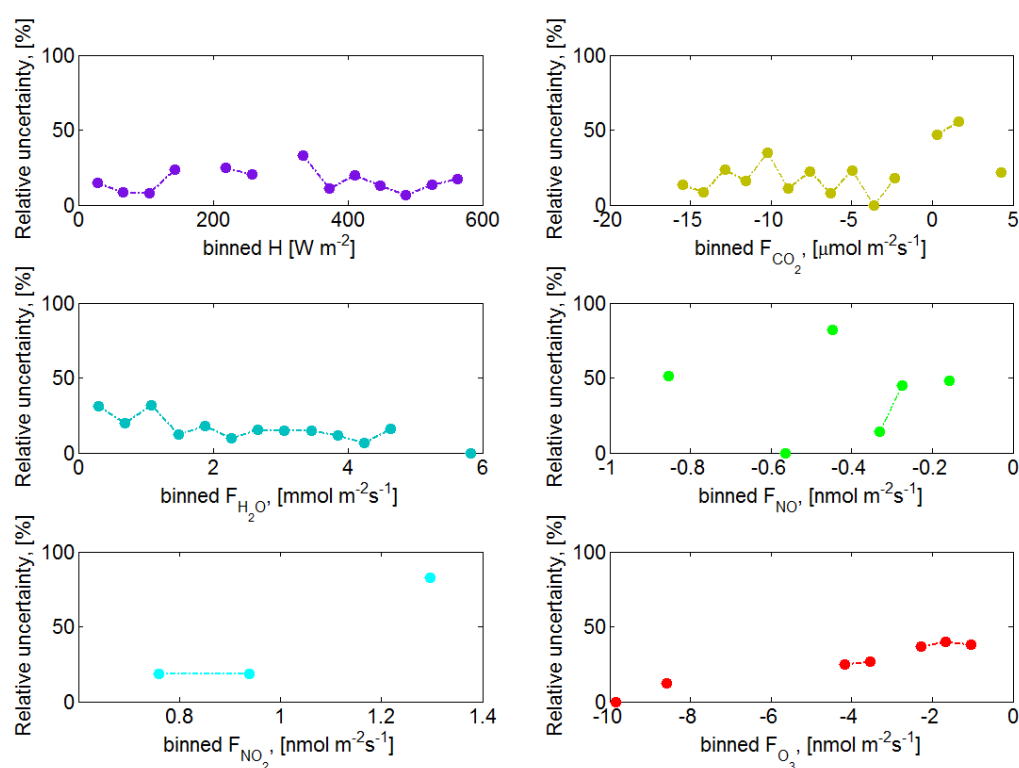


**Fig. 4.30.** Variation of relative uncertainties for (clockwise from top left) the fluxes  $H$ ,  $CO_2$ ,  $NO$ ,  $O_3$ ,  $NO_2$ , and  $H_2O$  against their respective fluxes each grouped into 16 bins from the average of daily differences between the golden days on MPI32.

Except for the  $CO_2$  flux on UBT36, relative errors were always smaller than the magnitude of their respective fluxes, i.e. the fluxes were significant and resolvable. When the results from the three methods were averaged (see the summary in Table 4.5), the results showed that the non-reactive species have smaller errors than those for the reactive species. The results were correlated to the flux quality flags shown in 4.5.3.

**Table 4.5.** Summary of the modal relative flux errors (MRFE) from the three methods

Flux	MRFE correlation coefficient method (%)	MRFE simultaneous flux method (%)	MRFE daily differencing method (%)	Average MRFE (%)
H	15/20/20	10	25	18
H <sub>2</sub> O	20/25/50*	15	25	21
CO <sub>2</sub>	20/25/25	15	15	20
NO	40/-/-	-	30	35
NO <sub>2</sub>	40/-/-	-	20	30
O <sub>3</sub>	40/-/-	-	25	33

\*This result was left out of the calculation for the average and was treated as an outlier

#### 4.5.5 Diel variation of the EC fluxes

In the previous section, the flux random errors were found to be in a range in which all the fluxes are significant. In this section, the diel variation of the EC fluxes during the IOP-2 golden days is shown and discussed.

##### **Energy fluxes**

The sensible heat flux, H (see Fig. 4.31), showed a good median diel pattern, starting around 0500 CET and with the fluxes going down to 0 W m<sup>-2</sup> around 1900 CET. The maximum heat flux of 650 W m<sup>-2</sup> occurred at around 1230 CET. The fluxes followed the diel variation of their driving force (global radiation; Fig. 4.2)

##### **Non-reactive trace gases**

The spruce forest ecosystem acted as a source of carbon dioxide (Fig. 4.31) between 0000 CET and 0600 CET. The CO<sub>2</sub> emissions can be attributed to the night time respiration by the ecosystem. The maximum flux during this period is 6 μmol m<sup>-2</sup> s<sup>-1</sup>. After 0600 CET, the ecosystem became a sink for CO<sub>2</sub> due to photosynthesis occurring with the onset of sunrise. Fluxes of CO<sub>2</sub> into the canopy rose to a maximum of -18 μmol m<sup>-2</sup> s<sup>-1</sup> at 0900 CET contrary to the expected maximum downward CO<sub>2</sub> flux coinciding with solar noon when PPFD is expected to be at its maximum.

The result suggests that CO<sub>2</sub> rather than PPFD is the limiting factor for photosynthesis at this site. This is assuming that the vegetation is the only significant sink for CO<sub>2</sub> at this site. Recall from the analysis of the trace gas mixing ratios in 4.3 that there is a CO<sub>2</sub> peak due to early to mid-morning advection from the nearby country road. It is the advected CO<sub>2</sub> that is assumed to have enhanced the

photosynthetic rate for the mid-morning period. After 1800 CET, the ecosystem changes from a sink to a source of CO<sub>2</sub> with CO<sub>2</sub> fluxes of about 6 μmol m<sup>-2</sup> s<sup>-1</sup> up to midnight.

Median diel water vapour fluxes had a normal, photosynthesis-dependent variation. Only emission fluxes of H<sub>2</sub>O were observed (expected result because fog events were removed from the raw data as part of the quality control process). Water vapour fluxes were observed starting from 0430 CET, coinciding with the rising of the sun and the opening of stomata. The H<sub>2</sub>O flux maximum was at 1300 CET with a nominal value of 4.5 mmol m<sup>-2</sup> s<sup>-1</sup>. Emission fluxes of H<sub>2</sub>O stopped at 2100 CET, presumably with the closing of stomata.

Analysing the fluxes of CO<sub>2</sub> and H<sub>2</sub>O provides information on the photosynthetic duration which in turn gives information on stomatal opening duration. This information is important in interpreting the fluxes of reactive trace gases later on in this thesis when stomatal uptake of reactive trace gases is considered.

### ***NO-O<sub>3</sub>-NO<sub>2</sub> triad***

#### *NO*

The exchange of NO between the forest and the atmosphere was effectively zero between 0000 CET and 0600 CET. After 0600 CET downward-directed fluxes of NO were observed reaching a maximum median value of -0.5 nmol m<sup>-2</sup> s<sup>-1</sup> at 0800 CET. After that, the downward-directed fluxes declined to zero at about 1230 CET and remained at zero until midnight. The NO fluxes were effectively observed only during the advection period described in 4.3. This result was unusual because most research published on NO fluxes above forests has shown emission fluxes.

The probable reason for the downward-directed fluxes of NO could be that during night-time, NO from soil biogenic activity is immediately converted to NO<sub>2</sub> by the high O<sub>3</sub> mixing ratios below the canopy, hence none of the NO has the chance to reach the top of the canopy and therefore there is zero flux of NO above the canopy during this time. Additionally, during the advection period, NO is advected towards the site from the country road. At the same time NO from soil biogenic activity is emitted but is all converted to NO<sub>2</sub> before it reaches the top of the canopy. Another reason could be that the NO that reaches the site from the country road is immediately converted to NO<sub>2</sub>. This may be the cause of the negative NO flux above the forest canopy.

#### *NO<sub>2</sub>*

The net NO<sub>2</sub> flux was out of the forest throughout the day (see Fig. 4.31), being highest during daytime and particularly during the advection period. The NO<sub>2</sub> flux can be interpreted as being coming from NO destruction by O<sub>3</sub> below the canopy, from advected NO<sub>2</sub>, and advected NO reacting with O<sub>3</sub>.

$O_3$

Ozone fluxes above the forest canopy were always deposited into the canopy. Between 0000 CET and 0600 CET the  $O_3$  flux had a magnitude of about  $-3 \text{ nmol m}^{-2} \text{ s}^{-1}$ . After 0600 CET they rose, reaching a maximum of  $-25 \text{ nmol m}^{-2} \text{ s}^{-1}$  around 1030 CET. They remained high until 1400 CET whereby the  $O_3$  fluxes started to decline. By 2100 CET,  $O_3$  fluxes were close to zero. They however increased slightly, rising to about  $-4 \text{ nmol m}^{-2} \text{ s}^{-1}$  between 2230 CET and 2330 CET.

The  $O_3$  fluxes' downward direction all the time can be interpreted as being a result of the conversion of NO to  $\text{NO}_2$ . The slightly higher  $O_3$  flux between 2230 CET and 2330 CET may be due to the occurrence of low level jets around that time on some of the golden days. In addition, the penetration of coherent structures deep into the forest canopy is believed to have caused occasional bursts of NO from the forest floor to travel further up the canopy which would then lead to a larger  $O_3$  sink at that time.

#### **4.6 Comparison of gradient methods to the EC standard**

Figure 4.31 shows the EC fluxes side by side with the AGM and the MBRM fluxes. The magnitudes of the median diel fluxes for H and the nonreactive trace gases are highly comparable using all three methods. The nonreactive trace gases however also show a higher standard deviation and variability during the advection dominated period, with the variability from the AGM being higher than from the MBRM.

For reactive trace gases, downward directed fluxes of NO were observed for both the MBRM and the AGM. The magnitudes and diel pattern was also comparable between all three methods. Upward directed fluxes of  $\text{NO}_2$  were observed during periods when there was no solar radiation (0000 CET – 0430 CET and 1900 CET to 2330 CET) and bidirectional fluxes of  $\text{NO}_2$  were observed during the daytime periods predominated by photolysis and advection. Downward-directed fluxes of  $O_3$  were observed during the 'dark' periods when there was no solar radiation (0000 CET – 0430 CET and 1900 CET to 2330 CET) while bidirectional fluxes of  $O_3$  were observed during the photolysis and advection dominated periods of the day.

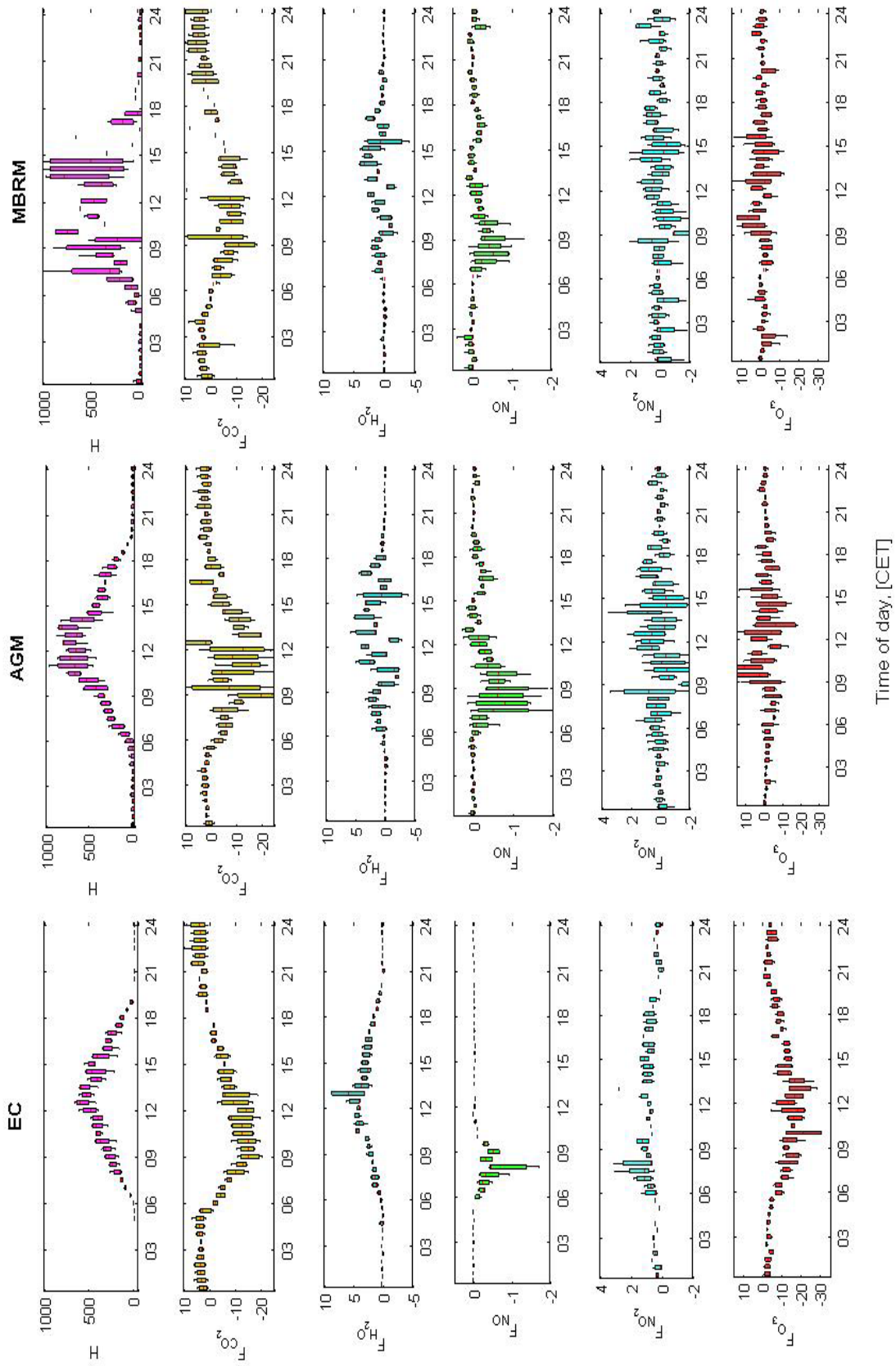


**Fig. 4.31.** Median diel variations of the EC flux (left column), RSL-corrected AGM fluxes (middle column), and MBRM fluxes (right column) for the IOP-2 Golden Days.

A plausible interpretation of the observations is that the atmospheric conditions above the forest at 32.5 m were vertically unstable (see Fig. 4.2 which shows the median diel variation of  $z/L$  for the golden days of IOP-2). Daytime  $\text{NO}$ ,  $\text{NO}_2$  and  $\text{O}_3$  transport was predominated by advection from the nearby country road as shown earlier. Therefore the combination of horizontal advection and vertical instability created variable concentrations of the triad constituents between the top of the canopy sampled by the lower inlet at 25 m and the top of the tower sampled by the inlet at 32.5 m. As a result the advected  $\text{NO}_2$  air mass produced either a negative or positive vertical concentration difference depending on which level it arrived at and its concentration compared to the  $\text{NO}_2$  emitted from the canopy. The EC method shows only emission fluxes of  $\text{NO}_2$  because all the  $\text{NO}_2$  is either coming out of the canopy or coming from advection. Therefore the net effect is an emission flux. The same situation occurred with the  $\text{O}_3$ .

$\text{NO}$  was however always deposited into the canopy at the local level also because it was all produced from the photolysis of advected  $\text{NO}_2$  and advective transport. The  $\text{NO}$  produced in situ above the canopy would have a tendency to rise up. The combination of the in situ produced  $\text{NO}$  and that from advection ensured that there was always a positive vertical concentration difference between 32 m and 25 m above the canopy and hence a downward-directed flux of  $\text{NO}$  when using gradient methods would be observed. The EC method would show a negative net flux because the  $\text{NO}$  would effectively get destroyed by the  $\text{O}_3$  at a rate faster than its production rate. The same goes for  $\text{O}_3$ .

Furthermore, the higher levels of  $\text{NO}$  at 32 m created a higher  $\text{O}_3$  sink at that level and hence a negative vertical concentration difference therefore a positive gradient-derived flux of  $\text{O}_3$  above the canopy).

This analysis has shown that the gradient methods are not useful for quantifying flux magnitudes in advection dominated environments on their own. An additional analysis of the incanopy processes in terms of turbulence, chemical transport and emission fluxes from the forest floor will help to complete analyses part of this thesis and fulfill the objectives of this thesis. This is done in the next sections.

#### **4.7 Effect of transport and chemistry on the reactive trace gas fluxes**

The study of reactive trace gases is complicated by the fact that one does not only have to consider turbulent transport when analysing and interpreting their fluxes but must also consider the effects of chemical conversion reactions during transport. Several tools introduced in the Materials and Methods chapter will be discussed in this section with a particular emphasis on how they relate to and can be used to interpret the reactive trace gas fluxes from this study. The tools that will be concentrated on

will be the forest-atmosphere coupling classes/turbulence exchanges regimes, the Damköhler number, and the segregation intensity.

#### 4.7.1 Forest-atmosphere coupling

The forest-atmosphere coupling classes are discussed in 2.1.4. Results for the coupling classes for IOP-2 (evaluated by Serafimovich et al. (2010)) show that when the canopy exchange regimes or coupling classes were grouped into 3 classes, it was seen that the most dominant class was *Ds*. In 44% of all cases during the four golden days, there was a decoupled sub-canopy dominated by sweeps (Fig. 4.32).

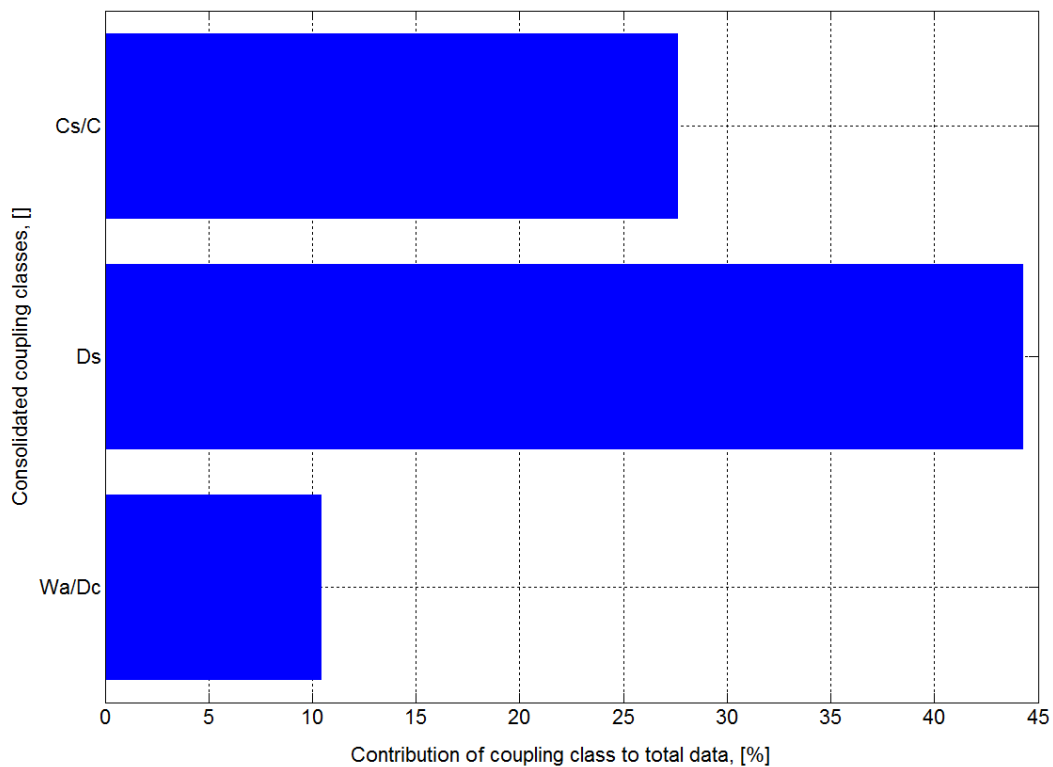


**Fig. 4.32.** Frequency distribution of the coupling classes consolidated into 3 classes.

Distribution of the turbulence timescale as a function of the turbulence exchange regime showed that, as expected, the highest turbulence timescales are related to the decoupled exchange regimes while the lowest turbulence timescales are associated with the coupled to fully coupled (*Cs/C*) exchange regimes. Figure 4.33 illustrates this.

Low level jets (LLJ) are suspected to have played a partial role in the forest-atmosphere coupling states, especially during the night. During the golden day's period, two LLJ events occurred, one on 01.07.2008 between 0100 CET and 0730 CET, then another one from 01.07.2008 to 02.07.2008 between 2230 CET and 0600 CET. The first LLJ event extended to a maximum height of 230 m a.g.l at 0530 CET with the maximum height corresponding to a maximum velocity of  $11.6 \text{ m s}^{-1}$ . The

second LLJ event had a maximum velocity of  $10.9 \text{ m s}^{-1}$  at 2330 CET corresponding to a height of 350 m a.g.l. See Foken et al. (2012) for more details.

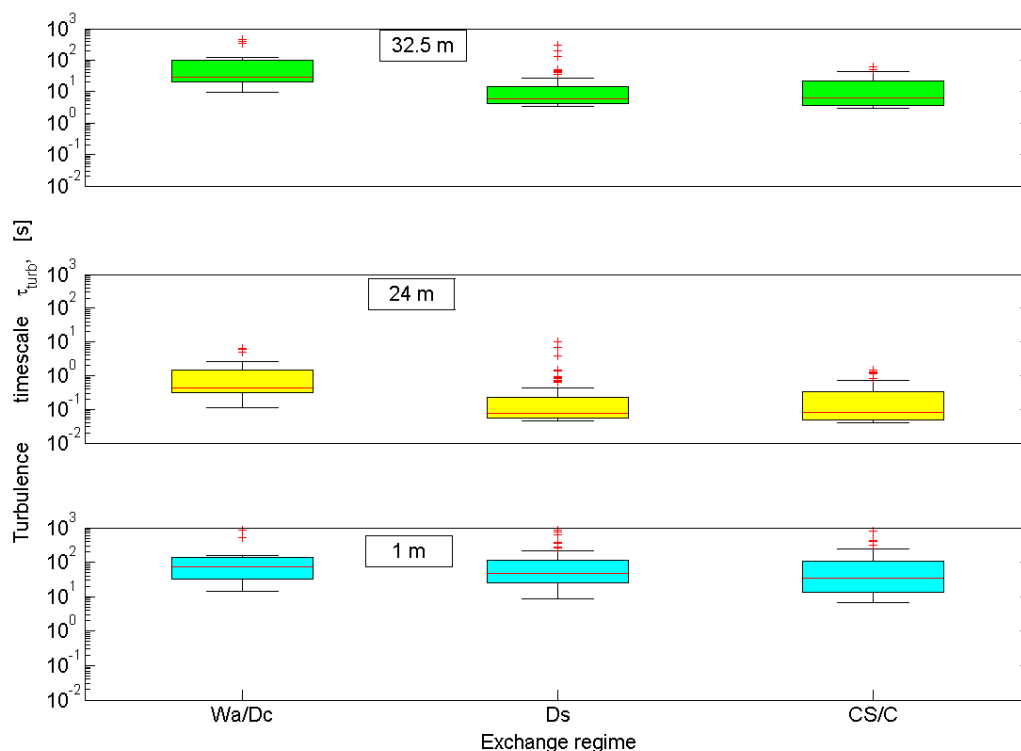


**Fig. 4.33.** Turbulence timescales classified according to exchange regimes for 32 m, 24 m, and 1 m during IOP-2.

### **Effect of coupling on the vertical concentration differences**

The forest-canopy coupling criteria were superimposed on vertical concentration differences of  $\text{CO}_2$  and  $\text{H}_2\text{O}$ . Results showed that for all the concentration differences  $Wa/Dc$  was mostly associated with the lowest concentration differences. This could indicate that when the canopy is decoupled from the atmosphere there is very little turbulent transfer of reactive trace gases from within the canopy, hence the lower concentration differences. Another reason could be that these exchange regimes occurred mostly during the night when turbulent transport was at its lowest. On the other hand the decoupled subcanopy class ( $Ds$ ) results showed mostly the highest concentration differences, a result which can be attributed to the exchange of trace gases from the higher part of the canopy, where there is vegetation, with the canopy. In contrast to the  $Wa/Dc$  class, the  $Ds$  class was predominant during the day. The combined coupled subcanopy/fully coupled ( $Cs/C$ ) exchange regime had no distinctly observable influence on the concentration differences of all the trace gases investigated during IOP-2.

### 4.7.2 Characteristic timescales of the NO-O<sub>3</sub>-NO<sub>2</sub> triad

Characteristic time scales for the individual species of the NO-O<sub>3</sub>-NO<sub>2</sub> triad were calculated and are presented in Fig. 4.36. Results showed that the timescale for NO varied between 10 and 100 s, while NO<sub>2</sub> timescales averaged about 150 s during the day and rose to infinity at night. Ozone timescales were in the order of 10<sup>4</sup> to 10<sup>5</sup> s. The timescale for the full triad, calculated according to the Lenschow method is shown also in Fig. 4.37. It varied between 50 and 160 s during the course of the golden days. The results confirm that there is no need for corrections for the NO and NO<sub>2</sub> mixing ratios as they travelled through the 53 m tubing. This is because the chemical timescales for NO and NO<sub>2</sub> are both higher than the residence time of NO and NO<sub>2</sub> in the tube (~9 s) (see Fig. 4.36).

Turbulence timescales were about 8 s during the day, rising to as high as 100 s during the night. However, the average night time value of the turbulence timescale was about 40 s.

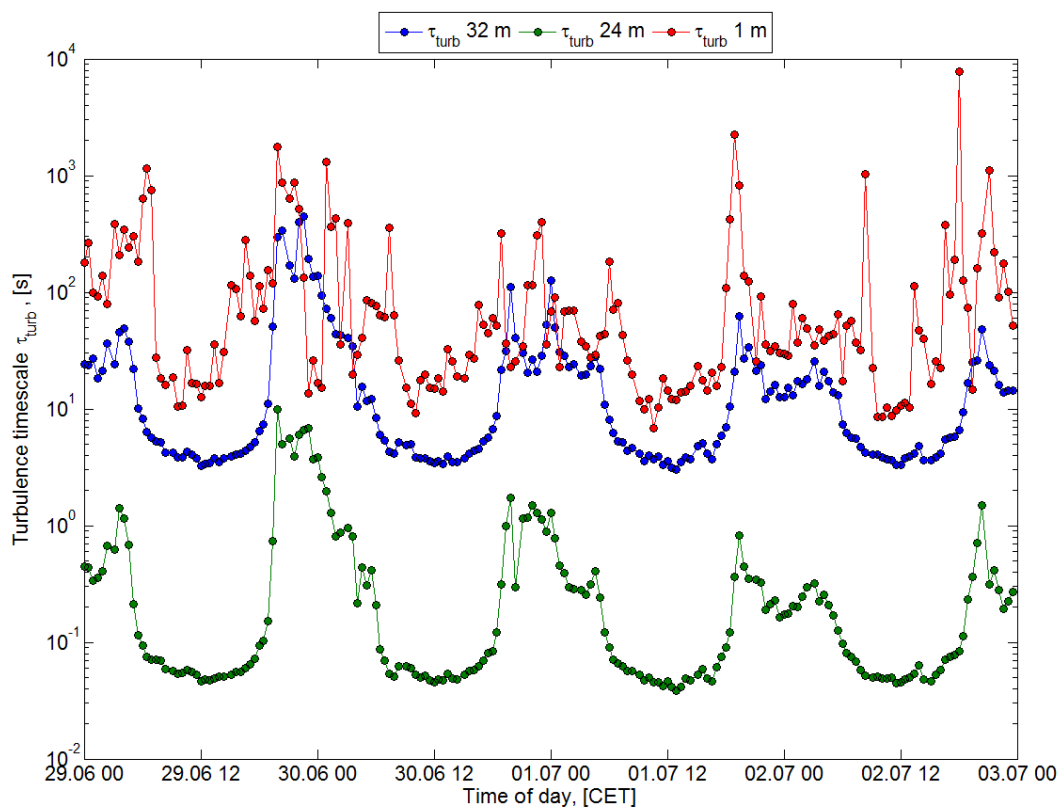


**Fig. 4.34.** Diurnal variation of the turbulence timescale at 32 m (blue), 24 m (green), and 1 m (red) during the IOP-2 Golden Days.

Distributions of chemical timescales (Fig. 4.35) above the canopy and at 1 m above the forest floor both showed that the lowest timescales were associated with the *Cs/C* while the highest were associated with the *Wa/Dc* class.

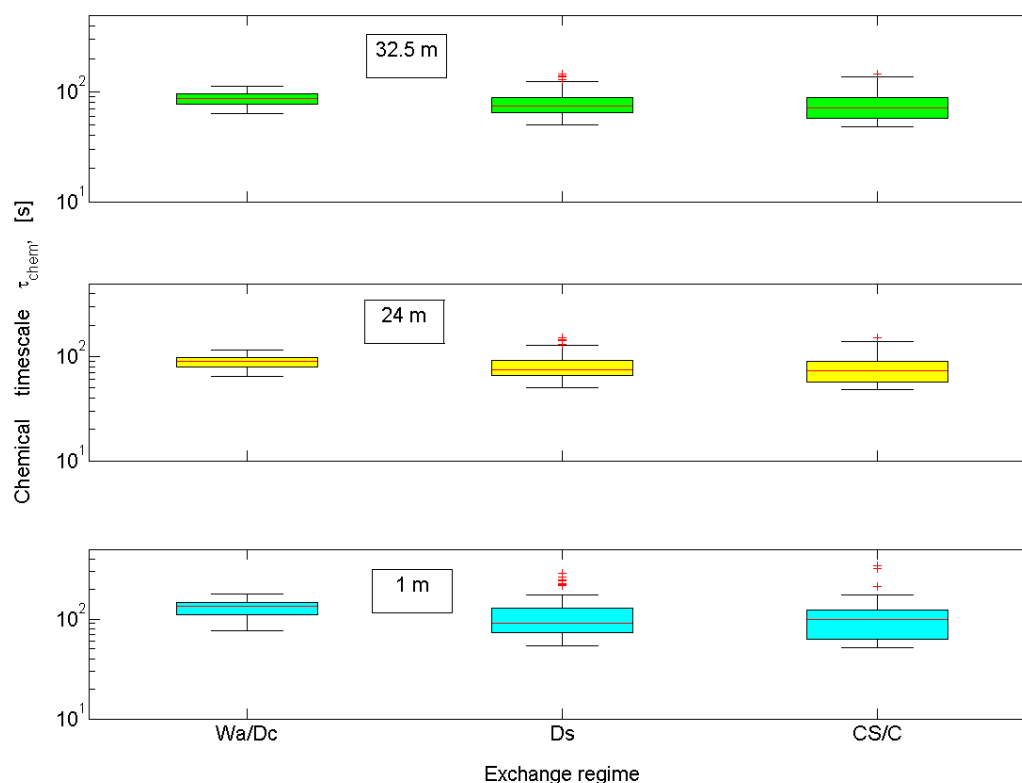


**Fig. 4.35.** Box plots showing the distribution of the chemical timescale with the combined turbulent exchange regimes  $Wa/Dc$ ,  $Ds$  and  $Cs/C$  at 32 m (top), 24 m (middle), and 1 m (bottom).

### 4.7.3 Damköhler numbers

Recall that the point  $Da = 0.1$  (also known as the critical Damköhler number) is usually defined as the threshold at which chemistry starts to influence the transport of a reactive trace gas.

In this thesis, the following classification was adopted for defining the rate of chemistry:

- **$Da < 0.1$ :** slow chemistry → reactants behaving as quasi-nonreactive trace gases.
- **$0.1 \leq Da \leq 1$ :** moderate chemistry → reactants moderately reacting with each other during turbulent transport, leading to slight chemical divergence.
- **$Da > 1$ :** fast chemistry → reactants affected by chemical reactions with each other during turbulent transport, leading to a strong likelihood of chemical divergence.

Figure 4.36 shows the diurnal variation of the chemical timescales for  $NO$ ,  $NO_2$  and  $O_3$  and also the respective Damköhler numbers. The results show that the chemical timescale for  $NO$  is the shortest while that for  $O_3$  is the longest. This suggests that  $O_3$  is much more stable in the air than  $NO$  with respect to chemical conversion.

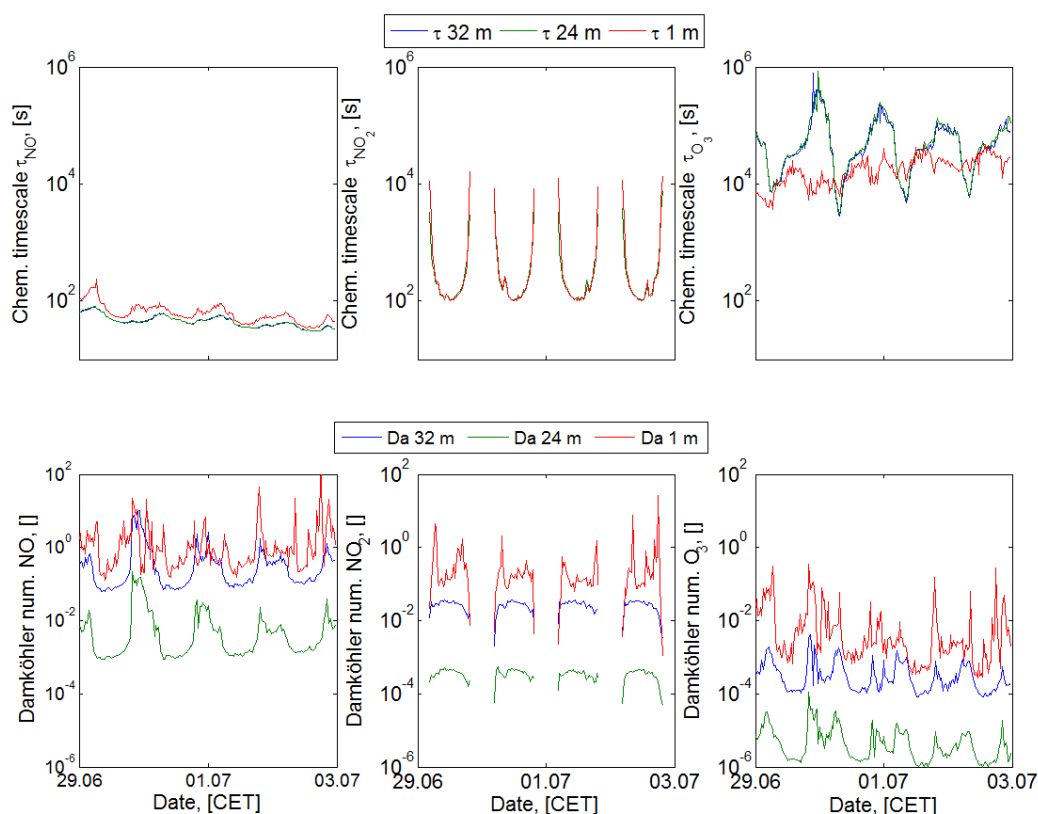


**Fig. 4.36.** Top: chemical timescales for NO (left), NO<sub>2</sub> (middle), and O<sub>3</sub> (right) at 32 m (blue), 24 m (green), and 1 m (red). Bottom: Damköhler numbers for NO (left), NO<sub>2</sub> (middle), and O<sub>3</sub> (right) at 32 m (blue), 24 m (green), and 1 m (red). All data presented is for the golden days IOP-2.

At 32 m, Damköhler numbers were below 0.1 between 0700 CET and 1800 CET and went up to 1 for the other time period. This was an indication of that there was little chemical influence on daytime fluxes of the triad at that level during their turbulent transport. At 24 m, which was the canopy height, Damköhler numbers were below 0.1 all the time – a condition that can be explained by the very short turbulence timescale at that level due to the effect of the enhanced turbulence at the canopy level. However, at 1 m, Damköhler numbers were greater than 0.1 in 98% of the cases due to the low turbulence regime inside the forest. NO from the soil was expected to be transformed rapidly to NO<sub>2</sub> by the action of O<sub>3</sub> within the first few meters above the ground.

The overall chemical timescale and the Damköhler number showed that both the chemical timescale and the Damköhler number for the NO-O<sub>3</sub>-NO<sub>2</sub> triad are heavily dependent on the magnitude of the mixing ratio of NO.

The median diel variation of Da above the forest at 32 m showed that the triad acted like quasi-nonreactive trace gases during the day (see 4.38) and became chemistry dominated during the periods

when there was no photolysis. At 1 m, the triad was under the influence of moderate to fast chemistry, a fact that can be attributed to the very low turbulence regime inside the forest.

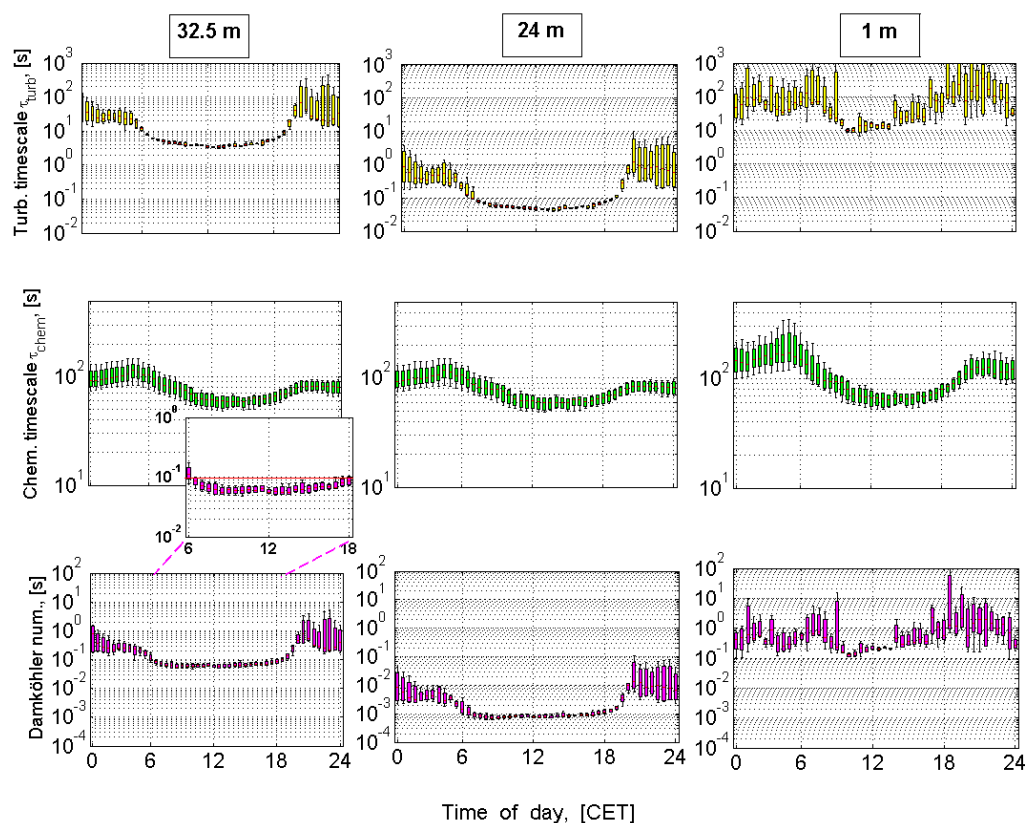


**Fig. 4.37.** Median diel variation of (top) the turbulence timescale at 32 m (left), 24 m (middle), and 1 m (right). Middle: The chemical timescales for the triad for the same three heights. Bottom: The Damköhler numbers for the same three heights during the Golden Days IOP-2. The red line on the insert in the plot for the Damköhler number at 32 m indicates the critical value of  $Da$ . The insert indicates the occurrence of the quasi-nonreactive nature of the  $NO-O_3-NO_2$  triad during daytime for this period.

#### 4.7.4 Intensity of segregation between $NO$ and $O_3$

Intensities of segregation between  $NO$  and  $O_3$  concentrations at 32 m (Fig. 4.38) showed values between  $-0.015$  and  $0.02$ . This is an indication that  $NO$  and  $O_3$  were in a state of almost perfect mixing during the course of the measurement period (0 indicates perfect mixing while  $-1$  indicates complete separation of two chemical compounds). Until now, all quoted values of  $I_s$  have been between 0 and  $-1$  ((de Arellano et al., 1993; de Arellano and Duynkerke, 1993). This is because the research has only dealt with cases where  $NO$  and  $O_3$  are always correlated. In the case of this study,  $NO$  and  $O_3$  are sometimes anti-correlated during the early to mid-morning period. This condition also explains the negative fluxes of  $NO$  apparent during this period. However the very small size of the segregation intensity indicates that segregation is not a conclusive indicator of the potential for flux divergence for

the NO-O<sub>3</sub>-NO<sub>2</sub> triad for the duration of the golden days measurement period (Dlugi, R, personal communication). The implication of this is that the likelihood of the two compounds reacting to generate NO<sub>2</sub> was high.

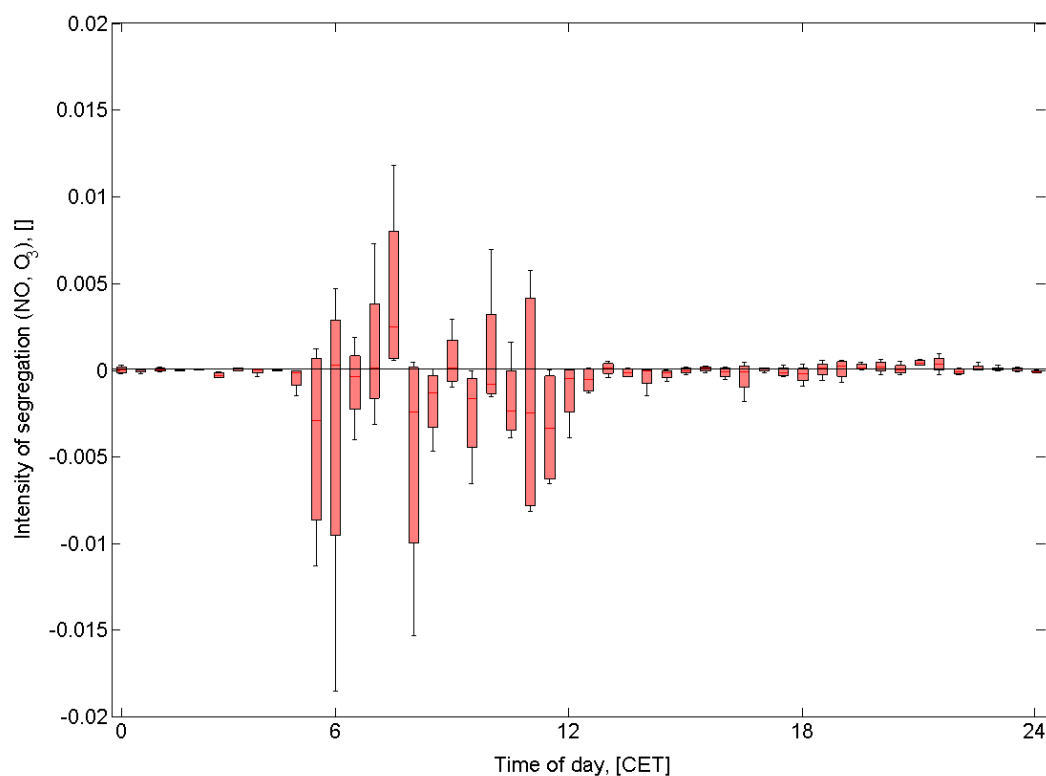


**Fig. 4.38.** Median diel variation of Intensities of segregation for the NO-O<sub>3</sub>-NO<sub>2</sub> during the golden days.

#### 4.8 Trace gas fluxes at the forest floor

It is known that the MOST cannot be applied in cases where the conditions are non-turbulent and the constant flux assumptions cannot be fulfilled. Such conditions exist below the forest canopy. It was desired to find out the exchange of trace gas fluxes at the forest floor. Having ascertained that there were periods of fully coupled conditions during the measurement period (whereby the conditions at the forest floor were as turbulent as those above the forest), it was decided to explore the possibility of evaluating below-canopy fluxes of the NO-O<sub>3</sub>-NO<sub>2</sub> triad. Except for O<sub>3</sub>, there was no EC station for reactive trace gases at the forest floor. The AGM was found to be unsuitable for this purpose because the temperature gradient measurements were not made at the same spot where the trace gas measurements were made. As a result of these limitations, and because of the availability of the EC flux of O<sub>3</sub> as well as gradient data of O<sub>3</sub>, the MBRM was chosen for evaluating the below-canopy trace gas fluxes.

Using the vertical gradient between 0.005 m and 0.9 m, fluxes were calculated using the MBRM for CO<sub>2</sub>, H<sub>2</sub>O, NO, NO<sub>2</sub>, and O<sub>3</sub>. Fluxes were picked only for those periods were:

- the coupling state was Cs/C;
- the vertical gradient was above 2σ of the detection limit for gradients (see 4.4.1).
- the friction velocity at 1 m was above 0.1 m s<sup>-1</sup>.

Coupling state Cs/C accounted for less than 20% of the golden days' data while vertical gradients above 2σ were prevalent because of the steep concentration gradient between 0.005 m and 0.9 m (see Fig. 4.39) which ensured that all vertical concentration differences were much higher than the 2σ significance level.

Median diel fluxes (MBRM) of H, CO<sub>2</sub>, and H<sub>2</sub>O at 1 m are shown in Fig. 4.39 while those for NO, NO<sub>2</sub> and O<sub>3</sub> are shown in Fig. 4.40. Also shown are the respective vertical concentration differences.

From midnight to 0800 CET, sensible heat fluxes hovered around zero. After 0800 CET, the sensible heat flux started to rise, reaching a maximum of 20 W m<sup>-2</sup> at 1000 CET before declining to zero again at 1500 CET. Between 1500 CET and 2330 CET, the sensible heat flux varied between 0 and -2 W m<sup>-2</sup>. This period coincided with the highest temperature gradient. The small heat flux is indicative of how dense the canopy is and its resistance to radiative and convective heat transfer. In addition, the absorption of incoming heat by the ground makes the net heat flux near the ground small. The positive heat fluxes measured are counter-gradient, i.e. the temperature gradient is almost always positive.

Night time CO<sub>2</sub> vertical concentration differences were as high as -70 μmol mol<sup>-1</sup>. This is indicative of biogenic activity by soil micro-organisms (e.g. soil respiration and decomposition of leaves on the soil surface). The flux of CO<sub>2</sub> was always out of the forest floor with maxima occurring at midnight (3.8 μmol m<sup>-2</sup> s<sup>-1</sup>), at midday (also 3.8 μmol m<sup>-2</sup> s<sup>-1</sup>), and at 2100 CET (2 μmol m<sup>-2</sup> s<sup>-1</sup>). The midday maximum, which occurred against a CO<sub>2</sub> vertical concentration difference minimum, may have been influenced by better mixing conditions during that period.

Water vapour vertical concentration differences were all negative close to the forest floor. This is evidence of the presence of dewfall, fog, and other forms of water vapour near the forest floor. The small negative concentration difference of H<sub>2</sub>O between midnight and 0600 CET is a strong indicator of the presence of fog. Results by (Sörgel et al., 2011) for IOP-1 show large concentrations of HONO at the same level and time of day, which typically forms in the presence of fog. Between 0600 CET and 2100 CET, the vertical concentration difference of H<sub>2</sub>O increases negatively. Conversely, the emission flux of H<sub>2</sub>O increased. This signifies the lifting of the fog as well as evaporation of water vapour from the forest floor. In addition, the water vapour from respiration at the forest floor could also have contributed to this.

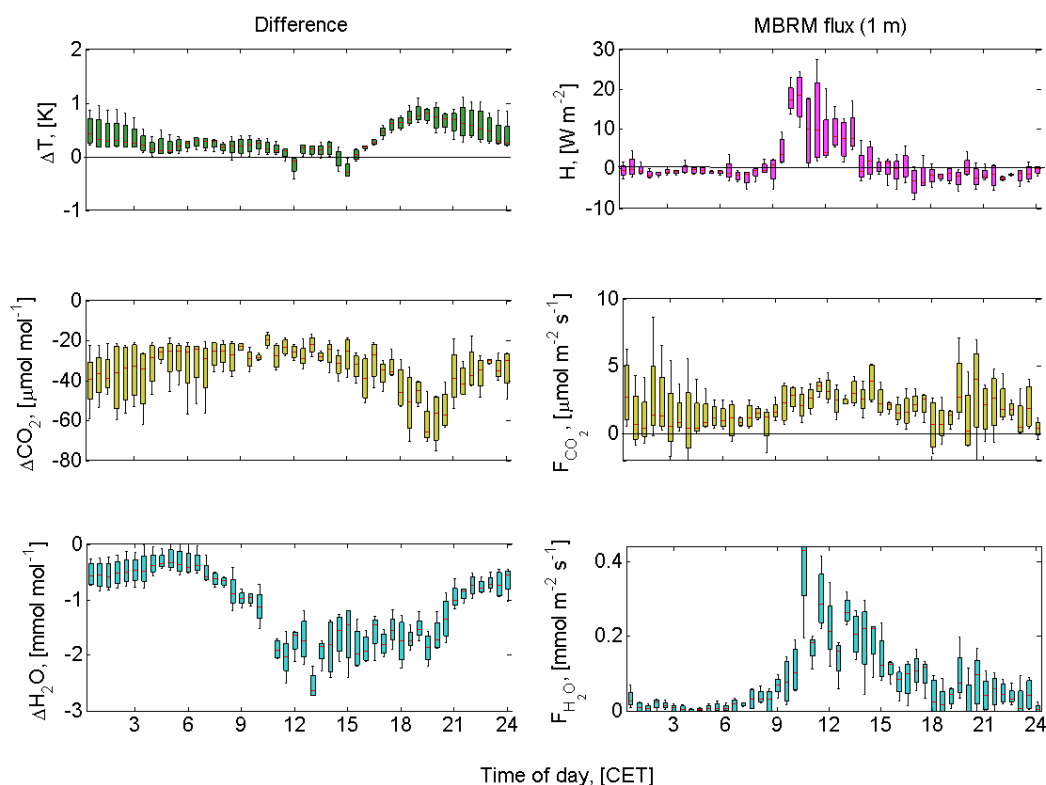


**Fig. 4.39.** The concentration difference between 0.005 m and 0.9 m (left) and the corresponding flux (right) using the Modified Bowen Ratio Method during the IOP-2 golden days.

The median diel vertical concentration differences of NO were all negative and ranged between -1.2 and -2.1 nmol mol<sup>-1</sup> throughout the day. Except for a small reduction in vertical concentration differences between 0900 CET and 1800 CET, there was no distinct diurnal variation in the differences. Fluxes of NO had a higher variability during night time and had their maximum during the day (0.25 nmol m<sup>-2</sup> s<sup>-1</sup> at 1000 CET). The fact that the NO flux out of the forest floor (assumed to be due to soil biogenic activity) is already so small at 1 m shows how strong the O<sub>3</sub> sink is throughout the canopy.

Nitrogen dioxide concentration differences were small and positive (averaging 0.5 nmol mol<sup>-1</sup>) between 0000 CET and 0900 CET. The differences became negative after 0900 CET and remained that way until the end of the day whereby they tended towards zero. In the same way, downward-directed fluxes of NO<sub>2</sub> were observed between 0000 CET and 0900 CET while emission fluxes of NO<sub>2</sub> were observed for the rest of the day. A possible explanation for the downward-directed flux of NO<sub>2</sub> at 1 m is that the NO<sub>2</sub> was getting converted to HONO and HNO<sub>3</sub> by the action of the early morning fog and dew discussed earlier.

Ozone vertical concentration differences between the forest floor and 1 m were positive throughout the golden days, ranging between 10 and 20 nmol mol<sup>-1</sup>. The corresponding fluxes were all negative

(as expected) and ranged between  $-0.1$  and  $-2.5 \text{ nmol m}^{-2} \text{ s}^{-1}$ . The maximum deposition flux of ozone occurred at 1200 CET and corresponded to  $-2.5 \text{ nmol m}^{-2} \text{ s}^{-1}$ . During night time,  $\text{O}_3$  fluxes were on average  $-0.5 \text{ nmol m}^{-2} \text{ s}^{-1}$ . However, between 2000 CET and 2330 CET,  $\text{O}_3$  fluxes rose to  $1 \text{ nmol m}^{-2} \text{ s}^{-1}$ . Ozone fluxes calculated by Riederer (2009) at the same site and height using the hydrodynamical multilayer model were of the same order of magnitude as the  $\text{O}_3$  fluxes by Zhu et al (2009) and in this study.

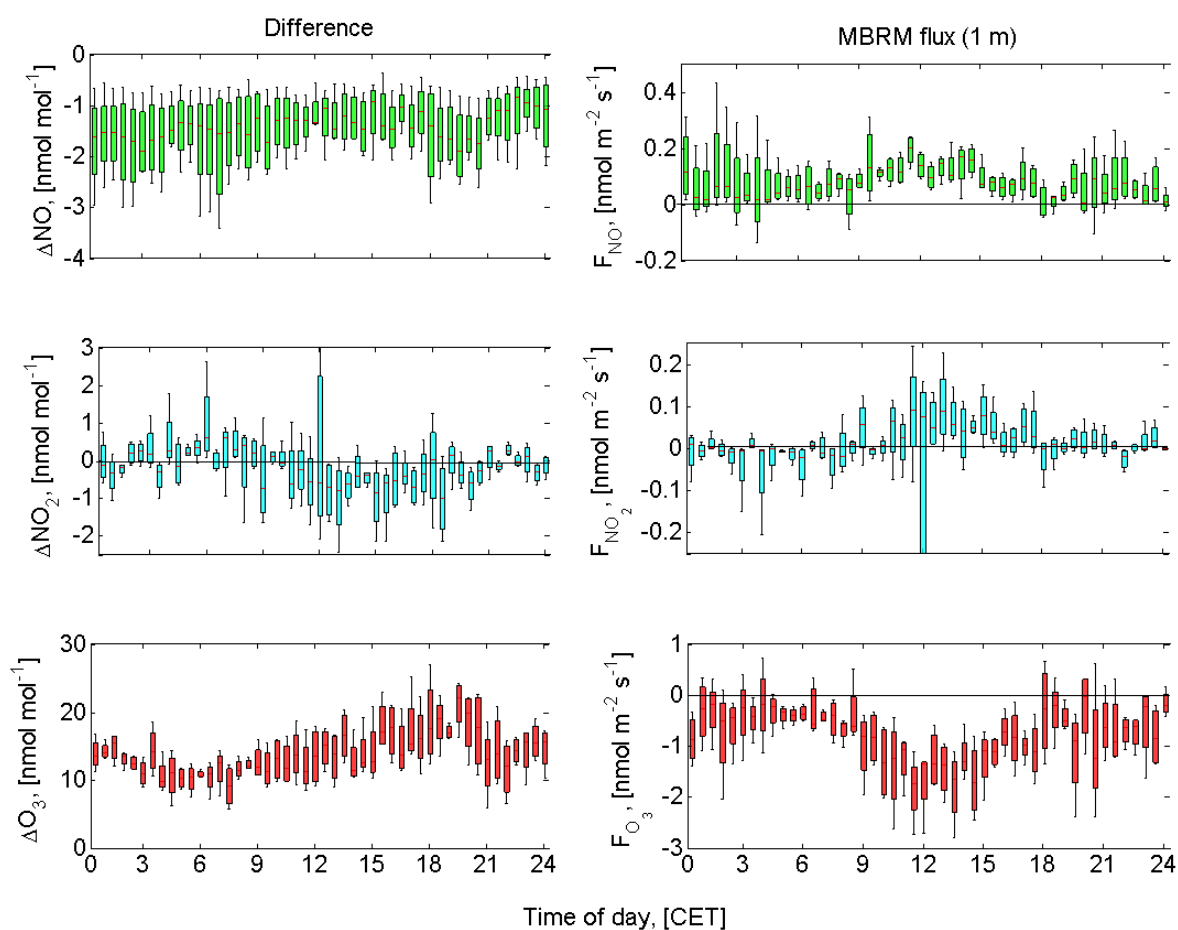


**Fig. 4.40.** The concentration difference between 0.005 m and 0.9 m (left) and the corresponding flux (right) for the reactive trace gases using the Modified Bowen Ratio Method during the IOP-2 golden days.

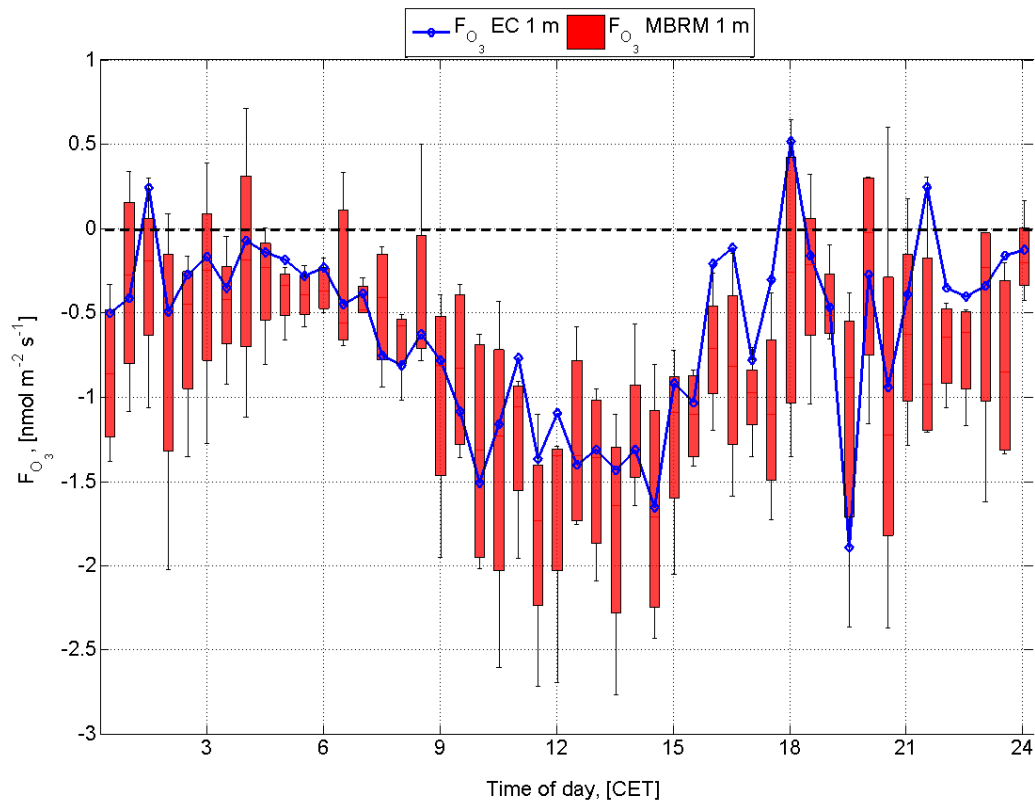


**Fig. 4.41.** Comparison of  $O_3$  fluxes from MBRM (red) and EC (blue) at 1 m during the IOP-2 golden days

**Table 4.6.** Summary of the directions of the above canopy fluxes in comparison to the below canopy fluxes.

Quantity	Below canopy diff	Above canopy diff	Below canopy flux	Above canopy flux
T	-	-	+/-	+
CO <sub>2</sub>	-	+/-	+	+/-
H <sub>2</sub> O	-	-	+	+
NO	-	+	+	-
NO <sub>2</sub>	+/-	+/-	+/-	+
O <sub>3</sub>	+	+/-	-	-

Using an algorithm developed by Meixner and Yang (2006) to derive net potential fluxes of NO as a function of the soil moisture, Falge et al. (2010) found that that the magnitude of the soil NO flux

from lab measurements and modelling was dependent on the understory vegetation (see Fig. 4.42). The model main input parameters were soil temperature, soil moisture, and understory cover. The soil NO flux results obtained at 0.9 m in this study are in closest agreement to those obtained by Falge et al. (2010) when the understory vegetation was moss and/or litter. The understory cover was moss/litter at the location of the inlets for the below canopy trace gas gradients. One cannot tell from which understory type the soil fluxes emerge but at 0.9 m above the soil surface, it is expected that the understory type directly below the trace gas inlets is likely to contribute the most to the flux footprint. The averaged soil NO flux from all the understory vegetation types was between 1.5 and 2  $\text{nmol m}^{-2} \text{s}^{-1}$ , being heavily biased by the results from the young spruce and blueberry understory types (see Fig. 4.42 a). Considering that the fluxes reported here were measured at 0.9 m above the soil surface and that they are not at optimum conditions, they are a reasonable comparison to the lab results since they are within the same order of magnitude in terms of mean diurnal values ( $0.1 \text{ nmol m}^{-2} \text{ s}^{-1}$  using MBRM,  $0.25 \text{ nmol m}^{-2} \text{ s}^{-1}$  using lab/modelling for moss/litter – see Fig. 4.42b). The lab results confirm the presence of flux divergence due to chemistry occurring faster than turbulence (hence the high Damköhler numbers at 1 m in Fig. 4.37) within the first meter above the forest floor.

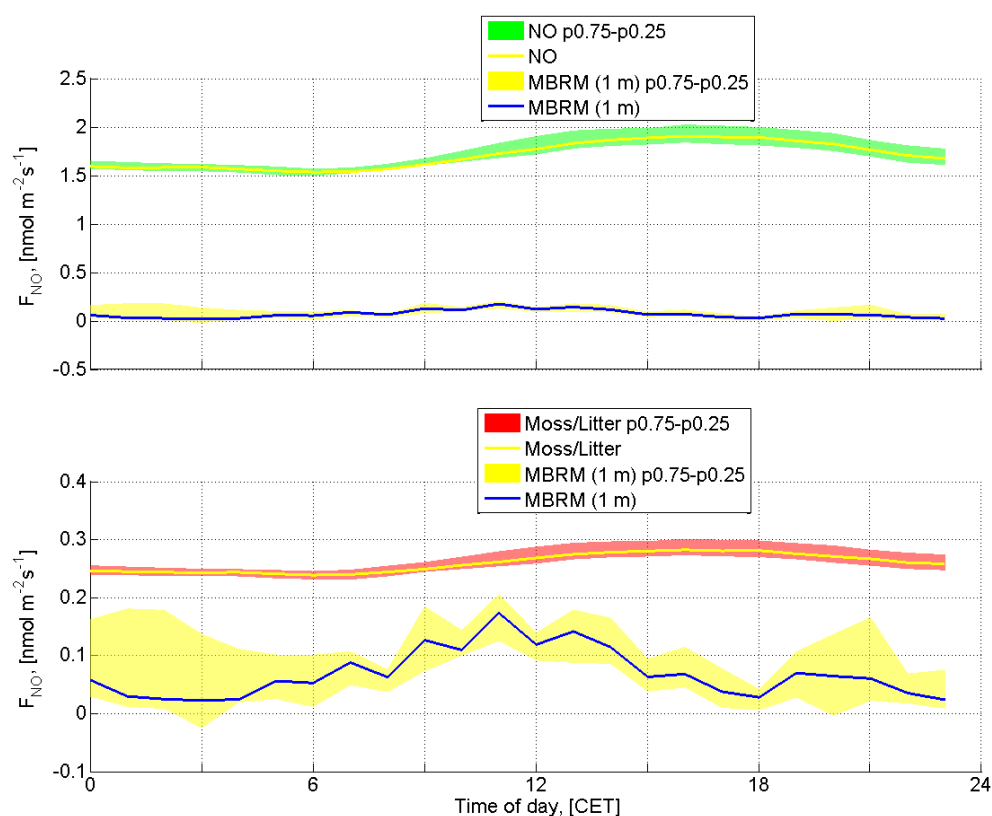


**Fig. 4.42.** Modelled soil NO fluxes according to Falge et al. (2010) for top/a: all understory covers, and bottom/b moss/litter cover. Note the different scales used for the vertical axes.

## 4.9 Fluxes of O<sub>3</sub>, NO<sub>2</sub> and NO under low NO<sub>x</sub> advection conditions on 29<sup>th</sup> of June 2008

The 29<sup>th</sup> of June 2008, the first golden day of EGER IOP-2 was unique in the sense that it was the only golden day on which there was very little NO<sub>x</sub> from advection (see 4.3). This was because it fell on a Sunday, a day on which there was less traffic on the country roads bordering the measurement site. Analysis of the meteorological conditions and the evolution of trace gas mixing ratios and fluxes on this day will help to complete the solution to the puzzle as to why the trace gas fluxes above the canopy are different from what is expected.

In the process of discussing this day in detail, the following steps will be followed:

- (1) The atmospheric conditions will be analysed in detail.
- (2) The chemical and turbulent driving forces as well as the forest-atmosphere exchange will be looked at.
- (3) The vertical concentration differences and the fluxes above the canopy and at the forest floor will be analysed and interpreted in relation to (1) and (2).
- (4) The result will be used to make a general interpretation and conclusion on the above canopy trace gas fluxes at this site.

### 4.9.1 Atmospheric conditions

It was the only day on which the mid-morning global radiation had a minimum value of 650 W m<sup>-2</sup>. The mid-morning period had brief periods of light cloud cover which lowered the global radiation to 650 W m<sup>-2</sup> from 900 W m<sup>-2</sup>. This was assumed not to have had any significant effect on the photolytic yield from the NO-O<sub>3</sub>-NO<sub>2</sub> triad reactions. A maximum global radiation intensity of 970 W m<sup>-2</sup> was achieved shortly after midday after which the global radiation followed a normal course, declining to zero at 2000 CET. The photolysis frequency had, as expected, the same diurnal course as the global radiation

The horizontal wind speed (measured at 31 m a.g.l as explained earlier) on this day was moderate and ranged between 1 m s<sup>-1</sup> and 4.5 m s<sup>-1</sup>. Maximum horizontal wind speed was achieved at midday, a time which corresponded to slightly unstable conditions. Friction velocities followed the same diurnal course as the horizontal wind speed. The mean diurnal wind direction (Fig. 4.42) was entirely in the North-Southwest to South-Northwest for that day. Wind coming from this sector is expected to have advected trace gas emission from a busy road in connecting Weißenstadt and Sparneck.

Atmospheric conditions were vertically unstable during the course of the day and stable during the night, an indicator of well-developed turbulence during the day. The stable conditions during the night were favourable to the accumulation of trace gases in the shallow boundary layer.

Relative humidity (Fig. 4.43) started out very high (~85-95%) and declined gradually, reaching a minimum of 40% at 1700 CET before rising again to reach 55% at the end of the day. The high relative humidity at the beginning of the day was due to moisture release from the soil and the canopy as a result of heavy rains the previous day (which was not a golden day). Conversely, air temperatures started out low (14 °C) before reaching a maximum of 22 °C at 1700 CET coincident with the minimum relative humidity. The air temperature then gradually declined to 18 °C at the end of the day.

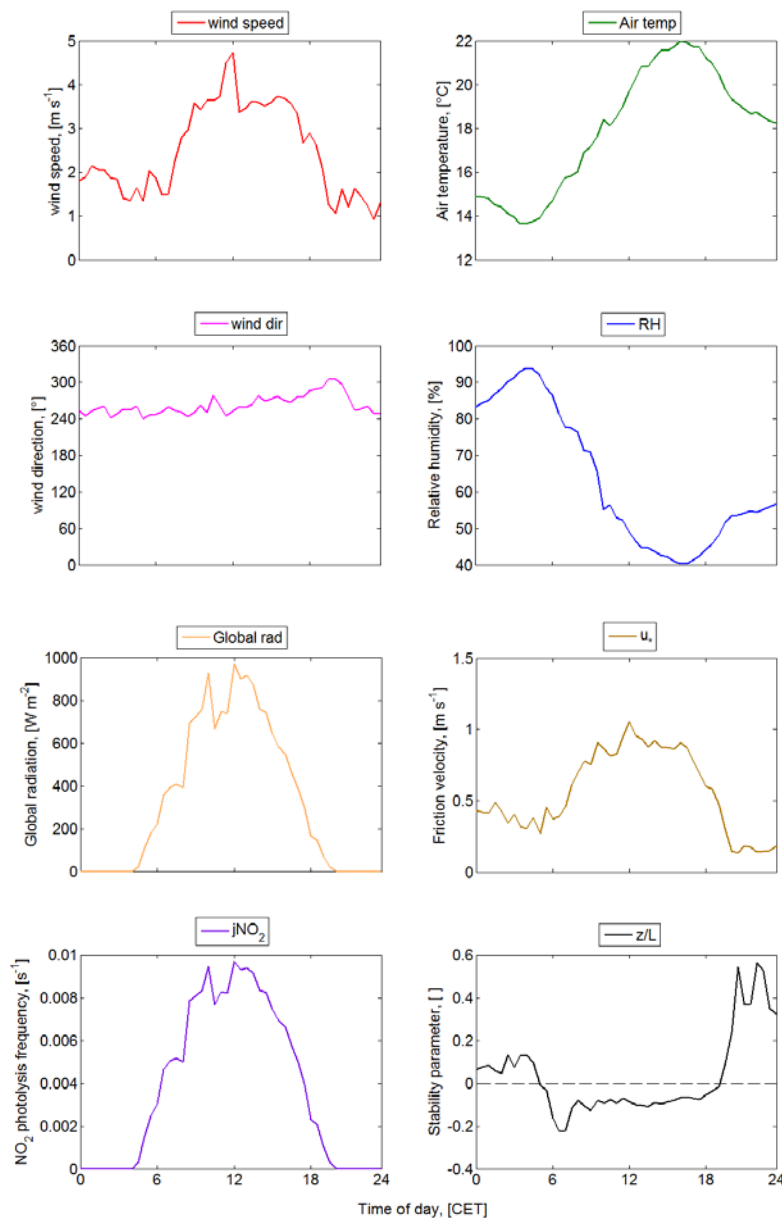


**Fig. 4.43.** Plots of the diel atmospheric conditions during the first golden day of IOP-2 (29.09.2008). Shown are the wind speeds (red), wind direction (pink), air temperature (green), relative humidity (blue), the global radiation (orange),  $j\text{NO}_2$  (violet), friction velocity (brown), and the stability parameter (black).

## 4.9.2 Trace gas vertical concentration differences and absolute concentrations

### ***Absolute concentrations***

The above canopy trace gas concentrations are shown in 4.3 and are described under the conditions for weekends. The below canopy mixing ratios of trace gases are shown in the figure below in the profile figures in the appendix.

### ***Dependence of mixing ratios on wind direction***

As explained in the previous section, the wind was blowing constantly from the same sector. The deviation in wind direction for the entire day was less than 60°. Therefore no conclusions could be drawn about mixing ratio dependence on wind direction.

### ***Vertical concentration differences***

#### *Nonreactive trace gases and temperature*

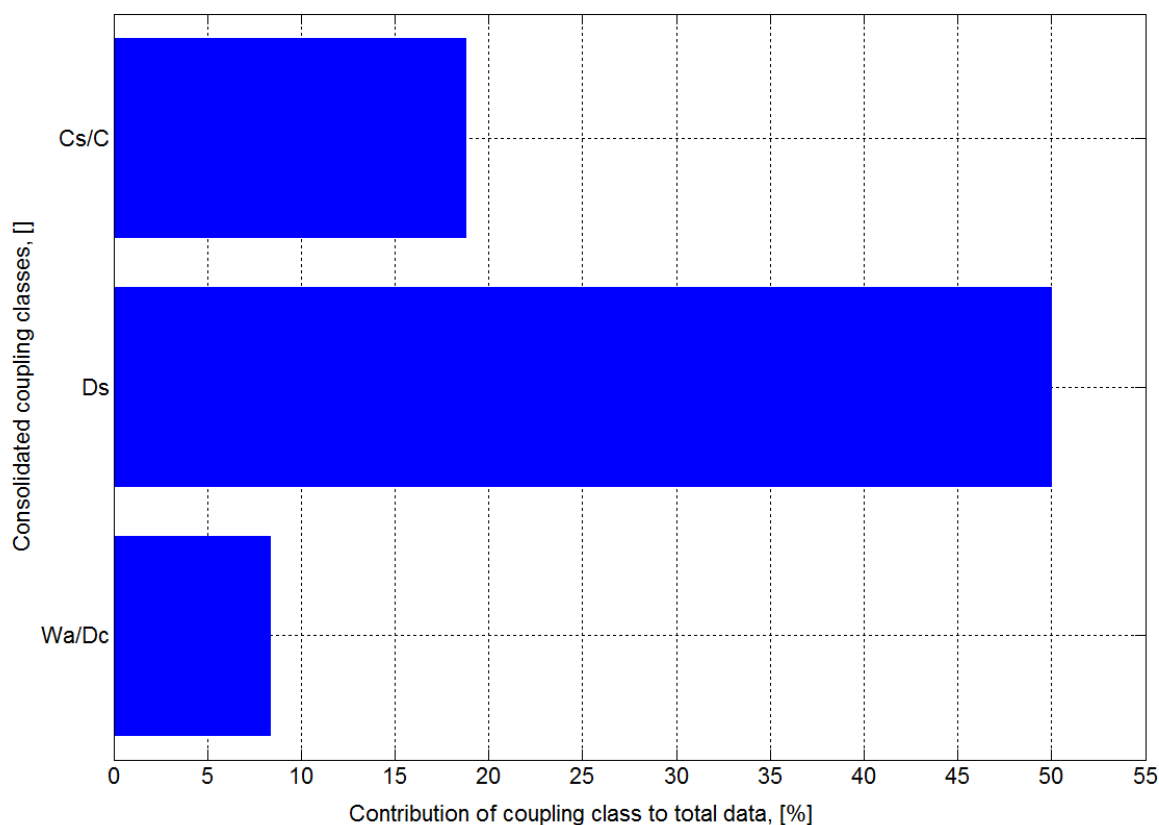
The vertical concentration differences for the nonreactive trace gases and temperature at 1 m are shown in Fig. 4.49. There was no significant difference between the concentration differences on this day and the median diel concentrations for all the golden days described in 4.8 and shown in Fig 4.39.

#### *Reactive trace gases*

The vertical concentration differences for the reactive trace gases at 1 m are shown in Fig. 4.50. The vertical concentration differences for NO were above the 75<sup>th</sup> percentile of the median diel variation shown in Fig. 4.40. This is an indication of the fact that there was less NO destruction on this day. The O<sub>3</sub> concentration differences support this point, being lower than the median diel O<sub>3</sub> concentration difference. Lower O<sub>3</sub> concentrations were available for converting NO to NO<sub>2</sub>, hence the larger NO concentration difference near the forest floor. In the same way there were slightly smaller NO<sub>2</sub> concentration differences.

## 4.9.3 Chemical and turbulent driving forces

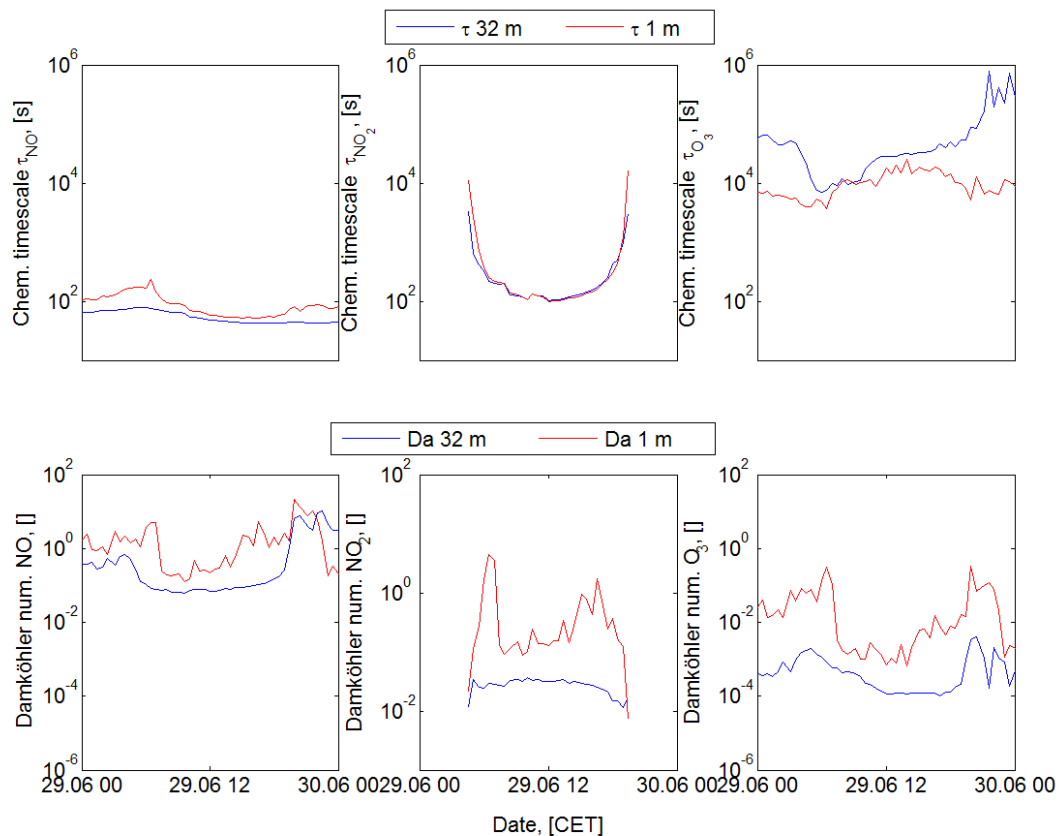
The forest-atmosphere coupling classes as shown in Fig. 4.44. Wa/Dc occurred 8% of the day while Ds occurred 50% of the day. Cs/C occurred 18% of the day. The coupling classes were indeterminate for the remainder of the time.



**Fig. 4.44.** Frequency distribution of the coupling classes consolidated into 3 classes for the first golden day of IOP-2.

The above canopy characteristic timescales for NO, O<sub>3</sub> and NO<sub>2</sub> and the Damköhler numbers on this day (see Figs 4.45 and 4.46) had the same orders of magnitude and variation as for the mean diel variation discussed in 4.7.2. For the below canopy case, the chemical timescale for NO,  $\tau_{\text{NO}}$ , was larger than that observed above the canopy as a result of the lower concentrations of O<sub>3</sub> at the forest floor ( $\tau_{\text{NO}}$  is inversely proportional to the O<sub>3</sub> concentration; see Eq. 2.75).

On the other hand, above canopy and below canopy chemical timescales for NO<sub>2</sub> were almost identical in magnitude and variation. This may have been caused by the differences in  $j_{\text{NO}_2}$  and concentrations between the two above canopy case and the below canopy case compensating for each other. The chemical timescale for O<sub>3</sub>,  $\tau_{\text{O}_3}$ , was an order of magnitude higher above the canopy than at the forest floor, particularly during night time periods. This is directly related to the concentration of NO at the respective levels since  $\tau_{\text{O}_3}$  is inversely proportional to the concentration of NO (see Eq. 2.77).



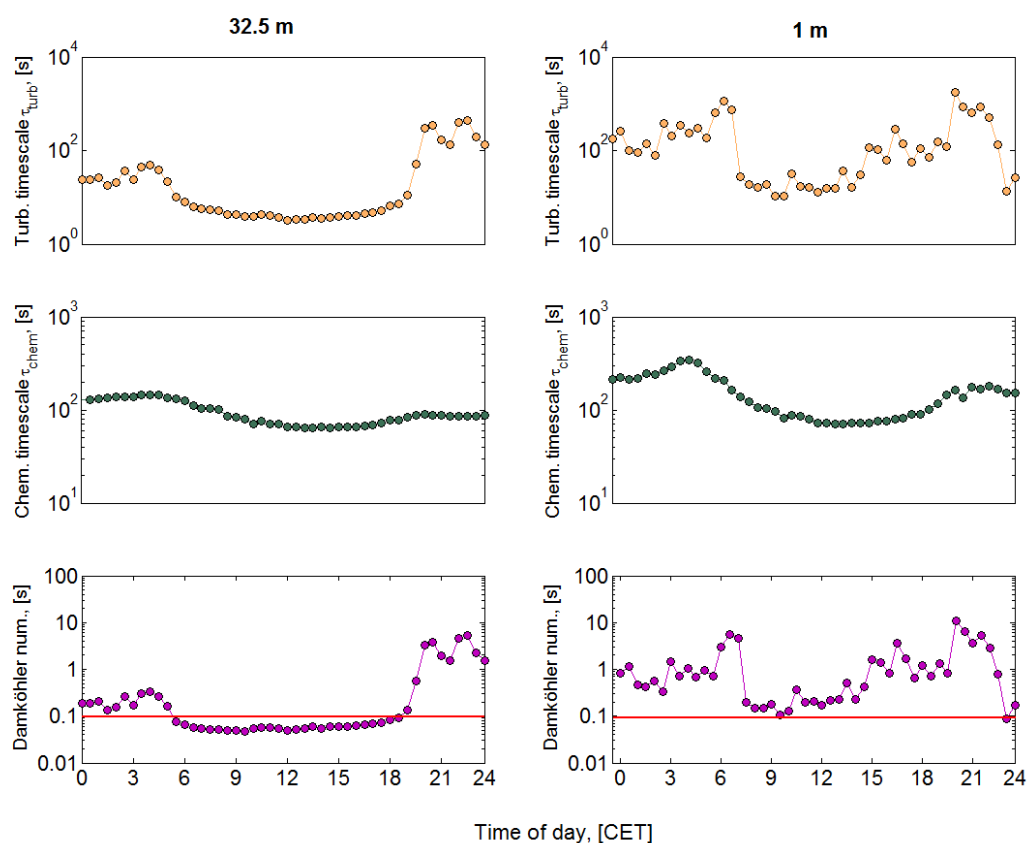
**Fig. 4.45.** Top: chemical timescales for NO (left), NO<sub>2</sub> (middle), and O<sub>3</sub> (right) at 32 m (blue) and 1 m (red). Bottom: Damköhler numbers for NO (left), NO<sub>2</sub> (middle), and O<sub>3</sub> (right) at 32 m (blue) and 1 m (red). All data presented is for the first golden day of IOP-2.

Figure 4.46 shows the turbulence timescales, the chemical timescales, and the corresponding Damköhler numbers for the NO-O<sub>3</sub>-NO<sub>2</sub> triad on the first golden day for the above canopy and the below canopy cases.

The turbulence timescale showed a strong similarity to the vertical stability parameter. During daytime, the magnitude of the turbulence timescale was less than 10 s but rose to a maximum of 500 s during the night. Below canopy turbulence timescales were lower during the day but were still at least twice as high as those above the canopy. During the night, the turbulence timescale at 1 m rose to as high as 1000s. It showed a much higher variability than the above canopy turbulence timescale. This can be attributed to the contribution of the different coupling states between the forest and the atmosphere. When coherent structures penetrated deeper into the canopy the turbulence timescale was correspondingly lower. This can be observed clearly for the period 2200 CET and 2330 CET where sweeps and ejections enhanced the turbulence regime at 1 m.

The chemical timescale ranged between 80 and 100 s above the canopy. It was dependent almost entirely on the characteristic timescale for NO, which was the highest common factor. Below the canopy, the chemical timescales ranged between 600 s during night time and early morning and 80 s during the day. In this case, O<sub>3</sub> appeared to be a stronger determinant for the chemical timescale due to the fact that its characteristic timescale was an order of magnitude lower than that above the canopy.

Damköhler numbers followed the same course as the chemical timescales. Above the canopy, the Damköhler number was below the critical value of 0.1 between 0530 CET and 1830 CET, indicating that turbulent transport was proceeding faster than chemical transformations. This time period was dominated by photolysis. During the night (dominated by low turbulence) and periods where photolysis was not occurring, the Damköhler number ranged between 0.5 and 10. For the below canopy case, the Damköhler number were at or above the critical value for the whole day (see Fig. 4.45). They ranged between 0.1 and 10, indicating that chemical transformations were moderate to fast.



**Fig. 4.46.** Median diel variation of (top) the turbulence timescale at 32 m (left), and 1 m (right). Middle: The chemical timescales for the triad for the same two heights. Bottom: The Damköhler numbers for the same two heights during the Golden Days IOP-2.

The segregation intensity between NO and O<sub>3</sub> during the first golden day is shown in Fig. 4.45. Only the period between 0530 CET and 1300 CET showed segregation. During this period, the segregation intensity ranged between 0.015 and -0.020, which is 1.5 to 2%. Even this segregation was too small to be considered significant and it can be concluded that segregation did not influence the NO-O<sub>3</sub>-NO<sub>2</sub> triad during the measurement period. There was homogenous mixing between NO and O<sub>3</sub> throughout the day.

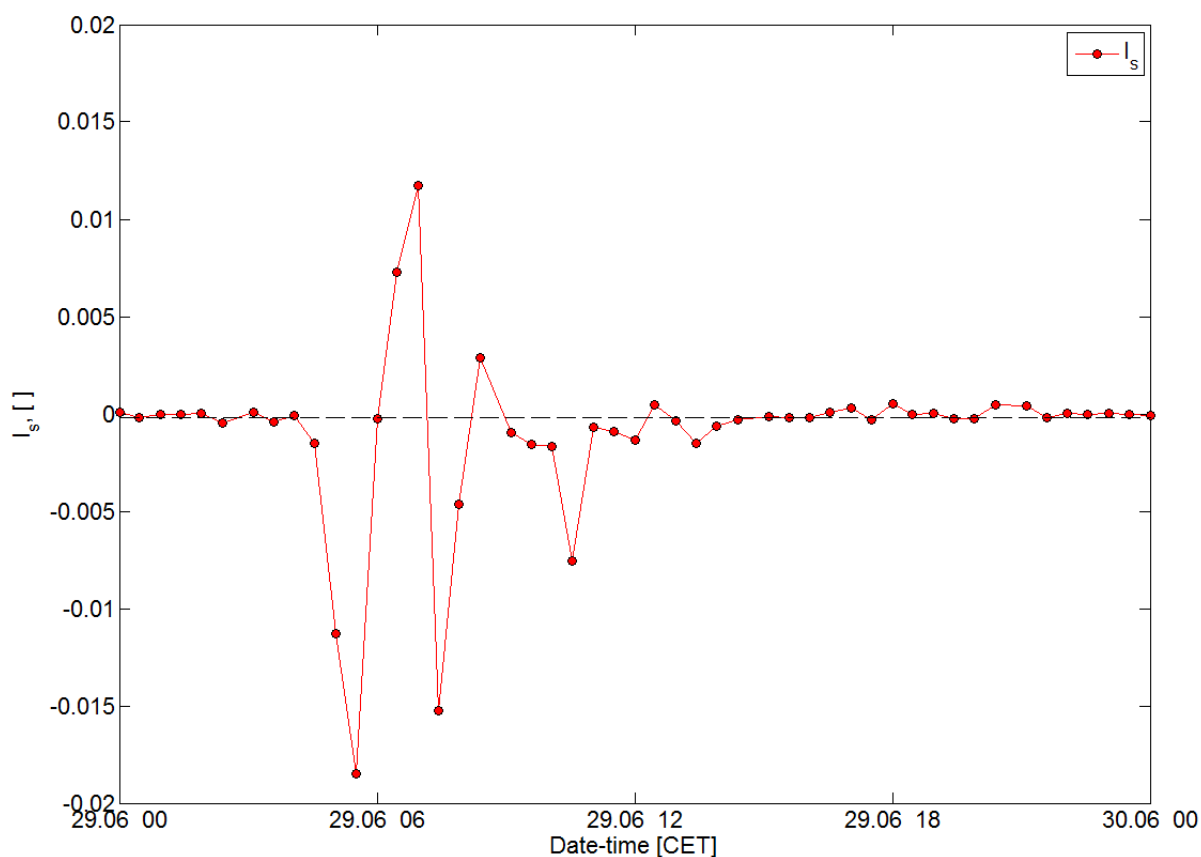


**Fig. 4.47.** Diurnal variation of intensities of segregation for the NO-O<sub>3</sub>-NO<sub>2</sub> during the first golden day.

#### 4.9.4 Fluxes

Here the energy and trace gas fluxes for the first golden day are presented. The above canopy fluxes are shown using the three flux evaluation methods while the below canopy fluxes are shown for the MBRM.

##### **Above canopy fluxes**

The above canopy fluxes are shown in Fig. 4.48.

### *Sensible heat*

The sensible heat flux on this showed a slightly negatively skewed bell shape with a maximum at  $800 \text{ W m}^{-2}$ . This was indicative of a good day with well-developed turbulence. There were no negative sensible heat fluxes observed for the entire day for all three methods.

### *CO<sub>2</sub> and H<sub>2</sub>O*

The CO<sub>2</sub> flux observed on this day had a clear, well-defined pattern with respiration during the night time periods and net photosynthesis during the daytime periods. Maximum net flux above the forest for CO<sub>2</sub> was  $20 \mu\text{mol m}^{-2} \text{ s}^{-1}$ , which was higher than the 75<sup>th</sup> percentile of the median diel value for all the golden days. The H<sub>2</sub>O flux also had a well-defined curve starting at 0300 CET with a maximum of  $9 \text{ mmol m}^{-2} \text{ s}^{-1}$  at midday and ending at 2100 CET.

### *NO*

The NO flux, like the median diel case described in 4.5.5, showed variation only between 0530 CET and 1000 CET for the EC case. The rest of the time there was no flux. The flux of NO had an observed maximum of  $0.5 \text{ nmol m}^{-2} \text{ s}^{-1}$  coinciding with 0900 CET. However, the gradient-based methods showed more variation in the daytime fluxes and some positive fluxes some of the time during the day. The magnitudes were within the same range for all three methods.

### *NO<sub>2</sub>*

Unidirectional net fluxes of NO<sub>2</sub> were observed from the EC evaluation with the fluxes also present only during daytime. The maximum NO<sub>2</sub> flux was  $2.5 \text{ nmol m}^{-2} \text{ s}^{-1}$ , observed at midday. Bidirectional daytime fluxes of NO<sub>2</sub> were observed from the gradient-based methods ranging between  $-2$  and  $2 \text{ nmol m}^{-2} \text{ s}^{-1}$ .

### *O<sub>3</sub>*

From the EC method, net downward-directed fluxes of O<sub>3</sub> were observed with a maximum value of  $-30 \text{ nmol m}^{-2} \text{ s}^{-1}$ . Fluxes were present from midnight until 2200 CET. The fluxes of O<sub>3</sub> from the gradient-based methods were predominantly downward directed but with some small emission fluxes during daytime. The magnitude of the gradient-based fluxes was approximately 3 times smaller than the EC fluxes. Fluxes of O<sub>3</sub> during the advection period were almost zero.

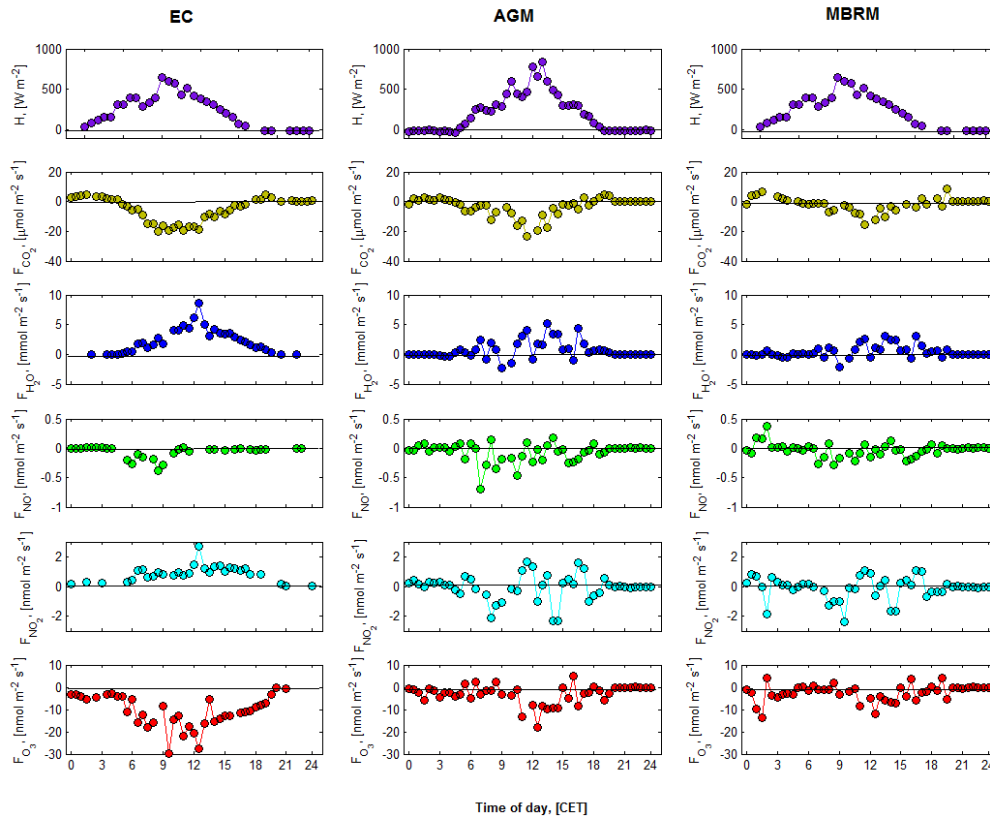


**Fig. 4.48.** Diurnal variations of the EC flux (left column), RSL-corrected AGM fluxes (middle column), and MBRM fluxes (right column) above the forest canopy (32 m) for the first IOP-2 golden day.

### Forest floor fluxes

#### Sensible heat

The sensible heat flux was only positive between 0900 CET and 1500 CET (Fig. 4.49). The negative sensible heat fluxes recorded during the other times of the day are an indication of the fact that soil temperatures were higher than the air temperatures above the soil. In a similar way to the median diel case, the positive heat fluxes are mostly counter-gradient. The fluxes were small, ranging between  $-5 \text{ W m}^{-2}$  and  $18 \text{ W m}^{-2}$ .

#### Nonreactive trace gases

Figure 4.49 shows the nonreactive trace gas fluxes. Emission fluxes of  $\text{CO}_2$  were observed at 1 m above the forest floor. The fluxes had their maximum values during night time with a peak value of  $9 \mu\text{mol m}^{-2} \text{ s}^{-1}$  at 0300 CET and another one of  $5 \mu\text{mol m}^{-2} \text{ s}^{-1}$  at 2100 CET. During the day the  $\text{CO}_2$  flux was consistently at approximately  $2 \mu\text{mol m}^{-2} \text{ s}^{-1}$  with some slight variation. At 0900 CET and

1800 CET the lowest fluxes were recorded which were between  $-0.5$  and  $-1 \mu\text{mol m}^{-2} \text{s}^{-1}$ . These were treated as artefacts resulting from periods where the EC ozone flux had a positive sign.

There was no water vapour flux between midnight and 0630 CET. A possible reason for this is the presence of vertically homogeneously distributed below-canopy fog. For the rest of the day,  $\text{H}_2\text{O}$  fluxes ranged between 0 and  $0.4 \text{ mmol m}^{-2} \text{s}^{-1}$  (which occurred at 1030 CET). This was due to evaporation of moisture from the soil and understory as a result of the previous day's rainfall event.

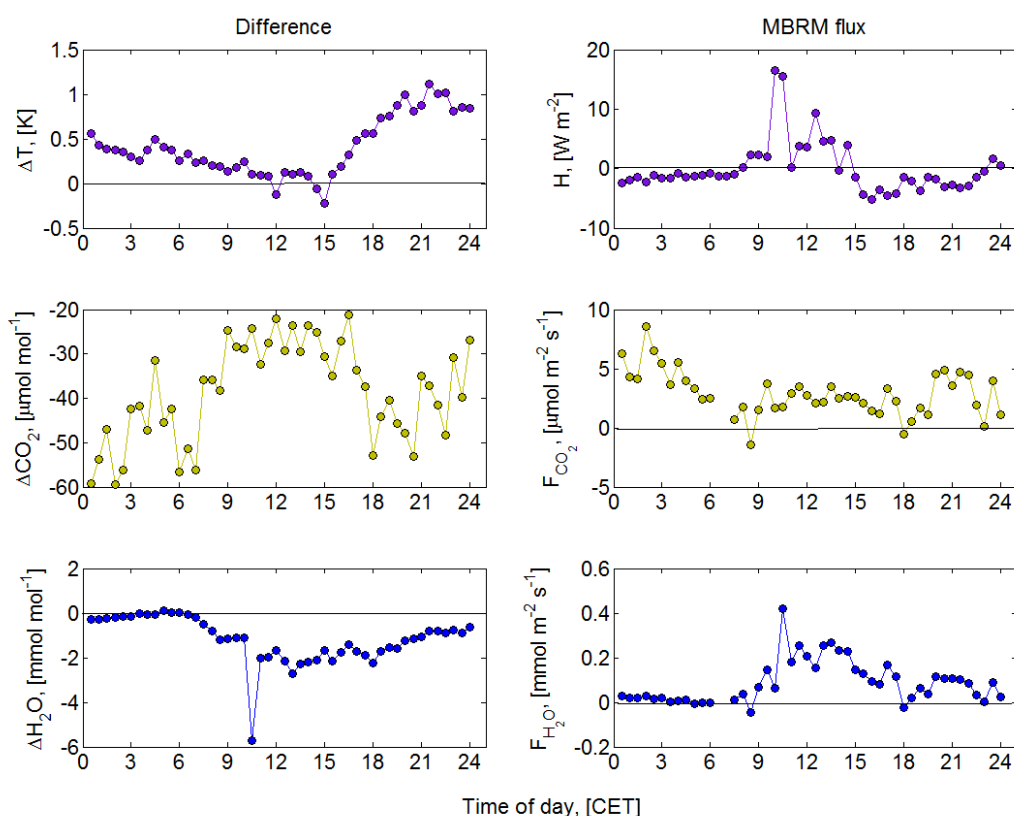


**Fig. 4.49.** Diurnal variation of  $H$ ,  $\text{CO}_2$ , and  $\text{H}_2\text{O}$  vertical concentration differences between  $0.005 \text{ m}$  and  $0.9 \text{ m}$ , and their corresponding fluxes calculated using the MBRM on the first golden day of IOP-2.

#### Reactive trace gases

The reactive trace gas fluxes are shown in Fig. 4.50. Nitrogen oxide emission fluxes were observed throughout the day. The  $\text{NO}$  flux was due to the soil biogenic activity which released  $\text{NO}$ . The  $\text{NO}$  released was of a higher concentration than the  $\text{O}_3$  could sink, hence the net emission flux. Nitrogen dioxide was being produced from the reaction between  $\text{NO}$  and  $\text{O}_3$  which was creating the  $\text{O}_3$  downward-directed fluxes. Therefore the  $\text{NO}_2$  fluxes would be expected to be positive. However, downward-directed fluxes of  $\text{NO}_2$  were observed between midnight and 0530 CET. A possible explanation for this is the reaction of the emitted  $\text{NO}_2$  with water vapour. It was explained earlier in this section that during this same time period, there was no  $\text{H}_2\text{O}$  flux, an indicator that there was a

dense fog event at this time at the forest floor and extending beyond the 1 m level. The water vapour would act as a sink for the  $\text{NO}_2$  and produce HONO and nitrates in the process. Unfortunately, no nitrate measurements were made during this campaign to confirm this. However, measurements of HONO at the forest floor confirm the validity of this explanation.

After 0800 CET, small emission fluxes of  $\text{NO}_2$  (maximum  $0.2 \text{ nmol m}^{-2} \text{ s}^{-1}$ ) were observed, with short periods of  $\text{NO}_2$  downward-directed in between. These were attributed to the reaction between  $\text{NO}$  emitted from the soil and  $\text{O}_3$  coming in from above the canopy. Ozone fluxes remained negative for the whole day, averaging  $1 \text{ nmol m}^{-2} \text{ s}^{-1}$ .

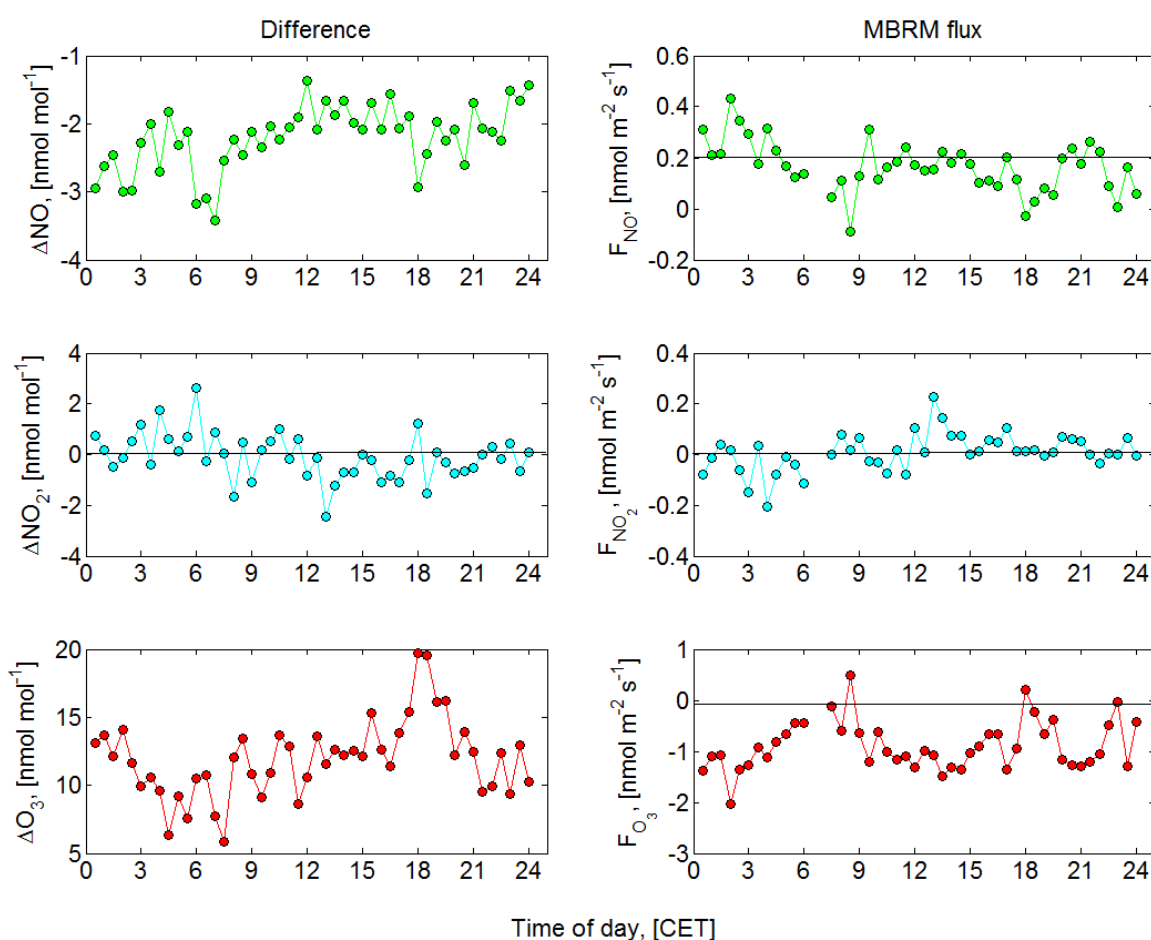


**Fig. 4.50.** Diurnal variation of  $\text{NO}$ ,  $\text{NO}_2$ , and  $\text{O}_3$  vertical concentration differences between 0.005 m and 0.9 m, and their corresponding fluxes calculated using the MBRM on the first golden day of IOP-2.

## Chapter 5: Summary and Conclusions

This chapter presents the major findings and conclusions from this experimental research. Initially the mixing ratios of the trace gases are summarised, followed by the fluxes derived from EC and their errors. Following that is a summary of the trace gas vertical differences, their precision limits and the fluxes derived from them using the gradient-based methods. Finally the influence of chemistry and forest-atmosphere coupling is summarised. Concluding remarks are made in the last section.

The main objectives of this study were to present reliable, high resolution simultaneous measurements of the mixing ratios and fluxes of the NO-O<sub>3</sub>-NO<sub>2</sub> triad above a spruce forest ecosystem using an eddy covariance system which consisted of a relatively novel NO analyser. The investigation of the source/sink relationship between the constituents of the NO-O<sub>3</sub>-NO<sub>2</sub> triad and the canopy-atmosphere was required. As a way of determining gradients and fluxes of the triad above the canopy under the influence of the roughness sublayer, the gradient-derived methods consisting of the Modified Bowen Ratio Method and the Aerodynamic Gradient Method were also applied and investigated firstly above the forest canopy and secondly below the forest canopy close to the forest floor. For the latter case, the aim was to determine reactive trace gas fluxes in the absence of eddy covariance instrumentation. Since the investigation of the NO-O<sub>3</sub>-NO<sub>2</sub> triad was the priority of this research, it was also an objective of this work to determine the timescales of the triad constituents during turbulent transport and the influence of the forest-atmosphere coupling.

To be able to evaluate fluxes of reactive trace gases in a rural forest ecosystem where levels of NO<sub>x</sub> are typically very low, a comprehensive data quality analysis was necessary to confirm the validity of the trace gas measurements as well as the performance of the analysers. This was done comprehensively for both eddy covariance measurements as well as the trace gas profile measurements. For the eddy covariance measurements, a random flux error analysis method derived from Lenschow's random flux error measurements as well as Wyngaard's turbulence time scale was used. Flux quality flags were also used for flagging the low quality data according to the method of Foken and Wichura. The eddy covariance analysers' response and suitability were checked by constructing power spectra, cospectra and ogives. Gradient-derived trace gas fluxes were quality controlled by using precision criteria which consisted of flagging data below the derived detection limit for concentration differences of the respective analyser. In addition, the influence of the roughness sublayer on the concentration differences as well as the gradient-derived fluxes above the forest canopy was investigated. Potential directional dependence of trace gas mixing ratios was investigated in view of the fact that there was a country road a kilometre away from the site which was a potential source of NO<sub>x</sub> emissions reaching the measurement site.

In order to understand and interpret the source/sink relationship between the atmosphere and the forest canopy, the forest-atmosphere coupling classes were used as well as turbulence timescales, chemical timescales of the triad and the Damköhler numbers for the triad. These were all important factors not only for interpreting the fluxes but also for determining the extent of the limitations of the flux results due to the influence of chemical inter-conversions.

### **5.1 Summary of data availability**

The evaluated data were chosen from those days (so-called ‘golden days’) when the skies were clear, with a lot of sunlight and no precipitation. The reasons for choosing such days being that (a) the trace gases NO, NO<sub>2</sub> and O<sub>3</sub> are reactive – therefore the absence of precipitation was required to ensure that there were no additional reactions with precipitation such as raindrops during the day and (b) chemical reactions of the NO-O<sub>3</sub>-NO<sub>2</sub> triad are driven by photolysis – therefore the presence of clear skies during the day to provide a continuous source of sunlight was required to make an unbiased analysis. A suitable period that fulfilled these conditions which was used for all the evaluations was 29.06 – 02.07.2008, although the total measurement period was 03.06 – 10.07.2008.

### **5.2 Summary of atmospheric conditions during the experiment**

Atmospheric conditions for the ‘golden days’ period were favourable for data analysis because they were characterized by lack of precipitation, moderate wind speeds, very low and infrequent cloud cover, and high radiation. These conditions, especially the high global radiation (and therefore high photolysis frequency) and the low cloud cover were important for the analysis of the light-dependent chemical reactions of the NO-O<sub>3</sub>-NO<sub>2</sub> triad.

IOP-2 was a summer experiment and it was dominated by cyclonic conditions, being under the influence of warmer air encircling cold air masses in the north. However, the golden days were characterised by dry summer weather conditions.

Horizontal wind speeds reported here were measured at 31 m (a.g.l) on top of the MT. This height was chosen because the meteorological standard of 11 m was within the canopy and would not give a reliable indication of the horizontal wind speed. IOP-2 was predominated by moderate wind speeds most of the day, only declining slightly in the evening. The wind speeds can be summarised as being moderate. Mean diel wind direction was in the East-Southeast to South-Southeast sector during most of the day.

Atmospheric conditions were unstable during the course of the day (indicating the development of turbulence) and slightly stable during the night. Low night-time friction velocities and neutral to stable night-time conditions were observed, which were expected to favour accumulation of those

trace gases that are normally emitted from the forest and the deposition of those trace gases that are normally deposited to the forest floor. The IOP-2 had medium-low daytime relative humidity, with values of 35% on average after midday.

The average time of sunrise was 0345 CET and sunset was 2030 CET. Median diel cycles of global radiation (Fig. 4.2) showed well defined almost bell shaped curves indicative of clear skies. These were the optimum conditions for studying photochemistry.

### **5.3 Summary of mixing ratios of the NO-O<sub>3</sub>-NO<sub>2</sub> triad**

The distribution of the mixing ratios of the NO-O<sub>3</sub>-NO<sub>2</sub> triad above the forest canopy (32 m) were analysed and the results grouped into all weekdays (Monday to Wednesday) and weekends (Sunday). The aim of such a grouping was to identify to what extent anthropogenic sources of NO<sub>x</sub> (such as cars and trucks on the country roads surrounding the measurement site) influence the mixing ratios of the reactive trace gases reaching the site because the traffic density is generally higher during the week than during weekends due to people commuting to and from work and trucks moving on the roads.

Diel variation of the NO-O<sub>3</sub>-NO<sub>2</sub> triad for all the days during IOP-2 showed a distinct pattern for all three constituents of the triad. Advected anthropogenic NO<sub>x</sub> from nearby country road traffic influenced early to mid-morning concentrations of the triad. A partitioning of the mixing ratio data into weekdays, weekends for the golden days showed that weekdays were influenced the most by the advected NO<sub>x</sub> and had their mixing ratios elevated. Sundays showed minimum influence from anthropogenic NO<sub>x</sub> presumably due to lower density traffic on the country roads. The NO and NO<sub>2</sub> mixing ratios showed higher mixing ratios when the wind was coming from sectors close to the country roads from the measurement site. This observation should be treated cautiously because the wind did not blow equally from all directions, with south-easterly winds being predominant during the weekdays and westerly winds on Sunday. Mixing ratios of O<sub>3</sub> were largely not influenced by the wind direction.

### **5.4 Summary of EC fluxes**

Eddy covariance fluxes of the reactive NO-O<sub>3</sub>-NO<sub>2</sub> triad, the non-reactive species (CO<sub>2</sub>, H<sub>2</sub>O and NO<sub>x</sub>) as well as sensible heat flux and momentum flux were all measured on the MT.

Where NO flux was present, only downward-directed fluxes were observed into the forest canopy. This was only during the high advection period, otherwise no NO fluxes were observed. On the other hand, NO<sub>2</sub> emission fluxes from the forest canopy were observed. The observed emission of NO<sub>x</sub> from the spruce forest canopy at this site contradicts measurements done on grassland and in the Amazon (Mayer et al 2010; Rummel et al., 2005, Kortner et al., 2006 (poster)). Only downward-directed fluxes of O<sub>3</sub> into the canopy were observed throughout the measurement period. The fluxes were in the same

range as those measured by Klemm and Mangold (2001) at the same site. Even at 1 m above the forest floor, downward-directed flux of O<sub>3</sub> was observed which was an order of magnitude smaller than that observed above the canopy (see also Zhu et al. (2008)).

Eddy covariance flux error analysis using the correlation coefficient method, the daily differencing method, and the simultaneous flux method showed an average modal relative error of 35%, 30%, and 33% for NO, NO<sub>2</sub>, and O<sub>3</sub> respectively. Table 5.1 shows a summary of the ranges of the EC fluxes during the golden days.

Cut-off frequencies for the fluxes were as follows: Momentum – 1.1 Hz, Sensible heat – 1.3 Hz, CO<sub>2</sub> – 0.96 Hz, H<sub>2</sub>O – 0.65 Hz, NO – 1.11 Hz, NO<sub>2</sub> – 1.17 Hz, O<sub>3</sub> – 0.79 Hz. They are indicative of high frequency damping. The fluxes of H<sub>2</sub>O, NO, and NO<sub>2</sub> suffered the most damping due to high frequency losses in the tubes during transport as well as sensor separation which were later corrected for using the Moore correction (Moore, 1986).

Flux losses were calculated from one minus the mean ratio of the sensible heat flux ogive to the ogive for each parameter at two different frequencies (0.067 Hz and 0.1 Hz). The results using mean half hourly ogives for the period 1100-1330 CET over 3 golden days were as follows: Momentum – 7.7%, CO<sub>2</sub> – 2.6%, H<sub>2</sub>O – 5.1%, NO – 2.1%, NO<sub>2</sub> – 7.5%, O<sub>3</sub> – 1.8%. At lower frequencies, the NO flux contribution lagged behind the heat flux contribution while the NO<sub>2</sub> flux contribution was always higher than the sensible heat flux contribution.

**Table 5.1.** A summary of the EC trace gas fluxes

Trace gas flux	Above canopy min	Above canopy	Below canopy	Below canopy
		max	min	max
CO <sub>2</sub> [ $\mu\text{mol m}^{-2} \text{s}^{-1}$ ]	-20	10		
H <sub>2</sub> O [ $\text{mmol m}^{-2} \text{s}^{-1}$ ]	0	7.5	-	-
NO [ $\text{nmol m}^{-2} \text{s}^{-1}$ ]	-1.75	0	-	-
NO <sub>2</sub> [ $\text{nmol m}^{-2} \text{s}^{-1}$ ]	0	2	-	-
O <sub>3</sub> [ $\text{nmol m}^{-2} \text{s}^{-1}$ ]	-25	0	0	-2.5

## 5.5 Summary of AGM and MBRM fluxes

Gradient-derived fluxes of all the species measured with EC described in 5.4 were evaluated from the measurement data on the MT above the forest canopy (32 m – 25 m) and below the forest canopy (1 m – 0.005 m). The gradient flux measurement techniques used were the AGM and the MBRM.

### 5.5.1 Above-canopy (32 m – 25 m)

Discontinuous sampling has a negative effect on trace gas flux calculations, particularly reactive trace gases to the extent that it can chance the sign of the calculated flux. This is especially noticeable in the presence of non-stationarity or photo-chemically favourable conditions whereby concentrations of substances change rapidly with time.

The presence of the roughness sublayer also changed the concentration regime at the lower level inlet level which was just at the canopy height. Since the AGM and MBRM fluxes were all mainly influenced by the vertical concentration difference, they were found to be highly comparable. The gradient-derived fluxes compared well with EC for H, CO<sub>2</sub>, H<sub>2</sub>O, and NO but not for NO<sub>2</sub> and O<sub>3</sub>. They both showed fluxes whose direction was mostly not in sync with their corresponding fluxes from EC. Additionally, their concentration differences showed distinct ramp-like structures which may be evidence of the influence of coherent structures. The duration of coherent structures occurring between the atmosphere and the forest is in the range of seconds. However the gradient measurement instruments measurements are in the range of minutes.

The precision of concentration differences was found to be an important factor in determining the validity of the results. A large percentage of gradient data for reactive trace gases did not satisfy the precision criteria, even at the 1- $\sigma$  criterion. This was particularly the case with NO<sub>2</sub>.

### 5.5.2 Below canopy (1 m – 0.005 m)

At 1 m above the ground, NO was always emitted from the ground. On the other hand, NO<sub>2</sub> downward-directed to the ground was present between 0000 CET and 0900 CET, most likely as a result of the conversion of NO<sub>2</sub> to HONO and the heterogeneous formation of HNO<sub>3</sub>. The O<sub>3</sub> fluxes were downward-directed. Table 5.1 shows a summary of the ranges of the gradient-derived trace gas fluxes during the golden days.

**Table 5.2.** *A summary of the gradient-derived trace gas fluxes*

Trace gas flux	Above canopy		Below canopy	
	min	max	min	max
CO <sub>2</sub> [ $\mu\text{mol m}^{-2} \text{s}^{-1}$ ]	-20	7.5	0	9
H <sub>2</sub> O [ $\text{mmol m}^{-2} \text{s}^{-1}$ ]	-3	5	0	0.4
NO [ $\text{nmol m}^{-2} \text{s}^{-1}$ ]	-1.75	0	0.1	0.45
NO <sub>2</sub> [ $\text{nmol m}^{-2} \text{s}^{-1}$ ]	-2	2	-0.2	0.3
O <sub>3</sub> [ $\text{nmol m}^{-2} \text{s}^{-1}$ ]	-10	10	-2.5	0

Using an algorithm developed by Meixner and Yang (2006) to derive net potential fluxes of NO as a function of the soil moisture, Falge et al. (2010) found that the magnitude of the soil NO flux from lab measurements and modelling was dependent on the understory vegetation (see Fig. 4.42). The model main input parameters were soil temperature, soil moisture, and understory cover. The soil NO flux results obtained at 0.9 m in this study are in closest agreement to those obtained by Falge et al. (2010) when the understory vegetation was moss and/or litter. The understory cover was moss/litter at the location of the inlets for the below canopy trace gas gradients. One cannot tell from which understory type the soil fluxes emerge but at 0.9 m above the soil surface, it is expected that the understory type directly below the trace gas inlets is likely to contribute the most to the flux footprint.

The averaged soil NO flux from all the understory vegetation was between 1.5 and 2.0  $\text{nmol m}^{-2} \text{s}^{-1}$ , being heavily biased by the results from the young spruce and blueberry understory types (see Fig. 4.42 a). Considering that the fluxes reported here were measured at 0.9 m above the soil surface and that they are not at optimum conditions, they are a reasonable comparison to the lab results since they are within the same order of magnitude in terms of mean diurnal values (0.1  $\text{nmol m}^{-2} \text{s}^{-1}$  using MBRM, 0.25  $\text{nmol m}^{-2} \text{s}^{-1}$  using lab/modelling for moss/litter – see Fig. 4.42b). The lab results confirmed the presence of flux divergence due to chemistry occurring faster than turbulence (hence the high Damköhler numbers at 1 m in Fig. 4.37) within the first meter above the forest floor.

## 5.6 Summary of chemical and turbulent effects on the net trace gas fluxes above the canopy

About 50% of the data from the triad showed a high likelihood of being diverted by chemical reactions occurring during turbulent transport, particularly during night time as evidenced by Damköhler numbers above 0.1. The intensity of segregation between NO and O<sub>3</sub> was very close to zero throughout the measurement period, indicating almost perfect mixing between the two

compounds. Coherent structures (see Serafimovich et al., 2009) and surface inhomogeneity close to the canopy may have contributed to the low segregation intensities.

For open systems, the Damköhler number in its current definition was found not to be a reliable indicator of the presence or absence of chemical divergence. The advection contribution must be included in the turbulence timescale definition. Strong  $O_3$  concentration above the canopy was found to decouple the above canopy NO from the below canopy NO.

The forest canopy was found to be a source of  $NO_2$ . The forest acts as a source of  $NO_2$  and a sink of NO and  $O_3$ . It was found to be difficult to quantify the amount of soil biogenic NO escaping from the canopy with the data that was available for this work. However a modelling approach using, for example, a 1-D box model might give an estimate of that, something that is recommended for future studies.

The MBR and the AGM performed well when compared to the EC standard method. Therefore they can be used to predict fluxes of reactive trace gases provided that a thorough precision analysis is done to find out the significance of the concentration differences. Care should be taken to ensure that the influence of chemistry is considered when measuring fluxes of reactive trace gases, particularly those with short chemical timescales.

During low advection conditions, fluxes of the NO- $O_3$ - $NO_2$  triad were significantly suppressed, as evidenced by the case study on Sunday the 29th of June 2008 which was a day characterised by low traffic (and therefore low trace gas) advection.

## 5.7 Conclusions

With the main objective being to find out the above canopy fluxes of the NO- $O_3$ - $NO_2$  triad above spruce forest canopy, a relatively novel, high precision chemiluminescence NO/ $NO_2$  EC measurement instrument (the CLD790 SR2) has been presented. The system used high efficiency photolytic converters for more reliable measurements of  $NO_2$ . It also used flow restrictors upstream of the sample inlets to ensure a reduced residence time such that conditions inside the 53 m long inert Teflon tubes remained as fully turbulent as possible. Rigorous quality assessment and evaluation of instrument performance and measured data proved that the system was suitable for the measurements. The results have proven that an EC system capable of measuring the full NO- $O_3$ - $NO_2$  fluxes at a sufficiently high frequency and precision can be developed as reported here.

Results from the EC measurements suggest that spruce forest ecosystems with low soil NO emissions are a net sink for NO but only in the presence of photolysis-inducing conditions and rapid  $NO_x$  advection from human-induced sources such as car exhaust plumes, otherwise there are neither upward-directed nor downward-directed detectable fluxes of NO.

Only upward-directed EC fluxes of  $\text{NO}_2$  were observed above the canopy throughout the measurement period. The main sources of the  $\text{NO}_2$  flux appeared to be the re-oxidation of photolysed NO formed from advected  $\text{NO}_2$  by  $\text{O}_3$ , and oxidation of NO to  $\text{NO}_2$  at the forest floor in the absence of light. Estimated fluxes of  $\text{NO}_2$  at the forest floor (not scaled to the whole site) were up to ten times smaller than those observed above the forest canopy. Below the forest canopy there is an unexpected sink for  $\text{NO}_2$  during night time and in the morning which may be due to the heterogeneous conversion to HONO (also observed and reported by Sörgel et al (2011) and possibly acid nitrates in the presence of fog and dew.

Damköhler numbers above the forest canopy showed that there was minimal influence of chemistry during day time turbulent transport of the reactive trace gases. This result was in contradiction to the intensity of segregation numbers which showed that NO and  $\text{O}_3$  were in a state of almost perfect homogenous mixing during the same time period.

Calculation of forest floor NO fluxes using a special case of the MBRM gave results that, when compared to those obtained using a modelling approach by Falge et al. (2010), showed divergence of all reactive trace gas fluxes due to fast chemical conversion of  $\text{NO}_x$  by  $\text{O}_3$ . Due to the large downward directed  $\text{O}_3$  flux penetrating the canopy from above, the NO from soil biogenic activity does not manage to reach the top of the canopy.

When the forest canopy is coupled to the atmosphere there is enhanced turbulence below the canopy and upward directed fluxes of  $\text{NO}_x$  are enhanced. When the forest is decoupled from the atmosphere, fluxes weaken and enhanced storage is observed.

The influence of chemistry cannot be ignored in the interpretation of the triad fluxes and has to be corrected for qualitatively and quantitatively. The presence of the roughness sublayer, coherent structures, wind shear as well as rapid chemical inter-conversions of the NO- $\text{O}_3$ - $\text{NO}_2$  triad constituents affect the stationarity above the canopy and lead to rapidly changing concentration differences which appear as spikes seen when evaluating concentration differences. This may also be the reason for the difference between the eddy covariance net flux above the canopy and the gradient derived fluxes above the canopy.

It can be concluded that the results expose the need for using fast, high precision sensors when doing eddy covariance measurements of reactive trace gases and that external sources of trace gases may play a bigger role (sometimes independent of the forest) in determining the net fluxes above the forest. More work needs to be done, particularly in determining reactive trace gas budgets of the trunk space and the top of the canopy where the situation is still unclear.

## 5.8 New contributions to science

A method of obtaining fast direct measurement of the NO-O<sub>3</sub>-NO<sub>2</sub> full triad above a spruce forest using state of the art quality control and assurance tools was demonstrated for the first time. The multi-faceted calculation of these reactive trace gas fluxes, including a comprehensive error analysis demonstrated in this study could be a useful starting point for further studies on the subject because of its consequences for model parameterisations. The reformulation and successful application of the correlation coefficient random flux method by applying Wyngaard's integral timescale formulation was demonstrated as a way of simplifying the calculation of random flux errors for EC fluxes. The use of the intensity of segregation of NO and O<sub>3</sub> in determining chemical divergence was demonstrated.

The effect of switching (discontinuous level sampling) and chemical transformations on gradients and gradient-derived fluxes of NO-O<sub>3</sub>-NO<sub>2</sub> triad has been studied for the first time in detail. The findings could find use in the design and customisation of reactive trace gas measurement sensors. The influence of coupling on stationarity and how this affects discontinuous gradient measurements was also shown for the first time.

## 5.9 Recommendations

For further research, an approach to partition above-canopy contributions of NO-O<sub>3</sub>-NO<sub>2</sub> fluxes from in-canopy contributions is highly recommended. This could include multi-level vertical EC flux measurements so that flux divergence can be detected. For this approach to work, more fast NO<sub>x</sub> and O<sub>3</sub> analysers would be needed. For the experimental site of this study, for instance, at least two additional analysers between the top of the canopy and a mast extending the tower to 40 m would have provided a lot of valuable data about the spatial dynamics of the reactive trace gas fluxes.

Although expensive, a multi-tower approach for measuring EC fluxes of the NO-O<sub>3</sub>-NO<sub>2</sub> triad simultaneously could give a lot more information about the evolution of these reactive trace gases in space and time. For instance, additional NO-O<sub>3</sub>-NO<sub>2</sub> analysers on the 36 m Turbulence Tower would have provided more data about the role of horizontal advection on the reactive trace gas fluxes.

Additionally, an in-canopy modelling procedure using a 1-D or 2-D box model might also be useful. In this approach, the in-canopy and above canopy regions would be divided into layers or boxes (layers for 1-D and boxes for 2-D). Simplified chemistry and transport would then be used to simulate what happens at in each layer from the ground right up to the top of the tower using a radioactive tracer with a suitable half-life. The data obtained would be very useful when used in conjunction with

the other methods outlined in this thesis to come up with a consolidated interpretation of the canopy-atmosphere processes of the NO-O<sub>3</sub>-NO<sub>2</sub> triad.

## References

- Amiro, B. D.: Comparison of turbulence statistics within three boreal forest canopies, *Boundary-Layer Meteorology*, 51, 99-121, 1990.
- Arya, S. P.: *Introduction to Micrometeorology*, Academic Press, San Diego, 415 pp., 2001.
- Aubinet, M., Grelle, A., Ibrom, A., Rannik, U., Moncrieff, J., Foken, T., Kowalski, A. S., Martin, P. H., Berbigier, P., Bernhofer, C., Clement, R., Elbers, J., Granier, A., Grunwald, T., Morgenstern, K., Pilegaard, K., Rebmann, C., Snijders, W., Valentini, R., and Vesala, T.: Estimates of the annual net carbon and water exchange of forests: The EUROFLUX methodology, *Advances in Ecological Research*, Vol 30, 30, 113-175, 2000.
- Aubinet, M., Clement, R., Elbers, J. A., Foken, T., Grelle, A., Ibrom, A., Moncrieff, J., Pilegaard, K., Rannik, U., and Rebmann, C.: Methodology for data acquisition, storage, and treatment, *Fluxes of Carbon, Water and Energy of European Forests*, 163, 9-35, 2003a.
- Aubinet, M., Heinesch, B., and Yernaux, M.: Horizontal and vertical CO<sub>2</sub> advection in a sloping forest, *Boundary-Layer Meteorology*, 108, 397-417, 2003b.
- Aubinet, M., Vesala, T., and Papale, D.: *Eddy Covariance: A Practical Guide to Measurement and Data Analysis*, Springer, 2012.
- Baldocchi, D.: Measuring biosphere-atmosphere exchange of biologically related gases with micrometeorological methods, *Ecology*, 69, 1331-1340, 1988.
- Beier, N., and Weber, M.: *Turbulente Austauschprozesse in der Grenzschicht - TUAREG : Schlußbericht ; Bewilligungszeitraum: 1.4.1988 bis 30.6.1991 ; Schlußbericht ; Förderprogramm Umwelt und Technologie, BMFT-Schwerpunkt Physikalisch-chemische Prozesse in der Atmosphäre, Meteorologisches Inst. der Univ., München, 1992.*
- Bergström, H., and Högström, U.: Turbulent exchange above a pine forest. II. Organized structures, *Boundary-Layer Meteorol.*, 49, 231-263, 1989.
- Berkowicz, R., and Prahm, L. P.: Evaluation of the profile method for estimation of surface fluxes of momentum and heat, *Atmos. Environ.*, 16, 2809-2819, 1982.
- Brodkey, R. S.: *Mixing Effects on Reactor Modeling and Scaleup .1. Fundamentals of Turbulent Motion, Mixing and Kinetics*, *Chem Eng Commun*, 8, 1-23, 1981.
- Brooks, I. M., and Rogers, D. P.: Aircraft Observations of Boundary Layer Rolls off the Coast of California, *J Atmos Sci*, 54, 1834-1849, 10.1175/1520-0469(1997)054<1834:aobl>2.0.co;2, 1997.
- Businger, J. A., Wyngaard, J. C., Izumi, Y., and Bradley, E. F.: Flux-profile relationships in the atmospheric surface layer, *Journal of Atmospheric Sciences*, 28, 181-189, 1971.
- Businger, J. A.: Evaluation of the accuracy with which dry deposition can be measured with current micrometeorological techniques, *J. Appl. Meteorol.*, 25, 1100-1124, 1986.
- Businger, J. A., and Oncley, S. P.: Flux measurement with conditional sampling, *Journal of Atmospheric and Oceanic Technology*, 7, 349-352, 1990.

- Businger, S., Johnson, R., and Talbot, R.: Scientific insights from four generations of Lagrangian smart balloons in atmospheric research, *Bulletin of the American Meteorological Society*, 87, 1539-+, Doi 10.1175/Bams-87-11-1539, 2006.
- Calvert, J. G., Yarwood, G., and Dunker, A. M.: An Evaluation of the Mechanism of Nitrous-Acid Formation in the Urban Atmosphere, *Res Chem Intermediat*, 20, 463-502, 1994.
- Cellier, P., and Brunet, Y.: Flux-gradient relationships above tall plant canopies, *Agricultural and Forest Meteorology*, 58, 93-117, 1992.
- Collineau, S., and Brunet, Y.: Detection of turbulent coherent motions in a forest canopy. Part I: Wavelet analysis, *Boundary-Layer Meteorol.*, 65, 357-379, 1993a.
- Collineau, S., and Brunet, Y.: Detection of turbulent coherent motions in a forest canopy. Part II: Time-scales and conditional averages, *Boundary-Layer Meteorol.*, 66, 49-73, 1993b.
- Crutzen, P. J.: Role of No and No<sub>2</sub> in the Chemistry of the Troposphere and Stratosphere, *Annu Rev Earth Pl Sc*, 7, 443-472, 1979.
- Damköhler, G.: The effect of turbulence on the combustion rate in gas compounds., *Z Elektrochem Angew P*, 46, 601-626, 1940.
- Danckwerts, P. V.: The Definition and Measurement of Some Characteristics of Mixtures, *Appl Sci Res*, 3, 279-296, 1952.
- de Arellano, J., Duynkerke, P. G., and Bultjes, P. J. H.: The Divergence of the Turbulent-Diffusion Flux in the Surface-Layer Due to Chemical-Reactions - the No-O<sub>3</sub>-No<sub>2</sub> System, *Tellus Series B-Chemical and Physical Meteorology*, 45, 23-33, 1993.
- de Arellano, J. V., and Duynkerke, P. G.: Influence of Chemistry on the Flux-Gradient Relationships for the NO-O<sub>3</sub>-NO<sub>2</sub> System, *Boundary-Layer Meteorology*, 61, 375-387, 1992.
- de Arellano, J. V. G., and Duynkerke, P. G.: 2nd-Order Closure Study of the Covariance between Chemically Reactive Species in the Surface-Layer, *Journal of Atmospheric Chemistry*, 16, 145-155, 1993.
- Delany, A. C., Fitzjarrald, D. R., Lenschow, D. H., Pearson, R., Wendel, G. J., and Woodruff, B.: Direct Measurements of Nitrogen-Oxides and Ozone Fluxes over Grassland, *Journal of Atmospheric Chemistry*, 4, 429-444, 1986.
- Denmead, D. T., and Bradley, E. F.: Flux-gradient relationships in a forest canopy, in: *The forest-atmosphere interaction*, edited by: Hutchison, B. A., and Hicks, B. B., D. Reidel Publ. Comp., Dordrecht, Boston, London, 421-442, 1985.
- Desjardins, R. L., MacPherson, J. I., Schuepp, P. H., and Karanja, F.: An evaluation of aircraft flux measurements of CO<sub>2</sub>, water vapor and sensible heat., *Boundary-Layer Meteorology*, 47, 55-69, 1989.
- Dickerson, R. R., Stedman, D. H., Chameides, W. L., Crutzen, P. J., and Fishman, J.: Actinometric Measurements and Theoretical Calculations of J(O<sub>3</sub>), the Rate of Photolysis of Ozone to O(1d), *Geophysical Research Letters*, 6, 833-836, 1979.
- Dlugi, R., Berger, M., Zelger, M., Hofzumahaus, A., Siese, M., Holland, F., Wisthaler, A., Grabmer, W., Hansel, A., Koppmann, R., Kramm, G., Mollmann-Coers, M., and Knaps, A.: Turbulent exchange and segregation of HO<sub>x</sub> radicals and volatile organic compounds above a deciduous forest, *Atmospheric Chemistry and Physics*, 10, 6215-6235, DOI 10.5194/acp-10-6215-2010, 2010.

- Eiden, R., Förster, J., Peters, K., Trautner, F., Herterich, R., and Gietl, G.: Air pollution and deposition, in: Forest decline and air pollution, edited by: Schulze, E.-D., Lange, O. L., and Oren, R., Ecological Studies, Springer Verlag, Berlin, Heidelberg, New York, 57-103, 1989.
- Enders, G., Dlugi, R., Steinbrecher, R., Clement, B., Daiber, R., Voneijk, J., Gab, S., Haziza, M., Helas, G., Herrmann, U., Kessel, M., Kesselmeier, J., Kotzias, D., Kourtidis, K., Kurth, H. H., Mcmillen, R. T., Roider, G., Schurmann, W., Teichmann, U., and Torres, L.: Biosphere Atmosphere Interactions - Integrated Research in a European Coniferous Forest Ecosystem, Atmospheric Environment Part a-General Topics, 26, 171-189, 1992.
- Falge, E., Bargsten, A., Behrendt, T., and Meixner, F. X.: Biogenic nitric oxide emission from a spruce forest soil in mountainous terrain, EGU General Assembly Conference Abstracts, May 1, 2010, 2010.
- Farmer, D. K., Wooldridge, P. J., and Cohen, R. C.: Application of thermal-dissociation laser induced fluorescence (TD-LIF) to measurement of HNO<sub>3</sub>, Sigma alkyl nitrates, Sigma peroxy nitrates, and NO<sub>2</sub> fluxes using eddy covariance, Atmospheric Chemistry and Physics, 6, 3471-3486, 2006.
- Farmer, D. K., and Cohen, R. C.: Observations of HNO<sub>3</sub>, Sigma AN, Sigma PN and NO<sub>2</sub> fluxes: evidence for rapid HO<sub>x</sub> chemistry within a pine forest canopy, Atmospheric Chemistry and Physics, 8, 3899-3917, 2008.
- Finkelstein, P. L., and Sims, P. F.: Sampling error in eddy correlation flux measurements, Journal of Geophysical Research-Atmospheres, 106, 3503-3509, 2001.
- Finnigan, J.: Turbulence in plant canopies, Annual Review of Fluid Mechanics, 32, 519-571, 2000.
- Foken, T., and Oncley, S. P.: Results of the workshop 'Instrumental and methodical problems of land surface flux measurements', Bulletin of the American Meteorological Society, 76, 1191-1193, 1995.
- Foken, T., and Wichura, B.: Tools for quality assessment of surface-based flux measurements, Agricultural and Forest Meteorology, 78, 83-105, 1996.
- Foken, T.: Genauigkeit meteorologischer Messungen zur Bestimmung des Energie- und Stoffaustausches über hohen Pflanzenbeständen, Ann. Meteorol., 37, 513-514, 1998.
- Foken, T.: Lufthygienisch-Bioklimatische Kennzeichnung des oberen Egertales, in: Bayreuther Forum Ökologie, 69+XLVIII, 2003.
- Foken, T.: Climate change in the Lehstenbach region, in: Biogeochemistry of Forested Catchments in a Changing Environment, A German Gase Study. Ecological Studies, edited by: Matzner, E., Springer, Berlin, Heidelberg, 59-66, 2004.
- Foken, T., Gockede, M., Mauder, M., Mahrt, L., Amiro, B., and Munger, W.: Post-field data quality control, Handbook of Micrometeorology: a Guide for Surface Flux Measurement and Analysis, 29, 181-208, 2004.
- Foken, T.: 50 years of the Monin-Obukhov similarity theory, Boundary-Layer Meteorology, 119, 431-447, 2006.
- Foken, T.: Micrometeorology, Springer, Berlin, Heidelberg, 308 pp., 2008.
- Foken, T., Meixner, F. X., Falge, E., Zetzsch, C., Serafimovich, A., Bargsten, A., Behrendt, T., Biermann, T., Breuninger, C., Dix, S., Gerken, T., Hunner, M., Lehmann-Pape, L., Hens, K., Jocher, G., Kesselmeier, J., Lüers, J., Mayer, J. C., Moravek, A., Plake, D., Riederer, M., Rütz, F., Scheibe,

- M., Siebicke, L., Sörgel, M., Staudt, K., Trebs, I., Tsokankunku, A., Welling, M., Wolff, V., and Zhu, Z.: Coupling processes and exchange of energy and reactive and non-reactive trace gases at a forest site – results of the EGER experiment, *Atmos. Chem. Phys.*, 12, 1923-1950, 10.5194/acp-12-1923-2012, 2012.
- Fuentes, J. D., Wang, D., Bowling, D. R., Potosnak, M., Monson, R. K., Goliff, W. S., and Stockwell, W. R.: Biogenic hydrocarbon chemistry within and above a mixed deciduous forest, *Journal of Atmospheric Chemistry*, 56, 165-185, DOI 10.1007/s10874-006-9048-4, 2007.
- Ganzeveld, L. N., Lelieveld, J., Dentener, F. J., Krol, M. C., Bouwman, A. J., and Roelofs, G. J.: Global soil-biogenic NO<sub>x</sub> emissions and the role of canopy processes, *Journal of Geophysical Research-Atmospheres*, 107, -, Artn 4298 Doi 10.1029/2001jd001289, 2002.
- Gao, W., Shaw, R. H., and PawU, K. T.: Observation of organized structure in turbulent flow within and above a forest canopy, *Boundary-Layer Meteorol.*, 47, 349-377, 1989.
- Garratt, J. R.: Flux profile relations above tall vegetation, *Quarterly Journal of the Royal Meteorological Society*, 104, 199-211, 1978.
- Garratt, J. R.: Surface influence upon vertical profiles in the atmospheric near surface layer, *Quarterly Journal of The Royal Meteorological Society*, 106, 803-819, 1980.
- Garratt, J. R.: Surface Influence Upon Vertical Profiles in the Nocturnal Boundary-Layer, *Boundary-Layer Meteorology*, 26, 69-80, 1983.
- Garratt, J. R.: *The atmospheric boundary layer*, Cambridge University Press, Cambridge, 316 pp., 1992.
- Gerstberger, P., Foken, T., and Kalbitz, K.: The Lehstenbach and Steinkreuz chatchments in NE Bavaria, Germany, in: *Biogeochemistry of Forested Catchments in a Changing Enivronment, A German Gase Study*. Ecological Studies, edited by: Matzner, E., Springer, Heidelberg, 15-41, 2004.
- Graefe, J.: Roughness layer corrections with emphasis on SVAT model applications, *Agricultural and Forest Meteorology*, 124, 237-251, 2004.
- Güsten, H., and Heinrich, G.: On-line measurements of ozone surface fluxes: Part I. Methodology and instrumentation, *Atmospheric Environment*, 30, 897-909, 1996.
- Gut, A., Scheibe, M., Rottenberger, S., Rummel, U., Welling, M., Ammann, C., Kirkman, G. A., Kuhn, U., Meixner, F. X., Kesselmeier, J., Lehmann, B. E., Schmidt, W., Muller, E., and Piedade, M. T. F.: Exchange fluxes of NO<sub>2</sub> and O<sub>3</sub> at soil and leaf surfaces in an Amazonian rain forest, *Journal of Geophysical Research-Atmospheres*, 107, -, Artn 8060 Doi 10.1029/2001jd000654, 2002a.
- Gut, A., van Dijk, S. M., Scheibe, M., Rummel, U., Welling, M., Ammann, C., Meixner, F. X., Kirkman, G. A., Andreae, M. O., and Lehmann, B. E.: NO emission from an Amazonian rain forest soil: Continuous measurements of NO flux and soil concentration, *Journal of Geophysical Research-Atmospheres*, 107, -, Artn 8057 Doi 10.1029/2001jd000521, 2002b.
- Harman, I. N., and Finnigan, J. J.: A simple unified theory for flow in the canopy and roughness sublayer, *Boundary-Layer Meteorology*, 123, 339-363, DOI 10.1007/s10546-006-9145-6, 2007.
- Harman, I. N., and Finnigan, J. J.: Scalar Concentration Profiles in the Canopy and Roughness Sublayer, *Boundary-Layer Meteorology*, 129, 323-351, DOI 10.1007/s10546-008-9328-4, 2008.

- Helmholtz, H. v.: Über discontinuirliche Flüssigkeits-Bewegungen, [Akademie der Wissenschaften zu Berlin], [Berlin], [p. [215]-228] pp., 1868.
- Hendl, M.: Globale Klimaklassifikation, in: Das Klimasystem der Erde, edited by: Hupfer, P., Akademie-Verlag, Berlin, 218-266, 1991.
- Hicks, B. B., Matt, D. R., and McMillen, R. T.: A Micrometeorological Investigation of Surface Exchange of O<sub>3</sub>, SO<sub>2</sub> and NO<sub>2</sub> - a Case-Study, *Boundary-Layer Meteorology*, 47, 321-336, 1989.
- Högström, U.: Non-dimensional wind and temperature profiles in the atmospheric surface layer: A re-evaluation, *Boundary-Layer Meteorology*, 42, 55-78, 1988.
- Holland, P. W., and Welsch, R. E.: Robust Regression Using Iteratively Re-Weighted Least-Squares, *Commun Stat a-Theor*, 6, 813-827, 1977.
- Hollinger, D. Y., Aber, J., Dail, B., Davidson, E. A., Goltz, S. M., Hughes, H., Leclerc, M. Y., Lee, J. T., Richardson, A. D., Rodrigues, C., Scott, N. A., Achuatavari, D., and Walsh, J.: Spatial and temporal variability in forest-atmosphere CO<sub>2</sub> exchange, *Global Change Biology*, 10, 1689-1706, DOI 10.1111/j.1365-2486.2004.00847.x, 2004.
- Hollinger, D. Y., and Richardson, A. D.: Uncertainty in eddy covariance measurements and its application to physiological models, *Tree Physiol*, 25, 873-885, 2005.
- Holmes, P., Lumley, J. L., and Berkooz, G.: Turbulence, coherent structures, dynamical systems and symmetry, Cambridge University Press, Cambridge, 420 pp., 1996.
- Horii, C. V., Munger, J. W., Wofsy, S. C., Zahniser, M., Nelson, D., and McManus, J. B.: Fluxes of nitrogen oxides over a temperate deciduous forest, *Journal of Geophysical Research-Atmospheres*, 109, 2004.
- Hosaynali Beygi, Z., Fischer, H., Harder, H. D., Martinez, M., Sander, R., Williams, J., Brookes, D. M., Monks, P. S., and Lelieveld, J.: Oxidation photochemistry in the Southern Atlantic boundary layer: unexpected deviations of photochemical steady state, *Atmos. Chem. Phys.*, 11, 8497-8513, 10.5194/acp-11-8497-2011, 2011.
- Hupfer, P.: Unsere Umwelt: Das Klima - Globale und lokale Aspekte, B.G. Teubner Verlagsgesellschaft, Stuttgart/ Leipzig, 335 pp., 1996.
- Hutchinson, B. A., Forest Environmental Measurements, C., Hutchison, B. A., Hicks, B. B., and Forest Environmental Measurements Conference, O. R.: The forest-atmosphere interaction, Reidel, Dordrecht ; Lancaster, xix,684p pp., 1985.
- Jenkin, M. E., Cox, R. A., and Williams, D. J.: Laboratory Studies of the Kinetics of Formation of Nitrous-Acid from the Thermal-Reaction of Nitrogen-Dioxide and Water-Vapor, *Atmospheric Environment*, 22, 487-498, 1988.
- Kaimal, J. C., and Finnigan, J. J.: Atmospheric boundary layer flows: Their structure and measurement, Oxford University Press, New York, NY, 289 pp., 1994.
- Karipot, A., Leclerc, M. Y., Zhang, G., Martin, T., Starr, G., Hollinger, D., McCaughey, J. H., and Hendrey, G. R.: Nocturnal CO<sub>2</sub> exchange over a tall forest canopy associated with intermittent low-level jet activity, *Theoretical and Applied Climatology*, 85, 243-248, 10.1007/s00704-005-0183-7, 2006.

- Karipot, A., Leclerc, M. Y., Zhang, G., Lewin, K. F., Nagy, J., Hendrey, G. R., and Starr, G.: Influence of nocturnal low-level jet on turbulence structure and CO<sub>2</sub> flux measurements over a forest canopy, *J. Geophys. Res.*, 113, D10102, 10.1029/2007jd009149, 2008.
- Karl, T., Harley, P., Emmons, L., Thornton, B., Guenther, A., Basu, C., Turnipseed, A., and Jardine, K.: Efficient Atmospheric Cleansing of Oxidized Organic Trace Gases by Vegetation, *Science*, 330, 816-819, 10.1126/science.1192534, 2010.
- Katul, G., Kuhn, G., Schieldge, J., and Hsieh, C.-I.: The ejection-sweep character of scalar fluxes in the unstable surface layer, *Boundary-Layer Meteorol.*, 83, 1-26, 1997.
- Kelvin, W. T. B.: Hydrokinetic solutions and observations, s.n., [[S.l., 16 p. pp., 1871.
- Klemm, O., and Mangold, A.: Ozone deposition at a forest site in NE Bavaria, *Water, Air and Soil Pollution: Focus*, 1, 223-232, 2001.
- Kolle, O., and Rebmann, C.: EddySoft : Dokumentation of a Software Package to Acquire and Process Eddy Covariance Data, MPI für Biogeochemie, 2007.
- Kolmogorov, A. N.: The Local-Structure of Turbulence in Incompressible Viscous-Fluid for Very Large Reynolds-Numbers, *P Roy Soc Lond a Mat*, 434, 9-13, DOI 10.1098/rspa.1991.0075, 1991.
- Kortner, M., Thielmann, A., Meixner, F.X., Göckede, M., Foken, T.: Eddy covariance flux measurements of the NO-NO<sub>2</sub>-O<sub>3</sub> triad over a mixed deciduous forest in a moderately polluted environment - quality assessment of fluxes and footprint analysis, European Geosciences Union General Assembly 2005, Vienna, 24-29.04.2005, 2005.
- Kramm, G., Müller, H., Fowler, D., Höfken, K. D., Meixner, F. X., and Schaller, E.: A modified profile method for determining the vertical fluxes of NO, NO<sub>2</sub>, Ozone, and HNO<sub>3</sub> in the atmospheric surface layer, *Journal of Atmospheric Chemistry*, 13, 265-288, 1991.
- Kramm, G., and Meixner, F. X.: On the dispersion of trace species in the atmospheric boundary layer: a re-formulation of the governing equations for the turbulent flow of the compressible atmosphere, *Tellus*, 51A, 500-522, 2000.
- Lee, X.: On micrometeorological observations of surface-air exchange over tall vegetation, *Agricultural and Forest Meteorology*, 91, 39-49, 1998.
- Leighton, P. A.: Photochemistry of Air Pollution, Academic Press, New York, 1961.
- Lenschow, D. H.: Reactive Trace Species in the Boundary-Layer from a Micrometeorological Perspective, *Journal of the Meteorological Society of Japan*, 60, 472-480, 1982.
- Lenschow, D. H., Mann, J., and Kristensen, L.: How long is long enough when measuring fluxes and other turbulence statistics?, *Journal of Atmospheric and Oceanic Technology*, 11, 661-673, 1994.
- Leuning, R.: The correct form of the Webb, Pearman and Leuning equation for eddy fluxes of trace gases in steady and non-steady state, horizontally homogeneous flows *Boundary-Layer Meteorology*, 123, 263-267, 2007.
- Liebenthal, C., and Foken, T.: On the significance of the Webb correction to fluxes, *Boundary-Layer Meteorology*, 109, 99-106, 2003.
- Liebenthal, C., and Foken, T.: On the significance of the Webb correction to fluxes, *Corrigendum, Boundary-Layer Meteorology*, 113, 301, 2004.

- Liu, H., and Foken, T.: A modified Bowen ratio method to determine sensible and latent heat fluxes, *Meteorologische Zeitschrift*, 10, 71-80, 2001.
- Lysak, P. D., Jenkins, D. M., Capone, D. E., and Brown, W. L.: Analytical model of an ultrasonic cross-correlation flow meter, part 1: Stochastic modeling of turbulence, *Flow Measurement and Instrumentation*, 19, 1-7, 10.1016/j.flowmeasinst.2007.08.004, 2008.
- Mann, J., and Lenschow, D. H.: Errors in airborne flux measurements, *Journal Geophysical Research*, 99, 1994.
- Mauder, M., and Foken, T.: Documentation and instruction manual of the eddy covariance software package TK2, *Arbeitsergebnisse, Universität Bayreuth, Abteilung Mikrometeorologie*, ISSN 1614-8916, 26, 42 pp., 2004.
- Mauder, M., and Foken, T.: Impact of post-field data processing on eddy covariance flux estimates and energy balance closure, *Meteorologische Zeitschrift*, 15, 597-609, 2006.
- Mayer, J. C., Hens, K., Rummel, U., Meixner, F. X., and Foken, T.: Moving measurement platforms - specific challenges and corrections, *Meteorologische Zeitschrift*, 18, 477-488, Doi 10.1127/0941-2948/2009/0401, 2009.
- McMillen, R. T.: An eddy correlation technique with extended applicability to non-simple terrain, *Boundary-Layer Meteorology*, 43, 231-245, 1988.
- Meixner, F. X., Andreae, M. O., van Dijk, S. M., Gut, U. A., Rummel, U. K., Scheibe, M., and Welling, M.: Biosphere-atmosphere exchange of reactive trace gases in a primary rainforest ecosystem : studies on interlinking scales., *Report Series in Aerosol Science*, 269-274, 2003.
- Meixner, F. X., and Yang, W. X.: Biogenic emissions of nitric oxide and nitrous oxide from arid and semi-arid land, edited by: D'Odorico, P., and Porporato, A., Springer Netherlands, 233-255, 2006.
- Meyers, T. P., Hall, M. E., Lindberg, S. E., and Kim, K.: Use of the modified Bowen-ratio technique to measure fluxes of trace gases, *Atmosph. Environ.*, 30, 3321-3329, 1996.
- Mölder, M., Lindroth, A., and Grelle, A.: Experimental determination of the roughness length for temperature over a field of tall grass in central Sweden, *Geogr Ann A*, 81A, 87-100, 1999.
- Monin, A. S., and Obukhov, A. M.: Osnovnye zakonomernosti turbulentnogo peremesivaniya v prizemnom sloe atmosfery (Basic laws of turbulent mixing in the atmosphere near the ground), *Trudy geofiz. inst. AN SSSR*, 24 (151), 163-187, 1954.
- Monteith, J. L., and Unsworth, M. H.: *Principles of environmental physics*, 2nd ed., Edward Arnold, London, 291 pp., 1990.
- Moore, C. J.: Frequency-Response Corrections for Eddy-Correlation Systems, *Boundary-Layer Meteorology*, 37, 17-35, 1986.
- Müller, H., Kramm, G., Meixner, F. X., Fowler, D., Dollard, G. J., and Possanzini, M.: Determination of HNO<sub>3</sub> dry deposition by modified Bowen ratio and aerodynamic profile techniques, *Tellus*, 45B, 346-367, 1993.
- Muller, J. B. A., Percival, C. J., Gallagher, M. W., Fowler, D., Coyle, M., and Nemitz, E.: Sources of uncertainty in eddy covariance ozone flux measurements made by dry chemiluminescence fast response analysers, *Atmos Meas Tech*, 3, 163-176, 2010.

- Munger, J. W., Wofsy, S. C., Bakwin, P. S., Fan, S. M., Goulden, M. L., Daube, B. C., Goldstein, A. H., Moore, K. E., and Fitzjarrald, D. R.: Atmospheric deposition of reactive nitrogen oxides and ozone in a temperate deciduous forest and a subarctic woodland .1. Measurements and mechanisms, *Journal of Geophysical Research-Atmospheres*, 101, 12639-12657, 1996.
- Munger, J. W., Fan, S. M., Bakwin, P. S., Goulden, M. L., Goldstein, A. H., Colman, A. S., and Wofsy, S. C.: Regional budgets for nitrogen oxides from continental sources: Variations of rates for oxidation and deposition with season and distance from source regions, *Journal of Geophysical Research-Atmospheres*, 103, 8355-8368, 1998.
- Obukhov, A. M.: Turbulence in an atmosphere with a non-uniform temperature, *Boundary-Layer Meteorology*, 2, 7-29, 1971.
- Oke, T. R.: *Boundary layer climates*, 2nd ed., Methuen, New York, 435 pp., 1987.
- Oncley, S. P.: Flux parameterization techniques in the atmospheric surface layer, Dissertation at the University of California, Irvine CA, 202 pp., 1989.
- Oncley, S. P., Businger, J. A., Itsweire, E. C., Friehe, C. A., LaRue, J. C., and Chang, S. S.: Surface layer profiles and turbulence measurements over uniform land under near-neutral conditions, 9th Symposium on Boundary Layer and Turbulence, Roskilde, Denmark, 1990, 237-240.
- Padro, J.: Seasonal Contrasts in Modeled and Observed Dry Deposition Velocities of O<sub>3</sub>, SO<sub>2</sub> and NO<sub>2</sub> over 3 Surfaces, *Atmospheric Environment Part a-General Topics*, 27, 807-814, 1993.
- Plake, D.: Vertikale Konzentrationsprofile und Flüsse von reaktiven und nicht reaktiven Spurengasen im Fichtelgebirge, Dip. Landschaftsökologie, Westfälische Wilhelms-Universität Münster, Münster, 144 pp., 2009.
- Pryor, S. C., Larsen, S. E., Sorensen, L. L., Barthelmie, R. J., Gronholm, T., Kulmala, M., Launiainen, S., Rannik, U., and Vesala, T.: Particle fluxes over forests: Analyses of flux methods and functional dependencies, *Journal of Geophysical Research-Atmospheres*, 112, -, Artn D07205 Doi 10.1029/2006jd008066, 2007.
- Rannik, U., Markkanen, T., Raittila, T., Hari, P., and Vesala, T.: Turbulence statistics inside and above forest: Influence on footprint prediction, *Boundary-Layer Meteorology*, 109, 163-189, 2003.
- Raupach, M. R., and Thom, A. S.: Turbulence in and above plant canopies, *Annual Review of Fluid Mechanics*, 13, 97-129, 1981.
- Raupach, M. R., Finnigan, J. J., and Brunet, Y.: Coherent eddies and turbulence in vegetation canopies: the mixing-layer analogy, *Boundary-Layer Meteorology*, 78, 351-382, 1996.
- Richardson, A. D., Hollinger, D. Y., Burba, G. G., Davis, K. J., Flanagan, L. B., Katul, G. G., Munger, J. W., Ricciuto, D. M., Stoy, P. C., Suyker, A. E., Verma, S. B., and Wofsy, S. C.: A multi-site analysis of random error in tower-based measurements of carbon and energy fluxes, *Agricultural and Forest Meteorology*, 136, 1-18, 2006.
- Rummel, U., Ammann, C., Gut, A., Meixner, F. X., and Andreae, M. O.: Eddy covariance measurements of nitric oxide flux within an Amazonian rainforest, *Journal Geophysical Research*, 107 (D20), 8050, 2002a.
- Rummel, U., Ammann, C., Gut, A., Meixner, F. X., and Andreae, M. O.: Eddy covariance measurements of nitric oxide flux within an Amazonian rain forest, *Journal of Geophysical Research-Atmospheres*, 107, -, Artn 8050 Doi 10.1029/2001jd000520, 2002b.

- Rummel, U., Ammann, C., and Meixner, F. X.: Characterizing turbulent trace gas exchange above a dense tropical rain forest using wavelet and surface renewal analysis, 15th Symposium on Boundary Layer and Turbulence, Wageningen, NL, 2002c, 602-605.
- Rummel, U., Ammann, C., Kirkman, G. A., Moura, M. A. L., Foken, T., Andreae, M. O., and Meixner, F. X.: Seasonal variation of ozone deposition to a tropical rain forest in southwest Amazonia, *Atmospheric Chemistry and Physics*, 7, 5415-5435, 2007.
- Schotanus, P., Nieuwstadt, F. T. M., and DeBruin, H. A. R.: Temperature measurement with a sonic anemometer and its application to heat and moisture fluctuations, *Boundary-Layer Meteorology*, 26, 81-93, 1983.
- Schulz, E. W., and Sanderson, B. G.: Stationarity of Turbulence in Light Winds during the Maritime Continent Thunderstorm Experiment, *Boundary-Layer Meteorology*, 111, 523-541, 10.1023/B:BOUN.0000016546.42602.0a, 2004.
- Seifert, W.: Klimaänderung und (Winter-) Tourismus im Fichtelgebirge - Auswirkungen, Wahrnehmung und Ansatzpunkte zukünftiger touristischer Entwicklung, Fakultät für Biologie, Chemie und Geowissenschaften, Universität Bayreuth, Bayreuth, 206 + XL pp., 2004.
- Seinfeld, J. H., and Pandis, S. N.: *Atmospheric chemistry and physics*, Wiley, New York, 1326 pp., 1998.
- Serafimovich, A., Thomas, C., and Foken, T.: Vertical and horizontal transport of energy and matter by coherent motions in a tall spruce canopy., *Boundary Layer Meteorology*, submitted., 2010.
- Serafimovich, A., Siebicke, L., Staudt, K., Lüers, J., Biermann, T., Schier, S., and Foken, T.: ExchanGE processes in mountainous Regions (EGER)- Documentation of the Intensive Observation Period (IOP1) September, 6th to October, 7th 2007, Universitätsbibliothek Bayreuth, Bayreuth, 2011a.
- Serafimovich, A., Siebicke, L., Staudt, K., Lüers, J., Hunner, M., Gerken, T., Schier, S., Biermann, T., Rütz, F., and Buttlar, J.: ExchanGE processes in mountainous Regions (EGER) Documentation of the Intensive Observation Period (IOP2) June, 1st to July, 15th 2008, Universitätsbibliothek Bayreuth, Bayreuth, 2011b.
- Sharan, M., Krishna, T. V. B. P. S. R., and Aditi: On the bulk Richardson number and flux-profile relations in an atmospheric surface layer under weak wind stable conditions, *Atmospheric Environment*, 37, 3681-3691, Doi 10.1016/S1352-2310(03)00409-6, 2003.
- Sörgel, M., Trebs, I., Serafimovich, A., Moravek, A., Held, A., and Zetzsch, C.: Simultaneous HONO measurements in and above a forest canopy: influence of turbulent exchange on mixing ratio differences, *Atmos. Chem. Phys.*, 11, 841-855, 10.5194/acp-11-841-2011, 2011.
- Spirig, C., Neftel, A., Ammann, C., Dommen, J., Grabmer, W., Thielmann, A., Schaub, A., Beauchamp, J., Wisthaler, A., and Hansel, A.: Eddy covariance flux measurements of biogenic VOCs during ECHO 2003 using proton transfer reaction mass spectrometry, *Atmospheric Chemistry and Physics*, 5, 465-481, 2005.
- Staudt, K., and Foken, T.: Documentation of reference data for the experimental areas of the Bayreuth Centre for Ecology and Environmental Research (BayCEER) at the Waldstein site, *Arbeitsergebnisse*, Universität Bayreuth, Abteilung Mikrometeorologie, ISSN 1614-8916, 35, 35, 2007.

- Stedman, D. H., Stuhl, F., Daby, E. E., and Niki, H.: Analysis of Ozone and Nitric-Oxide by a Chemiluminescent Method in Laboratory and Atmospheric Studies of Photochemical Smog, *Japca J Air Waste Ma*, 22, 260-&, 1972.
- Stella, P., Kortner, M., Ammann, C., Foken, T., Meixner, F. X., and Trebs, I.: Measurements of nitrogen oxides and ozone fluxes by eddy covariance at a meadow: evidence for an internal leaf resistance to NO<sub>2</sub>, *Biogeosciences Discuss.*, 10, 4461-4514, 10.5194/bgd-10-4461-2013, 2013.
- Street, J. O., Carroll, R. J., and Ruppert, D.: A Note on Computing Robust Regression Estimates Via Iteratively Reweighted Least-Squares, *Am Stat*, 42, 152-154, 1988.
- Stull, R. B.: *An Introduction to Boundary Layer Meteorology*, Kluwer Acad. Publ., Dordrecht, Boston, London, 666 pp., 1988.
- Thomas, C., and Foken, T.: Flux contribution of coherent structures and its implications for the exchange of energy and matter in a tall spruce canopy, *Boundary-Layer Meteorology*, 123, 317-337, 2007.
- Tillman, J. E.: The indirect determination of stability, heat and momentum fluxes in the atmospheric boundary layer from simple scalar variables during dry unstable conditions, *Journal of Climate and Applied Meteorology*, 11, 783-792, 1972.
- Trebs, I., Meixner, F. X., Slanina, J., Otjes, R., Jongejan, P., and Andreae, M. O.: Real-time measurements of ammonia, acidic trace gases and water-soluble inorganic aerosol species at a rural site in the Amazon Basin, *Atmos. Chem. Phys.*, 4, 967-987, 10.5194/acp-4-967-2004, 2004.
- Trebs, I., Bohn, B., Ammann, C., Rummel, U., Blumthaler, M., Königstedt, R., Meixner, F. X., Fan, S., and Andreae, M. O.: Relationship between the NO<sub>2</sub> photolysis frequency and the solar global irradiance, *Atmos Meas Tech*, 2, 725-739, 2009.
- Venkatram, A., Karamchandani, P. K., and Misra, P. K.: Testing a Comprehensive Acid Deposition Model, *Atmospheric Environment*, 22, 737-747, 1988.
- Vesala, T., Kljun, N., Rannik, U., Rinne, J., Sogachev, A., Markkanen, T., Sabelfeld, K., Foken, T., and Leclerc, M. Y.: Flux and concentration footprint modelling: State of the art, *Environmental Pollution*, 152, 653-666, 2008.
- Vickers, D., and Mahrt, L.: Quality control and flux sampling problems for tower and aircraft data, *Journal of Atmospheric and Oceanic Technology*, 14, 512-526, 1997.
- Webb, E. K., Pearman, G. I., and Leuning, R.: Correction of the flux measurements for density effects due to heat and water vapour transfer, *Quarterly Journal of the Royal Meteorological Society*, 106, 85-100, 1980.
- Wesely, M. L., Eastman, J. A., Stedman, D. H., and Yalvac, E. D.: An Eddy-Correlation Measurement of NO<sub>2</sub> Flux to Vegetation and Comparison to O<sub>3</sub> Flux, *Atmospheric Environment*, 16, 815-820, 1982.
- Wichura, B., Ruppert, J., Delany, A. C., Buchmann, N., and Foken, T.: Structure of carbon dioxide exchange processes above a spruce Forest, in: *Biogeochemistry of Forested Catchments in a Changing Environment, A German Gase Study*. Ecological Studies, edited by: Matzner, E., Ecological Studies, Springer, Berlin, Heidelberg, 161-176, 2004.
- Wilczak, J. M., Oncley, S. P., and Stage, S. A.: Sonic anemometer tilt correction algorithms, *Boundary-Layer Meteorology*, 99, 127-150, 2001.

- Wildt, J., Kley, D., Rockel, A., Rockel, P., and Segschneider, H. J.: Emission of NO from several higher plant species, *Journal of Geophysical Research-Atmospheres*, 102, 5919-5927, 1997.
- Wolfe, G. M., Thornton, J. A., Bouvier-Brown, N. C., Goldstein, A. H., Park, J. H., McKay, M., Matross, D. M., Mao, J., Brune, W. H., LaFranchi, B. W., Browne, E. C., Min, K. E., Wooldridge, P. J., Cohen, R. C., Crouse, J. D., Faloon, I. C., Gilman, J. B., Kuster, W. C., de Gouw, J. A., Huisman, A., and Keutsch, F. N.: The Chemistry of Atmosphere-Forest Exchange (CAFE) Model – Part 2: Application to BEARPEX-2007 observations, *Atmos. Chem. Phys.*, 11, 1269-1294, 10.5194/acp-11-1269-2011, 2011a.
- Wolfe, G. M., Thornton, J. A., McKay, M., and Goldstein, A. H.: Forest-atmosphere exchange of ozone: sensitivity to very reactive biogenic VOC emissions and implications for in-canopy photochemistry, *Atmos. Chem. Phys.*, 11, 7875-7891, 10.5194/acp-11-7875-2011, 2011b.
- Wolff, V., Trebs, I., Ammann, C., and Meixner, F. X.: Aerodynamic gradient measurements of the NH<sub>3</sub>-HNO<sub>3</sub>-NH<sub>4</sub>NO<sub>3</sub> triad using a wet chemical instrument: an analysis of precision requirements and flux errors, *Atmos Meas Tech*, 3, 187-208, 2010.
- Wyngaard, J. C., Cote, O. R., and Rao, K. S.: Numerical Studies of Convective Planetary Boundary-Layer, *B Am Phys Soc*, 18, 1488-1488, 1973.
- Wyngaard, J. C., Businger, J. A., Kaimal, J. C., and Larsen, S. E.: Comments on 'A reevaluation of the Kansas mast influence on measurements of stress and cup anemometer overspeeding', *Boundary-Layer Meteorology*, 22, 245-250, 1982.
- Zhu, Z., Tsokankunku, A., Andreae, M. O., Foken, T., and Meixner, F. X.: Use of spectral analysis method to evaluate the precision of different fast response ozone sonde and the effect on ozone fluxes., *EGU General Assembly 2009, Vienna*, 2009.

# Appendices

## A1: Roughness sublayer enhancement factors

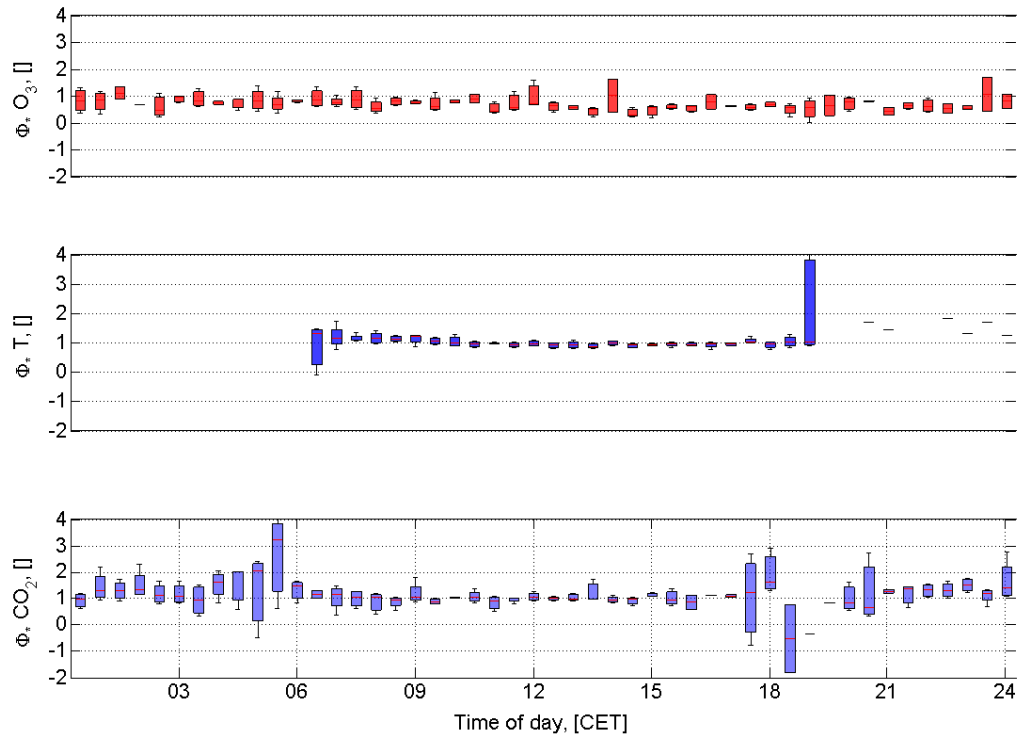


**Fig. A1.1.** Enhancement factors for  $O_3$  flux, sensible heat flux, and  $CO_2$  flux over the golden days of IOP-2.

## A2: Segregation intensities

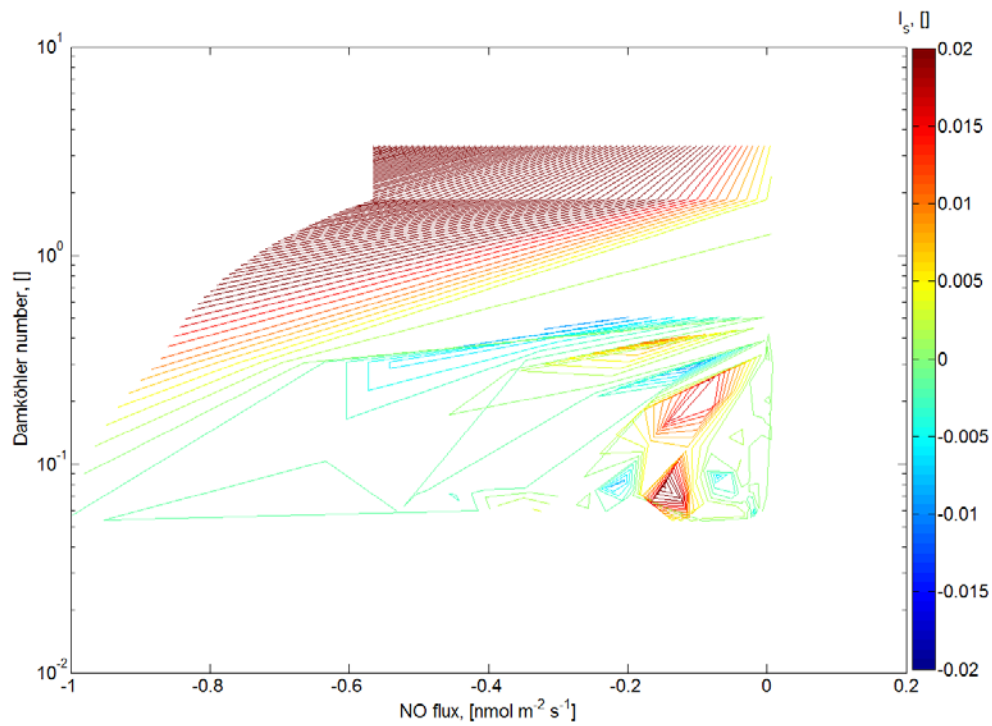


**Fig. A2.1.** Contour plot showing the dependence of the intensity of segregation on the Damköhler number and the NO flux.

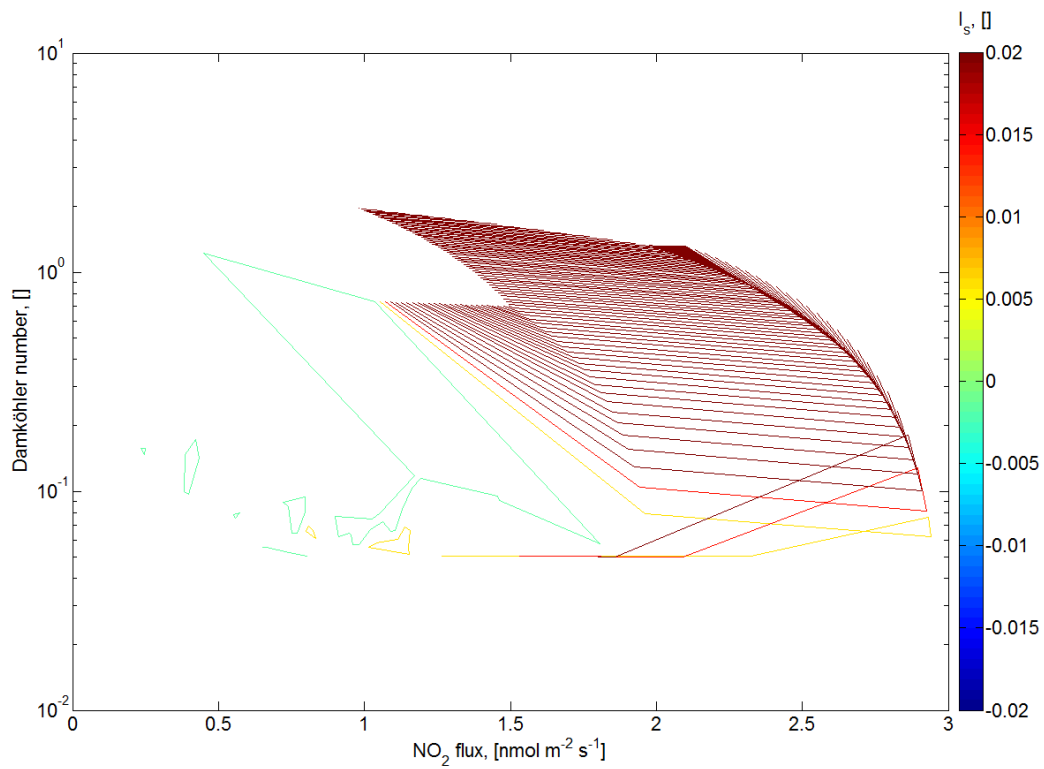


**Fig. A2.2.** Contour plot showing the dependence of the intensity of segregation on the Damköhler number and the  $\text{NO}_2$  flux.

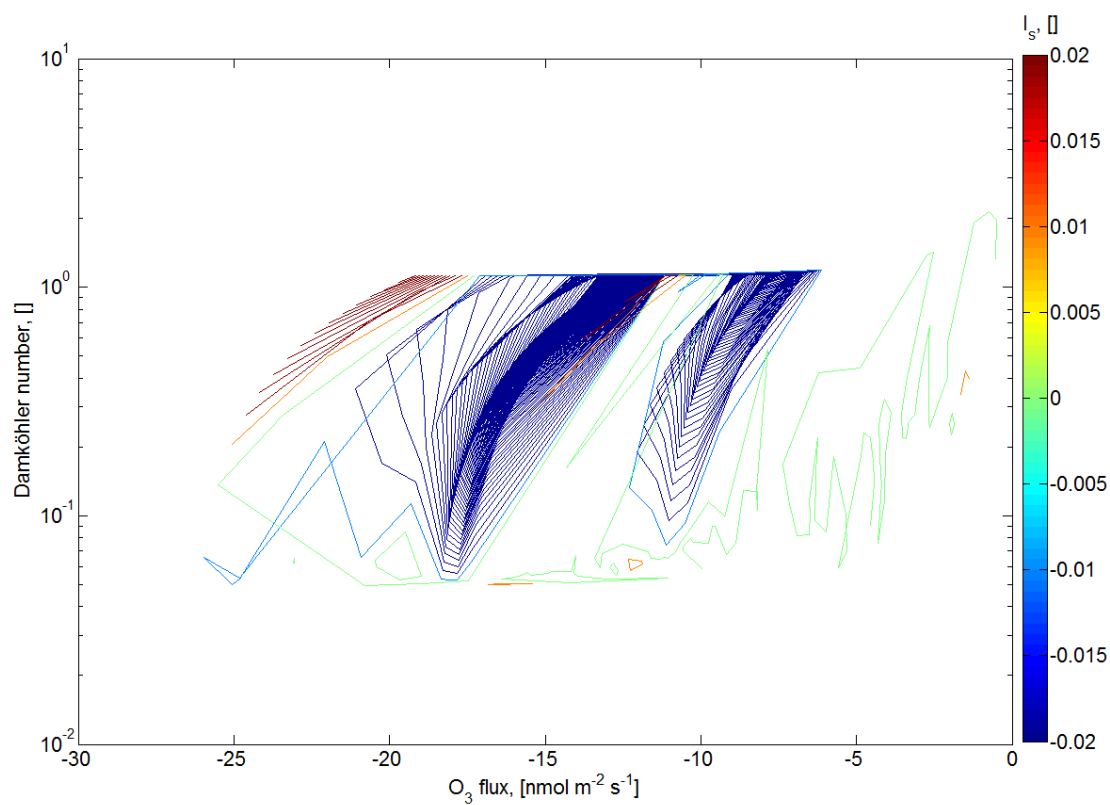


**Fig. A2.3.** Contour plot showing the dependence of the intensity of segregation on the Damköhler number and the  $O_3$  flux.

### A3: Mixing ratio profiles

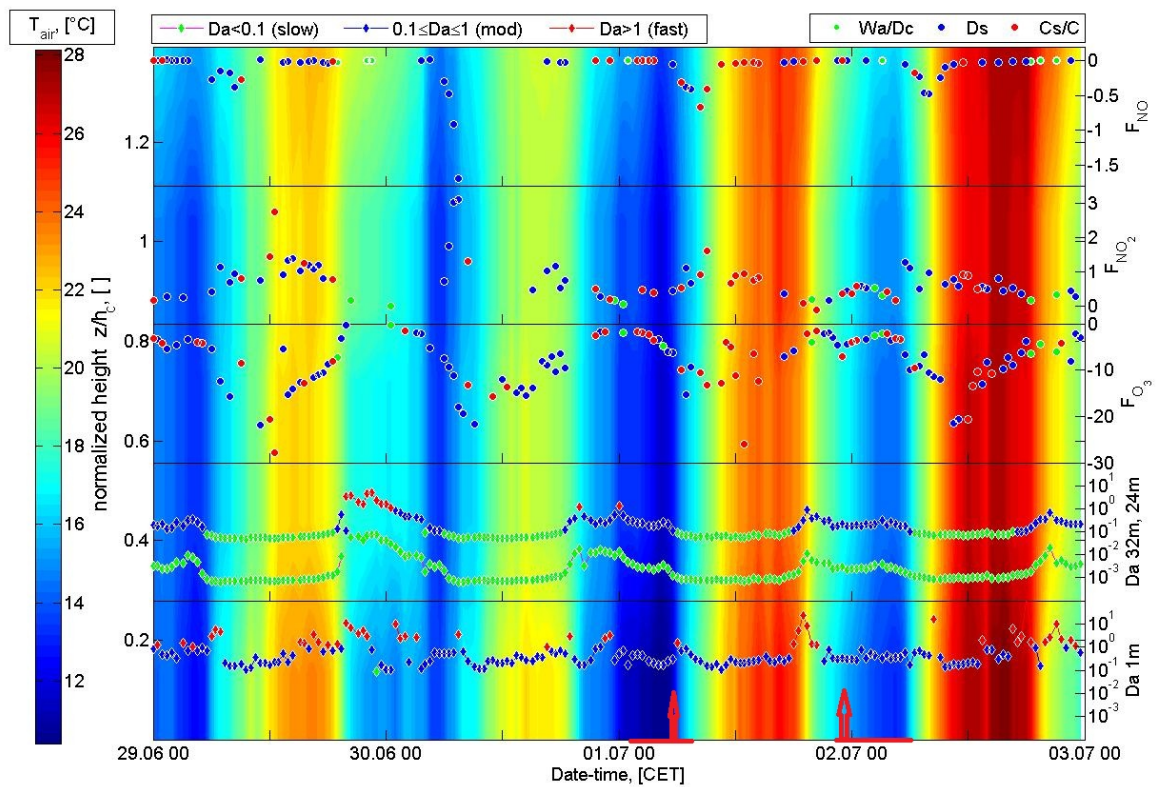


**Fig. A3.1.** Diurnal variation of the reactive trace gas fluxes from top:  $\text{NO}$ ,  $\text{NO}_2$  and  $\text{O}_3$  and the Damköhler numbers at 32 m and 24 m, and at 1 m. The data is overlaid on the contour plot of the temperature profile from the forest floor to the top of the MT. The red lines on the x-axes correspond to the duration of LLJ events and the red vertical arrows on them show the point of maximum velocity of each LLJ.

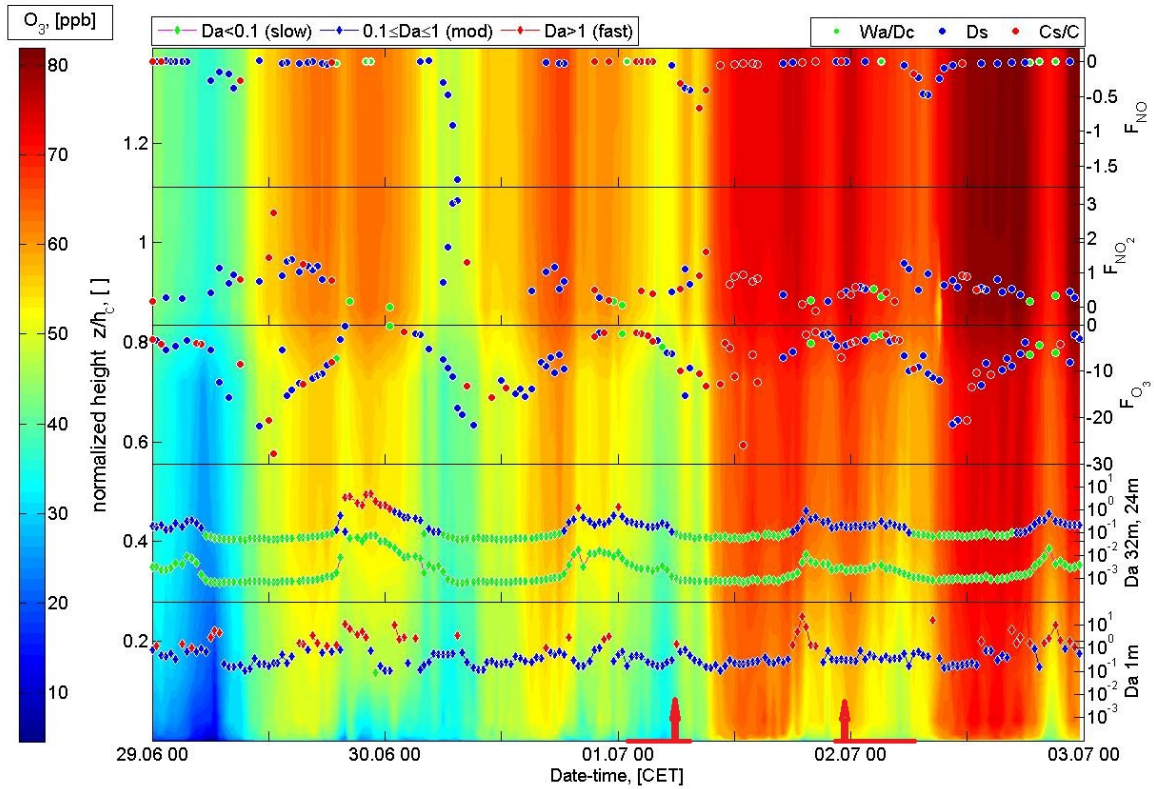


**Fig. A3.2.** Diurnal variation of the reactive trace gas fluxes from top: NO, NO<sub>2</sub> and O<sub>3</sub> and the Damköhler numbers at 32 m and 24 m, and at 1 m. The data is overlaid on the contour plot of the O<sub>3</sub> profile from the forest floor to the top of the MT. The red lines on the x-axes correspond to the duration of LLJ events and the red vertical arrows on them show the point of maximum velocity of each LLJ.

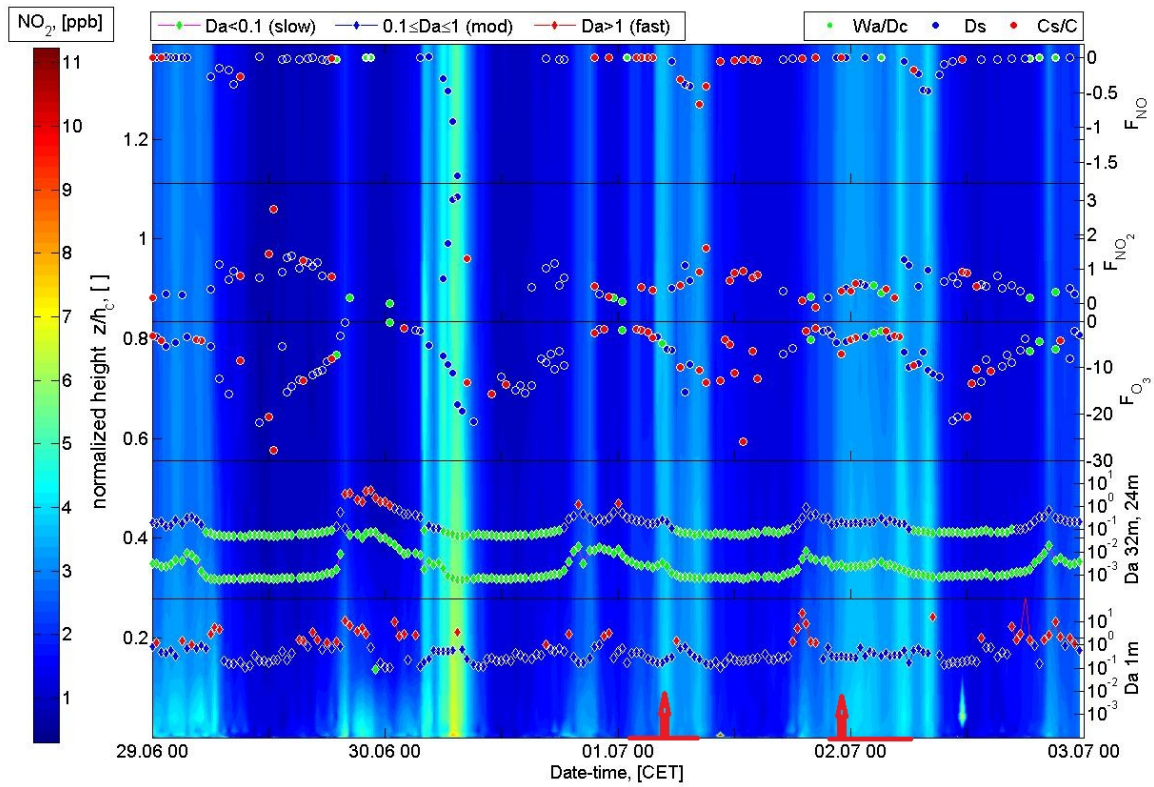


**Fig. A3.3.** Diurnal variation of the reactive trace gas fluxes from top:  $\text{NO}$ ,  $\text{NO}_2$  and  $\text{O}_3$  and the Damköhler numbers at 32 m and 24 m, and at 1 m. The data is overlaid on the contour plot of the  $\text{NO}_2$  profile from the forest floor to the top of the MT. The red lines on the x-axes correspond to the duration of LLJ events and the red vertical arrows on them show the point of maximum velocity of each LLJ.

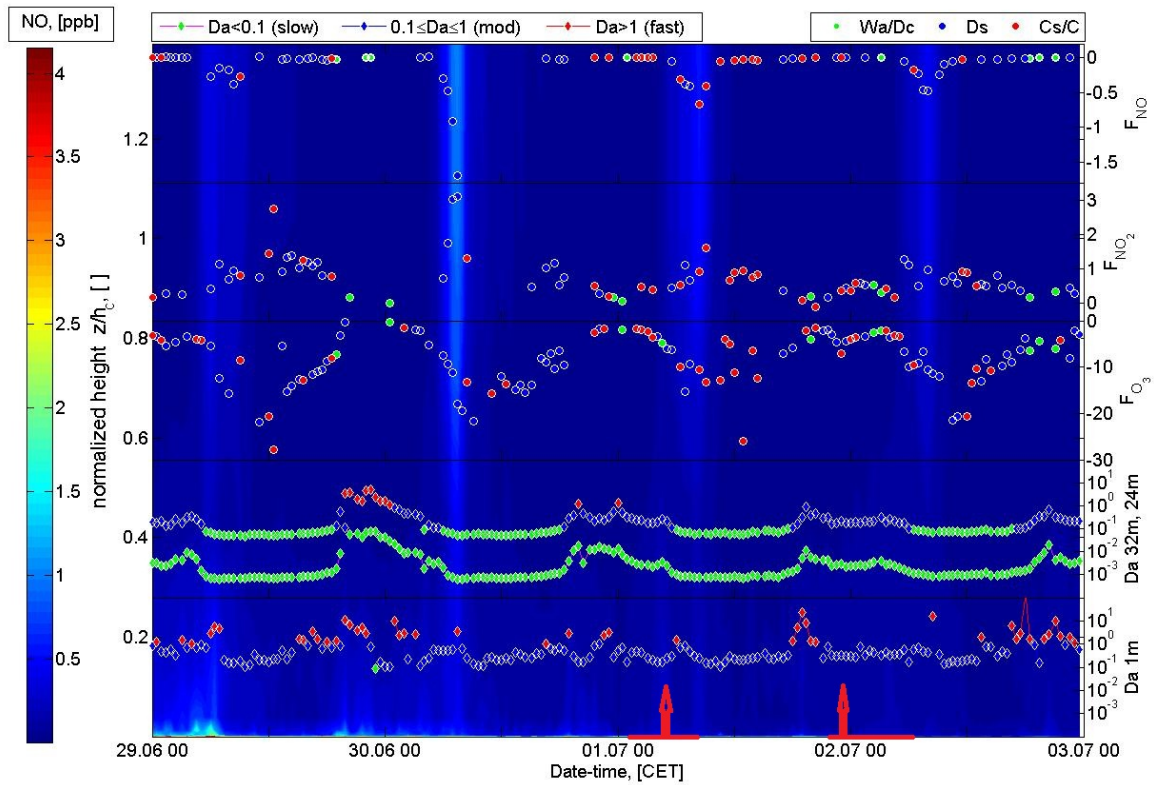


**Fig. A3.4.** Diurnal variation of the reactive trace gas fluxes from top:  $\text{NO}$ ,  $\text{NO}_2$  and  $\text{O}_3$  and the Damköhler numbers at 32 m and 24 m, and at 1 m. The data is overlaid on the contour plot of the  $\text{NO}$  profile from the forest floor to the top of the MT. The red lines on the x-axes correspond to the duration of LLJ events and the red vertical arrows on them show the point of maximum velocity of each LLJ.

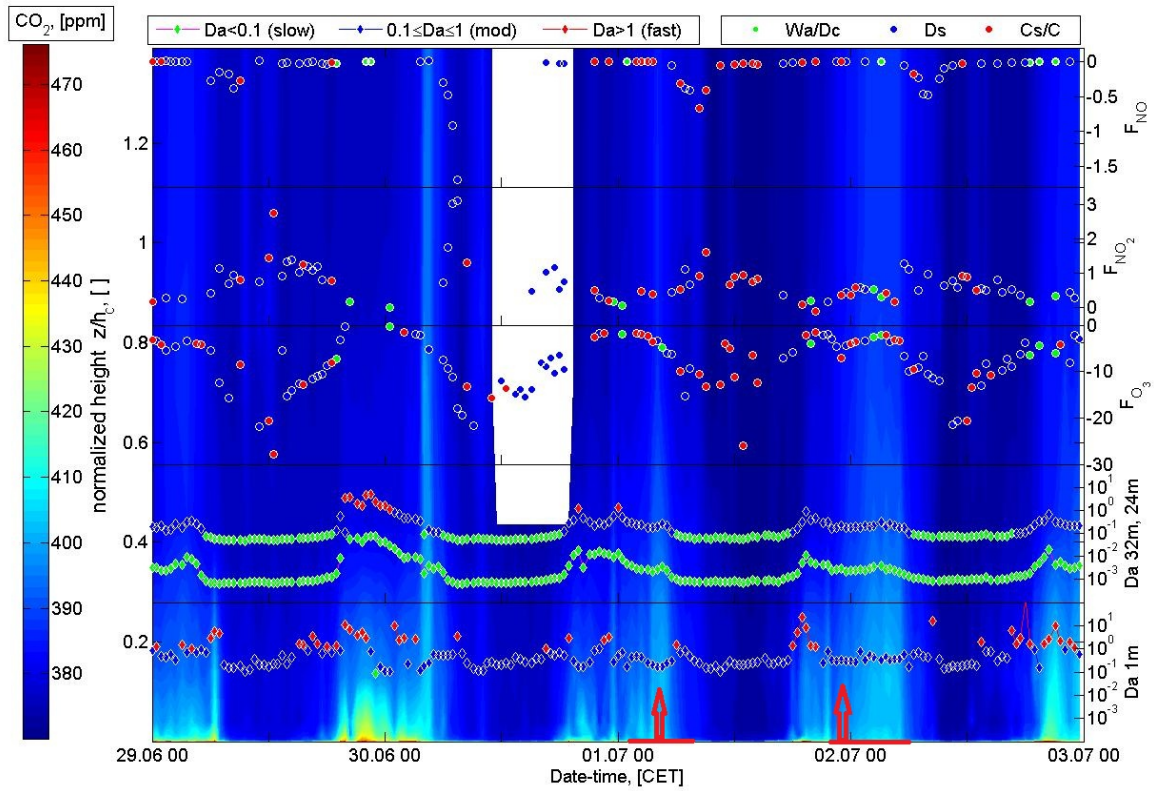


**Fig. A3.5.** Diurnal variation of the reactive trace gas fluxes from top:  $\text{NO}$ ,  $\text{NO}_2$  and  $\text{O}_3$  and the Damköhler numbers at 32 m and 24 m, and at 1 m. The data is overlaid on the contour plot of the  $\text{CO}_2$  profile from the forest floor to the top of the MT. The red lines on the x-axes correspond to the duration of LLJ events and the red vertical arrows on them show the point of maximum velocity of each LLJ.

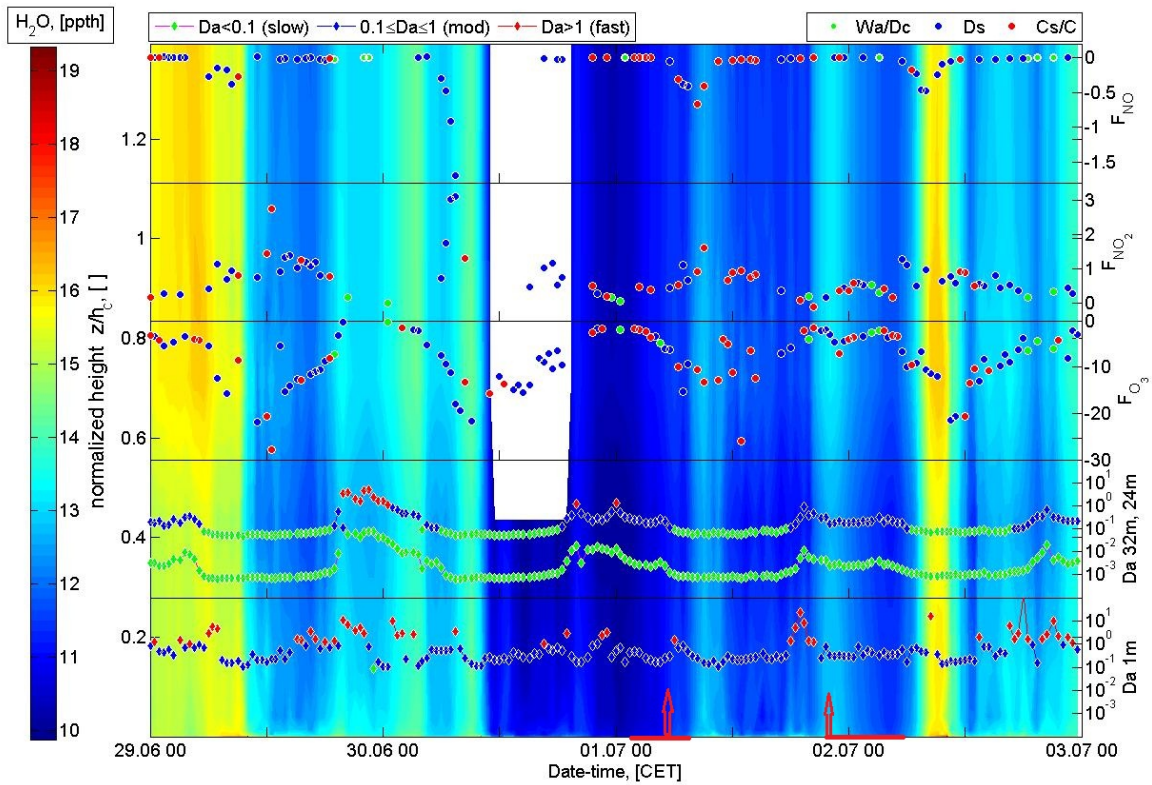


**Fig. A3.6.** Diurnal variation of the reactive trace gas fluxes from top:  $\text{NO}$ ,  $\text{NO}_2$  and  $\text{O}_3$  and the Damköhler numbers at 32 m and 24 m, and at 1 m. The data is overlaid on the contour plot of the  $\text{H}_2\text{O}$  profile from the forest floor to the top of the MT. The red lines on the x-axes correspond to the duration of LLJ events and the red vertical arrows on them show the point of maximum velocity of each LLJ.

## Table of abbreviations

### Abbreviations

$\text{NO}_c$  – sum total of nitrogen oxide and nitrogen oxide produced from photolysis of nitrogen dioxide

$\text{NO}_{BA}$  – nitrogen oxide of channel B calculated from correlation with channel A nitrogen oxide

$\mu\text{mol}$  - micromole

ABL – Atmospheric Boundary Layer

AGM – Aerodynamic Gradient Method

C - The atmosphere, the canopy and the subcanopy are in a fully coupled state.

CBL – convective boundary layer

CL – Canopy layer

$\text{CO}_2$  – carbon dioxide

Cs – coupling state characterised by the exchange between the above-canopy air and the subcanopy being forced by the strong sweep motion of coherent structures only.

D – molecular diffusion coefficient

Da – Damköhler number

Dc – coupling state characterised by the air above the canopy being decoupled from the canopy and subcanopy.

Ds – coupling state characterised by the atmosphere being coupled with the canopy, but decoupled from the subcanopy. The region of coherent exchange is limited to the canopy.

EC – eddy covariance

EZ – entrainment zone

FA – Free atmosphere

$\text{H}_2\text{O}$  - water

$\text{HNO}_3$  – Nitric acid

HONO – nitrous acid

IOP – Intensive Observation Period

Is – Intensity of segregation

ISL – Inertial Sublayer

ITC – Integral Turbulence Characteristic

LLJ – Low Level Jet

LOD – Limit of Detection

MBRM – Modified Bowen Ratio Method

ML – Mixing Layer

mmol - millimole

MOST – Monin-Obukhov Similarity Theory

MPI1– Max Planck Institute 1 m platform

MPI24 – Max Planck Institute 24 m platform

MPI32 – Max Planck Institute 32 m platform

MT – Main Tower

NBL – nocturnal boundary layer

nmol - nanomole

NO – nitrogen oxide

NO<sub>2</sub> – nitrogen dioxide

NO<sub>x</sub>-nitrogen oxides (NO + NO<sub>2</sub>)

O· – oxygen radical

O<sub>2</sub> – oxygen

O<sub>3</sub>-ozone

PAN-peroxyacetylnitrate

PMT – photomultiplier

ppm – parts per million

ppt – parts per trillion

Q – chemical source

RETGAP – reactive trace gas profile

RL – residual layer

RSL – roughness sublayer

S – chemical sink

SBL – stable boundary layer

TT – turbulence tower

UBT – University of Bayreuth

UBT23 – University of Bayreuth 23 m measurement platform

UBT32 – University of Bayreuth 32 m measurement platform

UBT36 – University of Bayreuth 23 m measurement platform

VOC – volatile organic compound

Wa – coupling state due to wave motion

*CE* – conversion efficiency

*FFT* - fast Fourier transform

*Ls*- sample length

## **Roman Symbols**

a, b, c – planar fit coefficients

$B_1$  – constant for determination of  $j\text{NO}_2$  according to the method of Trebs

$B_2$  – constant for the determination of  $j\text{NO}_2$  according to Trebs

$c_p$	specific heat capacity at constant pressure
$d$	displacement height
$f$	frequency
$f_0$	initial frequency
$f_{NO}$	counts per second per ppm for NO
$F, F_1, F_2$	flux
$g$	acceleration due to gravity
$G$	global radiation
$h$	Planck constant
$h_c$	canopy height
$I_s$	intensity of segregation
$P_0$	air pressure of 1000 mBar
$P$	air pressure
$z$	height
$H$	sensible heat flux
$LE$	latent heat flux
$L$	Obukhov length
$m$	ratio of an upper level to a lower level
$T$	temperature
$T_d$	dew-point temperature
$u$	horizontal wind speed
$\Delta u$	difference in horizontal wind speed between 2 levels
$u_*$	friction velocity
$u_{p*}$	friction velocity derived from the profile method

## Table of abbreviations

---

$v$  – horizontal velocity perpendicular to  $u$

$w$  – vertical wind velocity

$w'$  – fluctuation in vertical wind velocity

$J_{NO_2}$  – photolysis frequency of  $NO_2$

$k_1$  – rate constant for a first order reaction

$z$  – vertical height above ground

$z_m$  – mean vertical height

$\Delta z$  – difference in mean height between 2 levels

$z_*$  – height of the roughness sublayer

$R_L$  – universal gas constant

$Ri$  – Richardson number

$Ri_c$  – critical Richardson number

$Pr_t$  – turbulent Prandtl number

$F_M$  – momentum flux

$F_N$  – normalized flux

$F_\chi$  – flux due to a trace gas  $\chi$

$K_\chi$  – turbulent exchange coefficient according to trace gas  $\chi$

$Sc_t$  – turbulent Schmidt number

$N_{O_3}$  – number density of  $O_3$

$N_{NO}$  – number density of  $NO$

$N_{NO_2}$  – number density of  $NO_2$

$S_{NO}$  –  $NO$  signal from chemiluminescence detector

$ZERO_{NET}$  – zero signal from chemiluminescence detector

**Greek symbols**

$\sigma$  – detection limit or standard deviation

$\sigma_F$  – flux relative error

$\sigma_{\psi_H}$  – error in the integrated stability parameter for sensible heat flux and trace gases

$\sigma_{u_{p^*}}$  - error in the friction velocity according to the profile method

$\sigma_{\Delta\chi}$  – error in vertical concentration difference

$\sigma_w$  – standard deviation of vertical wind velocity component

$\theta$  – potential temperature

$\Delta\theta$  – difference in potential temperature between two vertical levels

$\tau_{turb}$  – turbulence timescale

$\tau_{NO}$  – timescale of NO

$\tau_{NO_2}$  – timescale of NO<sub>2</sub>

$\tau_{O_3}$  – timescale of O<sub>3</sub>

$\tau_{chem}$  – timescale of chemistry

$\varepsilon$  – error due to the difference between two random EC fluxes

$\zeta$  – stability parameter

$\chi$  – mixing ratio of trace gas

$\delta_{i3}$  – kronecker delta

$\partial$  - partial differential

$\Psi$  – integrated stability parameter

$\kappa$  – von Kármán's constant

$\xi$  – Obukhov stability parameter

$\pi$  - pi

$\rho$  –air density

$\lambda$  – wavelength

$\lambda_{NO}$  – NO interference factor

$u_m$  – mean wind component in the horizontal direction

$v_m$  – mean wind component perpendicular to  $u$

$w_m$  – mean wind component in the vertical direction

$\tau$  – shear stress

$\phi$  – phase angle

$\psi$  – integrated stability parameter

$\psi_M$  – integrated stability parameter for momentum

$\psi_H$  – integrated stability parameter for heat flux; also applied for trace gases

$z_1$  – height of measurement level 1

$z_2$  – height of measurement level 2

$\kappa$  – kappa (=0.4)

$\Delta\chi$  – mixing ratio difference

$\chi$  – trace gas concentration

$\chi_*$  – trace gas concentration at the roughness sublayer height

$\varphi_{*M}$  – enhancement factor for momentum in the roughness sublayer

$\varphi_{*H}$  – enhancement for heat flux and trace gases in the roughness sublayer

$\varphi_M$  – stability parameter for momentum

$\varphi_H$  – stability parameter for heat and trace gases

$\varphi_Q$  – stability parameter for humidity

$\theta_*$  – potential temperature at the height of the roughness sublayer

$\infty$  – infinity

## **(Eidesstattliche) Versicherungen und Erklärungen**

### **(§5 Nr. 4 PromO)**

*Hiermit erkläre ich, dass keine Tatsachen vorliegen, die mich nach gesetzlichen Bestimmungen über die Führung akademischer Grade zur Führung eines Doktorgradess unwürdig erscheinen lassen.*

### **(§8 S. 2 Nr. 5 PromO)**

*Hiermit erkläre ich mich damit einverstanden, dass die elektronische Fassung meiner Dissertation unter Wahrung meiner Urheberrechte und des Datenschutzes einer gesonderten Überprüfung hinsichtlich der eigenständigen Anfertigung der Dissertation unterzogen werden kann.*

### **(§ 8 S. 2 Nr. 7 PromO)**

*Hiermit erkläre ich eidesstattlich, dass ich die Dissertation selbständig verfasst und keine anderen als die von mir angegebenen Quellen und Hilfsmittel benutzt habe.*

### **(§8 S. 2 Nr. 8 PromO)**

*Ich habe die Dissertation nicht bereits zur Erlangung eines akademischen Grades anderwertig eingereicht und habe auch nicht bereits diese oder eine gleichartige Doktorprüfung endgültig nicht bestanden.*

### **(§ 8 S. 2 Nr. 9 PromO)**

*Hiermit erkläre ich, dass ich keine Hilfe von gewerbliche Promotionsberatern bzw. Vermittlern in Anspruch genommen habe und auch künftig nicht nehmen werde.*

Anywhere Tsokankunku

Mainz, 23.07.2014

.....

Ort, Datum, Unterschrift